INVESTIGATIONS ON STRUCTURAL, OPTICAL AND MULTIFERROIC PROPERTIES OF MODIFIED $BiFeO_3$ CERAMICS

Thesis submitted in fulfillment of the requirements for the degree of

DOCTOR OF PHILOSOPHY

By

MANPREET KAUR

(Regn. No. 901212006)

School of Physics and Materials Science

Thapar Institute of Engineering & Technology,

Patiala -147004, Punjab, INDIA

(Declared as Deemed-to-be-University u/s of the UGC act, 1956)

December, 2017

Dedicated to
my family...

Certificate

This is to certify that the thesis entitled "***INVESTIGATIONS ON STRUCTURAL, OPTICAL AND MULTIFERROIC PROPERTIES OF MODIFIED $BiFeO_3$ CERAMICS***" in the partial fulfilment of the requirements for the award of the degree of Doctor of Philosophy in the School of Physics and Materials Science, Thapar University, Patiala is an authentic record of my own work carried out under the supervision of Dr. Poonam Uniyal. The thesis has not been submitted in part or full to any other university or institute for the award of any degree.

Manpreet kaur
(901212006)

Date: 26th Feb, 2018

This is to certify that the above statement made by the candidate is correct and true to the best of my knowledge.

Dr. Poonam Uniyal
(Associate Professor)
School of Physics and Materials Science
Thapar University
Patiala-147004 (INDIA)

Acknowledgment

I begin with the thanks to "The Almighty God" and my parents for the patience, perseverance and courage they bestowed on me in every field of life.

I would like to express my deep sense of gratitude to my mentor, Dr. Poonam Uniyal, Associate Professor, School of Physics and Materials Science, Thapar University, Patiala, for her guidance throughout the research work.

I am highly thankful to Sr. Prof. O. P. Pandey, Dean Research and Sponsored Projects, Prof. kulvir Singh and Prof. Manoj K. Sharma for proving necessary support and laboratory facilities during their tenure of Chairpersonship. I am also grateful to my doctoral committee members Dr Puneet Sharma, Dr S. D. Tiwari, Dr Bonamali Pal for their constructive suggestions, lively discussion and continuous encouragement at various stages of my research work. I want to convey my regards to all faculty members of School of Physics and Materials Science for their moral support.

My warmest thanks are due to Prof. K L Yadav, Head of Department, Department of Physics, IIT Roorkee for providing me the platform for my research work. I would like to thank, Prof. N K Verma, Dr Manoj Kumar (Assistance professor, JIIT Noida) and Dr Sachin tyagi (Scientist, CSIR-CSIO Chandigarh) for providing the necessary laboratory facilities and cooperation. I am also very grateful to Dr Piyush Kumar Patel (Assistance Professor, Vardhaman College, Bijnor) for their constant help and motivation during the research work.

I am thankful to Director of IIT Roorkee for providing FESEM and TEM facilities; especially Mr. Shiv Kumar Singh for his timely technical assistance. I am also grateful to SAI Labs, Thapar University for providing XRD facility.

I would like to thank all my friends and well wishers for their love and affections. I would like to extend my cordial thanks to the technical staff for their co-operation and departmental support during my research.

Words are not enough to express the respect and my feelings to my husband Mr Rahul Sharma and brother Mr Amritpal Singh for their unconditional love, munificence and support for me to pursue this endeavour.

Manpreet kaur

List of publications/conference/workshops

I. Papers published in SCI Journals

1) "Multiferroic and optical studies on the effects of Ba^{2+} ions in $BiFeO_3$ nanoparticles" Manpreet Kaur, K. L. Yadav, Poonam Uniyal, *J Mater Sci: Mater Electron* (2016) **27 (5)**:4475–4482.
2) "Investigation on the effect of Ti doping on dielectric, impedance and magnetic properties of Ba^{2+}-substituted $BiFeO_3$ ceramics" Manpreet Kaur, Poonam Uniyal, *J Mater Sci: Mater Electron* (2016) **27 (12)**:12539–12549.
3) "Study on Structural, Multiferroic, Optical and Photocatalytic Properties of Ferroelectromagnetic Nanoparticles: $Bi_{0.9}Ba_{0.1}Fe_{0.8}Ti_{0.2}O_3$" Manpreet Kaur, Poonam Uniyal, *J Supercond Nov Magn* (2017) **30 (2)**: 431-439.
4) "Ho^{3+} doping induced dielectric, magnetic and optical properties of $BiFeO_3$ ceramics" Manpreet Kaur, Poonam Uniyal (Under Review in *Materials of chemistry and physics*).

II. ***Papers in Non-SCI Journals***

1) "Investigations on multiferroic, optical and photocatalytic properties of lanthanum doped bismuth ferrite nanoparticles" Manpreet Kaur, K. L. Yadav, Poonam Uniyal, *Adv. Mater. Lett.* (2015) **6 (10)**:895-901.
2) "Effect of dysprosium doping on structural, dielectric and ferroelectric properties of PLZT (65/35) ceramics" Manpreet Kaur, Nandini Sharma, Poonam Uniyal, *AIP Conference Proceedings* (2016) **1536:** 1045.
3) "Synthesis and characterization of $BiFeO_3$ for photocatalytic degradation of azo dye" Manpreet Kaur, Poonam Uniyal, *AIP Conference Proceedings* (2015) **1675:** 030019.
4) "Study of phase transformation and microstructure of alcohol washed titania nanoparticles for thermal stability" Manpreet Kaur, Gaganjot Singh, Keshav Bimbraw, Poonam Uniyal, *AIP Conference Proceedings* (2015) **1675:** 030049.

III. ***Conference Presentations***

1. "Synthesis of $BiFeO_3$ at Low Temperature for Photocatalytic Applications", Manpreet Kaur, Poonam Uniyal (ICCMP-2014) Shimla-171005, Himachal Pradesh, INDIA.

IV. ***Conference***

1. 19th National Conference on Liquid Crystals (NCLC-19), Nov. 21-23, 2012, Thapar University, Patiala-147004, Punjab, INDIA.
2. International Conference on Recent Trends in Applied Physics & Material Science (RAM-2013), Feb. 1-2, 2013, Govt. College of Engineering & Technology, Bikaner-334004, Rajasthan, INDIA.
3. 58th DAE Solid State Physics Symposium (DAE-SSPS-2013), Dec. 17-21, 2013, Thapar University, Patiala-147004, Punjab, INDIA.
4. International Conference on Condensed Matter Physics 2014 (ICCMP-2014), Nov. 4-6, 2014, Himachal Pradesh University, Shimla-171005, Himachal Pradesh, INDIA.
5. 4th National Conference on Advanced Materials and Radiation Physics (AMRP-2015) March 13-14, 2015, SLIET (Deemed University), Longowal-148106, Distt. Sangrur, INDIA.

V. ***Workshop***

1. National Workshop on Advanced Techniques for Surface Characterization, Oct. 28-30, 2015, Thapar University, Patiala-147004, Punjab, INDIA.

Index

List of Figures

List of Tables

Abstract

Multiferroism is a wide and interdisciplinary area of research that has been growing explosively worldwide in past few years. Multiferroic materials are those materials having two or all primary ferroic orders, i.e. ferromagnetism, ferroelectricity, ferroelasticity much more recently ferrotoroidic, coexist in the same phase. These materials attract now considerable attention due to its applicability in fundamental research and potential devices as information storage, spintronics, magnetically modulated transducers, actuators, sensor devices, ultrafast optoelectronic devices etc. Bismuth ferrite (*BFO)* is a well known multiferroic material with Néel temperature T_N = ~ 643K, Curie temperature T_C = ~ 1103 K and coupling phenomena of various ferroic order parameters at room temperature.

BFO based ceramics doped with rare earth (La^{3+}, Ho^{3+}) and alkaline earth metal (Ba^{2+}) has been investigated for structural, morphological, dielectric, magnetic and optical properties. Subsequently, the effect of Ti^{4+} at Fe site for $Bi_{0.9}A_{0.1}Fe_{1-y}Ti_yO_3$ (A= La^{3+}, Ho^{3+}, Ba^{2+}) ceramics is studied. The present thesis is organized into five chapters:

Chapter 1 contains the general introduction to the broad area of multiferroics along with different types of multiferroic materials. A summarized review of single phase BFO with its perovskite structure, origin of ferroelectricity and magnetism are well described. Further, historical journey, literature survey on recent developments and motivation to carry out research are also highlighted.

Chapter 2 deals with the experimental part of the entire thesis work, wherein the detailed aspects of synthesis and characterization methods of pure, doped and codoped BFO nanostructures are elucidated. Thus, for synthesis process sol-gel auto combustion reaction route and for characterization, the physical principle of X-ray diffraction (XRD), Transmission electron microscopy (TEM), Field emission scanning electron microscopy (FESEM) for the investigation of structural properties, Dielectric measurement, Impedance and ferroelectric analysis for electrical properties, Vibrating samples magnetometer (VSM) for magnetic behaviour, Fourier transform infrared (FTIR) spectroscopy, UV-Visible spectrometer and Photoluminescence (PL) spectroscopy for optical studies are discussed in details.

Chapter 3 features the detailed results obtained during La^{3+}, Ho^{3+} and Ba^{2+} doping at Bi^{3+} site in BFO i.e. $Bi_{1-x}A_xFeO_3$ (A- La^{3+}, Ho^{3+} and Ba^{2+}, x=0.0, 0.1 and 0.2) ceramics. Various aspects of structural, microstructural, dielectric, electric, magnetic and optical responses for different concentrations of La^{3+}, Ho^{3+} and Ba^{2+} were examined. XRD patterns illustrate single phase formation for all modified BFO ceramics. Refined crystal structure is confirmed rhombohedral symmetry for BFO and Ba^{2+} doped nanoparticles, whereas structural phase transition from rhombohedral (*R3c*) to orthorhombic (*Pnma*) phase has been observed for $La^{3+}$and Ho^{3+} substituted nanoparticles at x=0.1. FESEM analysis has revealed the spherical shaped grains together with a grain size<0.1µm. The enhancement in dielectric behavior for $La^{3+}$and Ho^{3+} substituted ceramics with very less loss at x=0.1 is observed by analyzing dielectric measurements. The weak ferroelectric behavior of BFO with the effects of La^{3+}, Ho^{3+} and Ba^{2+} doping ions are also incorporated in this chapter. However, a large enhancement in magnetization has been observed with increasing La^{3+}, Ho^{3+} and Ba^{2+} doping concentration with maximum magnetization of 1.417 emu g^{-1} for $Bi_{0.8}Ba_{0.2}FeO_3$ ceramic. In addition to multiferroic properties, interesting optical properties along with the possible application of modified BFO ceramics are also summarized at the end of same chapter.

In the next **Chapter 4**, the effect of Titanium (Ti^{4+}) substitution at the Fe^{3+} site in modified BFO on the structural, morphological, dielectric, magnetic and optical properties were examined. XRD patterns demonstrate single phase formation of co-substituted BFO ceramics and further analyzed by Rietveld refinement. Rietveld refinement of XRD patterns demonstrated the phase transformation in Ba^{2+}-Ti^{4+} co-doped samples with tetragonal structure (*P4mm*), whereas, La^{3+}-Ti^{4+} and Ho^{3+}-Ti^{4+} substituted samples indicated the existence of orthorhombic phase (*Pnma*) for all compositions. Room temperature ferromagnetism in co-substituted BFO ceramics has been observed. The substitution of Ti^{4+} ions at Fe^{3+} site along with fixed La^{3+}/Ho^{3+}/Ba^{2+} concentration at Bi^{3+} site in BFO further improve the magnetic and dielectric properties of BFO ceramics. Optical properties of the samples are also studied, indicating their potential optical applications in visible range and can be utilized in photocatalytic decomposition of organic contaminants in the future.

Finally, **Chapter 5** summarizes the key results and conclusions obtained from the above mentioned experimental results. In addition, thesis ends with the future scope and related issues of single-site and double-site doped BFO ceramics.

LIST OF ACRONYMS & ABBREVIATIONS
(Alphabetically)

AFM	Antiferromagnetic
Ba	Barium
BFO	Bismuth Ferrite
BBFO	Barium doped Bismuth Ferrite
BHFO	Holmium doped Bismuth Ferrite
BLFO	Lanthanum doped Bismuth Ferrite
BBFTO	Barium and Titanium co-doped Bismuth Ferrite
BHFTO	Holmium and Titanium co-doped Bismuth Ferrite
BLFTO	Lanthanum and Titanium co-doped Bismuth Ferrite
CT	Charge Transfer
DM	Dzyaloshinskii-Moriya
E	Electric Field
E_a	Activation Energy
EDX	Energy Dispersive X-ray
FESEM	Field Emission Scanning Electron Microscopy
FM	Ferromagnetic
FTIR	Fourier Transforms Infrared Spectroscopy
H	Magnetic Field
H_C	Coercive Field
Ho	Holmium
ICSD	Inorganic Crystal Structure Database
K	Force Constant
L	Lanthanum
M	Magnetization
ME	Magnetoelectric
M_{max}	Maximum Magnetization
M-H	Magnetization-Magnetic Field
M_r	Remnant Magnetization
P	Polarization

P-E	Polarization-Electric Field
PL	Photoluminescence
P_{max}	Maximum Polarization
P_r	Remnant Polarization
RE	Rare earth
SAED	Selected Area Electron Diffraction
SMSS	Space Modulated Spiral Structure
T_C	Curie Temperature
TEM	Transmission Electron Microscope
Ti	Titanium
T_M	Transition Metal
T_N	Néel Temperature
VSM	Vibrating Sample Magnetometer
XRD	X-Ray Diffraction
Z	Complex Impedance
a b c	Lattice Constant
σ_{ac}	Ac Conductivity
χ	Susceptibility
λ	Wavelength
τ	Relaxation Time
t	Tolerance Factor
θ	Angle
ϵ	Microstrain
ε	Dielectric Constant
tan δ	Dissipation factor

CHAPTER I

INTRODUCTION

This chapter contains the general introduction to the broad area of multiferroics along with different types of multiferroic materials. A summarized review of single phase BFO with its perovskite structure, origin of ferroelectricity and magnetism are well described. Further, historical journey, literature survey on recent developments and motivation to carry out research are also highlighted.

Most of the new discovery is observed to be accidental. In 1820, scientist named "Hans Christian Oersted" accidently observed that a magnetic field is produced around a conducting wire when current passes through it. This outstanding event fascinated many scientists for centuries and then, in 1873, a scottish physicist "J. C. Maxwell" established the coupling between magnetic and electric interactions. After this discovery, scientists placed a great emphasis on interplay of magnetism and electricity in the category of real materials. In 1888, W. C. Röntgen **[1]** and in 1894, P. Curie **[2]** also pointed out this type of coupling in crystals.

Over the 65 years or so following W. C. Röntgen's and P. Curie's observation, L. D. Landau and E. M. Lifshitz theoretically confirmed the possibility of this coupling in one material **[3]**. Later, I. E. Dzyaloshinskii predicted theoretically **[4]** and then, in 1960, D. Astrov experimentally **[5]** proved this coupling in antiferromagnetic Cr_2O_3, which is now termed as "*LINEAR MAGNETOELECTRIC EFFECT"*.

1.1 MAGNETOELECTRIC EFFECT

According to Landau theory, the magnetoelectric effect (or say *ME* effect) is an unusual phenomenon of coupling between magnetic $\vec{H}$ and electric field $\vec{E}$ in materials **[6]**, can be written as:

$$F\left(\vec{E},\vec{H}\right) = F_0 - P_i^s E_i - M_i^s H_i - \frac{1}{2}\varepsilon_0\varepsilon_{ij} E_i E_j - \frac{1}{2}\mu_0\mu_{ij} H_i H_j - \alpha_{ij} E_i H_j - \frac{1}{2}\beta_{ijk} E_i H_j H_k - \frac{1}{2}\gamma_{ijk} H_i E_j E_k - \frac{1}{4}\delta_{ijkl} H_i H_j E_k E_l - \cdots \quad Eq.1.1$$

where F is the free energy associated with the materials. The term $\frac{1}{2}\varepsilon_0\varepsilon_{ij} E_i E_j$ describes the contribution of electrical response, where ε_{ij} corresponds to relative permittivity. The term $\frac{1}{2}\mu_0\mu_{ij} H_i H_j$ is the magnetic equivalent to $\frac{1}{2}\varepsilon_0\varepsilon_{ij} E_i E_j$, where μ_{ij} corresponds to relative permeability. The term $\alpha_{ij} E_i H_j$ elucidates linear magnetoelctric coupling via α_{ij}. The very next terms represent higher-order coefficients of magnetoelectric coupling.

Differentiation of **equation 1.1** leads to polarization expressed as

$$P_i\left(\vec{E},\vec{H}\right) = -\frac{\partial F}{\partial E_i} = P_i^s + \varepsilon_0\varepsilon_{ij} E_j + \alpha_{ij} H_j + \frac{1}{2}\beta_{ijk} H_j H_k + \gamma_{ijk} H_i E_j + \frac{1}{4}\delta_{ijkl} H_k H_j E_l \quad Eq.1.2$$

and the magnetization expressed as

$$M_i(\vec{E},\vec{H}) = -\frac{\partial F}{\partial H_i} = M_i^s + \mu_0\mu_{ij}H_j + \alpha_{ij}E_j + \beta_{ijk}H_jE_i + \frac{1}{2}\gamma_{ijk}E_jE_k + \frac{1}{4}\delta_{ijkl}H_jE_kE_l \qquad Eq.1.3$$

More than 80 compounds display *ME* effect **[6]**. The largest coefficient of magnetoelectric coupling was reported in yttrium iron garnet (*YIG*) films (~30 ps/m) **[7]**, $LiCoPO_4$ (~ 30.6 ps/m) **[8]** and $TbPO_4$ (~ 36.7 ps/m) **[9]** which is not enough strong to be used in technological *ME* devices. Unfortunately, the coefficient of linear magnetoelectric effect (α_{ij}) is limited by the following relation

$$\alpha_{ij}^2 < \varepsilon_{ii}\mu_{jj} \qquad Eq.1.4$$

Or, more rigorously

$$\alpha_{ij}^2 < \chi_{ii}^e\chi_{jj}^m \qquad Eq.1.5$$

along with the electrical (χ^e) and magnetic (χ^m) susceptibilities. According to the above mentioned **equation 1.4** and **equation 1.5** only ferroelectric and/or ferromagnetic materials can possess large *ME* coupling effect.

Astonishingly, it was observed that few materials exhibit two or more primary "ferroic" orders which can coexist even in the absence of external fields and in 1994, H. Schmid **[10]** called such materials as "*MULTIFERROICS*".

1.2 MULTIFERROICS

By definition, multiferroic materials are those materials having two or all primary ferroic orders, *i.e.* ferromagnetism, ferroelectricity, ferroelasticity. Much more recently ferrotoroidicity is also included **(Figure 1.1) [11, 12]**. The well known ferroic orderings *i.e.* ferromagnetism, ferroelectricity and ferroelasticity can be controlled via their own conjugate magnetic, electric and stress fields, respectively. Moreover, a most tempting aspect of multiferroism is their magnetoelectric (*ME*) coupling which is neither equivalent nor irrelevant to it. This leads to additional functionality of cross coupling which allows them to be tuned by external fields that are different from their own conjugates. Physicists are also investigating the feasibility of new ferroic order "ferrotoroidics" which should be adjustable by crossed magnetic and electric fields—that will likely enrich future research.

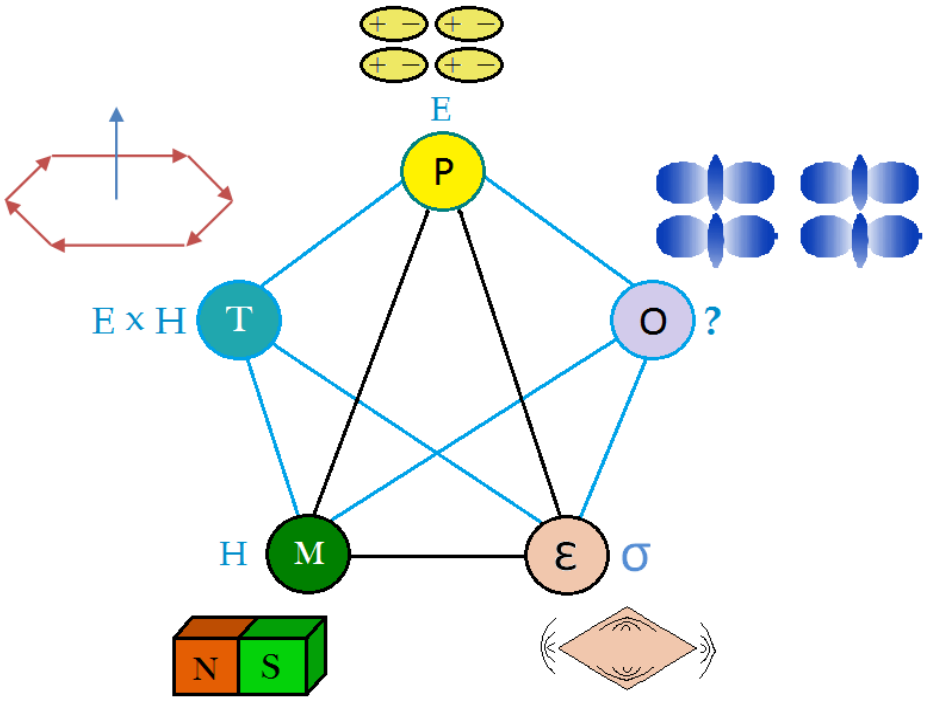

Figure 1.1 Interactions in multiferroics. (The "O" corresponds to other possibilities—such as spontaneous switchable orbital orderings, vortices, and chiralities) **[13].**

Further, multiferroics are categorized into two different types because it includes both ferroic and antiferroic ordered materials.

1.2.1 Multiferroic -Type I

Type I multiferroic materials are those materials which are capable enough to originate both ferroelectricity and magnetism independently.

a. ABO_3 perovskites

In this structural class, ferroelectric order can be originated either by a lone electron pair at A-site or by a transition metal ions at B-site which exhibits d^0 electron configuration. On the other hand, magnetism induced by partially filled d- electron shell of transition metal ions at B-site or via. rare earth ions (RE-ions) at A-site. Some common combination of compositions such as $BaTiO_3$, $BiFeO_3$, $Pb(Fe_{2/3}W_{1/3})O_3$ etc. can lead to multiferroicity in materials.

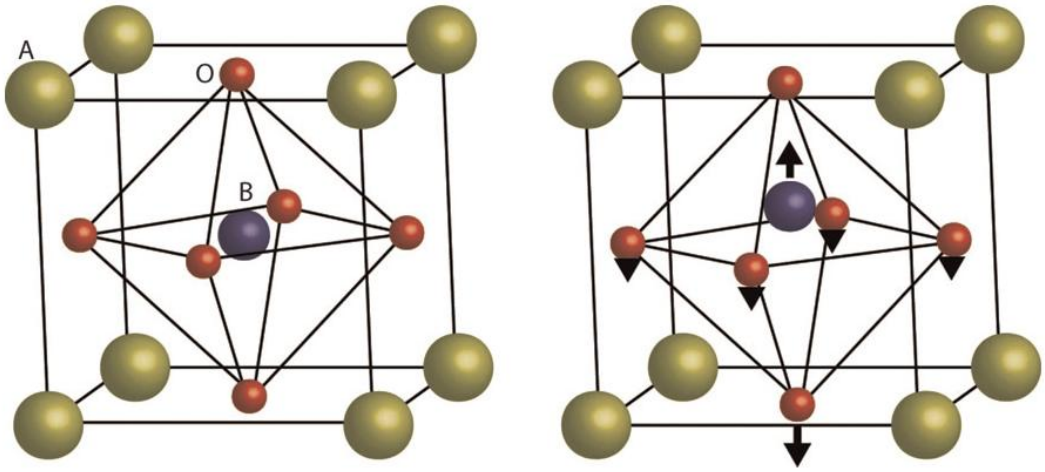

Figure 1.2 Crystal structure of a perovskite ABO_3 with a tetragonal ferroelectric distortion **[14]**.

b. $M_3B_7O_{13}X$ boracites

In boracites system, *M* and *X* corresponds to a divalent metal ions and halogen family, respectively. The multiple interatomic interactions with in the unit cell of boracites have made it difficult to figure out the actual factors causing magnetism and ferroelectric ordering in this system.

c. Organic–inorganic hybrids

Similar to ABO_3 perovskites, these materials have structure of composition ABX_3, where A is cationic organic molecule, B-site are filled with transition metal cation and X is small organic anion or halide. For Example, $((CH_3)_2NH_2)Mn(HCOO)_3$ where at A-site=$[(CH_3)_2NH_2]^+$, at B-site=Mn^{2+} and at X-site=$HCOO^-$.

d. Geometric ferroelectrics

Compositional identity of geometric ferroelectrics (*GF*) is same as that of ABO_3 perovskites such as $AMnO_3$, $RFeO_3$ etc. but the structure of these materials is completely different. For example, $AMnO_3$ contains MnO_5 triangular bipyramids sheets which are connected to AO_7 polyhedra. Therefore, ferroelectric ordering in $AMnO_3$ occurs due to the shift of A^{3+} ions within its coordination sphere whereas RE-ions at A-site or d^4 electron configuration of Mn^{3+} ions at B-site are responsible to originate magnetism.

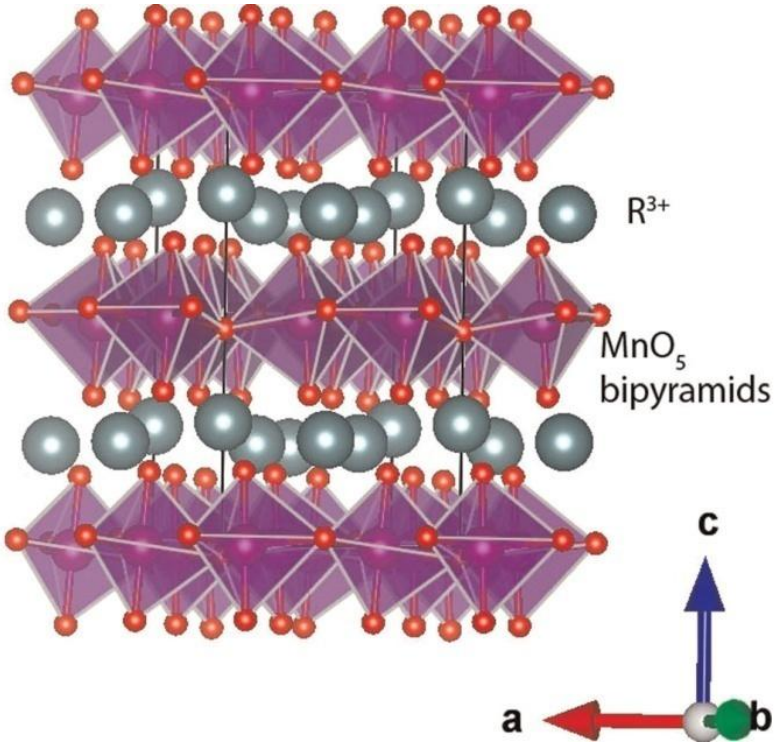

Figure 1.3 Crystal structure of a hexagonal manganite $RMnO_3$, with R a rare-earth element **[14]**.

e. Charge order

In this class of multiferroic, ferroelectric polarization is driven with inherent charge frustration. $R_{1-x}Ca_xMnO_3$ (R =RE ions) and $LuFe_2O_4$ are common charged order multiferroic materials.

1.2.2 Multiferroic -Type II

Previously, ferroelectric ordering was not expected in orthorhombic perovskites $TbMnO_3$ and $DyMnO_3$, as these compounds exhibit inversion symmetry. Type II multiferroic materials are those materials in which inversion symmetry can be broken with the help of spin order to induce improper ferroelectricity. Type II multiferroic materials are sub divided to cycloidal spin spirals ($RMnO_3$), p–d Hybridization, proper screw spin order, symmetric exchange striction and ferroaxial multiferroics ($CaMn_7O_{12}$) based upon distinct magnetoelectric coupling mechanisms. **Table 1.1** below summarizes the type of multiferroics and their mechanism that causes ferroelectricity along with relevant examples.

Table 1.1 Type of multiferroics and their mechanism that causes ferroelectricity along with relevant examples.

Type of multiferroics	Mechanism	Examples
Type I	Lone-pair effects	$BiFeO_3$, $BiMnO_3$
	Geometric frustration	$YMnO_3$
	Charge ordering	$LuFeO_4$
Type II	Magnetic ordering	$TbMnO_3$, $TbMn_2O_4$

However, the applications of multiferroic materials are still uncertain due to the two possible reasons **a.** *ME* coupling is too weak, **b.** temperatures at which *ME* coupling occur are too low. Therefore, the synthesis of new multiferroic materials is very essential. Till date, more than 100 single phased multiferroic materials were synthesized in the form of discrete composition or as solid solution/composites. Some natural occurring and synthesized multiferroic materials are summarized in **Table 1.2.**

Table 1.2 Different multiferroic materials with their structure and transition temperature.

Multiferroic materials	Crystal structure	Magnetic ion	$T_C/T_M/T_N$	Reference
$RFe_3(BO_3)_4$ (R=Gd, Tb...)	*R32*	R^{3+}	38K, 37K	[15, 16]
$Pb(B_{1/2}B'_{1/2})O_3$ (B=Fe, Mn and B′=Nb, W)	*Pm3m*	B′	385K, 143K	[17-21]
$BiFeO_3$	*R3c*	Fe^{3+}	1103K, 647K	[22-24]
$BiMnO_3$	*C2*	Mn^{3+}	750K, 105K	[25-27]
$ScMnO_3$	*H*, $P6_3cm$	Mn^{3+}	130K	[28]
$(Y,Yb)MnO_3$	*H*, $P6_3cm$	Mn^{3+}	950K, 80K	[29]
$HoMnO_3$	*H*, $P6_3cm$	Mn^{3+}	875K, 72K	[30]
$ErMnO_3$	Hexagonal (*H*)	Mn^{3+}	830K, 80K	[31]
$LuMnO_3$	*H*, $P6_3cm$	Mn^{3+}	900K, 90K	[28]
$Ca_3Co_{2-x}Mn_xO_7$	*R3c*	Co^{2+}, Mn^{4+}	16.5K, 16K	[32]
RMn_2O_5 (R= Tb, Dy,Tm...)	*Pbam*	Mn^{3+}, Mn^{4+}	38K, 43K	[33-35]
$DyFeO_3$	*Pbnm*	Fe^{3+}, Dy^{3+}	3.5K, 645K	[36]
$YCrO_3$	Monoclinic *P21*	Cr^{3+}	475K, 140K	[37]
$Bi_{0.9-x}Tb_xLa_{0.1}FeO_3$	*R3c*	Fe^{3+}	518K	[38]
$GaFeO_3$	O, *Pc21n*	Fe^{3+}	220K, 225K	[39]

$BiCrO_3$	Cubic	Cr^{3+}	440K, 114K	[40]
$Cd_{0.5}Fe_{0.5}Cr_2S_4$	FCC, *Fd3m*	Fe, Cr	137K, 137K	[41]
$Bi_xCo_{2-x}MnO_4$	Spinel, *Fd3m*	Mn	350K, 182K	[42]
$BiMn_2O_5$	Orthorhombic (O)	Mn^{2+},Mn^{3+}	35K, 39K	[43]
$Ni_3B_7O_{13}I$	-	-	64K, 64K	[44]
$Ni_3B_7O_{13}Br$	-	-	398K, 30K	[45]
$LuFe_2O_4$	$R\bar{3}m$	Fe^{2+}, Fe^{3+}	330K, 250K	[46]

The most studied and a favorable multiferroic material to date is *bismuth ferrite*.

1.3 BISMUTH FERRITE

Since 1950, Bismuth ferrite ($BiFeO_3$, or abbreviated as *BFO)* is a well known multiferroic material in which ferroelectricity exists along with anti-ferromagnetism at room temperature. In fact, BFO sets an ultimate standard for new multiferroic materials in the global search. Due to coupling phenomena of various ferroic order parameters and technological applications for magnetoelectric as well as optoelectronic devices, adequate consideration has been imparted to BFO. Nevertheless, even in BFO the *ME* coupling is quite weak. Still, it holds the future for theoretical/practical research, especially in nanoscience. It's both antiferromagnetic ordering below Néel temperature, T_N = ~643K and ferroelectric ordering with a high ferroelectric Curie temperature T_C = ~1103 K are well above room temperature.

1.3.1 STRUCTURE OF BFO

BFO acquires perovskite structure (with chemical formula; ABO_3) and not the ferrite structure, regardless of its nomenclature. BFO has six oxygen anions (O^{2-}) creating FeO_6 octahedra with Fe^{3+} ions (B-site) via chemical bonding **[47]**. Further, these FeO_6 octahedra connect to each other and the vacant spaces *i.e.* A-site between the octahedra are occupied by Bi^{3+} ions as illustrated in **Figure 1.4**. As, Bi^{3+} ions can't fill the vacant sites completely because of its smaller ionic radius, the octahedra is tilted by ~11 -14° towards [111] $_{pseudocubic}$ direction. This results into rhombohedrally distorted ABO_3-type symmetry at room temperature.

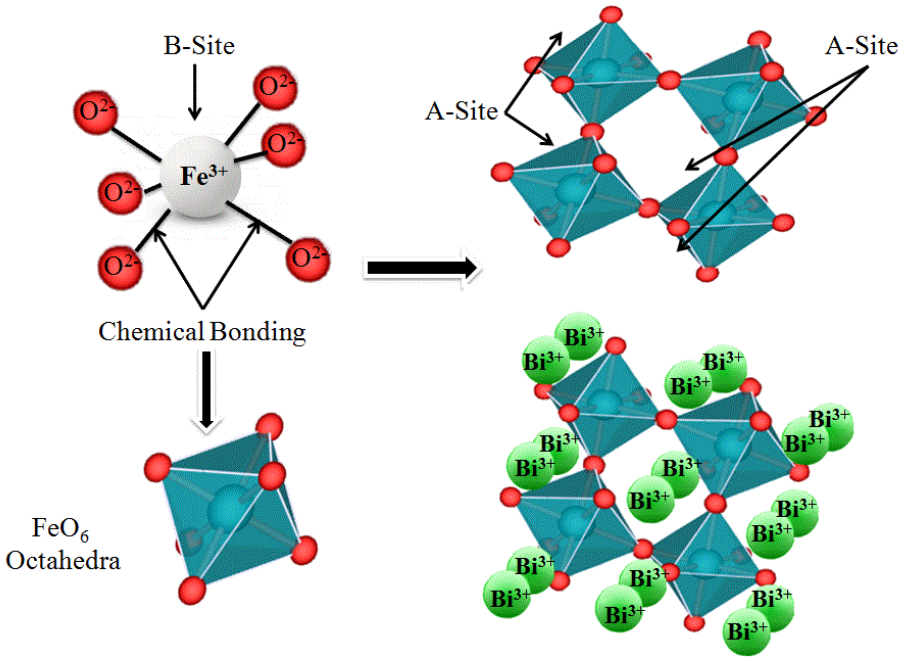

Figure 1.4 Pictorial representation of BFO crystal structure.

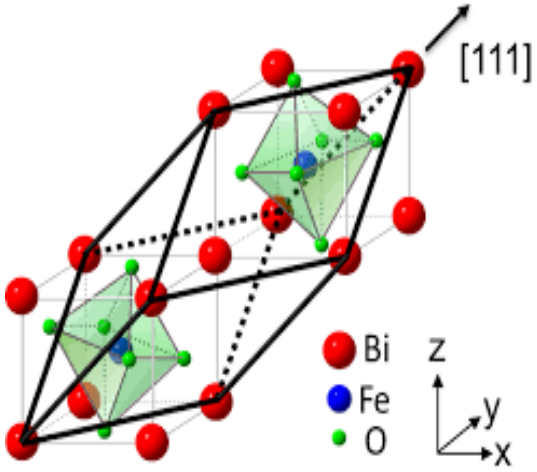

Figure 1.5 Crystal structure of BFO shows octahedral rotation along [111] axis **[48]**.

The BFO unit cell has a lattice parameter (a_{rh}) of 3.965 Å and a rhombohedral angle (α_{rh}) of approximately 89.3-89.4° along with ferroelectric polarization of ~100 μC cm^{-2} which is oriented in <111> pseudocubic axes. The ABO_3-type unit cell of BFO can also be expressed in a hexagonal frame of reference as $[001]_{hexagonal} \parallel [111]_{pseudocubic}$ and lattice parameters are $a_{hex}=b_{hex}=5.58$ Å and $c_{hex}=13.90$ Å **[49]**.

1.3.2 ORIGIN OF FERROELECTRICITY

Bi^{3+} ions at A-site play an important role in BFO perovskite to originate ferroelectricity as shown in **Figure 1.6**. Bi^{3+} ions have $6s^2$ electrons in its outer most shell and due to their reactive nature, they either make Bi $6s^2$ lone pair **[50]**, or create a covalent bond with (sp)-hybridized states (usually sp^2 or sp^3) along with neighboring oxygen anions (Bi 6sp-O 2p) **[51]**. According to the microscopic phenomenon, the particular orientation of Bi $6s^2$ lone pairs (or dangling bonds), may create local electric dipole moments, which finally gets aligned to produce ferroelectric polarization along $[111]_{pseudocubic}$ axis.

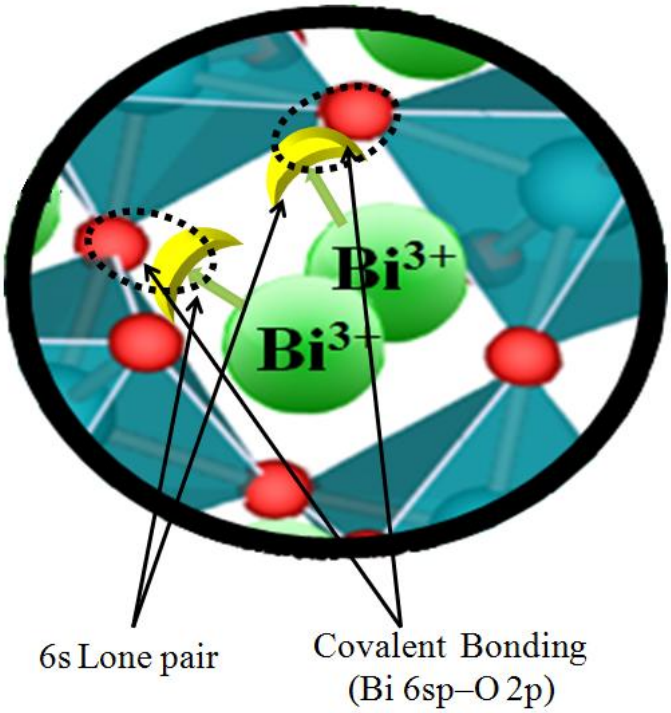

Figure 1.6 In BFO the ordering of lone pairs (yellow "lobes") of Bi^{3+} ions (green), contributes to the polarization.

This phenomenon of polarization can also be possible along eight other axis (which includes positive and negative orientations), giving rise to four structural variants as depicted in **Figure. 1.7**. Early measurements of ferroelectricity in bulk BFO yielded only small value of ferroelectric polarization ~6.1 µC cm^{-2} as reported by Teague *et al.* **[52]** in 1970.

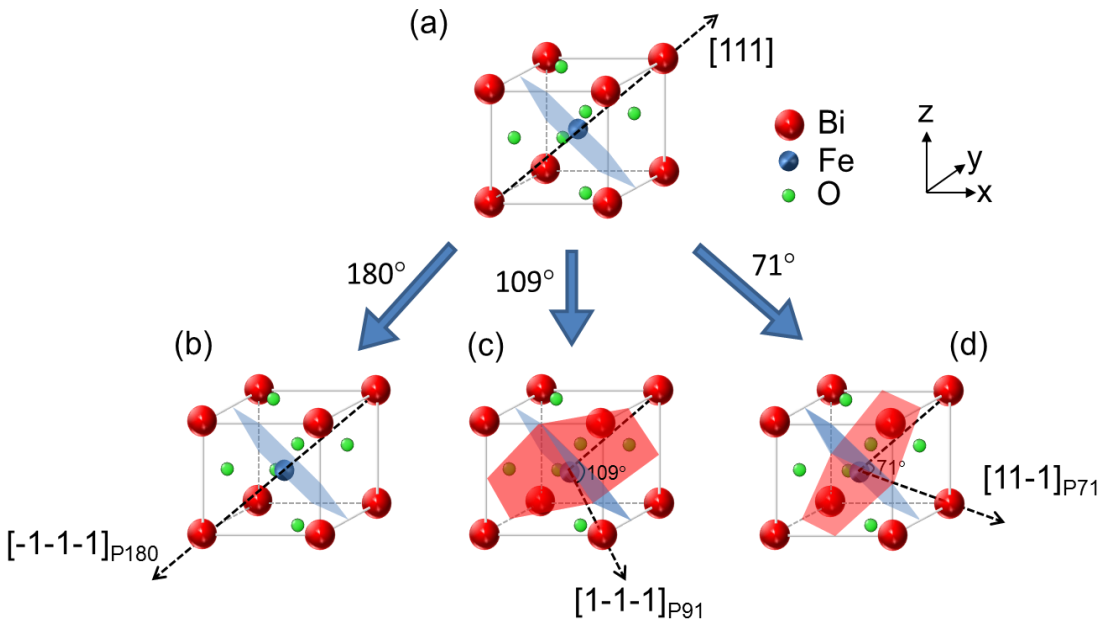

Figure 1.7 Representations of the eight possible polarization variants and three possible domain walls related to it **[48].**

1.3.3 ORIGIN OF MAGNETISM

$3d^5$-orbital of Fe^{3+} ions at B-site are responsible to induce magnetism in BFO. According to crystal field theory, the degenerate d-orbital states of Fe^{3+} ions (located at the center of FeO_6 octahedra) are split into two states, *i.e.* e_g doublet state and t_{2g} triplet state with field splitting energy of $10D_q$. Every electron of Fe^{3+} ions in 3d orbital have parallel spins generating 5 μB per Fe^{3+} ion. Moreover, the localized nature of half filled 3d-orbital is strong to create such a local magnetic moment very easily through on-site electron correlation. But, they are not that much stronger to prohibit inter-site exchange interaction. In fact, they do not hop spatially to a neighboring Fe^{3+} site and interaction can only be acquired through 2p orbital of O^{2-} anions for magnetic ordering. Partially filled 3d orbital of Fe^{3+} ion with 5 electrons creates spherical symmetry. This symmetry provides the option of interaction between magnetic moment of Fe^{3+} ion with nearby six local spins of Fe^{3+} ions through the similar exchange integral, that is, G-type antiferromagnetic **[53, 54]**. On the other hand, the dominant exchange interaction is produced between neighboring half filled e_g orbitals via 2p σ-bonding of O^{2-} anions. Consequently, t_{2g} state allows for antiferromagnetic spin arrangement between the adjacent planes. The exhibited antiferromagnetic spins are not completely antiparallel because of the feeble canting moment caused by local magnetoelectric coupling. Overlay on this canting, though, is also a long-range

spin structure consisting of a spiral modulated spin structure (SMSS) of the antiferromagnetically ordered sub lattices. The spin cycloid has an extended repetitive distance of approximately 620 Å with propagation vector along [110] axis (**Figure 1.8**). In 1982, the existence of a spiral modulated spin structure in BFO was first experimentally predicted by Sosnovska *et al.* **[55]** and later its theoretical interpretation was proposed in 1995 **[56]**.

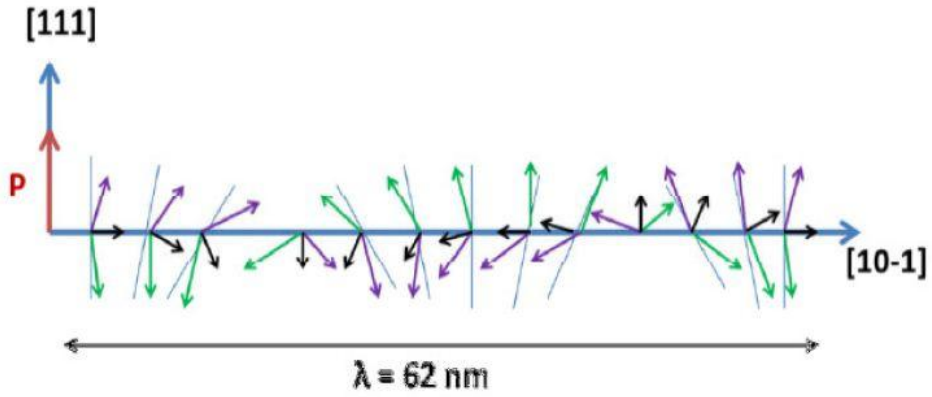

Figure 1.8 G-type antiferromagnetic order with weak ferromagnetic moment superimposed by a spiral spins cycloidal modulation **[57]**.

1.4 LITERATURE REVIEW

BFO was first synthesized by Royen *et al.* 1957 **[58]**. Prior to describing its unique aspects, it would be great to explore the historical journey of BFO, which can be separated into two eras as follows:

Historical era (1957-2003)

In this frame of time, investigation on BFO was just nominal due to lack of its structural knowledge, difficulty in synthesis as well as various ambiguities in its properties. However, in 1960, Filepev *et al.* **[59]** showed that BFO possesses the perovskite structure which then triggered the vigorous experimental and theoretical/computational research on BFO. Then after, numerous features for BFO were discovered like antiferromagnetic G-type ordering below T_N (Kiselev *et al.* 1963 **[60]**), ferromagnetic ordering (Teague *et al.* 1970 **[52]**), spiral modulated spin structure (SMSS) in BFO (Sosnowska *et al*. 1982 **[55]**), quadratic magnetoelectric effect (Tabares-Munoz *et al*. 1985 **[61]**; Murashov *et al*. 1990 **[62]**) etc. Meanwhile Smolenskii *et al.* **[55]** pioneered the investigation on BFO, but was appearing to be in vain due to its highly

conducting nature. Again they tried to overcome the conductivity problem by adopting various techniques, but no technological device applications were obtained.

Revival era (2003-2017)

The research on BFO got high momentum when surprisingly large remnant polarization (~55μC/cm^2, approx. 15 times larger) along with a large ferromagnetism (~1.0 μ_B /unit cell) reported by Ramesh *et al.* in 2003 **[63]**. A huge amount of investigation has been done on BFO throughout the world after 2003 which opens an avenue to study the host BFO for various functional device applications in information storage, spintronics, actuators, sensors, etc. Even though, BFO exhibits room temperature multi-functionality, yet its low resistivity, large loss factor, weak remnant magnetization and low-magnetoelectric coupling obstruct its use in the devices. Scientists in India, UK, USA, Germany, France, South Korea, Russia, China and Japan have been working ceaselessly to improve the quality of BFO. Consequently, variety of synthesis techniques and numerous doping strategies at A-site, B-site and A- B- site simultaneously have been employed to enhance its magnetoelectric properties. These are described below:

i) Adopting various synthesizing techniques to obtain single phase BFO ceramics without any impurity phase.

Conventional solid state reaction technique was most common and widely used method as it was simple, economical and suitable for mass-production. However, its slow kinetic rate leads to more impurities *i.e.* $Bi_2Fe_4O_9$ and $Bi_{25}FeO_{40}$, leaky ferroelectric hysteresis loops and loss of stoichiometric. On the other hand, rapid liquid sintering provides acceptable results, but this technique was limited by the synthesis temperature gap. Wang *et al.* **[64]** synthesized $BiFeO_3$ ceramics by conventional solid state reaction technique followed by rapid liquid phase sintering. A saturated ferroelectric hysteresis loop has been observed for these ceramics at room temperature. The spontaneous polarization of 8.9 μC cm^{-2}, remnant polarization of 4.0 μC cm^{-2} and coercive field of 39 kV cm^{-1} was obtained under an applied field of 100 kV cm^{-1}. Kolte *et al.* **[65]** reported that the nanocrystalline $BiFeO_3$ prepared by microwave sintering technique shows much higher resistivity (~1.8 GΩ-cm) as compared to BFO prepared by conventional solid state route.

The fine powder of BFO with improved homogeneity, high densifications and purity was obtained by wet chemical methods (e.g. sol–gel method, the hydrothermal method and the co-precipitation method). Xu *et al.* **[66]** obtained homogenous and pure phase BFO nanopowders synthesized via a simple sol gel technique. Hou *et al.* **[67]** investigated the effect of external magnetic field on magnetic behavior and morphology of BFO particles prepared by hydrothermal method. High magnetic fields of 4T, 8T and 12T greatly affected the grain growth of $BiFeO_3$ and changed the morphology from regular cube→irregular sphere→chain like structure with increasing magnetic field. Moreover, auto-combustion method was a novel and cost-efficient approach for the formation of nanostructured materials, ceramics and composites for advanced device applications. Hengky *et al.* **[68]** synthesized the nanostructures of BFO via sol gel auto combustion method and reported the effect of fuel concentration, calcination temperature and duration on the phase formation of BFO.

ii) Chemical substitution for A- and B- site, *i.e.* Bi^{3+} and Fe^{3+}

Bi^{3+} ions at A-site play a significant role in ferroelectricity, whereas $3d^5$-orbital of Fe^{3+} ions at B-site are responsible to induce magnetism in BFO. A partial ionic substitution to $Bi_{1-x}A_xFeO_3$ (A is a lanthanide ion, alkali earth metal or lead) and $BiFe_{1-x}M_xO_3$ (M is, typically, another 3d transition metal) alters the dielectric, ferroelectric and magnetic properties of BFO. In literature, more or less every possible combination has been tried.

a) Common ions substitution at A-site (*i.e.* Bi^{3+}- site) in BFO as follows:

Table 1.3 List of ions substitution at A-site (*i.e.* Bi^{3+}- site) in BFO.

Subvalent (2^+)	**Isovalent (3^+)**	**Supervalent (4^+,5^+)**	**References**
Ca, Sr, Ba, Pb, Cd, Mg	Nd, La, Ho, Gd, Eu, Sm, Tb, Dy, Y	Ce, Pr	**69-73**

- Song *et al.* **[69]** studied the effect of Ho^{3+} doped in $BiFeO_3$ and found that Ho^{3+} act as sintering aid as well as promote the densification of $Bi_{0.95}Ho_{0.05}FeO_3$ and $Bi_{0.9}Ho_{0.1}FeO_3$ samples. The observed value of P_r and M_r was 23 and 35 times as high for $Bi_{0.9}Ho_{0.1}FeO_3$ as that of BFO, respectively.

- Phase transformation of rhombohedral→orthorhombic for 20 mol% of La^{3+} substitution and orthorhombic→tetragonal for 30 mol% of La^{3+} substitution in BFO has been observed by Cheng *et al.* **[70]**. The La doping ions also significantly reduce electric leakage as well as enhanced the ferromagnetic moment of the samples due to the broken cycloid spin structure.
- Ting *et al.* **[71]** synthesized the 5 mol%, 10 mol% and 15 mol% Ba^{2+} substituted BFO ceramics and observed the structural transformation from low-symmetry rhombohedral → to high-symmetry pseudocubic phase. Enhanced magnetization was observed in 15 mol% Ba^{2+} doped BFO ceramics.
- Sati *et al.* **[72]** investigated the effect of Dy on the magnetic as well as the optical properties of BFO ceramics. Maximum remnant magnetization of 0.2103 emu/g has been reported for 12 mol% of Dy substitution in BFO system. Whereas, the value of the energy band gap was observed to decrease from ~2.25eV to 2.09 eV with the doping of Dy content.
- Multiferroic behavior of $Bi_{0.8}A_{0.2}FeO_3$ ceramics as a function of A= Ca, Sr, Pb doping has been reported by Khomchenko *et al.* **[73]**. The value of conductivity was observed to increase with the substitution of Ca and Sr. It has also been observed that Ca and Sr-doping reproduced the antiferromagnetic behavior in ceramics, whereas, with the Pb-substitution, onset of a weak ferromagnetism was obtained.

b) Common ions substitution at B-site (*i.e.* Fe^{3+}-site) in BFO as follows:

Table 1.4 List of ions substitution at B-site (*i.e.* Fe^{3+}-site) in BFO.

Subvalent (2^+)	**Isovalent (3^+)**	**Supervalent (4^+,5^+)**	**References**
Ga, Zn	Co, Cr, Ni, Sc	Ti, Zr, V, Mn, Nb, Ta	**74-78**

- Bernardo *et al.* **[74]** prepared the $BiFeO_3$ and $BiFe_{0.95}Ti_{0.05}O_3$ nominal composition and found that with the substitution of Ti grain size of the samples decreased. The high resistivity of ~$10^{11}\Omega$ cm and ferromagnetic behavior was reported for this sample.

- Rao *et al.* **[75]** used conventional solid state reaction method to prepare the Sc doped compounds with composition $BiFe_{1-x}Sc_xO_3$ where x=0.0, 0.05, 0.1, 0.15. It was reported that the ac conductivity of the prepared compounds decreases with the addition of Sc content. The suppressed anomaly in dielectric data has also been observed at 220 °C with Sc substitution.
- Layek *et al.* **[76]** studied the magnetic behavior of $BiFe_{1-x}Cr_xO_3$ (x = 0.0, 0.05 and 0.1) nanoparticles. On increasing the amount of Cr, rhombohedral phase was evident with average particle size around 40 nm for 10 mol% Cr-doped $BiFeO_3$ nanoparticles. It has also been reported that the values of magnetization and coercive field increases with the addition of 10 mol% Cr ions.
- Xu *et al.* **[77]** studied the effect of divalent Mg^{2+} ions doped $BiFeO_3$ and found that the compositions obtained are simultaneously ferromagnetic and super-paramagnetic at room temperature.
- Kumar *et al.* **[78]** reported the room temperature magnetoelectric coupling effect in $BiFe_{0.75}Ti_{0.25}O_3$ ceramics. The electrical resistivity was observed to be ~$5.5x10^{10}$ Ω cm with enhanced dielectric behavior in $BiFe_{0.75}Ti_{0.25}O_3$ ceramics.

c) Co-substitution at A- and B-site in BFO simultaneously as follows **[79-89]**:

Table 1.5 List of ions substitution at A- and B-site in BFO simultaneously.

Doping at A-site	***Doping at B-site***	***Doping at A-site***	***Doping at B-site***
La, Pr	-	La	Nb
La, Nd	-	Ba	Gd
Pb	Ti	-	Co, Ta
La	Tb	Pr	Sc
La	Ti	La	Mn
Ba	Mn	Sm	Ti
Pr, Ba	-	Ca, Sr, Pb	-
Nd	Ti	Ba	Ti

- Kumar *et al.* **[79]** synthesized the $Bi_{1-x}La_xFe_{1-x}Ti_xO_3$ with x = 0.000-0.250 via tartaric acid modified sol–gel technique. Doping of La and Ti in $BiFeO_3$ makes the phase transformation from rhombohedral (*R3c*) to orthorhombic (*Pnma*). This phase transformation enhance the dielectric constant with less value of *tanδ* (0.03) and reduces M_S, M_r and H_C of the samples for more than 10 mol% of La and Ti co-substitution.
- As reported by Reetu *et al.* **[80]** the doping of Ti at B-site in $Bi_{0.8}La_{0.2}Fe_{1-x}Ti_xO_3$ maintains the rhombohedral symmetry upto 5 mol% and transformed to tetragonal for 10 mol% and 15 mol% substitution. The high resistivity and remnant magnetization was found in 10 mol% Ti and 15 mol% Ti samples.
- He *et al.* **[81]** investigated the effect of Pr and Mg co-substitution in $BiFeO_3$ nanoparticles and found that Pr and Mg effectively reduce the leakage current and enhanced the dielectric properties of $BiFeO_3$ samples. The observed magnetization was five-fold higher in magnitude for $Bi_{0.95}Pr_{0.03}Mg_{0.02}FeO_3$ ceramics with simultaneously improved electrical properties than $BiFeO_3$.
- Manjunath *et al.* **[82]** synthesized $Bi_{1-x}Ca_xFe_{1-x}Mn_xO_3$ ($0 \leq x \leq 0.4$) ceramics with different average grain sizes via conventional solid state reaction method. It was observed that the room temperature magnetization increases with increasing Ca and Mn substitution, showing weak ferromagnetism. The $Bi_{1-x}Ca_xFe_{1-x}Mn_xO_3$ samples represented maximum dielectric values in the mixed *R3c*→*Pbnm* phase region.
- Karthik *et al.* **[83]** studied the A-site lattice disorder effect due to the variance between RE^{3+} cation (Gd^{3+}, Tb^{3+}, Dy^{3+}) and Bi^{3+} cation and its multiferroic behavior. Doping of 10 mol% RE^{3+} -ion allows the coexistence of orthorhombic Bragg's reflection along with rhombohedral phase. Also, the slight red shift in the position of d-d transition band was observed with the substitution of RE^{3+} -ions. Moreover, the decrease in T_N was also observed upon addition of RE^{3+} -ions.
- It has been reported by Mao *et al.* **[84]** that the grain size of $BiFeO_3$ nanoparticles decrease with the doping of Dy and Cr co-doping (*i.e.* 71.14 nm for BFO and 69.31 nm for $Bi_{0.95}Dy_{0.05}Fe_{0.95}Cr_{0.05}O_3$), and it greatly enhanced the magnetic and ferroelectric properties for device applications.
- Ahmmad *et al.* **[85]** investigated the effect of Ba and Ti co-doped $BiFeO_3$ materials prepared by ultrasonication method. The maximum leakage current density was reported

for $Bi_{0.7}Ba_{0.3}Fe_{0.9}Ti_{0.1}O_3$ material after ultrasonication of 60 minutes. It was also observed that the net value of magnetization of co-doped material reduces than that of undoped material.

- Ramachandran *et al.* **[86]** prepared calcium and barium doped polycrystalline $BiFeO_3$ via an ethanol mediated sol-gel route. They obtained significantly reduced grain sizes (~200-500 nm) for doped samples as compared to that of BFO (~10-20 µm). It was also observed that the transition temperature shift towards higher temperatures with the substitution of Ca^{2+} and Ba^{2+}-Ca^{2+} ions in BFO.
- The codoping effect of Y and Zr for $Bi_{1-x}Y_xFe_{1-y}Zr_yO_3$ ceramics with x=0.05, 0.1, 0.15, and y=0.05 has been carried out by Xu *et al.* **[87]**. Enhancement in dielectric and ferroelectric properties has been reported in Y and Zr co-doped samples due to the reduction of oxygen vacancies. The double hysteresis loop-like M-H curve with a significantly enhanced remnant magnetization of 0.4149 emu/g was found in $Bi_{0.85}Y_{0.15}Fe_{0.95}Zr_{0.05}O_3$ sample.
- Xu *et al.* **[88]** studied the abnormal variation of band gap for $Bi_{0.9}La_{0.1}FeO_3$ and $Bi_{0.9}La_{0.1}Fe_{0.99}Zn_{0.01}O_3$ nanoparticles. The X-ray photoelectron spectra revealed that the addition of Zn increases the oxygen vacancies, which could contribute to the enhancement of leakage current density. The energy band gap was also found to increase from 2.13(84) eV to 2.17(26) eV with the substitution of Zn.
- Priyadharsini *et al.* **[89]** reported the enhanced multiferroic behavior in La and Ce co-substituted $BiFeO_3$ nanoparticles. They found that $Bi_{0.9}La_{0.075}Ce_{0.025}FeO_3$ sample exhibit superior P–E loop along with the enhanced remnant polarization equal to 3.169 µC/cm^2. The observed value of ac conductivity was several orders lesser in magnitude than undoped BFO ceramics.

1.5 Motivation

On the basis of above discussion, it has been found that A-site, B-site and A- B-site substitution is very fascinating and well studied. Even a minute substitution at A-site of BFO increases magnetocrystalline anisotropy, as a result, making cycloidal spin spiral structure energetically unfavorable. However, B-site substitution greatly enhanced the magnetization in nano multiferroic BFO ceramics. But, a large loss tangent associated with BFO still degrades its

dielectric and magnetic properties, and therefore, it is necessary to synthesize new ceramics in nano range that have very low tangent loss. It is also important to study the systematic variation in dielectric and magnetic properties of doped and co-doped BFO ceramics in the wide composition range. Therefore, the following objectives were framed and have been achieved.

- To synthesize and characterize $Bi_{1-x}A_xFeO_3$ (A: Ba, La, Ho; $0<x<0.2$) ceramics.
- To investigate the effect of Ti doping at Fe site for $Bi_{0.9}A_{0.1}Fe_{1-y}Ti_yO_3$ ($0<y<0.2$) ceramics.
- To investigate the variation of the dielectric properties (dielectric constant and dielectric loss) with temperature and frequency. Also to measure the ferroelectric, magnetic and optical properties at room temperature.

References

1. Röntgen W. C., *Annalen Der Physik*, (1888), *271*(10), 264-270.
2. Curie P., *Journal De Physique*, (1894), 3, 393-415.
3. Landau L. D., Lifshits E. M., Electrodynamics of continuous media, Fizmatgiz, Moscow, (1959).
4. Dzyaloshinskii I. E., *Soviet Physics Jetp-Ussr*, (1960), *10*(3), 628-629.
5. Astrov D. N., *Soviet Physics, JETP*, (1960), *11*(3), 708-709.
6. Fiebig M., *Journal of Physics D: Applied Physics*, (2005), *38*(8), R123-R152.
7. Krichevtsov B. B., Pavlov V. V., Pisarev R. V., *JETP Letters*, (1989), *49*(8), 535-539.
8. Rivera J. P., *Ferroelectrics*, (1994), *161*(1), 147-164.
9. Rado G. T., Ferrari J. M., Maisch W. G., *Physical Review B*, (1984), *29*(7), 4041-4048.
10. Schmid H., *Ferroelectrics*, (1994), *162*(1), 317-338.
11. Eerenstein W., Mathur N. D., Scott J. F., *Nature*, (2006), *442*(7104), 759-765.
12. Khomskii D. I., *Journal of Magnetism and Magnetic Materials*, (2006), *306*(1), 1-8.
13. Spaldin N. A., *MRS Bulletin*, (2017), *42*(5), 385-390.
14. Buurma A. J. C., Blake G. R., Palstra T. T. M., Adem U., Reference Module in Materials Science and Materials Engineering, from Encyclopedia of Materials: Science and Technology (Second Edition), (2006), 1-7.

15. Gavriliuk A. G. E., Kharlamova S. A., Lyubutin I. S. E., Troyan I. A., Ovchinnikov S. G. E., Potseluiko A. M., Eremets M. I., Boehler R., *JETP Letters*, (2004), *80*(6), 426-432.
16. Mo H., Nelson C. S., Bezmaternykh L. N., Temerov V. T., *Physical Review B*, (2008), *78*(21), 214407(1-9).
17. Venevtsev Y. N., Gagulin V. V., *Ferroelectrics*, (1994), *162*(1), 23-31.
18. Smolenskii G. A., Agranovskaya A. I., Isupov V. A., *Soviet Physics-Solid State*, 1(6), (1959), 907-908.
19. Bokov V. A., Mylnikova I. E., Smolenskii G. A., *Soviet Physics JETP-Ussr*, (1962), *15*(2), 447-449.
20. Yan L., Li J., Viehland D., *Journal of Applied Physics*, (2007), *101*(10), 104107(1-5).
21. Yang Y., Liu J. M., Huang H. B., Zou W. Q., Bao P., Liu Z. G., *Physical Review B*, (2004), *70*(13), 132101(1-4).
22. Wang Y. P., Zhou L., Zhang M. F., Chen X. Y., Liu J. M., Liu Z. G., *Applied Physics Letters*, (2004), *84*(10), 1731-1733.
23. Zhang S. T., Lu M. H., Wu D., Chen Y. F., Ming N. B., *Applied Physics Letters*, (2005), *87*(26), 262907(1-3).
24. Yuan G. L., Or S. W., Chan H. L. W., Liu Z. G., *Journal of Applied Physics*, (2007), *101*(2), 024106(1-4).
25. Atou T., Chiba H., Ohoyama K., Yamaguchi Y., Syono Y., *Journal of Solid State Chemistry*, (1999), *145*(2), 639-642.
26. Dos Santos A. M., Cheetham A. K., Atou T., Syono Y., Yamaguchi Y., Ohoyama K., Chiba H., Rao C. N. R., *Physical Review B*, (2002), *66*(6), 064425(1-4).
27. Son J. Y., Shin Y. H., *Applied Physics Letters*, (2008), *93*(6), 062902(1-3).
28. Tomuta D. G., Ramakrishnan S., Nieuwenhuys G. J., Mydosh J. A., *Journal of Physics: Condensed Matter*, (2001), *13*(20), 4543-4552.
29. Filippetti A., Hill N. A., *Journal of Magnetism and Magnetic Materials*, (2001), *236*(1), 176-189.
30. Dela Cruz C., Yen F., Lorenz B., Wang Y. Q., Sun Y. Y., Gospodinov M. M., Chu C. W., *Physical Review B*, (2005), *71*(6), 060407(1-4).
31. Vermette J., Jandl S., Gospodinov M. M., *Journal of Physics: Condensed Matter*, (2008), *20*(42), 425219(1-5).

32. Choi Y. J., Yi H. T., Lee S., Huang Q., Kiryukhin V., Cheong S. W., *Physical Review Letters*, (2008), *100*(4), 047601(1-4).
33. Harris A. B., Kenzelmann M., Aharony A., Entin-Wohlman O., *Physical Review B*, (2008), *78*(1), 014407(1-15).
34. Kobayashi S., Kimura H., Noda Y., Kohn K., *Journal of the Physical Society of Japan*, (2005), *74*(1), 468-472.
35. Moskvin A. S., Pisarev R. V., *Physical Review B*, (2008), *77*(6), 060102(1-4).
36. Tokunaga Y., Iguchi S., Arima T., Tokura Y., *Physical Review Letters*, (2008), *101*(9), 097205(1-4).
37. Ramesha K., Llobet A., Proffen T., Serrao C. R., Rao C. N. R., *Journal of Physics: Condensed Matter*, (2007), *19*(10), 102202(1-8).
38. Palkar V. R., Kundaliya D. C., Malik S. K., Bhattacharya S., *Physical Review B*, (2004), *69*(21), 212102(1-3).
39. Sun Z. H., Cheng B. L., Dai S., Cao L. Z., Zhou Y. L., Jin K. J., Chen Z. H., Yang G. Z., *Journal of Physics D: Applied Physics*, (2006), *39*(12), 2481-2484.
40. Zheng Y., Wang B., Woo C. H., *Applied Physics Letters*, (2006), *89*(6), 062904(1-3).
41. Yan L. Q., Sun Z. H., Peng X. D., Luo W. J., He L. H., Wang F. W., *Journal of Physics D: Applied Physics*, (2007), *40*(10), 3239-3242.
42. Rajeevan N. E., Pradyumnan P. P., Kumar R., Shukla D. K., Kumar S., Singh A. K., Patnaik S., Arora S. K., Shvets, I. V., *Applied Physics Letters*, (2008), *92*(10), 102910(1-3).
43. Shukla D. K., Mollah S., Kumar R., Thakur P., Chae K. H., Choi W. K., Banerjee A. *Journal of Applied Physics*, (2008), *104*(3), 033707(1-10).
44. Smolenskii G. A., Agranovskaia A. I., Popov S. N., Isupov V. A., *Soviet Physics-Technical Physics*, (1958), *3*, 1981-1982.
45. Smolenskiĭ G. A., Chupis I. E., *Soviet Physics Uspekhi*, (1982), *25*(7), 475-493.
46. Zhang Y., Yang H. X., Ma C., Tian H. F., Li J. Q., *Physical Review Letters*, (2007), *98*(24), 247602(1-4).
47. Yang C. H., Kan D., Takeuchi I., Nagarajan V., Seidel J., *Physical Chemistry Chemical Physics*, (2012), *14*(46), 15953-15962.
48. Naganuma H., *In Ferroelectrics-Physical Effects*. InTech., (2011).

49. Catalan G., Scott J. F., *Advanced Materials*, (2009), *21*(24), 2463-2485.
50. Shishidou T., Mikamo N., Uratani Y., Ishii F., Oguchi T., *Journal of Physics: Condensed Matter*, (2004), *16*(48), S5677-S5683.
51. Seshadri R., Hill N. A., *Chemistry of Materials*, (2001), *13*(9), 2892-2899.
52. Teague J. R., Gerson R., James W. J., *Solid State Communications*, (1970), *8*(13), 1073-1074.
53. Anderson P. W., *Physical Review*, (1950), *79*(2), 350-356.
54. Goodenough J. B., Magnetism and the Chemical Bond, John Wiley & Sons, New York, London, 1963.
55. Sosnowska I., Neumaier T. P., Steichele E., *Journal of Physics C: Solid State Physics*, (1982), *15*(23), 4835-4846.
56. Sosnowska I., Zvezdin A. K., *Journal of Magnetism and Magnetic Materials*, (1995), *140*, 167-168.
57. Lebeugle D., Colson D., Forget A., Viret M., Bataille A. M., Gukasov A., *Physical Review Letters*, (2008), *100*(22), 227602(1-4).
58. Royen P., Swars K., *Angewandte Chemie*, (1957), *69*(24), 779-779.
59. Filip'ev V. S., Smolyaninov N. P., Fesenko E. G., Belyaev I. N., *Kristullograjiya*, (1960), 5, 958-960.
60. Kiselev S. V., Ozerov R. P., Zhdanov G. S., *In Soviet Physics Doklady*, (1963), 7, 742-753.
61. Tabares-Muñoz C., Rivera J. P., Bezinges A., Monnier A., Schmid H., *Japanese Journal of Applied Physics*, (1985), *24*(S2), 1051-1053.
62. Murashov W. A., Rakov D. N., Dubienko I. S., Zvezdin A. K., Ionov W. M., *Krystalografia*, (1990), *35*, 912-917.
63. Wang J. B. N. J., Neaton J. B., Zheng H., Nagarajan V., Ogale S. B., Liu B., Viehland D., Vaithyanathan V., Schlom D. G., Waghmare U. V., Spaldin N. A., *Science*, (2003), *299*(5613), 1719-1722.
64. Wang Y. P., Zhou L., Zhang M. F., Chen X. Y., Liu J. M., Liu Z. G., *Applied Physics Letters*, (2004), *84*(10), 1731-1733.
65. Kolte J., Salame P. H., Daryapurkar A. S., Gopalan P., *AIP Advances*, (2015), *5*(9), 097164(1-11).

66. Xu J. H., Ke H., Jia D. C., Wang W., Zhou Y., *Journal of Alloys and Compounds*, (2009), *472*(1), 473-477.
67. Hou L., Zuo K. H., Sun Q. B., Ren Z. M., Zeng Y. P., Li X., *Applied Physics Letters*, (2013), *102*(8), 082901(1-4).
68. Hengky C., Dunn S., Singh V., Loh L., *NSTI-Nanotech.*, (2010), *1*, 570-573.
69. Song G. L., Song Y. C., Su J., Song X. H., Zhang N., Wang T. X., Chang F. G., *Journal of Alloys and Compounds*, (2017), *696*, 503-509.
70. Cheng Z. X., Li A. H., Wang X. L., Dou S. X., Ozawa K., Kimura H., Zhang S. J., Shrout T. R., *Journal of Applied Physics*, (2008), *103*(7), 07E507(1-3).
71. Ting Y., Tu C. S., Chen P. Y., Chen C. S., Anthoniappen J., Schmidt V. H., Lee J. M., Chan T. S., Chen W. Y., Song R. W., *Journal of Materials Science*, (2017), *52*(1), 581-594.
72. Sati P. C., Arora M., Chauhan S., Kumar M., Chhoker S., *Journal of Physics and Chemistry of Solids*, (2014), *75*(1), 105-108.
73. Khomchenko V. A., Kiselev D. A., Vieira J. M., Kholkin A. L., Sá M. A., Pogorelov Y. G., *Applied Physics Letters*, (2007), *90*(24), 242901(1-3).
74. Bernardo M. S., Jardiel T., Peiteado M., Mompean F. J., Garcia-Hernandez M., Garcia M. A., Villegas M., Caballero A. C., *Chemistry of Materials*, (2013), *25*(9), 1533-1541.
75. Rao T. D., Kumari A., Niranjan M. K., Asthana S., *Physica B: Condensed Matter*, (2014), *448*, 267-272.
76. Layek S., Saha S., Verma H. C., *AIP Advances*, (2013), *3*(3), 032140(1-9).
77. Xu J., Xie D., Teng C., Zhang X., Zhang C., Sun Y., Ren T. L., Zeng M., Gao X., Zhao Y., *Journal of Applied Physics*, (2015), *117*(22), 224101(1-6).
78. Kumar M., Yadav K. L., *Journal of Applied Physics*, (2006), *100*(7), 074111(1-4).
79. Kumar P., Panda C., Kar M., *Smart Materials and Structures*, (2015), *24*(4), 045028(1-12).
80. Reetu, Agarwal A., Sanghi S., Ahlawat N., *Journal of Physics D: Applied Physics*, (2012), *45*(16), 165001(1-9).
81. He P., Hou Z. L., Wang C. Y., Li Z. J., Jing J., Bi S., *Ceramics International*, (2017), *43*(1), 262-267.

82. Manjunath B., Thakuria P., Joy P. A., *Materials Research Express*, (2017), *4*(1), 016104(1-13).
83. Rao T. D., Karthik T., Srinivas A., Asthana S., *Solid State Communication*, (2012), 152(23), 2071-2077.
84. Mao W., Wang X., Chu L., Zhu Y., Wang Q., Zhang J., Yang J., Li X. A., Huang W., *Physical Chemistry Chemical Physics*, (2016), *18*(9), 6399-6405.
85. Ahmmad B., Kanomata K., Koike K., Kubota S., Kato H., Hirose F., Billah A., Jalil M. A., Basith M. A., *Journal of Physics D: Applied Physics*, (2016), *49*(26), 265003(1-8).
86. Ramachandran B., Dixit A., Naik R., Lawes G., Ramachandra Rao M. S., *Journal of Applied Physics*, (2012), *111*(2), 023910(1-5).
87. Xu J., Xie D., Yin C., Feng T., Zhang X., Li G., Zhao H., Ma S., Ren T. L., Guan Y., *Journal of Applied Physics*, (2013), *114*(15), 154103(1-5).
88. Xu X., Liu W., Wu P., Zhang H., Guo M., Han Y., Zhang C., Gao J., Rao G., Wang S., *Applied Physics Letters*, (2015), *107*(4), 042905(1-5).
89. Priyadharsini P., Pradeep A., Sathyamoorthy B., Chandrasekaran G., *Journal of Physics and Chemistry of Solids*, (2014), *75*(7), 797-802.

CHAPTER II

EXPERIMENTAL TECHNIQUES

This chapter deals with the experimental part of the entire thesis work, wherein the detailed aspects of synthesis and characterization methods of pure, doped and co-doped BFO nanostructures are elucidated.

2.1 SAMPLE PREPARATION

Sol gel auto combustion method is used for synthesis of nanoparticles in the present study. This method involves a self-propagating high-temperature reaction in homogeneous solution of metal nitrates with the addition of fuels like urea, glycine, hydrazides etc. The resultant solution was then heated with simultaneous mixing and stirring using a magnetic stirrer. Then after, it involves thermally induced self-reaction of xerogel which is formed by the mixture of metal nitrates and fuel. Generally, metal nitrates are used to synthesize metal ferrites due to the easy solubility of nitrates in distilled water at lower temperatures. In addition, the fuel to metal nitrate ratio act as a significant parameter to decide the reaction temperature of the solution and particle size etc. A systematic presentation of sol-gel auto combustion method is illustrated in the **Figure 2.1**.

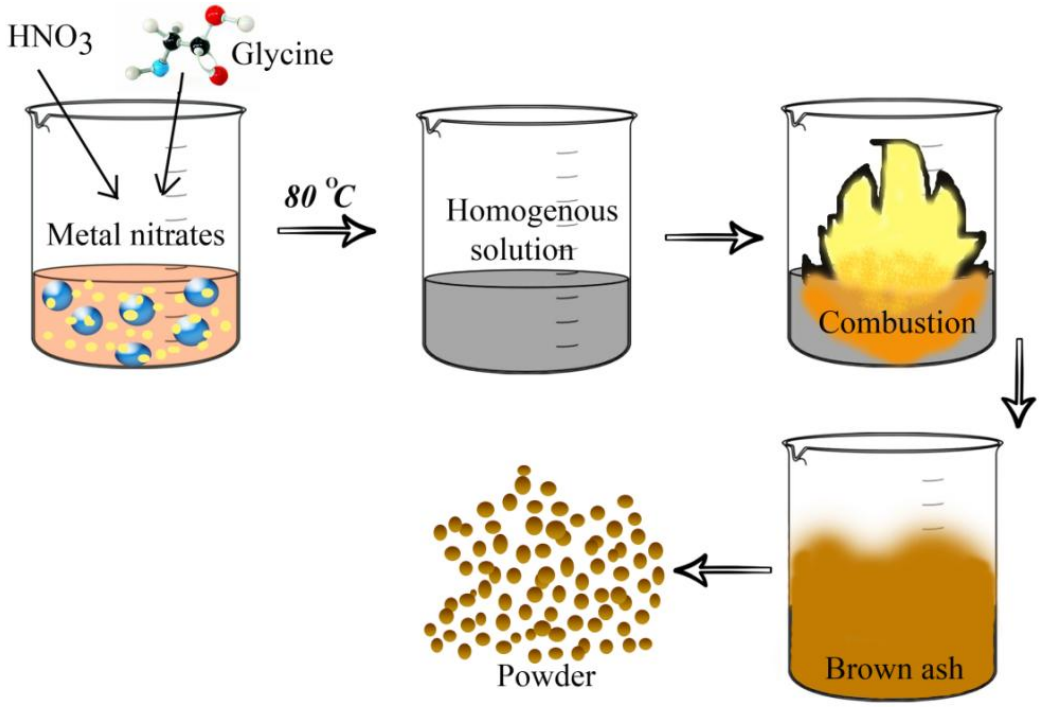

Figure 2.1 Pictorial view of auto combustion method.

Bismuth ferrite ceramics were synthesized by taking bismuth nitrate ($Bi(NO_3)_3 \cdot 5H_2O$) and iron nitrate ($Fe(NO_3)_3.9H_2O$), of Loba Chemie (~99.0%) as precursor and glycine (NH_2CH_2COOH) as fuel. In case of substitution of doping content in BFO, nitrate of substituted element was taken. The ratio amongst glycine to metal nitrates (G/N) has taken 1.56 so that the O^{2-} content of the oxidizer can be reacted to absorb entire glycine and no extra heat exchange is required for the

completion of reaction. Then after, bismuth nitrate in nitric acid (HNO_3), and iron nitrate in deionized water were mixed and stirred using a magnetic stirrer for 30 minutes to obtain a homogeneous transparent solution. The temperature of solution was sustained at 80 °C and the solution was stirred vigorously for 30 minutes. After auto-ignition, within a few minutes, brownish color ash was acquired. The ash was then dried at 100 °C in an electric oven for an hour and the fine powder obtained after drying was ground, calcined and sintered at a suitable temperature. A flow chart for the synthesis of BFO ceramics by same method is shown in **Figure 2.2**. Details about substituted elements in BFO ceramics are given in the respected chapters.

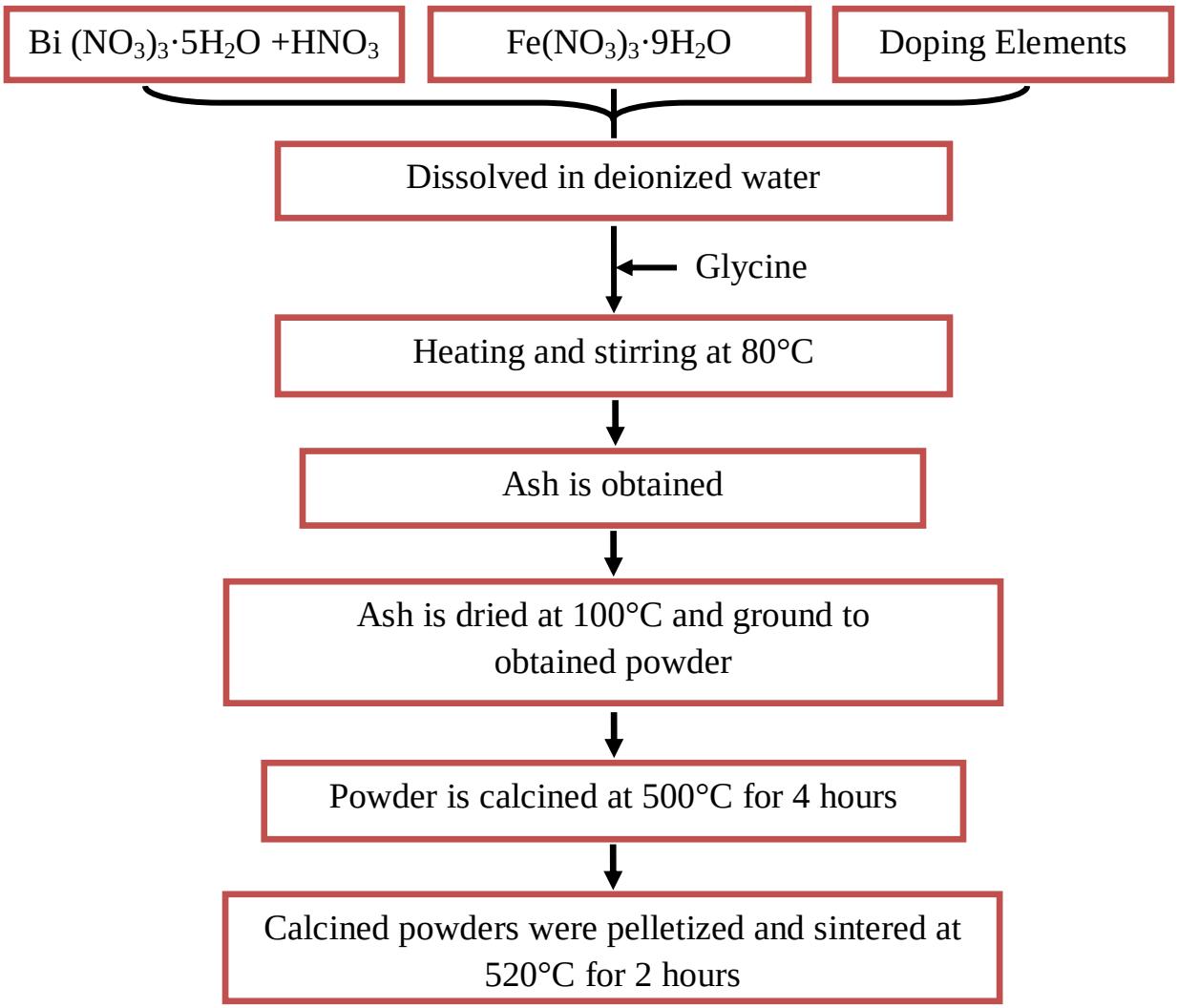

Figure 2.2 The detailed steps for the synthesis of the studied materials by sol-gel autocombustion method.

2.2 CHARACTERIZATION TECHNIQUES

The details of adopted technique are described below:

2.2.1 X-RAY DIFFRACTION (XRD)

X-ray diffraction is used for structure and phase identification of the material from which lattice constant, crystallite size and strain can be easily determined. The basic phenomenon of XRD is based on the principle of Bragg's Law. It relates the direction of constructive interference to the inter-planar spacing of the crystals as follows:

$$2dsin\theta = n\lambda \qquad Eq.\ 2.1$$

Where 'd' is the spacing between planes, 'θ' is Bragg's angle, 'n' is diffraction order and 'λ' is the wavelength of the X-rays.

The XRD of samples were performed using the *X'pert PRO PANalytical diffractometer* operating at 40 kV & 30 mA with CuK_α radiation (λ=1.5406 Å). The data was collected at room temperature for all samples within the angle range of 20°-70° and scan step size of 0.02. The phase formation of samples was identified using standard reference card (ICSD-Code 08-2614) and rietveld refinement.

Moreover, Williamson–Hall equation was used to compute the crystallite size (d) of all samples as follows:

$$\beta_{hkl}\, cos\theta_{hkl} = \frac{k\lambda}{d} + 4 \in sin\theta_{hkl} \qquad Eq.\ 2.2$$

Where "β_{hkl}" is the full width half maximum (FWHM) of the diffraction peak, "θ" the Bragg angle, "k"=0.9 is the correction factor, "λ"=1.5406 Å is the wavelength of Cu target, "d" is the crystalline size and "∈" corresponds to strain. Both the instrumental and sample dependent effects have contributed to the broadening of Bragg diffraction peak. In order to calculate the correct broadening β_{hkl} of samples, instrumental effects need to be eliminated using the relation:

$$\beta_{hkl}^2 = \beta_{measured}^2 - \beta_{instrumental}^2 \qquad Eq.\ 2.3$$

The plot of $\beta_{hkl}\, cos\theta_{hkl}$ as a function $4\, sin\theta_{hkl}$ is obtained using **equation 2.2** and **equation 2.3.** Therefore, the crystallite size (d) is estimated from the intercept of the plot whereas slope of the line gives the value of strain (∈).

2.2.2 SCANNING ELECTRON MICROSCOPY (SEM)

The microstructure of the samples was studied using SEM *Model ULTRA plus, Germany*. SEM provides the information regarding size, shape of grains, grain boundaries, porosity etc. of the materials which strongly influence its physical properties. For SEM analysis, the calcined powder was pressed down to pellets at a pressure of 6 MPa with a diameter of 10 mm and sintered at 520 ℃ for 2 h. Sintered pellets were coated with an ultrathin layer of gold, deposited on the surface of sample by low vacuum sputtering method. Then, gold sputtered pellets mounted on specimen stub. A high energy beam of electrons in a raster pattern scan the surface of sample at magnifications of 10x to 300,000x, with a virtually unrestricted depth of field. Various radiations including backscattered electrons, characteristic X-ray, secondary electrons etc. released during this process and collected by electron detector to form SEM image.

2.2.3 TRANSMISSION ELECTRON MICROSCOPY (TEM)

Particles morphology and size of BFO samples was investigated using *TEM (TECNAI G^2 20)*. For TEM analysis, calcined powder was dispersed in ethanol and ultrasonicate for half an hour. Then, the sample solution was placed on the carbon coated grid with a dropper. A high energy beam of electrons scan the sample. TEM uses electromagnetic and electrostatic lenses to control the accelerated electron beam and focus it to create an image of the sample.

2.2.4 DIELECTRIC ANALYSIS

The dielectric analysis can define in terms of permittivity and conductivity of material properties. The dielectric measurements were performed for silver coated pellets using *SOLARTRON analytical LCR meter (model SI-1260)*. Dielectric constant (ε) was calculated using values of capacitance measured via two probe methods and can be written as

$$\varepsilon = \frac{Cd}{A\varepsilon_o} \qquad Eq.\ 2.4$$

Where‘d’, ‘A’ and ‘ε_o’ corresponds to the distance between electrodes, area of the sample and permittivity of the free space (8.85 x 10^{-12} F/m), respectively.

Further, the same *SOLARTRON analytical LCR meter* was used to measure the complex resistance (or say impedance) of an electric circuit that is faced by the current when it passes through the circuit consisting capacitors, resistors and inductors. Impedance has its real and

imaginary components. Real part exhibits the capability of circuit to oppose the current and imaginary part shows the ability to store electrical energy which is displayed in terms of following parameters:

Complex impedance;

$$Z^* = Z' - jZ'' = \frac{1}{j\omega C_o \varepsilon^*} \qquad Eq.2.5$$

where $\omega=2\pi f$ is the angular frequency, $j=\sqrt{-1}$, Z' and Z'' are real and imaginary components of impedance, respectively.

The plot between Z' on the x-axis and Z'' on the y-axis is known as Nyquist plots as shown in **Figure 2.3**. In general, if any signal in Nyquist plots is applied to a pure resistive system, then the complex impedance $Z^*= R$ (resistance) or if it is applied to the pure capacitive system then the complex impedance $Z^* = \frac{1}{j\omega C_o}$.

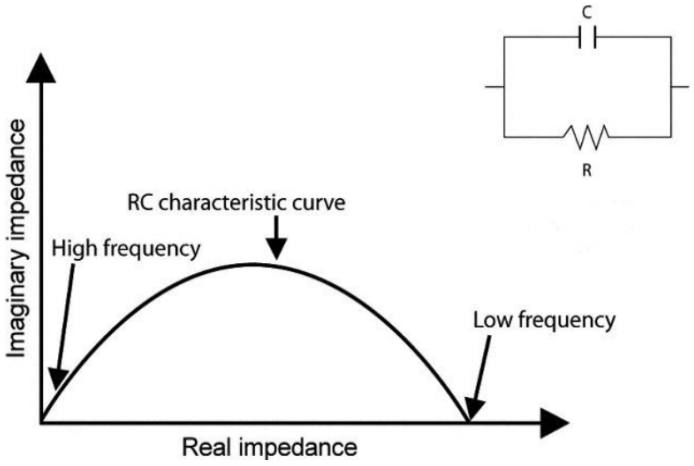

Figure 2.3 Nyquist plots.

The data were collected for all samples from room temperature to 450 °C at 100 Hz, 1 kHz, 10 kHz, 100 kHz and 1 MHz.

2.2.5 FERROELECTRIC (*P-E*) MEASUREMENTS

The imperative feature of a ferroelectric substance is to exhibit the hysteresis behavior. A *P-E* loop tracer is used to plot of polarization developed when an alternating electric field is applied to the sample at a given frequency. The basic principle of the PE test system is based on sawyer tower circuit states that when AC voltage is applied to the capacitors connected in series, then the charge on both the capacitors will be same. Moreover, the internal capacitance must be

larger than material's capacitance in order to achieve complete saturation, as shown in **Figure 2.4**.

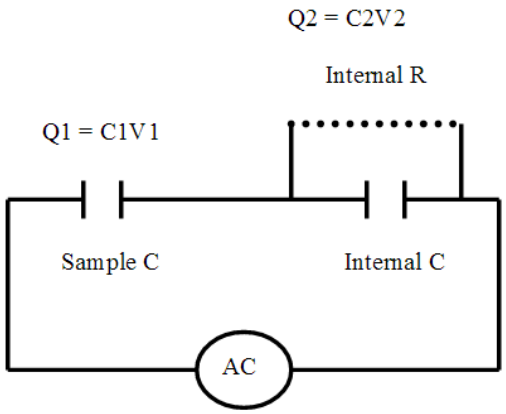

Figure 2.4 Schematic representation of sawyer-tower circuit.

The ferroelectric measurements of BFO samples were carried out using *PE* loop tracer *(Marine India).*

2.2.6 MAGNETIC *(M-H)* MEASUREMENTS

Vibrating sample magnetometer (VSM) technique helps in verifying the magnetic moment of a material at a high accuracy rate. VSM stands by the Faraday's law which states that whenever there is a change in flux through the coil, electromagnetic forces starts generating. Therefore, the produced electric field can be measured which further used to extract the information regarding change in magnetic field.

Magnetic properties of BFO samples were investigated using VSM *(Model Lakeshore 7400 Series).*

2.2.7 FOURIER TRANSFORM INFRARED SPECTROSCOPY (FTIR)

To identify every different type of material, IR spectroscopy is used which provides a unique impression for each material. A specific IR radiation is absorbed by the materials that communicate to the vibrational frequency between the atomic bonds of the materials. Since each material has its own different combinations of atoms, corresponding to different functional group is obtained.

IR spectroscopy has its own pros and corns but the slow scan rate was the main difficulty. A method was needed that measure all IR signals at the same time rather than individually. This

can be accomplished by interferometer which produces a unique kind of signals that consisting of all IR frequencies encoded into it and decoded by a very well-known mathematical technique "FOURIER TRANSFORMATION".

FTIR investigation of BFO samples was recorded on *Perkin Elmer-Spectrum* at 1 cm^{-1} resolution with a scan range of 400–700 cm^{-1} using KB_r powder.

2.2.8 *UV*-VISIBLE ABSORPTION SPECTROSCOPY

The ultraviolet absorption spectroscopy helps to probe the bonding characteristic of the particles. *UV* spectroscopy stands by the Beer-Bouguer-Lambert law states that when an amount of light is passed through a sample solution, the attenuation in intensity of radiation is directly proportional to the concentration of the solution as well as incident radiation and can be written as-

$$A = log\left(\frac{I_o}{I}\right) = Ecl \qquad Eq.2.6$$

Where A, I_o, I, E, C and l corresponds to absorbance, intensity of light incident upon sample cell, intensity of light leaving sample cell, molar absorptivity, molar concentration of solute and length of sample cell.

The absorption optical properties of the resultant doped BFO samples were characterized using a *Hitachi U-3900H spectrophotometer.*

2.2.9 PHOTOLUMINESCENCE (PL)

PL spectroscopy is an efficient and nondestructive technique to probe the optoelectronic structure of semiconductor materials. This spectroscopy involves spontaneous emission of light from the surface of material which provides

- Detailed information of discrete electronic states of the material
- Understanding of recombination mechanisms
- Band gap determination
- Assessment of the material quality
- Detection of defects and impurity levels

A Photoluminescence spectrum of BFO samples was performed on *Cary eclipse.*

CHAPTER III

STUDY OF PURE AND Bi-SITE SUBSTITUTED $BiFeO_3$ CERAMICS

This chapter features the detailed study of pure and Bi-site substituted BFO ceramics. Primarily, BFO powders were synthesized via. sol gel auto combustion technique. Then, the effect of calcination temperature on the phase formation of BFO has been investigated. Also, various aspects of structural, microstructural, dielectric, ferroelectric, magnetic and optical responses for different concentrations of doped elements were examined. The following polycrystalline multiferroic materials have been synthesized in the present chapter:

a)	$Bi_{1-x}La_xFeO_3$;	where x = 0.0, 0.1 and 0.2
b)	$Bi_{1-x}Ho_xFeO_3$;	where x = 0.0, 0.05 and 0.1
c)	$Bi_{1-x}Ba_xFeO_3$;	where x = 0.0, 0.1 and 0.2

3.1 $Bi_{1-x}La_xFeO_3$ (x=0.0, 0.1 and 0.2) ceramics

3.1.1 SYNTHESIS

$Bi_{1-x}La_xFeO_3$ (x=0.0, 0.1 and 0.2) ceramics were synthesized via. auto combustion technique by taking $Bi(NO_3)_3 \cdot 5H_2O$, $Fe(NO_3)_3.9H_2O$ and $La(NO_3)_3 \cdot 3H_2O$, as precursor and glycine as fuel. $Bi(NO_3)_3 \cdot 5H_2O$ in nitric acid (HNO_3), and $Fe(NO_3)_3.9H_2O$ in deionized water were mixed. Then the mixed solution was stirred using a magnetic stirrer for 30 minutes to obtain a homogeneous transparent solution. The transparent solution was stirred vigorously at 80 °C and within few minutes self sustained reaction occurred. The brown colored ash was acquired and then dried at 100 °C in an electric oven for an hour. The fine powder obtained after drying was ground and calcined at 500 °C. The compositions of $Bi_{1-x}La_xFeO_3$ where x=0.0, 0.1 and 0.2 was signified as BFO, BLFO-0.1 and BLFO-0.2, respectively.

The phase formation and crystal structure was examined using XRD in an X'pert PROPANalytical diffractometer using CuKα radiation followed by rietveld refinement. The calcined powder was pressed down to pellets of dia. 10 mm and sintered at 520 °C for 2 hours. The prepared samples were characterized by TEM, FESEM for the investigation of microstructural properties, dielectric measurement, impedance and ferroelectric analysis for electrical properties, VSM for magnetic behavior. The optical properties were carried out using FTIR spectroscopy, *UV*-Visible spectrometer and PL spectroscopy.

3.1.2 X-RAY DIFFRACTION ANALYSIS

Figure 3.1 shows the X-ray diffraction patterns of BFO powder samples calcined at **(a)** 400 °C, **(b)** 450 °C, **(c)** 500 °C, **(d)** 550 °C, and **(e)** 600 °C for 4 hours. The sample calcined at 400 °C is found to be amorphous with small characteristic peaks of $Bi_2Fe_4O_9$. The sample calcined at 450 °C shows BFO peaks along with a few peaks of $Bi_2Fe_4O_9$. The observed weak diffraction peaks of BFO can be ascribed to rhombohedrally distorted ABO_3-type structure (*R3c* space group), in accordance with the standard ICSD-Code 08-2614 of the crystal $BiFeO_3$. Pure phase BFO is obtained at 500 °C without any impurity peak. The degree of crystallinity increases as the temperature rises to 550 °C and 600 °C.

After optimizing the synthesis conditions for pure BFO nanoparticles, rest of the single doped BFO nanoparticles studied in the present chapter have been prepared by combustion route with the set calcination temperature at 500 °C for 4 hours.

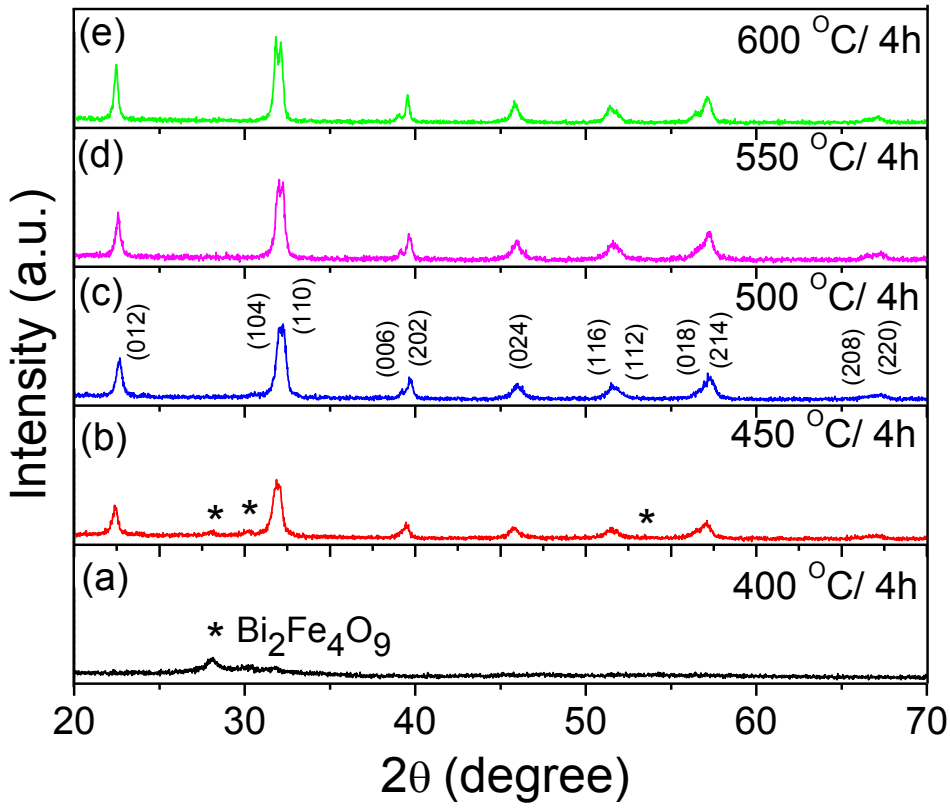

Figure 3.1 XRD patterns of BFO nanoparticles calcined at different various temperatures (400 – 600 °C).

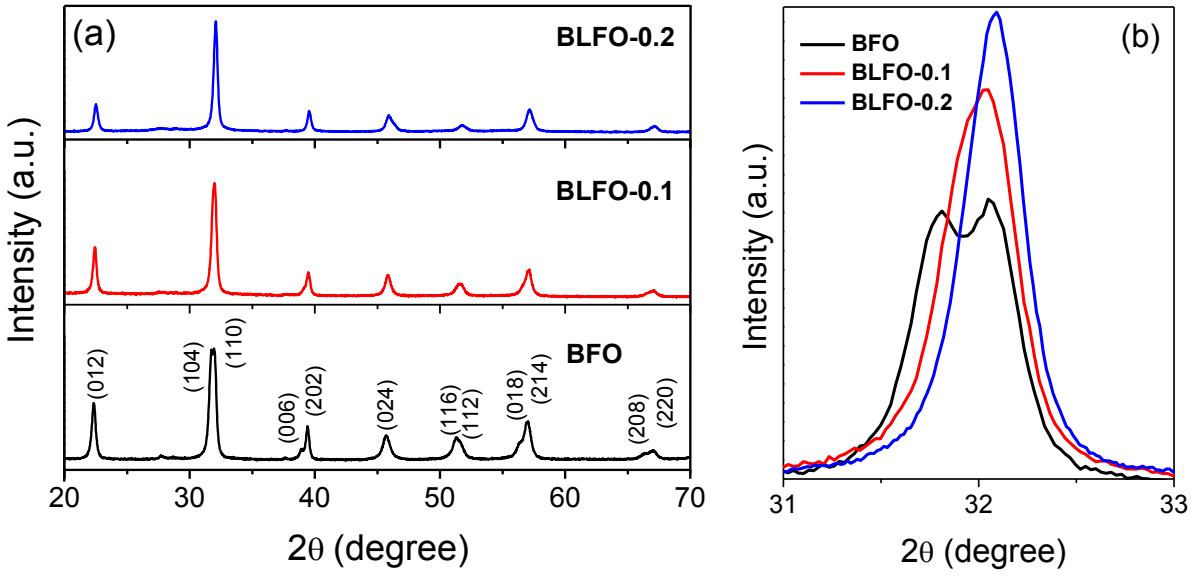

Figure 3.2 (a) X-ray diffraction patterns of $Bi_{1-x}La_xFeO_3$ (x=0.0, 0.1 and 0.2) nanoparticles **(b)** Enlarged view of the characteristic peak.

Figure 3.2 (a) shows the XRD patterns of $Bi_{1-x}La_xFeO_3$ (x=0.0, 0.1 and 0.2) nanoparticles. Enlarged view of characteristic peak is given in **Figure 3.2 (b)**. The structural phase transformation from rhombohedral (*R3c*) to orthorhombic (*Pnma*) is observed for BLFO-0.1 and is evidenced by merging of the split diffraction peaks into one peak indexed as (104) (110), (006) (202) and (116) (122) around the angle 2θ=32°, 2θ=39° and 2θ=51°. In fact, for further La^{3+} substitution, samples only reflect the orthorhombic phase similar as $LaFeO_3$ (ICSD-Code 08-4941). Such type of structural transformation has also been reported in other RE doped BFO **[1-4]**.

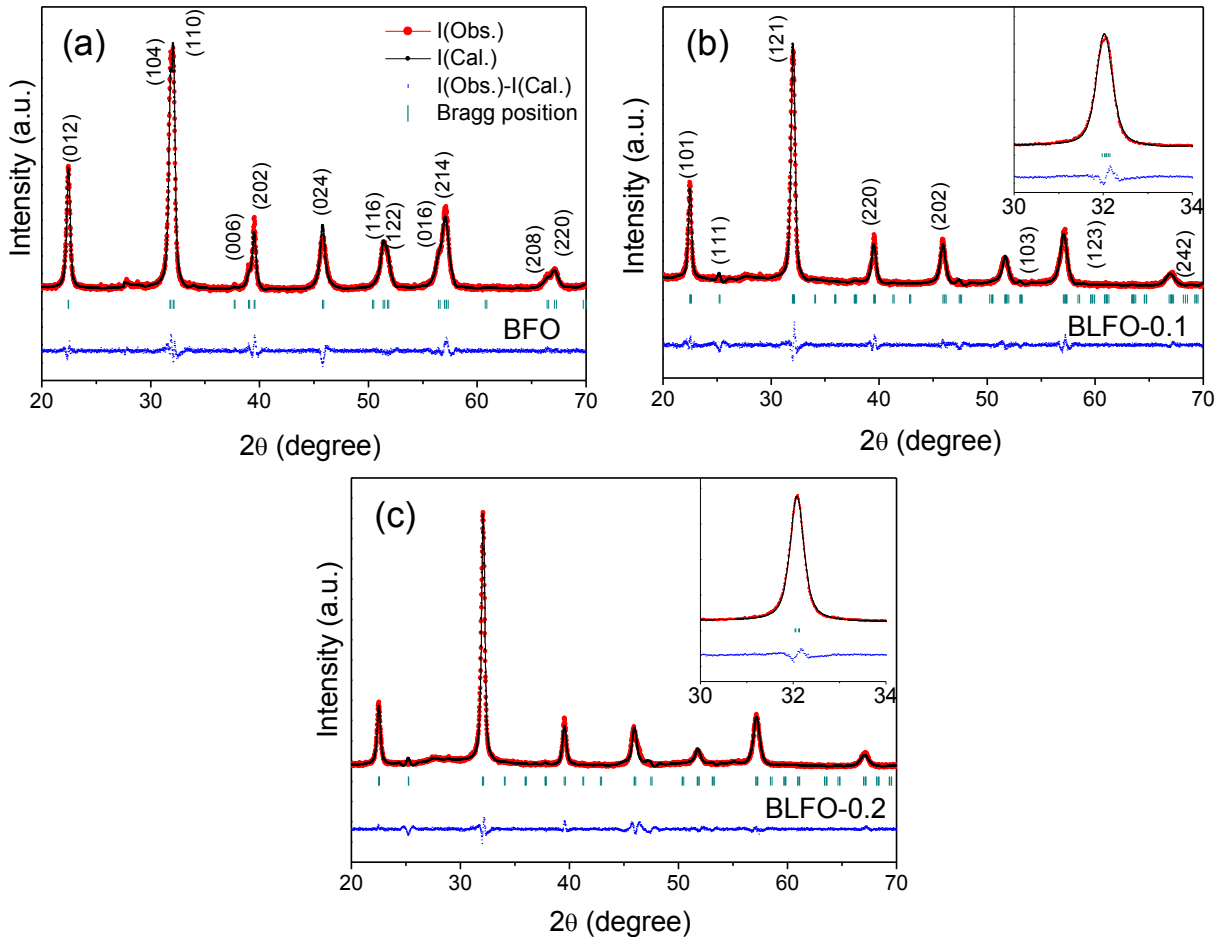

Figure 3.3 Rietveld refinements of the XRD patterns of **(a)** BFO **(b)** BLFO-0.1 and **(c)** BLFO-0.2 nanoparticles.

To investigate the various structural parameters, rietveld refinement of the crystal structure of BFO nanoparticles has been performed as shown in **Figure 3.3 (a)**. The refinement for BFO nanoparticles was carried out using the rhombohedral crystal symmetry with *R3c* space group in a hexagonal lattice. Best fits between the experimental and simulated profiles along

with relatively lower R_p and R_{wp} (<10%) values were obtained. Rhombohedral crystal model could not fit to the observed XRD patterns for BLFO-0.1 and BLFO-0.2 nanoparticles. Therefore, the refinement for La^{3+} substituted nanoparticles were performed with an orthorhombic structural model (space group: *Pnma*). The rietveld fit between the experimental and simulated profiles of La^{3+} doped samples are shown in **Figures 3.3 (b and c)**, while the refined structural parameters, Fe–O bond lengths and Fe–O–Fe bond angles are listed in **Table 3.1**. All these resultant parameters suggest a lattice distortion which involves Fe^{3+} or Bi^{3+} ion displacement with the structural phase transformation which enhances the Fe-O-Fe bond angle along with contraction of the unit cell volume.

Table 3.1 Refined **s**tructural parameters for $Bi_{1-x}La_xFeO_3$ nanoparticles ($0.0 \leq x \leq 0.2$).

Composition of $Bi_{1-x}La_xFeO_3$	**Atom**	**Fractional coordinates**			**Lattice Parameter [Å]**	**Bond angle [°]**	**Bond Length [Å]**	**Statistical Parameter (%)**
		x	**y**	**z**				
BFO	Bi	0.0000	0.0000	0.0000	a =5.57	Fe-O-Fe	Bi-O=2.16	R_p=3.72
R3c	Fe	0.0000	0.0000	0.2212	c =13.84	=156.66	Fe-O=2.17	*Rwp*=4.85
V=372.95 (Å^3)	O	0.4748	0.0178	-0.0563				R_{exp}=3.41
								χ^2=2.02
BLFO-0.1	Bi/La	0.0357	0.2500	0.9946	a =5.58	Fe-O1-Fe	Bi/La-O1	R_p= 4.38
Pnma	Fe	0.0000	0.0000	0.5000	b = 7.87	=139.19	= 2.10	*Rwp*=5.76
V=245.88 (Å^3)	O1	0.5111	0.2500	0.1303	c = 5.59	Fe-O2-Fe	Bi/La-O2	R_{exp}=3.98
	O2	0.2677	0.5291	0.2174		=166.20	=3.10	χ^2=2.09
							Fe-O1=2.09	
							Fe-O2=2.18	
BLFO-0.2	Bi/La	0.0393	0.2500	0.9953	a =5.58	Fe-O1-Fe	Bi/La-O1 =2.36	R_p=3.57
Pnma	Fe	0.0000	0.0000	0.5000	b =7.88	=153.69	Bi/La-O2 =2.76	*Rwp*=4.79
V=245.84 (Å^3)	O1	0.5170	0.2500	0.0808	c =5.58	Fe-O2-Fe	Fe-O1=2.02	R_{exp}= 3.09
	O2	0.2067	0.5445	0.2034		=151.62	Fe-O2=2.04	χ^2=2.41

Williamson-Hall plot of $\beta_{hkl}\, cos\theta_{hkl}$ as a function 4 $sin\theta_{hkl}$ was used to calculate the crystallite size (*d*) as shown in **Figure 3.4 [5, 6]**. The crystallite size was calculated to be 43.32 nm, 32.47 nm and 29.94 nm for BFO, BLFO-0.1 and BLFO-0.2 nanoparticles, respectively. The corresponding strain values are 0.00394, 0.01037 and 0.0114 for BFO, BLFO-0.1 and BLFO-0.2 nanoparticles respectively.

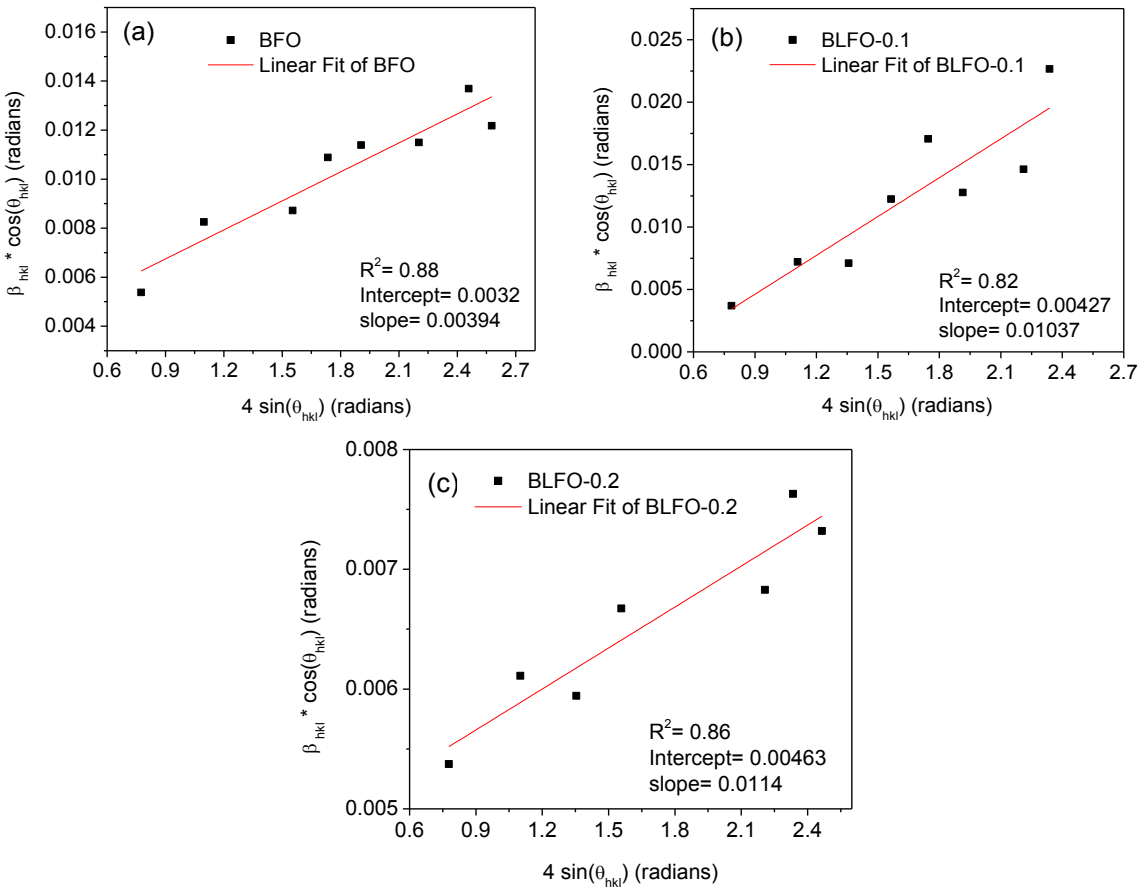

Figure 3.4 Williamson–Hall plots of BFO, BLFO-0.1 and BLFO-0.2 nanoparticles.

According to thermodynamic analysis, the distortion in BFO nanoparticles due to the substitution of La^{3+} doping ions can qualitatively be verified by using Pauling's equation and is written as **[7]**

$$I_{AB} = 1 - exp\frac{-|X_A - X_B|}{4} \qquad Eq.\ 3.1$$

Here I_{AB} is the ionic bond strength of ions, X_A is electronegativity of cation and X_B is electronegativity of anion. The obtained results reveal that the La-O bond has more ionic strength, $I_{\text{La-O}}$=0.442 over the Bi-O bond, $I_{\text{Bi-O}}$=0.319 by using electronegativity values 1.9, 1.10 and 3.44 for Bi^{3+}, La^{3+} and O^{2-} ions respectively in the above mentioned **equation (3.1)**. Moreover, the enthalpy of formation (ΔH_f) is a function of ionic bond strength I_{AB} and is written as

$$\Delta H_f = P_{AB} * \left[\varepsilon_{AB} - \frac{1}{2}\left(\varepsilon_{AA} + \varepsilon_{BB}\right)\right] \qquad Eq.3.2$$

Where, P_{AB} corresponds to number of A-B bonds (Bi-O or La-O bonds) and ε is the energy of A-B bonds which is directly proportional to the negative of ionic bond strength I_{AB} of ions. The much negative enthalpy of formation (ΔH_f) is observed in BLFO-0.1 and BLFO-0.2 nanoparticles, as La^{3+} substituted samples has more ionic strength in comparison of BFO. Therefore, this negative enthalpy of formation leads to the more negative free energy of formation ($\Delta G_f = \Delta H_f - T\Delta S_f$) will enhance the more stability in the perovskite phase of La^{3+} substituted nanoparticles.

3.1.3 MORPHOLOGICAL STUDIES

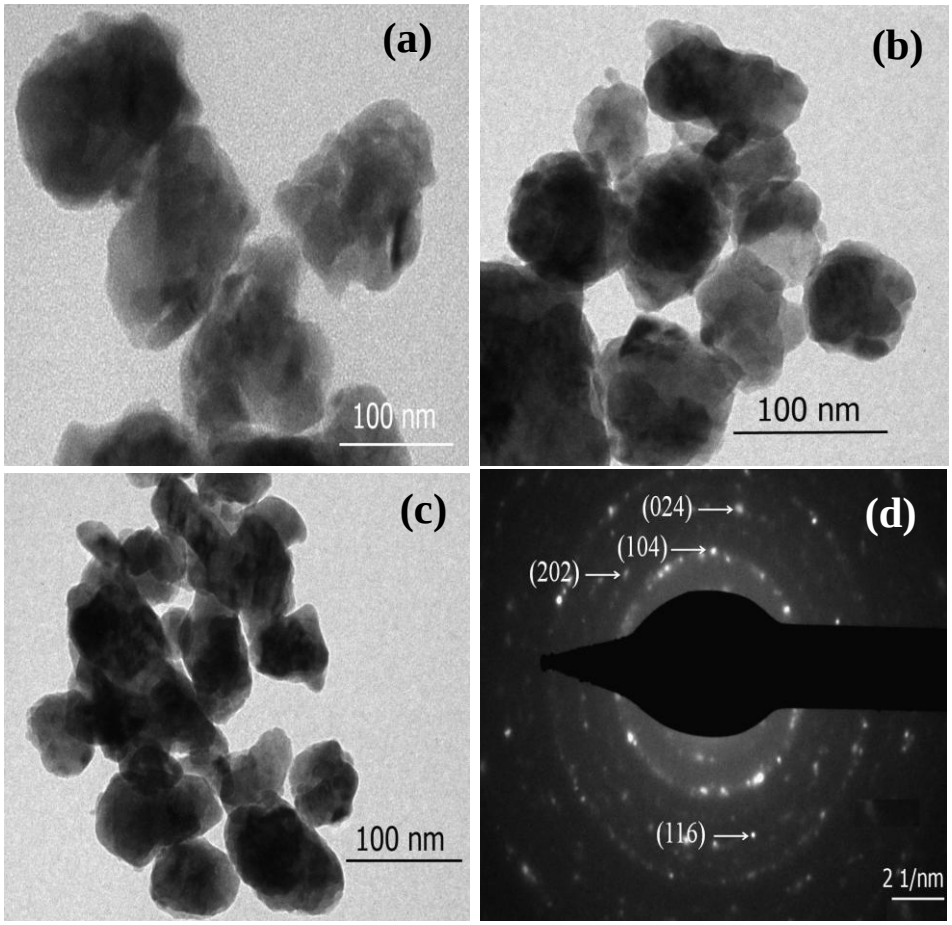

Figure 3.5 TEM images of **(a)** BFO **(b)** BLFO-0.1 **(c)** BLFO-0.2 and SAED patterns of **(d)** BFO nanoparticles.

Figure 3.5 exhibit the TEM morphology and SAED of $Bi_{1-x}La_xFeO_3$ (x=0.0, 0.1 and 0.2) nanoparticles at the scale of 100 nm. Agglomerate particles are acquired due to the high surface energy of uniform particles with fairly narrow size. The mean particle size of the BFO sample is

~132 nm as can be observed in **Figure 3.5 (a)** which decreases with increase the La^{3+} doping content, to ~68 nm for BLFO-0.2. Similar decrement in the size of particles has also been reported in RE doped BFO ceramics **[8, 9]**.

The SAED pattern taken for BFO nanoparticles exhibits the discrete rings indicating well developed polycrystalline nature as shown in **Figure 3.5 (d)**. The calculated lattice spacing is 2.84 Å, 2.28 Å, 1.96 Å and 1.79 Å which correspond to (104), (202), (024) and (116) lattice planes, respectively.

Figure 3.6 shows the surface morphology of $Bi_{1-x}La_xFeO_3$ (x=0.0, 0.1 and 0.2) ceramics. It can be seen from **Figure 3.6 (a)** that grains of BFO ceramic are uniform. The surface morphology of BFO has number of pores or voids that are ascribed to many gases which are liberated during combustion process. The average grain size of BFO ceramics is ~422 nm. The grain size is found to reduce with La^{3+} substitution as shown in **Figure 3.6 (b and c)**, resulting better grain connectivity. The decrease in size of grains may be attributed to the suppression of the oxygen vacancy (Vo^{2+}) concentration and consequently inhibits the grain growth **[10]**.

The EDX spectrum of ceramic surface shows almost similar elemental distribution as have taken primarily. The initial and obtained stoichiometry from EDX analysis for BFO, BLFO-0.1 and BLFO-0.2 samples are shown in the inset of **Figure 3.6 (d-f)**.

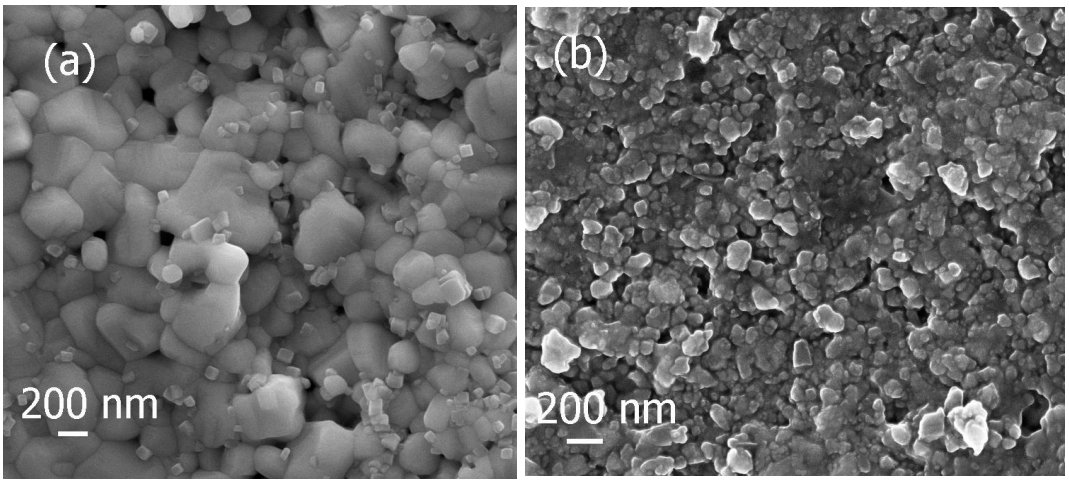

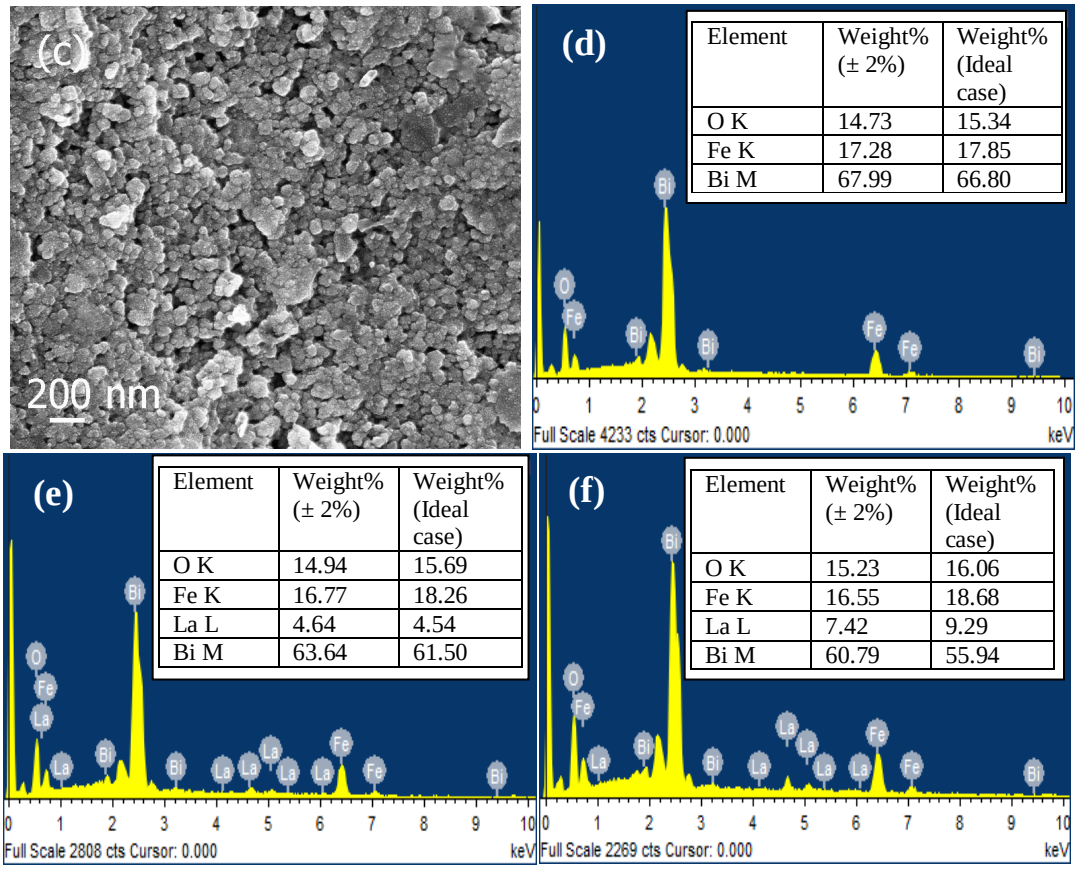

Figure 3.6 FESEM micrographs and EDX patterns of **(a, d)** BFO **(b, e)** BLFO-0.1 and **(c, f)** BLFO-0.2 samples.

3.1.4 DIELECTRIC STUDIES

Figure 3.7 shows the variation of the **(a)** dielectric constant (ε) and **(b)** loss ($tan\ \delta$) for $Bi_{1-x}La_xFeO_3$ (x=0.0, 0.1 and 0.2) ceramics with frequency at room temperature. Both ε and $tan\ \delta$ are found to decrease with increase in frequency and then remain constant at higher frequencies for BFO. The observed variation of both ε and $tan\ \delta$ indicate frequency dispersion due to the Maxwell-Wagner model related to interfacial space charge relaxation **[11, 12]**. This space charge originate in BFO ceramics via oxygen vacancies (Vo^{2+}) which occurs from Bi volatility and via transitions from Fe^{3+}-Fe^{2+}. Moreover, space charge follows the applied alternating field in low frequency region but beyond a certain level they begin to lag behind the field polarity as frequency increases. It happens because assembly of space charges does not have sufficient time to line-up their axis to rapidly changing applied field. As a result, low values of ε are obtained at high frequency. Whereas, presence of all type of polarization factors (interfacial dislocations,

dipolar, ionic, and electronic) which became significant at lower frequency gives the high values of ε.

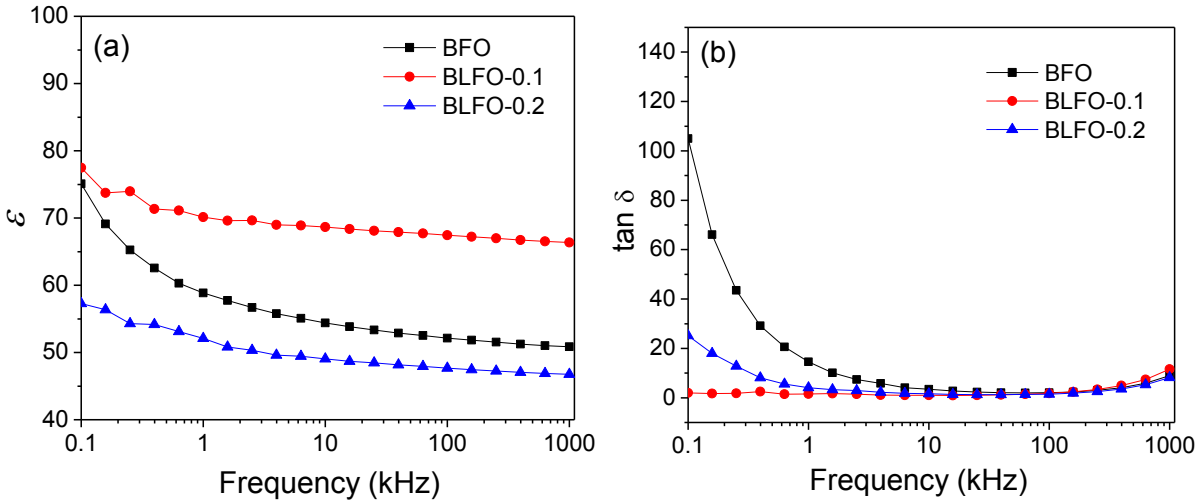

Figure 3.7 Variation of **(a)** dielectric constant (*ε*) and **(b)** dielectric loss (*tan δ*) for BFO, BLFO-0.1 and BLFO-0.2 samples as a function of frequency.

The value of *ε* is found to be almost 1.5 times higher in BLFO-0.1 ceramics than that of BFO at 1 kHz. The enhanced values of *ε* with the incorporation of La^{3+} ions could be ascribed to the size effect of grains in ceramics. La^{3+} ions reduce the size of the grains (as evidenced from FESEM) and hence increase the volume fraction of grain boundaries which results in high value of ε. Similar kind of enhancement in *ε* has also been reported in Pr doped and La-Nd co-doped BFO ceramics **[13, 14]**. Moreover, *tan δ* is observed to decrease for BLFO-0.1 and then it increases with further La^{3+} ions substitution in BFO. The change in *tan δ* with the substitution of La^{3+} ions correlates with corresponding variation in electrical resistivity.

The temperature dependence of the dielectric constant (*ε*) and loss (*tan δ*) for $Bi_{1-x}La_xFeO_3$ (*x*=0.0, 0.1 and 0.2) ceramics at different frequencies (100 Hz to 1 MHz) are shown in **Figures 3.8 (a-f)**. From **Figure 3.8 (a)**, the observed dielectric constant is found to increase with increase in temperature up to 380 °C and then it decreases with further increase in temperature for all the applied frequencies. This peak corresponds to an antiferromagnetic Neél temperature (T_N) and may be ascribed to reflect the change in electric dipole order state from one to another because of antiferromagnetic transitions/possible magnetoelectric coupling effects which was predicted by the Landau-Devonshire theory of phase transition in magnetoelectrically ordered systems **[15, 16]**. Similar trend of ε has also been observed for BLFO-0.1 and BLFO-0.2

ceramics as shown in **Figure 3.8 (c and e)**, respectively. Moreover, this type of anomaly has also been observed in loss (*tan δ*) for BFO, BLFO-0.1 and BLFO-0.2 ceramics shown in **Figures 3.8 (b, d and f)** respectively.

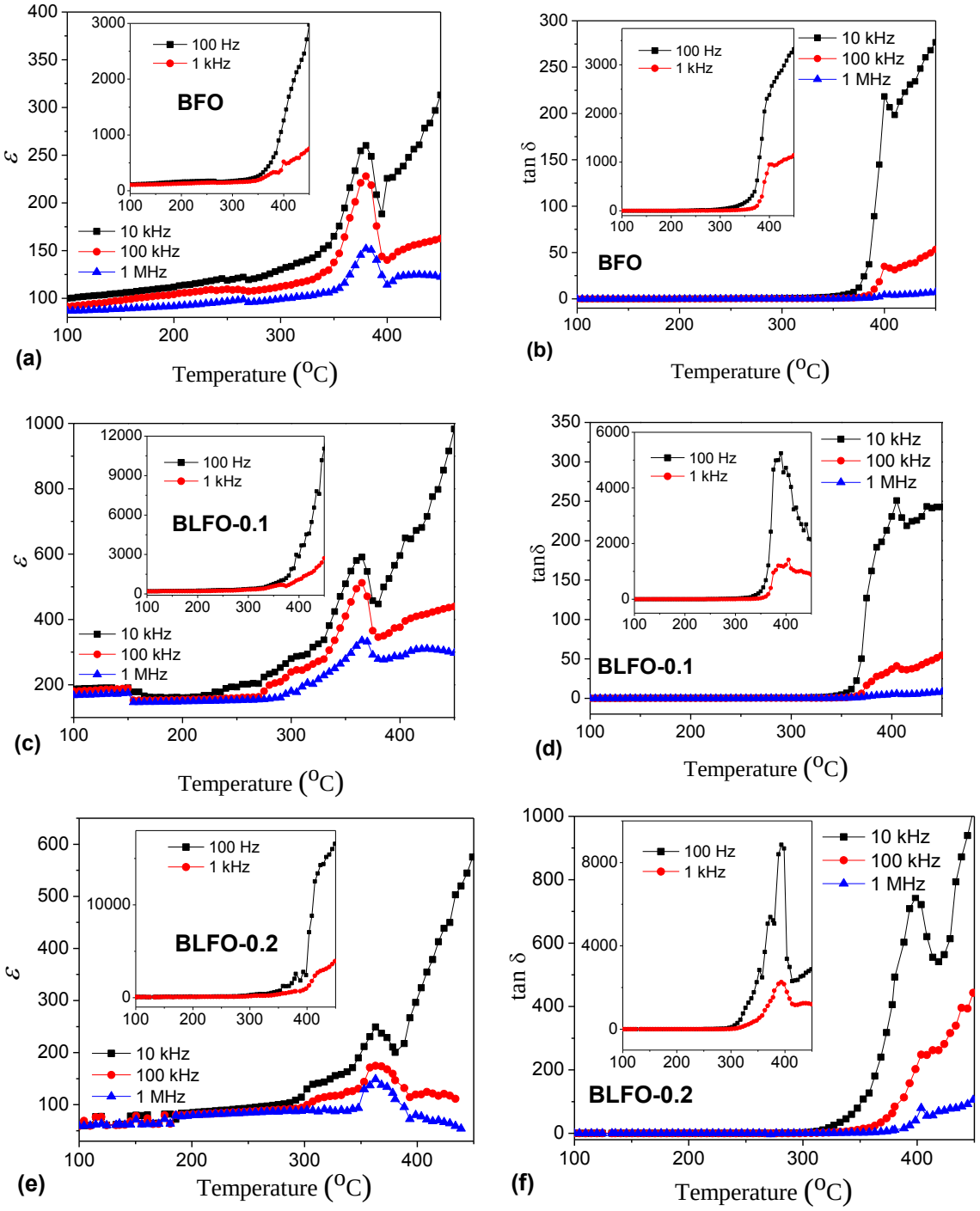

Figure 3.8 Dielectric constant (*ε*) and dielectric loss (*tan δ*) versus temperature curves for $Bi_{1-x}La_xFeO_3$ samples at 100 Hz, 1 kHz, 10 kHz, 100 kHz and 1 MHz.

The antiferromagnetic Neél temperature (T_N) is found to decrease with the substitution of La^{3+} ions in BFO ceramics. The obtained value of T_N is 380 °C, 365 °C and 362 °C for BFO, BLFO-0.1 and BLFO-0.2 ceramics, respectively. A similar trend of decrease in T_N has also been reported earlier in La doped BFO ceramics **[17, 18]**. This shift in T_N could be correlated to changes in spin canted Fe-O-Fe angle due to structural modification **[19, 20]**.

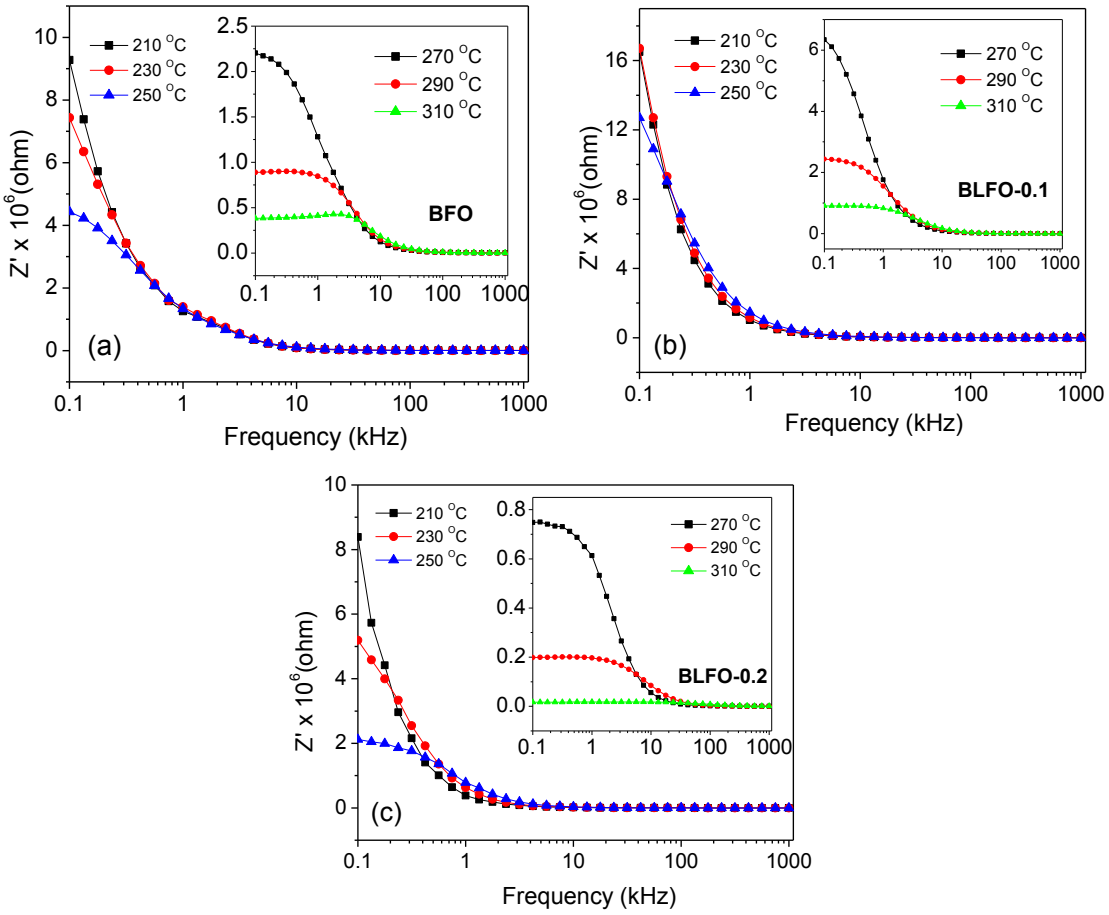

Figure 3.9 Frequency dependent real (Z') part of impedance for **(a)** BFO **(b)** BLFO-0.1 and **(c)** BLFO-0.2 samples at 210 °C, 230 °C and 250 °C, the inset shows the variation of impedance at 270 °C, 290 °C and 310 °C.

Impedance analysis has been carried out to study the conduction mechanism in $Bi_{1-x}La_xFeO_3$ (x=0.0, 0.1 and 0.2) ceramics. **Figure 3.9** shows the variation in the real part of impedance (Z') with frequency at different temperatures (210 °C to 310 °C). It is observed from **Figure 3.9 (a)** that Z' decreases with the increase in frequency at 210 °C, followed by a saturation region, which lowers the barrier properties of BFO ceramics. Moreover, Z' for BFO is found to decrease with increase in temperature as well, showing negative temperature coefficient of resistance (NTCR) behavior of ceramics. These observations reveal the possibility of increase

in a.c. conductivity in the ceramics **[21]**. Similar trend of Z' with respect to frequency at entire temperature range has also been observed for BLFO-0.1 and BLFO-0.2 ceramics as shown in **Figure 3.9 (b and c)**, respectively. A noticeable increment in the magnitude of Z' is observed for BLFO-0.1, which indicates the reduction in electrical conductivity with the La^{3+} substitution in BFO ceramics. Whereas, further La^{3+} doping increase electrical conductivity of the ceramics **[22]**.

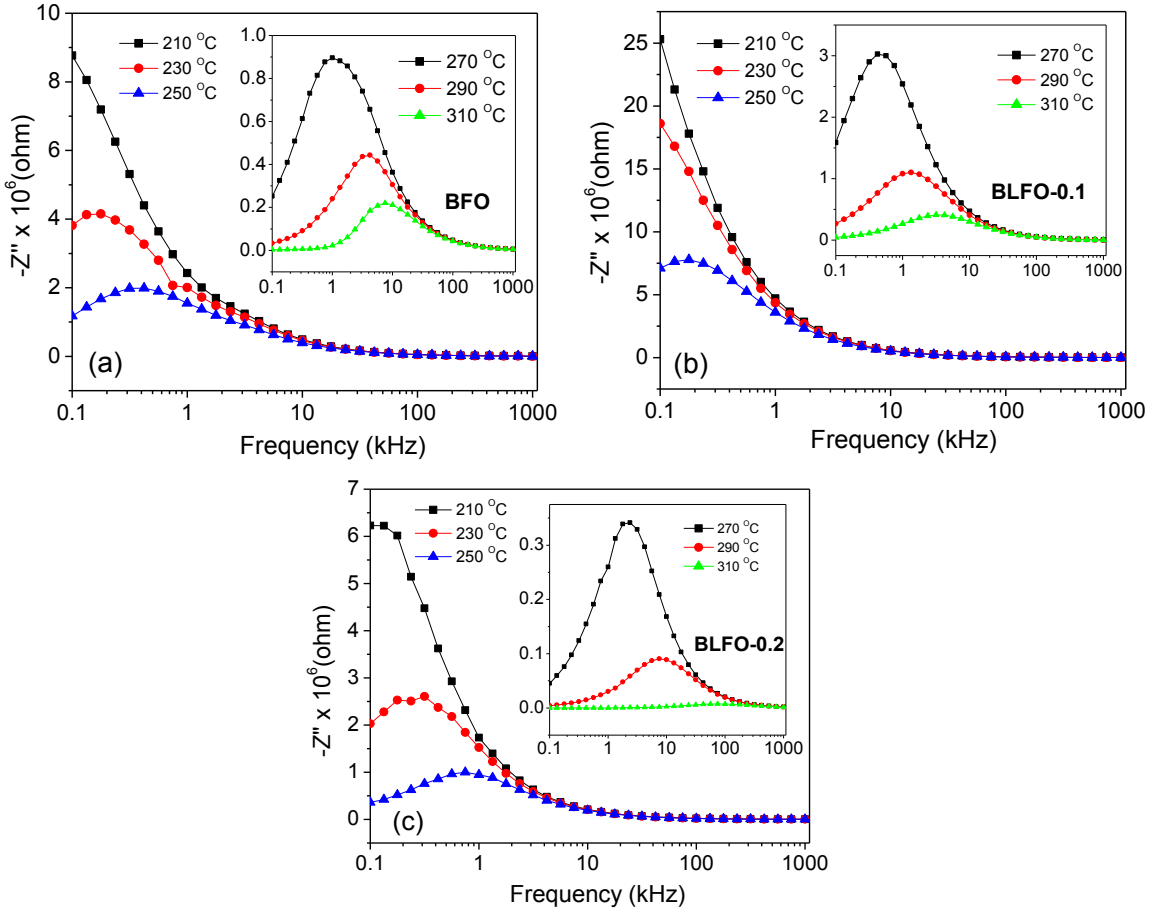

Figure 3.10 Frequency dependent imaginary (Z'') part of impedance for **(a)** BFO **(b)** BLFO-0.1 and **(c)** BLFO-0.2 samples at 210 °C, 230 °C and 250 °C, the inset shows the variation of impedance at 270 °C, 290 °C and 310 °C.

Figure 3.10 depicts the variation in the imaginary part of impedance (Z'') as a function of frequency at different temperatures (210 °C to 310 °C). It can be seen from **Figure 3.10 (a)** that the Z'' decreases monotonically with increase in frequency at 210 °C. However, at higher frequencies, the value of Z'' remains constant which could be ascribed to the occurrence of a thermally activated dielectric relaxation process in the ceramics **[23]**. At higher temperatures, a

broad peak at a particular frequency f_{max} (called relaxation frequency) is observed. As temperature increases, a noticeable shift of f_{max} towards the high frequency side is observed which exhibit strong dispersion in Z″. This shift suggests the asymmetry in the peak pattern and decrease of relaxation time in the ceramics. The above mentioned observations of Z" are also noticed in BLFO-0.1 and BLFO-0.2 ceramics as shown in **Figure 3.10 (b and c)** respectively. **Figure 3.11 (a-f)** show the nyquist plots (Z" versus Z') of $Bi_{1-x}La_xFeO_3$ (x=0.0, 0.1 and 0.2) ceramics at different temperatures (210 °C to 310 °C). At lower temperature, the straight lines with large slopes are observed whereas the bends of the lines decreased and hence, semicircles are generated at higher temperature. The intercept of the semicircles on Z'-axis gives the value of resistance. The obtained value of resistance is of the order of ~10^7 Ω for BFO. However, resistance is found to increase for BLFO-0.1 and then it decreases with further increase in La^{3+} substitution.

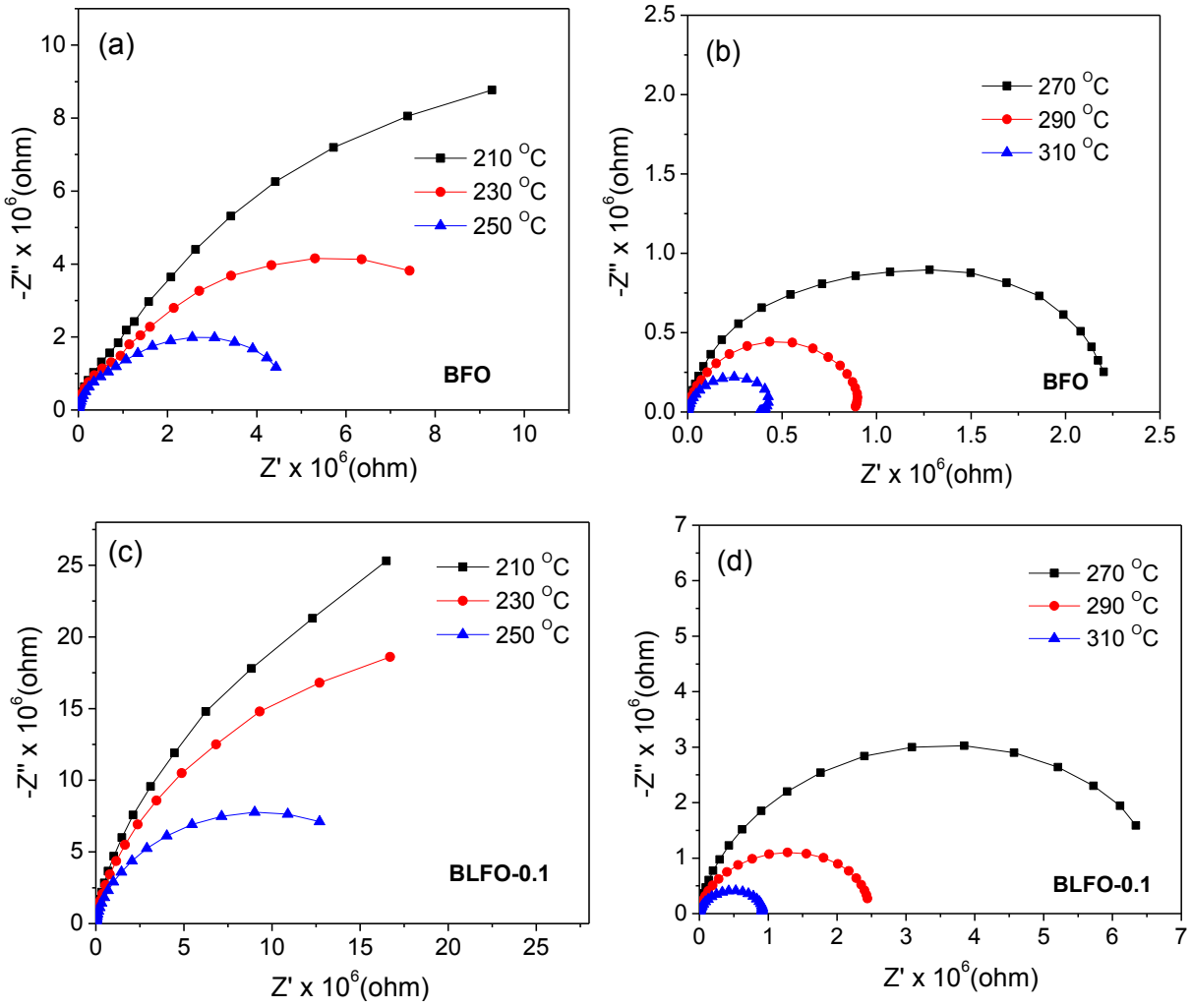

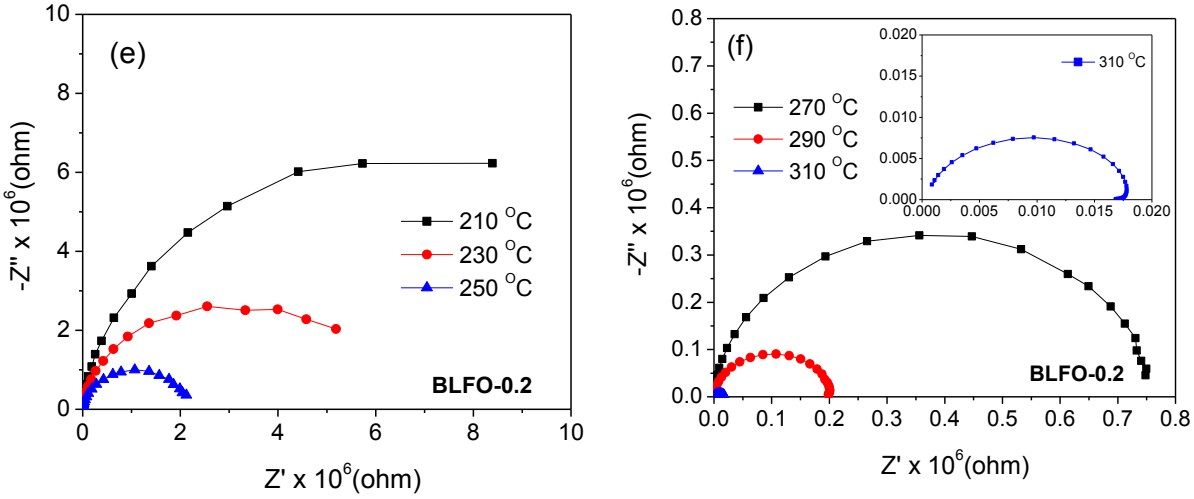

Figure 3.11 Variation of imaginary part Z'' with respect to real part Z' of complex impedance (Nyquist plots) for **(a, b)** BFO **(c, d)** BLFO-0.1 and **(e, f)** BLFO-0.2 samples.

The temperature dependent ac conductivity (σ_{ac}) follows the Arrhenius activation law and the activation energy can be determined as the slope of the straight line in plot of In (σ_{ac}) versus 1000/T as shown in **Figure 3.12**. The calculated value of activation energy is 0.69 eV for BFO, 0.58 eV for BLFO-0.1 and 1.07 eV for BLFO-0.2 ceramics. The obtained values of activation energy suggest the mixed type conducting process due to ionic polaronic and singly ionized oxygen vacancies **[23]**.

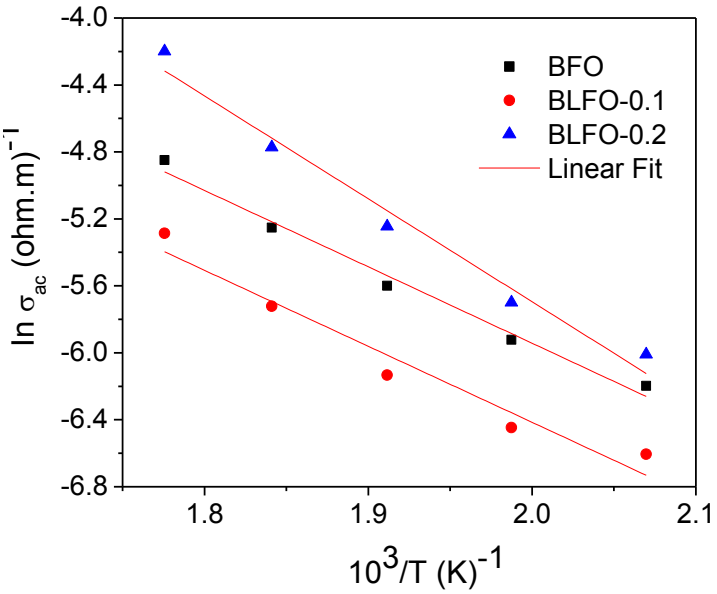

Figure 3.12 Arrhenius plot with temperature for BFO, BLFO-0.1 and BLFO-0.2 samples.

3.1.5 FERROELECTRIC STUDIES

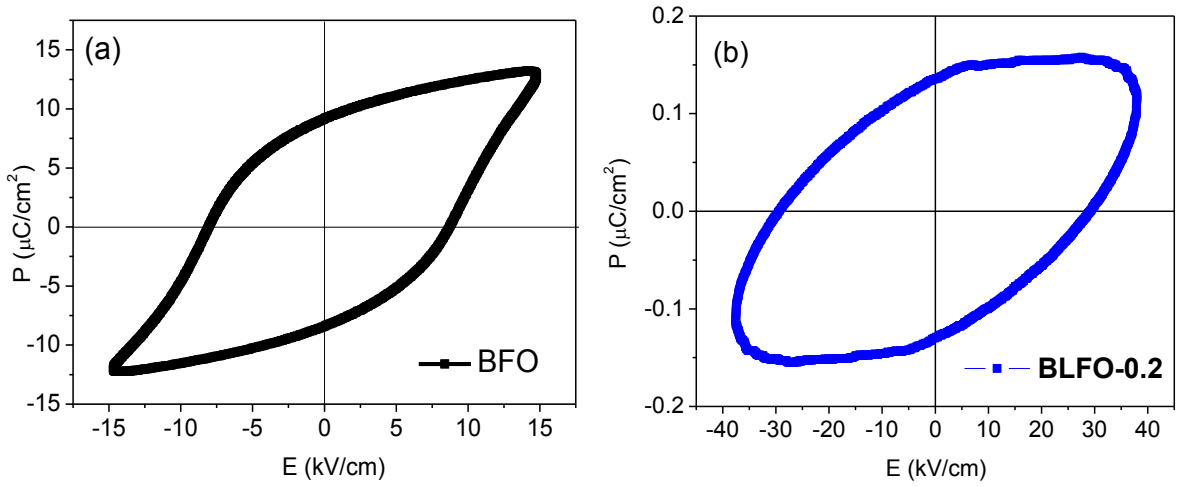

Figure 3.13 Room temperature polarization vs. electric field hysteresis loops of BFO and BLFO-0.2 ceramics.

Figure 3.13 shows the *P-E* hysteresis loops measured for BFO and BLFO-0.2 ceramics at 12 kV/cm. It is observed that BFO represent ferroelectric behavior with maximum polarization (P_{max}) of 12.72 μC/cm^2, remnant polarization (P_r) of 8.79 μC/cm^2, and coercivity (E_c) of about 8.38 kV/cm. It is also clearly seen that the loops are not really saturated and its ferroelectric behavior is degraded by substitution of La^{3+} ions. The observed behavior is directly attributed to the high leakage current **[24, 25]**. In addition, a decrease in polarization with increasing La^{3+} ions could also be ascribed to the fact that structural distortion decreases considerably (as evidenced by c/a ratio) with increase in substitution of La^{3+} ions.

3.1.6 MAGNETIC ANALYSIS

Room temperature *M-H* plots of $Bi_{1-x}La_xFeO_3$ (x=0.0, 0.1 and 0.2) nanoparticles are shown in **Figure 3.14**. At an applied field of 10 kOe, BFO nanoparticles show a weak ferromagnetic hysteresis loop because of the lattice strain-induced spin canting **[26]**. It is also noticed from the figure that La^{3+} substitution enhanced the magnetization (M_{max}) of BFO nanoparticles. Whereas, for BLFO-0.2 nanoparticles it is significantly lower, which is likely to occur because of the collinear antiferromagnetic ordering in the orthorhombic crystal symmetry which decreases the resultant M_{max} value **[27, 28]**. The obtained magnetic parameters for BFO, BLFO-0.1 and BLFO-0.2 nanoparticles are listed in **Table 3.2**. The observed hysteresis loops for all samples are not saturated even at 10KOe. The noticeable enhancement of ferromagnetism in

BLFO-0.1 and BLFO-0.2 than BFO nanoparticles could be due to modification of the spin spiral structure into linear **[29]** caused by change in bond angle Fe–O–Fe associated with the large distortion due to the considerable ionic mismatches between Bi^{3+} ions and La^{3+} ions. The obtained value of maximum magnetization (M_{max}) is higher for BLFO-0.2 than the earlier reported M-H measurements of La doped BFO ceramics **[4, 8]**.

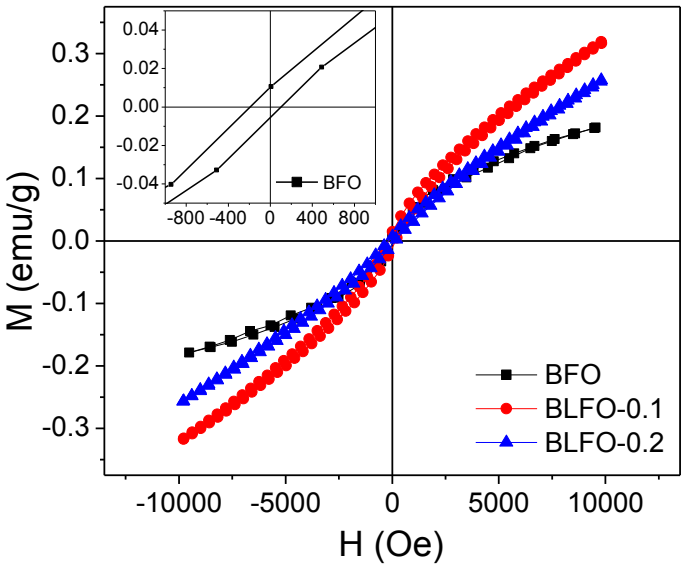

Figure 3.14 Room temperature magnetic hysteresis loops of BFO, BLFO-0.1 and BLFO-0.2 nanoparticles. Inset shows enlarged view of *M-H* loop for BFO nanoparticles.

Table 3.2 Room temperature magnetic parameters for $Bi_{1-x}La_xFeO_3$ (x=0.0, 0.1 and 0.2) nanoparticles.

Compositions	M_{max} **(emu/g)**	M_r **(emu/g)**	H_C **(Oe)**
BFO	0.180	0.0077	145.71
BLFO-0.1	0.318	0.0121	165.55
BLFO-0.2	0.257	0.0066	163.37

It is noticed that the substitution of La^{3+} ions increases H_c for BLFO-0.1 nanoparticles, whereas decreases with further increase in La^{3+} substitution. The increase in the coercivity could be attributed to decrease in the particle size from ~132 nm for BFO to ~91.37 nm for BLFO-0.1 because of lattice strain-induced spin canting or ferromagnetism in nanoscale **[26]**. Other contributing factor towards the change in coercivity is anisotropy (magnetocrystalline anisotropy, magnetoelastic anisotropy, shape anisotropy). Out of these, contribution of shape anisotropy could be excluded because of the spherical nature of nanoparticles as evidenced form

TEM. Therefore, the enhancement in the coercivity as observed for BLFO-0.1 ceramics might be caused by magnetocrystalline anisotropy and magnetoelastic anisotropy **[3, 30]**. However, further substitution of La^{3+} decreases the coercivity which could be ascribed to the decrease in magnetocrystalline anisotropy and thermal effects **[30, 31]**.

3.1.7 FTIR STUDIES

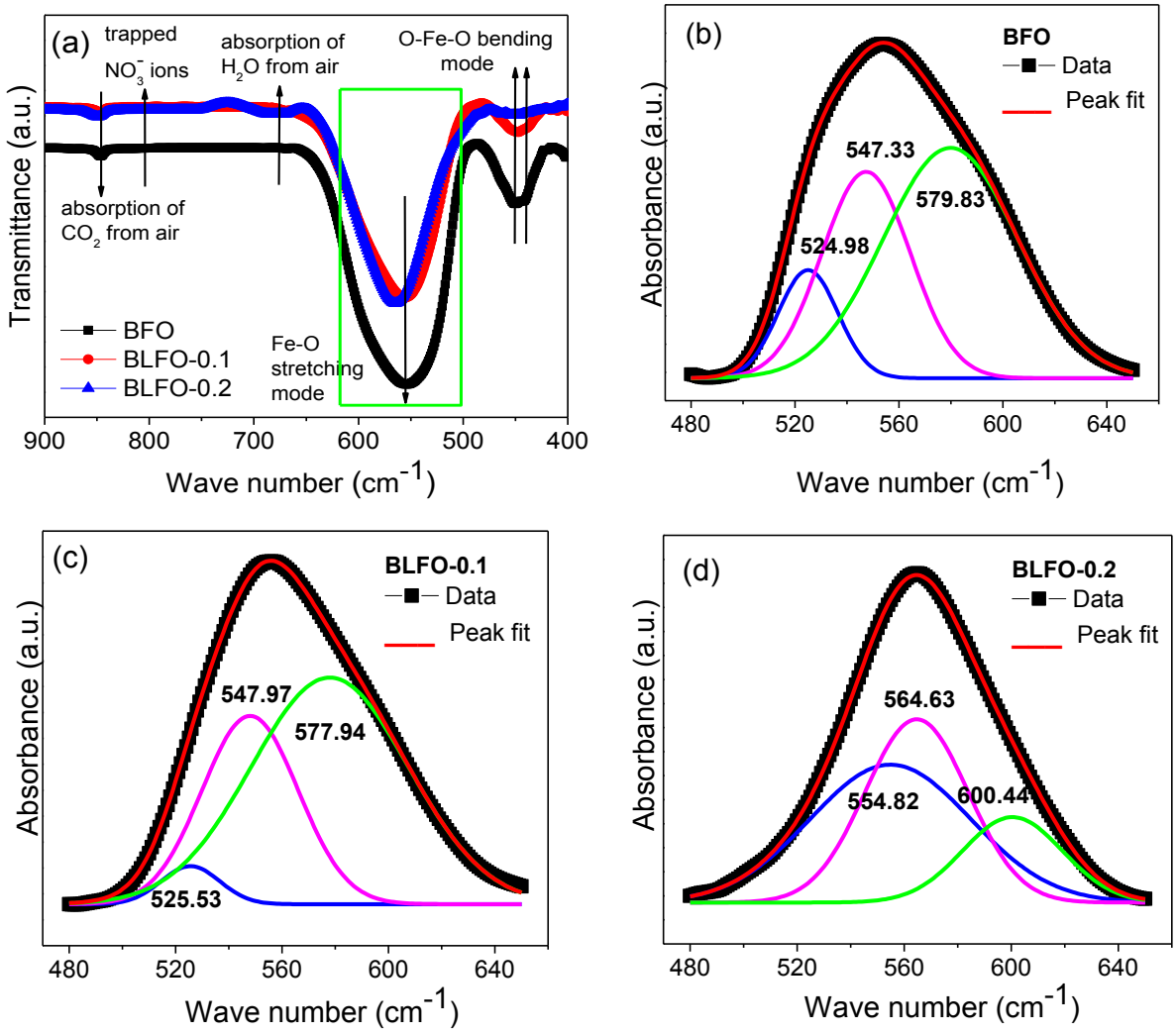

Figure 3.15 (a) FTIR spectra and **(b-d)** Gaussian fitting of FTIR spectra for BFO, BLFO-0.1 and BLFO-0.2 nanoparticles.

FTIR spectra of $Bi_{1-x}La_xFeO_3$ (x=0.0, 0.1 and 0.2) nanoparticles are shown in **Figure 3.15**. The broad band around 565 and 454 cm^{-1} in BFO are attributed to the overlapping of Fe-O bending and stretching mode in FeO_6 octrahedra and BiO_6 octahedral structure unit, respectively

[19, 32]. The presence of this metal-oxide band directly indicates the formation of highly crystalline BFO perovskite phase. However, the broad characteristic band as well as most complex part of the spectrum is the region from 480 to 660 cm^{-1}, which gets less broadened with the substitution of La^{3+} ions. For clarity, the spectra were deconvoluted in the wave number range of 470-650 cm^{-1} using the Gaussian type functions and is shown in **Figures 3.15 (b-d)**.

The IR peaks located at 524.98, 525.53, 554.82 cm^{-1} are attributed to Bi/La-O bond and the peaks at 547.33, 547.97, 564.97 cm^{-1} corresponds to Fe-O bond. In addition, sharp IR peaks located at 579.83, 577.94, 600.44 cm^{-1} are assigned to out of phase vibrations of oxygen atoms for BFO, BLFO-0.1 and BLFO-0.2 nanoparticles, respectively **[30]**. The observed shift in the position of the peaks with La^{3+} doping could be associated with change in the corresponding ionic sizes as well as the structural change, resulting in changed bond lengths and angles **[33]**. Bond length (r) of BFO, BLFO-0.1 and BLFO-0.2 nanoparticles can be determined from the position of the band (mentioned above) using an equation

$$k = \frac{17}{r^3} \qquad Eq.\ 3.3$$

where, k is average force constant and the average bond length of Fe-O and Bi/La-O can be correlated to the force constant of the nanoparticles which is given by;

$$\nu = \frac{1}{2\pi c}\sqrt{\frac{k}{\mu}} \qquad Eq.\ 3.4$$

Here the vibrational frequency of Fe-O and Bi/La-O bonds is related to their wave number (ν), average force constant (k) and effective mass (μ). However, the effective mass for BFO, BLFO-0.1 and BLFO-0.2 nanoparticles can be obtained by the equation;

For Fe-O bond,

$$\mu = \frac{M_O \times M_{Fe}}{M_O + M_{Fe}} \qquad Eq.\ 3.5$$

For Bi/La-O bond,

$$\mu = \frac{M_O \times [xM_{L_a} + (1-x)M_{B_i}]}{M_O + [xM_{L_a} + (1-x)M_{B_i}]} \qquad Eq.\ 3.6$$

where M_{Bi}, M_{La}, M_{Fe} and M_O are atomic weight of Bi^{3+}, La^{3+}, Fe^{3+} and O^{2-}, respectively. Thus, the values of effective mass and bond length (r) are extracted by using above mentioned

equations (3.3)-(3.6) and are listed in **Table 3.3**. The bond length values of Fe-O and Bi/La-O bonds are duly matched with the average bond lengths evaluated from rietveld refinement.

Table 3.3 Wave number, effective mass, force constant, Fe-O and Bi/La-O bond lengths calculated from FTIR spectra for $Bi_{1-x}La_xFeO_3$ (x=0.0, 0.1 and 0.2) nanoparticles.

Compositions		**BFO**	**BLFO-0.1**	**BLFO-0.2**
Fe-O bonds	**Wave number (cm^{-1})**	547.33	547.97	564.63
	Effective mass μ (10^{-26} kg)	2.065	2.065	2.065
	Force constant k (N cm^{-1})	2.196	2.201	2.337
	Bond Length (Å) (From FTIR)	1.978	1.976	1.937
	Bond Length (Å) (From Refinement)	2.171	2.143	2.036
Bi/La-O bonds	**Wave number (cm^{-1})**	524.98	525.53	554.82
	Effective mass μ (10^{-26} kg)	2.467	2.461	2.455
	Force constant k (N cm^{-1})	2.414	2.413	2.682
	Bond Length (Å) (From FTIR)	1.916	1.917	1.850
	Bond Length (Å) (From Refinement)	2.166	2.604	2.564

3.1.8 *UV*-VISIBLE ABSORPTION STUDIES

Figure 3.16 (a-c) shows the *UV*-Vis absorption spectra of $Bi_{1-x}La_xFeO_3$ (x=0.0, 0.1 and 0.2) nanoparticles where the absorption cutoff wavelengths are seen at 638.58 nm, 627.82 nm and 513.061 nm respectively as shown in the inset of **Figure 3.16 (a-c)**. This decrease in cutoff wavelength indicates the disturbance in electronic structure of BFO with the addition of La^{3+} ions and an obvious blue shift towards the lower wavelength due to the oxygen vacancies **[34, 35]**. The energy band gap of the nanoparticles calculated using Tauc's relationship,

$$\alpha h\nu = A(h\nu - E_g)^n \qquad Eq.\ 3.7$$

using n = ½. The observed band gap values of the nanoparticles increases from 2.04, 2.13 to 2.65 eV with increase in La^{3+} content from x=0.0 to 0.2 respectively, which is quite comparable with other reports **[34, 36, 37]**. Therefore increase in the band gap of the samples, increases the efficiency of photocatalytic activity in $Bi_{1-x}La_xFeO_3$ nanoparticles **[38]**.

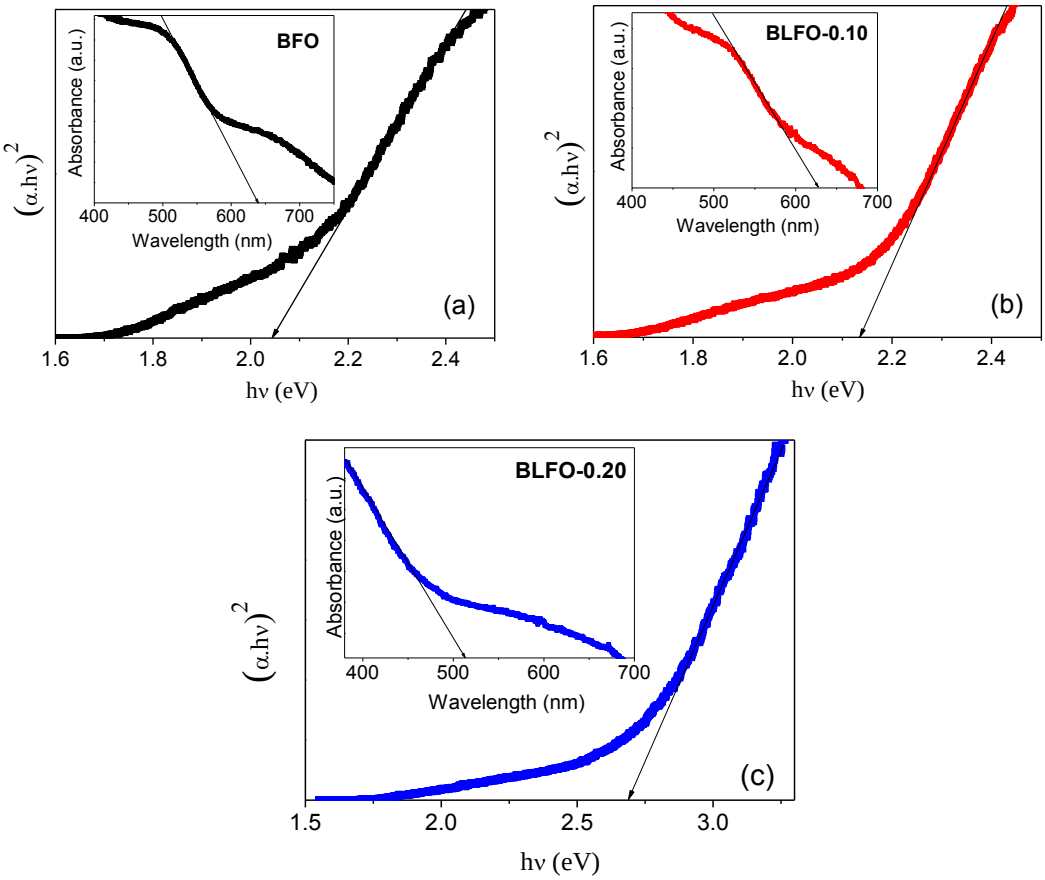

Figure 3.16 Tauc's plots **(a)** BFO, **(b)** BLFO-0.1 and **(c)** BLFO-0.2 nanoparticles. Inset shows the *UV*-Vis absorption spectra of nanoparticles.

3.1.9 PHOTOLUMINESCENCE STUDIES

To look into the active site properties of the metal oxide surface, PL spectra for $Bi_{1-x}La_xFeO_3$ (x=0.0, 0.1 and 0.2) nanoparticles at an excitation wavelength of 380 nm has been studied at room temperature. A blue emission nearly 488 nm is observed in the PL spectra of BFO which corresponds to the self-activated center as shown in **Figure 3.17**. The strong influence of La^{3+} doping in $Bi_{1-x}La_xFeO_3$ nanoparticles is evident from the shifting of the blue emission band towards lower wavelength **[39]**. This shifting of peak from 488.02 to 481.95 nm wavelength could be ascribed to the increase in band gap due to the small particle size of La^{3+} doped samples. Another high intensity peak is seen in the PL spectra, besides 488.02 nm wavelength. This green band emission around 528nm can be attributed to the transition of $5p^6$ electrons in La^{3+}. La^{3+}content in $BiFeO_3$ affect the green band emission by shifting the position of the band towards lower wavelength in few nm.

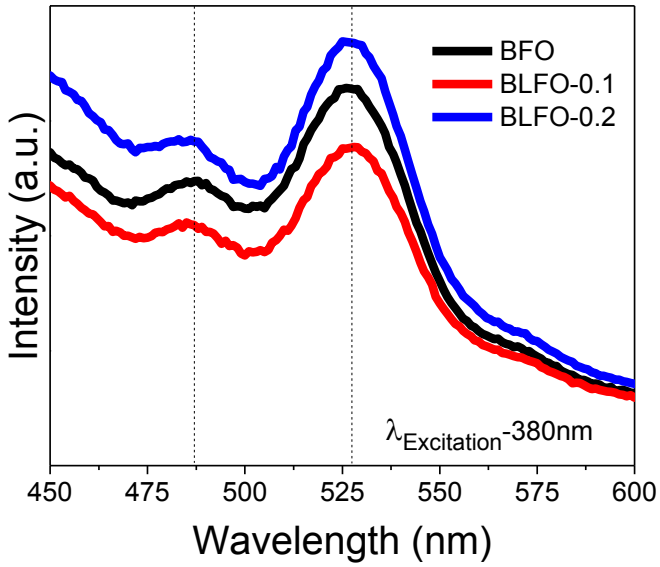

Figure 3.17 Photoluminescence spectra of BFO, BLFO-0.1 and BLFO-0.2 nanoparticles.

3.2 $Bi_{1-x}Ho_xFeO_3$ ($0.0 \leq x \leq 0.1$) ceramics

3.2.1 SYNTHESIS

Auto combustion method was used to fabricate $Bi_{1-x}Ho_xFeO_3$ (x=0.0, 0.05 and 0.1) ceramics. $Bi(NO_3)_3 \cdot 5H_2O$, $Fe(NO_3)_3.9H_2O$ and $Ho(NO_3)_3 \cdot 5H_2O$ were taken as precursor in appropriate amount. Bismuth nitrate and iron nitrate were dissolved in HNO_3 and deionized water, respectively. The solution was stirred using a magnetic stirrer for 30 minutes and $Ho(NO_3)_3 \cdot 5H_2O$ was added as doping element and glycine as fuel. The temperature of solution was sustained at 80 °C and the solution was stirred vigorously for 30 minutes. After auto-ignition, within a few minutes, brownish color ash was acquired. The ash was then dried at 100 °C in an electric oven for an hour and the fine powder obtained after drying was ground and calcined at 500 °C. The powder obtained was palletized to 10 mm with a pressure of 6 MPa and then sintered for 2 hours at 520 °C. The compositions of $Bi_{1-x}Ho_xFeO_3$ where x=0.0, 0.05 and 0.1 was signified as BFO, BHFO-0.05 and BHFO-0.1, respectively. The prepared samples were characterized by X-ray diffraction, TEM, FESEM for the investigation of structural properties, dielectric measurement, impedance and ferroelectric analysis for electrical properties, VSM for magnetic behavior, FTIR spectroscopy, *UV*-Visible spectrometer and PL spectroscopy for optical studies.

3.2.2 X-RAY DIFFRACTION STUDIES

The XRD analysis of $Bi_{1-x}Ho_xFeO_3$ nanoparticles and their refinements were executed to determine the change in structural parameters and their crystallite sizes as a result of Ho^{3+} doping. It is confirmed from the matching of the diffraction peaks with standard ICSD-Code 08-2614, that BFO has rhombohedral crystal symmetry with *R3c* space group as shown in **Figure 3.18 (a)**. Moreover, a noticeable change in the intensity and a shift in the position of diffraction peaks for BHFO-0.05 and BHFO-0.1 nanoparticles are also observed. **Figure 3.18 (b)** demonstrates that the splitting of (104) and (110) peaks are converged in case of BHFO-0.1 nanoparticles, which has been well described in previous published research articles as distortion in the crystal structure of the samples from rhombohedral to other symmetry **[1-3, 40]**. This structural or phase transformation is further confirmed by rietveld refinement using Fullprof as a tool.

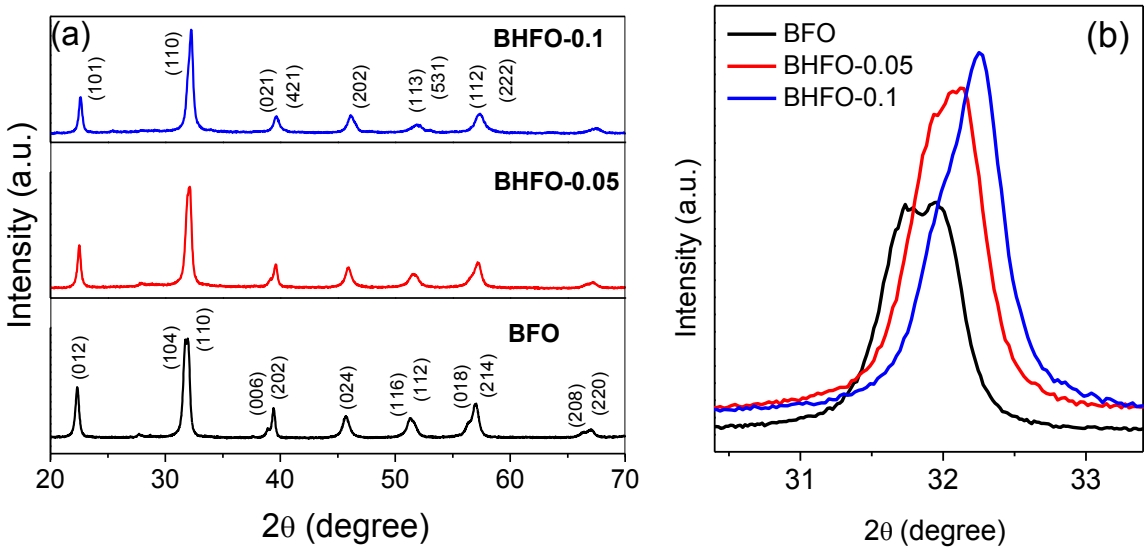

Figure 3.18 (a) X-ray diffraction patterns of $Bi_{1-x}Ho_xFeO_3$ nanoparticles ($0.0 \leq x \leq 0.1$) **(b)** Enlarged view of the characteristic peak.

The refinements for BFO and BHFO-0.05 nanoparticles were executed within the space group "*R*3*c*", where the closely spaced two most intense diffraction peaks (104) and (110) are fitted well with rhombohedral structural model. However, the rhombohedral structural model could not fit the observed crystal structure for BHFO-0.1 nanoparticles. Therefore, the refinement of XRD patterns for BHFO-0.1 was performed with an orthorhombic structural model and could be indexed using the orthorhombic phase "*Pnma*" which suggests the structural phase transformation at BHFO-0.1. Such type of structural transformation has also been reported

in RE doped BFO **[1-3, 40].** The observed, calculated and their difference of XRD profiles for BFO, BHFO-0.05 and BHFO-0.1 nanoparticles are shown in **Figure 3.19** and refined lattice parameters along with Fe-O-Fe bond angles are enlisted in **Table 3.4**.

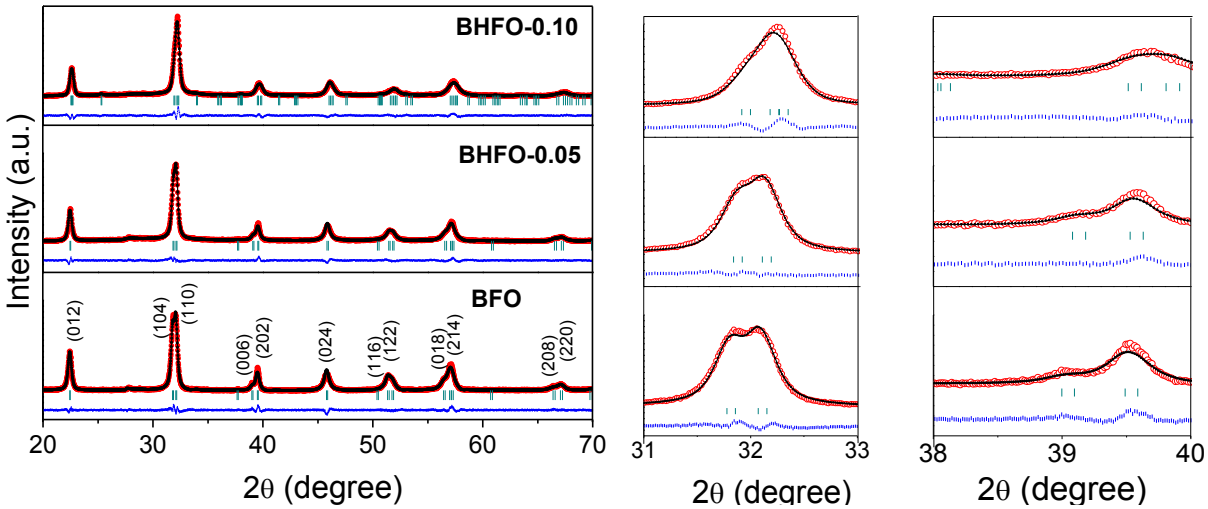

Figure 3.19 Rietveld refinements of the XRD patterns of BFO, BHFO-0.05 and BHFO-0.1 nanoparticles.

Table 3.4 Refined structural parameters for $Bi_{1-x}Ho_xFeO_3$ nanoparticles ($0.0 \leq x \leq 0.1$).

Composition of $Bi_{1-x}Ho_xFeO_3$	**Atom**	**Fractional coordinates**			**Lattice Constant [Å]**	**Bond angle [°]**	**Bond length [Å]**	**Statistical Parameter (%)**
		x	**y**	**z**				
BFO	Bi/Ho	0.0000	0.0000	0.0000	a=5.57	Fe-O-Fe	Bi-O=2.16	R_p=3.72
R3c	Fe	0.0000	0.0000	0.2212	c=13.84	=156.66	Fe-O=2.17	*Rwp*=4.85
V=372.95(Å^3)	O	0.4748	0.0178	-0.0563	c/a ratio-2.48			R_{exp}=3.41
								χ^2=2.02
BHFO-0.05	Bi/Ho	0.0000	0.0000	-0.2233	a=5.57	Fe-O-Fe	Bi/Ho-O =2.38	R_p=3.29
R3c	Fe	0.0000	0.0000	0.2062	c=13.81	= 164.6	Fe-O =2.025	*Rwp*=4.25
V=371.51(Å^3)	O	0.4748	0.0178	-0.0563	c/a ratio-2.47			R_{exp}=2.72
								χ^2=2.45
BHFO-0.1	Bi/Ho	0.0065	0.2500	0.0191	a= 5.60	Fe-O1-Fe	Bi/Ho-O1 =2.60	R_p=3.61
Pnma	Fe	0.0000	0.0000	0.5000	b= 7.84	= 161.53	Bi/Ho-O2 =2.68	*Rwp*=4.61
V= 243.52(Å^3)	O1	0.4450	0.2500	0.0149	c= 5.54	Fe-O2-Fe	Fe-O1=1.98	R_{exp}=2.74
	O2	0.1988	0.5344	0.2050	c/a ratio-0.98	= 153.43	Fe-O2=1.99	χ^2= 2.82

Williamson–Hall equation is used to calculate average crystallite size of the nanoparticles **[6, 7]** are shown in **Figure 3.20**. The obtained crystallite sizes of BFO, BHFO-0.05 and BHFO-0.1 nanoparticles are found to be 43.23 nm, 39.61 nm and 37.47 nm, respectively. The corresponding microstrain values are 0.00394, 0.00356 and 0.0041 for BFO, BHFO-0.05 and BHFO-0.1 nanoparticles, respectively. It is well known that the change in crystallite size of

ratify the modification of structural parameters as a result of Ho^{3+}-doping. The variation of c/a ratio and unit cell volume in terms of Ho^{3+} doping is shown in **Table 3.4**. It is observed that the normalized c/a ratio decreases with increasing Ho^{3+} substitution which has been described in previous reports as the diminution of rhombohedral symmetry and onset of orthorhombic symmetry. Also, a continual decrease in unit cell volume is due to the small difference in ionic radius of Bi^{3+} (ionic radii = 1.17 Å) and Ho^{3+} (ionic radii = 1.015 Å). Also, the observed change in Fe-O-Fe angle may cause changes in the tilting of FeO_6 octahedron, and subsequently a modification in magnetic and electrical properties is expected for $Bi_{1-x}Ho_xFeO_3$ nanoparticles **[41]**.

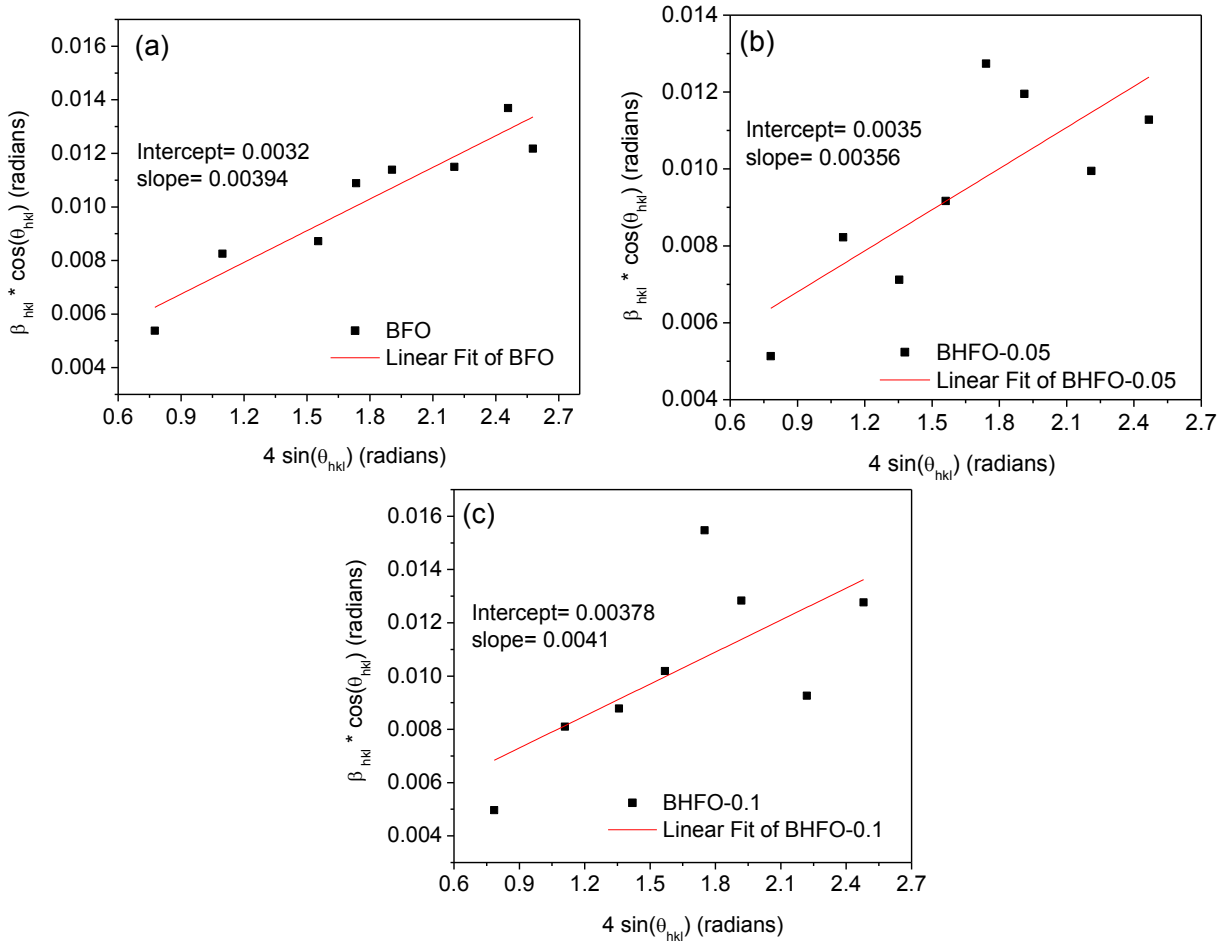

Figure 3.20 Williamson–Hall plots of BFO, BHFO-0.05 and BHFO-0.1 nanoparticles.

3.2.3 MORPHOLOGICAL STUDIES

The FESEM micrographs are shown in **Figures 3.21 (a-c)** reveal the effect of Ho^{3+}-doping on the morphology and the grain size of the $Bi_{1-x}Ho_xFeO_3$ ceramics. It is observed that BFO exhibits uniform grains throughout the surface together with an average grain size of ~422 nm. The average grain size gradually becomes smaller with the partial substitution of Ho^{3+} ions. The decrease in grain size for BHFO-0.05 and BHFO-0.1 suggests that Ho^{3+} ions act as grain growth inhibitor due to their relatively low diffusivity **[42, 43]**.

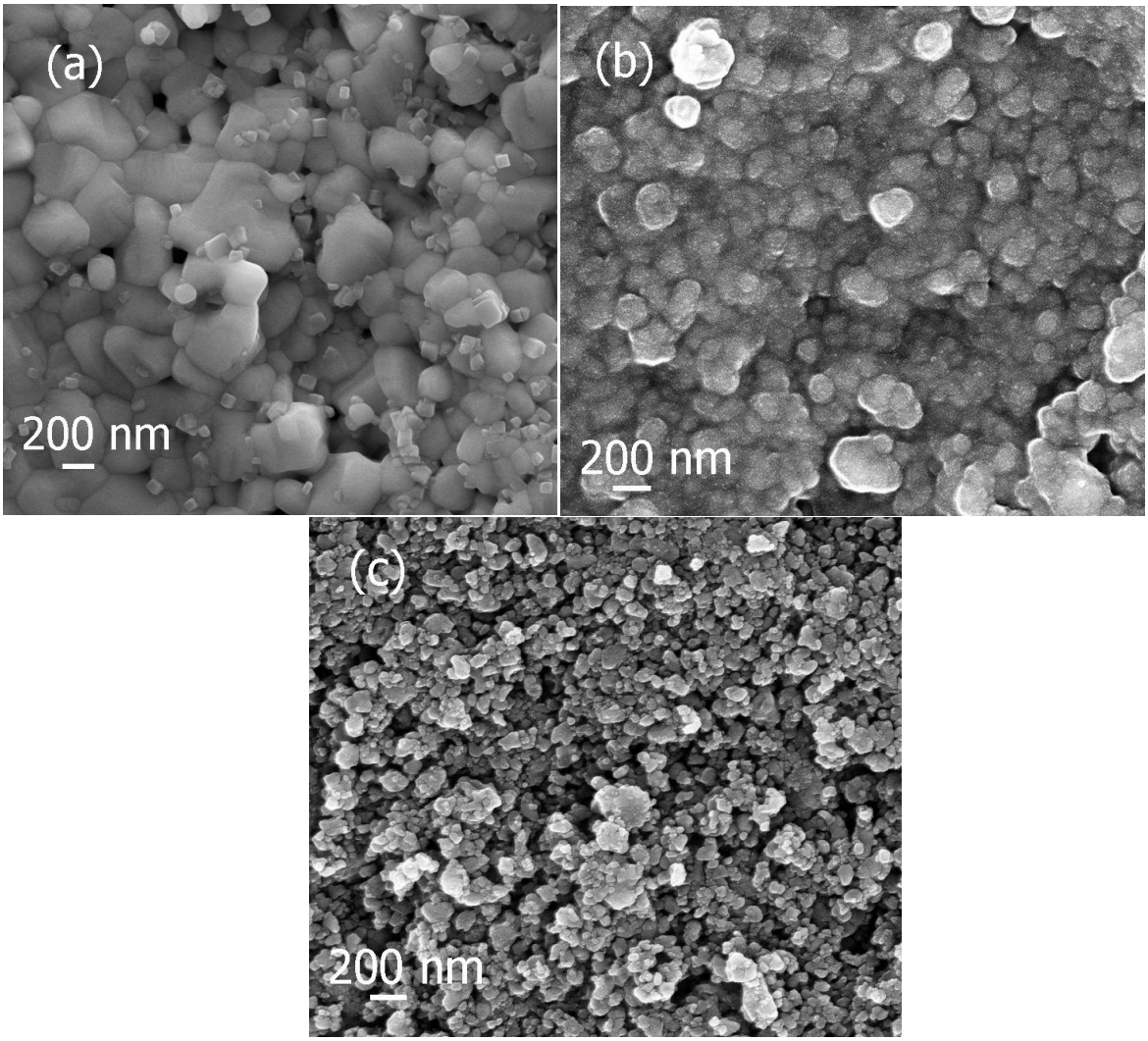

Figure 3.21 FESEM micrographs of **(a)** BFO **(b)** BHFO-0.05 and **(c)** BHFO-0.1 samples.

3.2.4 DIELECTRIC STUDIES

Figure 3.22 (a and b) shows the dielectric behavior for $Bi_{1-x}Ho_xFeO_3$ (x=0.0-0.1) ceramics as a function of frequency. Both ε and $tan\ \delta$ are observed to decrease significantly with

increase in frequency up to 10^4 Hz and thereafter, became frequency independent for all ceramics. It is also important to see that, with increasing Ho^{3+} doping ions, the value of ε decreased for BHFO-0.05 and increased for BHFO-0.1. The higher values of ε with the substitution of Ho^{3+} ions could be ascribed to the size effect of grains in ceramics. Ho^{3+} ions reduces the size of the grains and hence enhanced the volume fraction of grain boundaries which results in high value of ε. Dielectric loss (*tan* δ) is observed to decrease over the whole frequency range which indicates the rise in electrical resistivity with increase in Ho^{3+} ions substitution.

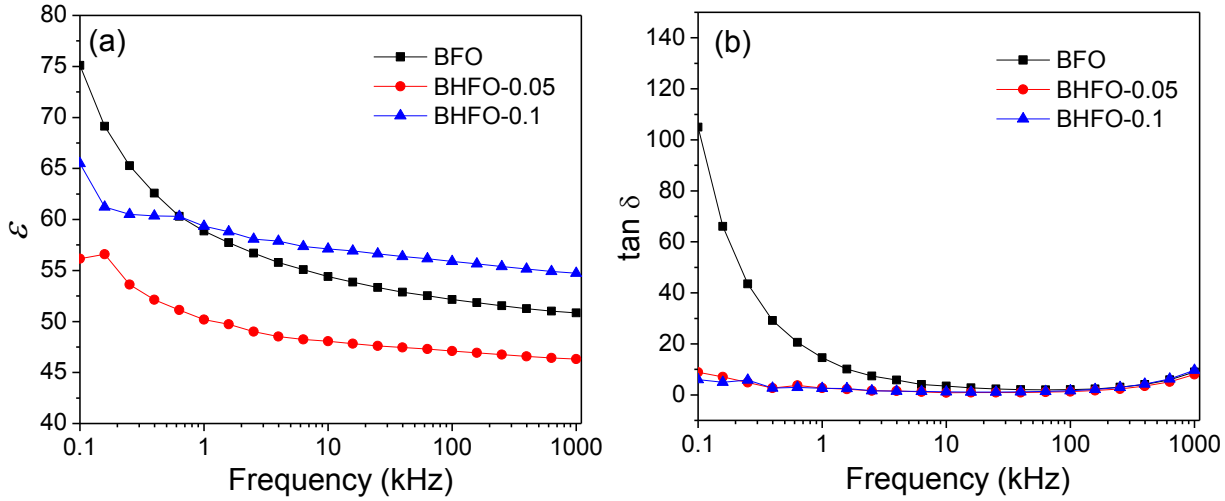

Figure 3.22 Variation of **(a)** dielectric constant (ε) and **(b)** dissipation factor (*tan* δ) for BFO, BHFO-0.05 and BHFO-0.1 samples as a function of frequency.

Figure 3.23 shows the temperature dependent dielectric behavior for $Bi_{1-x}Ho_xFeO_3$ (x=0.0-0.1) ceramics at different frequencies (100 Hz to 1 MHz). It is observed from the **Figure 3.22 (a)** that ε for BFO increases monotonically with increase in temperature at 100 Hz. Above 100 Hz, ε increases up to a certain peak temperature at all applied frequencies, attains its maximum value and decrease with further increase in temperature. The obtained peak temperature corresponds to an antiferromagnetic Neél temperature (T_N). However, the observed dielectric anomaly was attributed to the effect of vanishing spin ordering over dipole order **[15, 16]**. The variation of ε with the effect of Ho^{3+} substitution is shown in **Figures 3.23 (c-e),** which indicates an increase in T_N value for BHFO-0.05 and decreases with the further Ho^{3+} ion substitution. A noticeable shift in T_N may be attributed to the variation in the spin canted Fe-O-Fe angle due to the lattice modification. Similar dielectric anomaly has also been obtained in *tan* δ for $Bi_{1-x}Ho_xFeO_3$ (x=0.0-0.1) ceramics as shown in **Figures 3.23 (b, d and f)**.

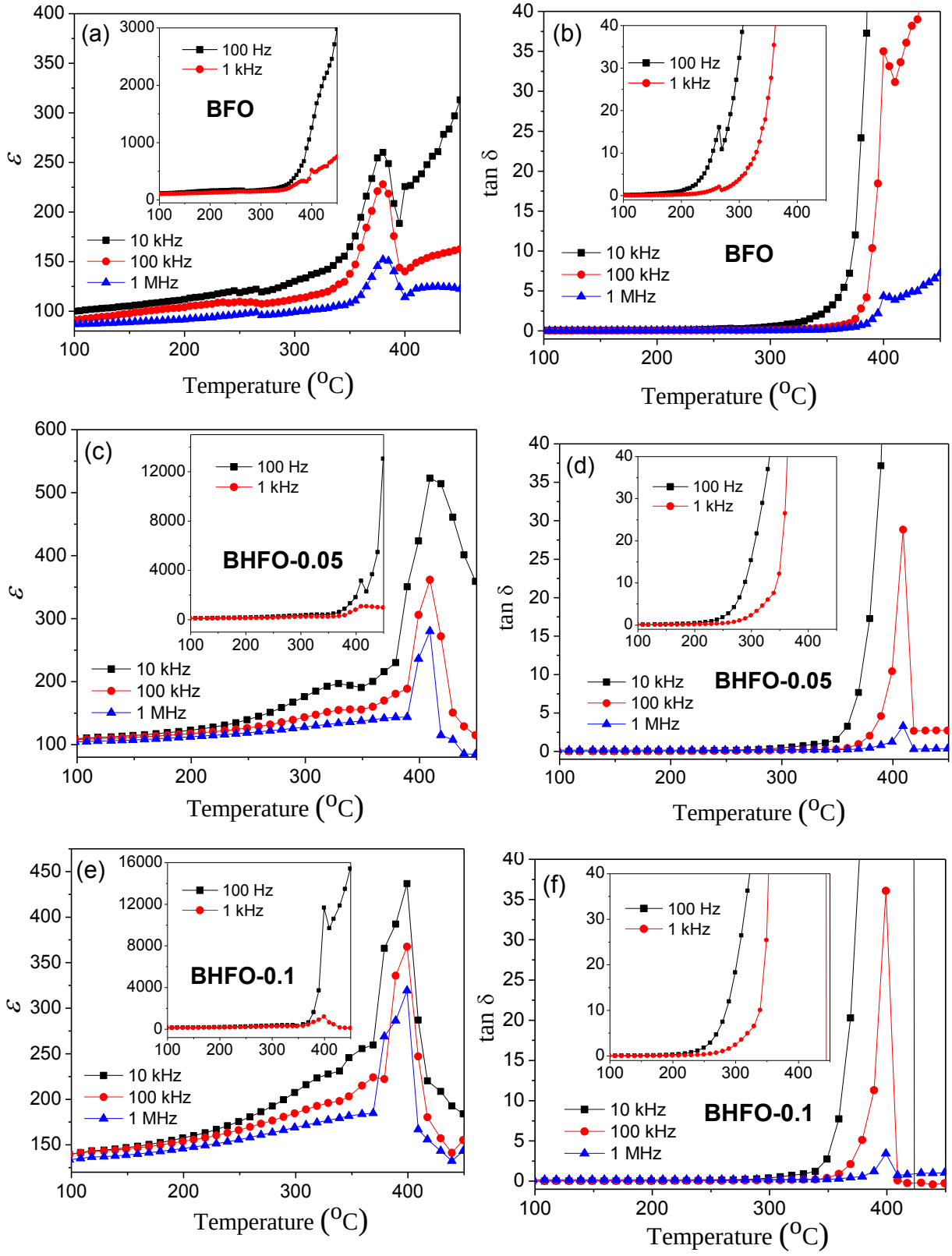

Figure 3.23 Dielectric constant (ε) and dissipation factor ($tan\ \delta$) versus temperature curves for $Bi_{1-x}Ho_xFeO_3$ samples at 100 Hz, 1 kHz, 10 kHz, 100 kHz and 1 MHz.

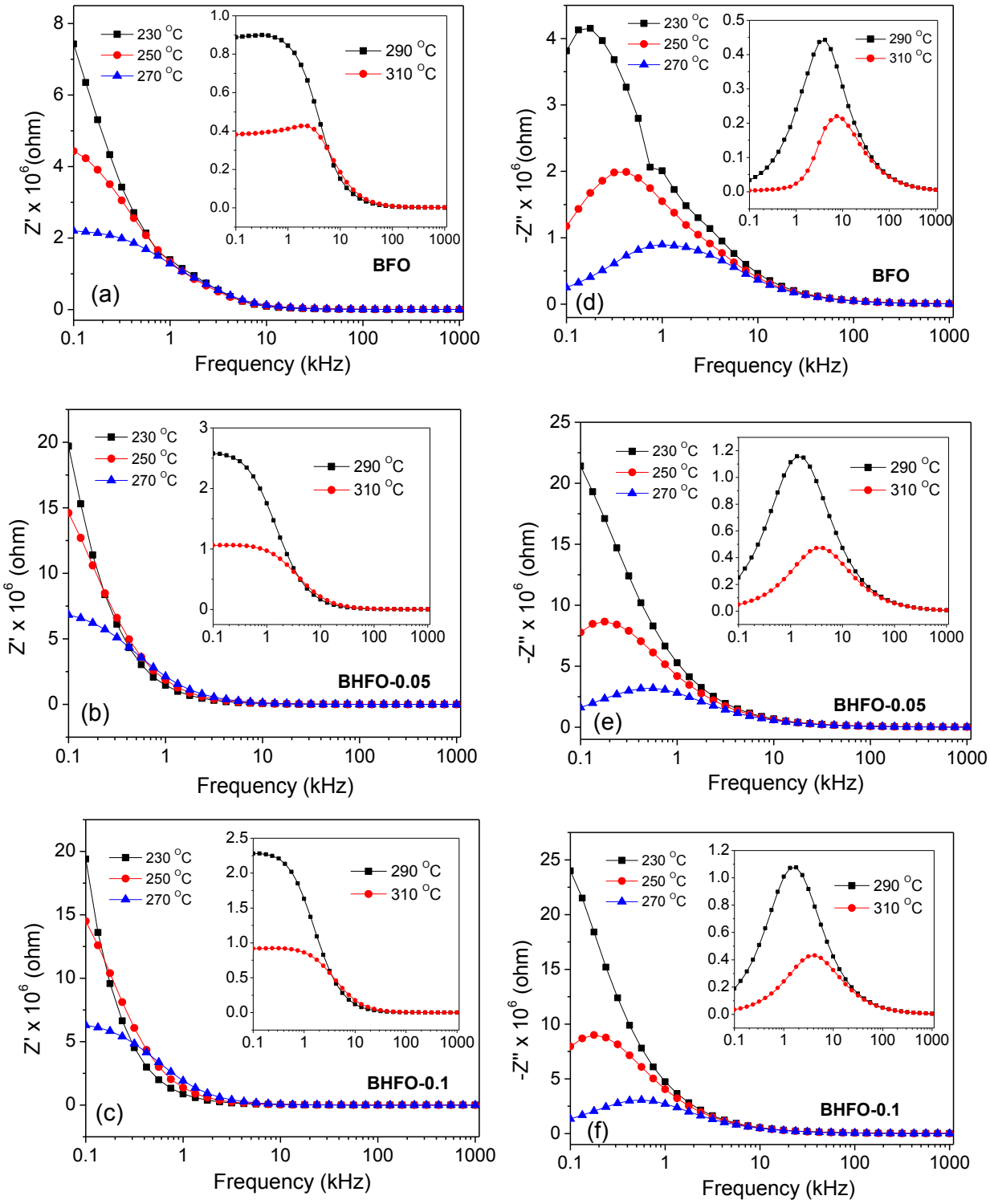

Figure 3.24 Frequency dependent real (Z') and Imaginary (Z'') part of impedance for BFO, BHFO-0.05 and BHFO-0.1 at 230 °C, 250 °C and 270 °C, the inset shows the variation of impedance at 290 °C and 310 °C.

Figure 3.24 shows the frequency dependence of the real (Z') and imaginary (Z'') part of impedance at various temperature for $Bi_{1-x}Ho_xFeO_3$ (x=0.0-0.1) ceramics. A monotonous decrease in Z' with the increase in frequency up to 10^4 Hz is observed at all temperatures (230 °C- 310 °C). Above 10^4 Hz, Z' spectra is found to coincide with each other for all temperatures. Therefore, the high values of Z' at lower frequencies along with merging tendency at higher frequency zone normally indicate the release of space charge polarization in ceramics **[21]**. However, the magnitude of Z' is observed to increase with increasing Ho^{3+} concentration (**Figures 3.24 (b and c))** which attributes to the decrease in conductivity of doped ceramics **[22]**.

It can be seen from the **Figure 3.24 (d)** that the Z'' frequency pattern also decreases monotonically with increase in frequency range of low temperature (at 230 °C). While, the appearance of a broad peak at a particular frequency f_{max} (called relaxation frequency) is observed at higher temperatures **[23]**. A clear shift of f_{max} towards the high frequency side with the rise in temperature is obtained. Moreover, the magnitude of peak is also found to decrease with increasing temperature. This behavior indicates the presence of an activated relaxation process in $Bi_{1-x}Ho_xFeO_3$ ceramics and may be considered due to **(a)** accumulation of space charge, **(b)** temperature dependent electrical relaxation phenomenon with a decrease in the mean relaxation time ($\tau = 1/2\Pi f_{max}$) and **(c)** increase in the distribution of τ, indicating a non-Debye relaxation process occurring in ceramics. The above observations are also observed in BHFO-0.05 and BHFO-0.1 ceramics as shown in **Figures 3.24 (e-f)** respectively.

Figures 3.25 (a-f) shows temperature dependent nyquist plots (Z'' vs. Z') for $Bi_{1-x}Ho_xFeO_3$ (x=0.0-0.1) ceramics at different temperatures (230 °C- 310 °C). The onset of a semicircle with large slopes at low temperature zone doesn't exhibit a unique relaxation time. However, the apparent single arc at high temperature region for each sample is directly indicative of an individual conduction and relaxation process in ceramics. Moreover, the value of resistance is obtained when semicircle intercepts the Z'-axis. The resistance is found to increase with Ho^{3+} substitution.

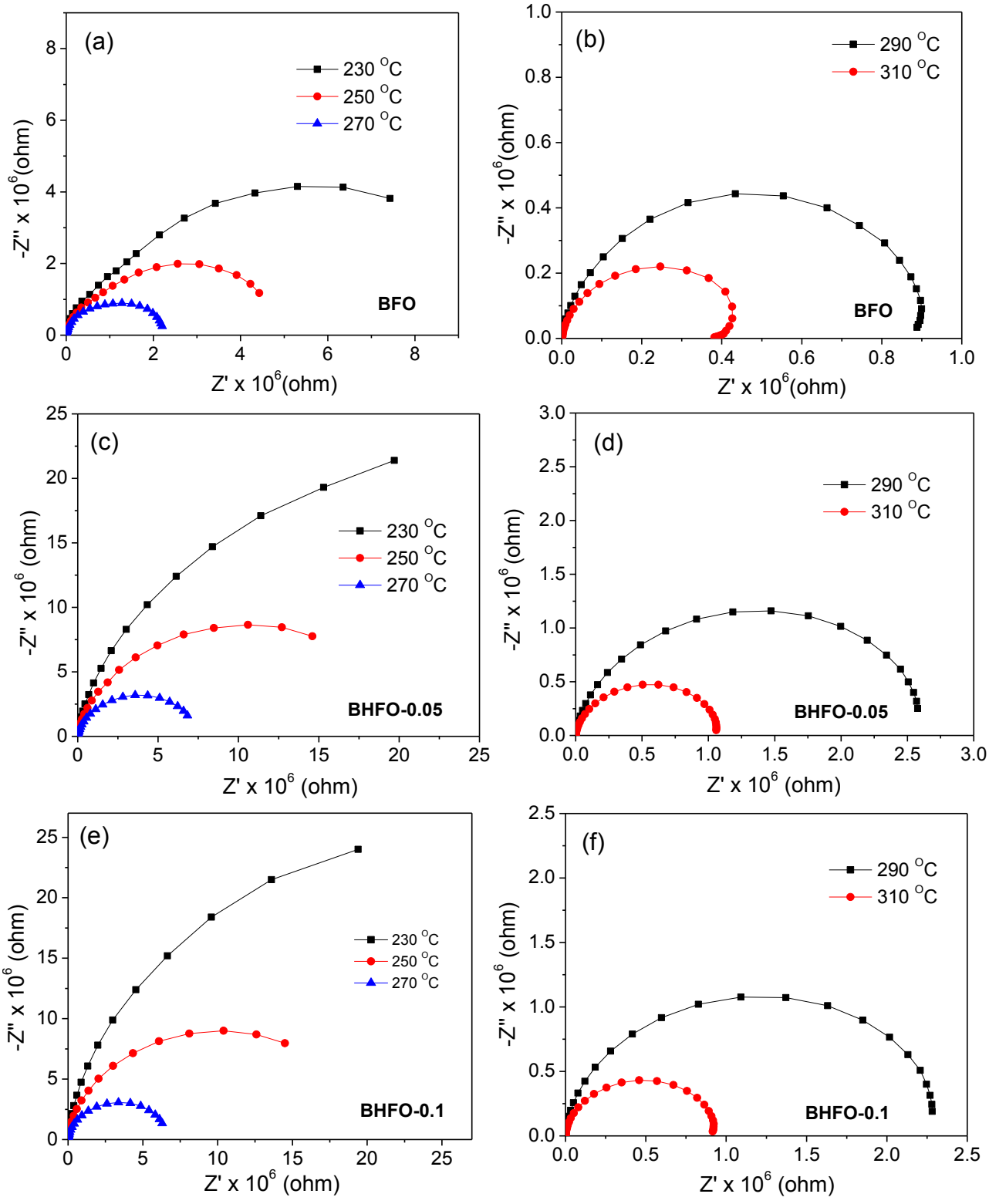

Figure 3.25 Variation of imaginary part Z'' with respect to real part Z' of complex impedance (Nyquist plots) for **(a, b)** BFO **(c, d)** BHFO-0.05 and **(e, f)** BHFO-0.1 samples.

The variation of ac conductivity (σ_{ac}) with respect to the inverse of temperature for $Bi_{1-x}Ho_xFeO_3$ (x=0.0-0.1) ceramics is shown in **Figure 3.26.** The calculated value of activation energy is 0.83 eV for BFO, 0.90 eV for BHFO-0.05 and 0.93 eV for BHFO-0.1 ceramics. The activation energy lie in a temperature range of 510 K-650 K, suggesting the conducting behavior of the ceramics due to the contribution of short range hopping movement of oxygen vacancies **[23]**.

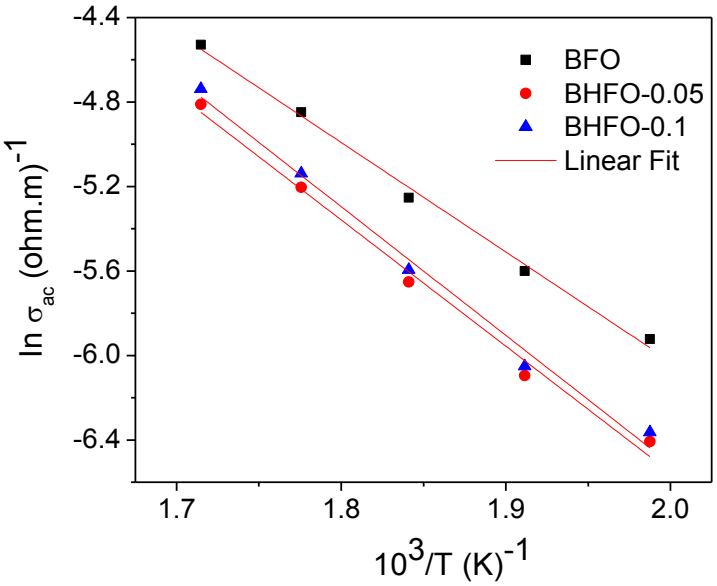

Figure 3.26 Arrhenius plot with temperature for BFO, BHFO-0.05 and BHFO-0.1 samples.

3.2.5 FERROELECTRIC STUDIES

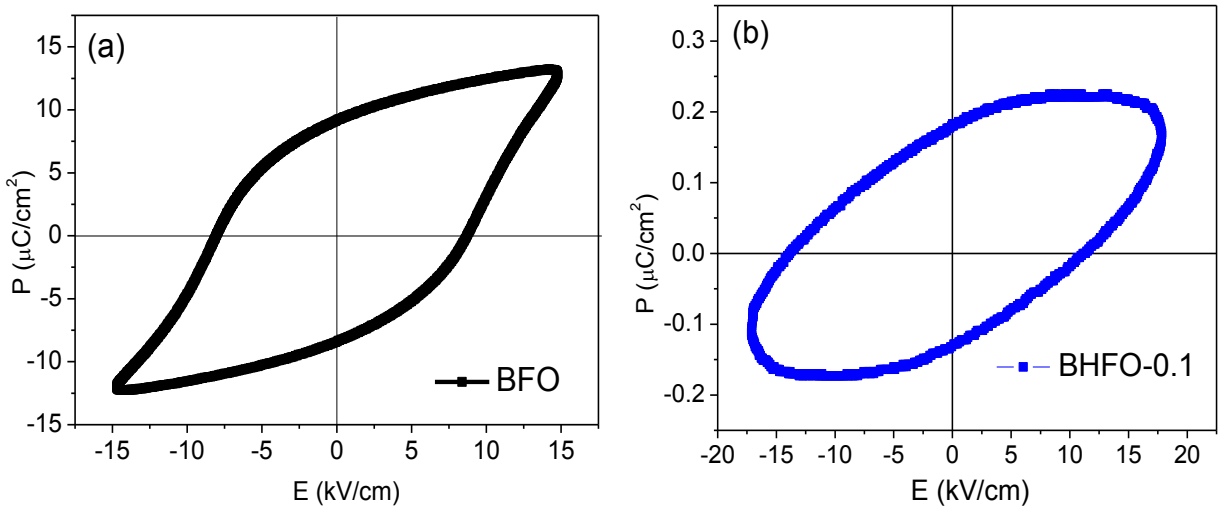

Figure 3.27 Polarization vs. electric field hysteresis loops of BFO and BHFO-0.1 ceramics.

The *P–E* hysteresis loops of BFO and BHFO-0.10 ceramics are shown in **Figure 3.27** which actually demonstrate the effect of Ho^{3+}-doping and particle size reduction. It is observed that BFO represent ferroelectric behavior with maximum polarization (P_{max}) of 12.72 μC/cm^2, remnant polarization (P_r) of 8.79 μC/cm^2, and coercivity (E_c) of about 8.38 kV/cm. In case of BHFO-0.10, nanoparticles have smaller crystalline sizes as compared to BFO, so the grain boundary is larger, therefore, the leakage current may be increased, and hence, the electrical property is degraded **[24, 25].**

3.2.6 MAGNETIC ANALYSIS

Figure 3.28 shows the *M-H* loops of $Bi_{1-x}Ho_xFeO_3$ nanoparticles with a magnetic field of 10kOe at room temperature. *M-H* loops indicate the weak ferromagnetic nature of BFO nanoparticles with maximum magnetization (M_{max}) of 0.180 emu/g, remnant magnetization (M_r) of 0.0101 emu/g and coercivity (H_c) 145.71 Oe, respectively. It is evident from the **Figure 3.28 (a)** that M_r and M_{max} for all the nanoparticles increase with the increment of Ho^{3+} doping content and obtained values of M_{max} and M_r are listed in **Table 3.5**. The observed onset of ferromagnetism in BFO, BHFO-0.05 and BHFO-0.1 nanoparticles could be due to collapse of the spin cycloid structure by Ho^{3+} doping in addition to structural distortion which is quantified from XRD data as variation in Fe-O-Fe bond angles (**Table 3.4**) **[23]**. However, the variation in bond angle alters the tilting angle of FeO_6 octahedral which may be suppressing the spin spiral structure and, hence, outset net magnetization in Ho^{3+} doped nanoparticles **[44, 45]**.

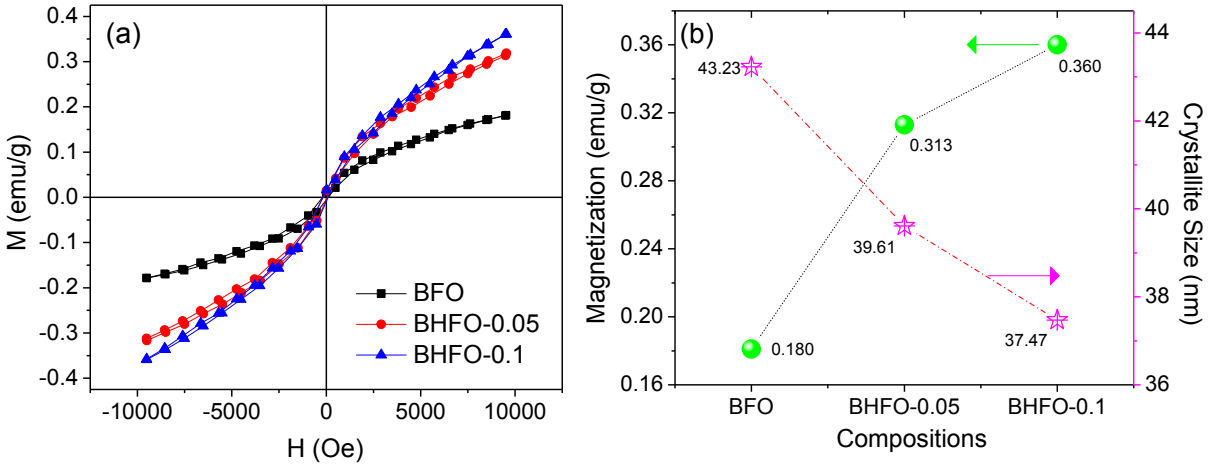

Figure 3.28 (a) Room temperature magnetic hysteresis loops of BFO, BHFO-0.05 and BHFO-0.1 nanoparticles. **(b)** Variation of magnetization and crystallite size with the concentration of the nanoparticles.

The calculated coercivity H_c is 145.71 Oe for BFO nanoparticles. It is clear that the substitution of Ho ions significantly decreases H_c of 113.19 Oe for BHFO-0.05 nanoparticles. However, a further increment of Ho increases the value of H_c from 113.19 to 135.58 Oe for BHFO-0.1 nanoparticles. The larger values of H_c in nanoparticles may be related to their magneto-crystalline anisotropy and magnetoelastic anisotropy **[3, 28-29]**.

Table 3.5 Room temperature magnetic parameters for $Bi_{1-x}Ho_xFeO_3$ nanoparticles ($0.0 \leq x \leq 0.1$).

Compositions	M_{max} **(emu/g)**	M_r **(emu/g)**	H_C **(Oe)**
BFO	0.180	0.0077	145.71
BHFO-0.05	0.313	0.0095	113.19
BHFO-0.1	0.360	0.0122	135.58

As magnetic properties are size dependent, **Figure 3.28 (b)** shows the correlation between magnetism, Ho^{3+} doping and crystallite size of BFO, BHFO-0.05 and BHFO-0.1 nanoparticles. It is visualized from the figure that the magnetization has been found to increase drastically with the increase in Ho^{3+} doping as well as decreasing crystallite size. This could be ascribed to incomplete spin compensation at the surface of antiferromagnetic BFO which becomes measurable on reducing its size **[46]**. Hence, the surface-to-volume ratio increases and so does the contribution of non-compensated spins present on particle's surface. In addition, the Fe-O-Fe bond angle reduces with the decreasing crystallite size for all nanoparticles. The antiferromagnetic super exchange interaction weakens with reducing the bond angle which results in a spin canting bit away from the perfect antiferromagnetic structure and introduce weak ferromagnetic interaction in the nanoparticles. The weakening of antiferromagnetic interaction could be one of the significant factors behind the apparent rise of magnetization with decreasing crystallite size. Furthermore, *M-H* loops are not saturated even at high applied magnetic field of 10 kOe indicating the sluggish transformation of G-type antiferromagnetic nature of BFO into weak ferromagnetic Ho^{3+} doped nanoparticles.

3.2.7 FTIR STUDIES

FTIR spectra of BFO, BHFO-0.05 and BHFO-0.1 nanoparticles are shown as **Figure 3.29 (a)**. Expected O-Fe-O bending and Fe-O stretching vibration of the FeO_6 octahedral unit is

observed near the absorption band at 448 cm^{-1}. Similar band is also attributed to BiO_6 octahedral structure unit that exhibits absorption at 457 cm^{-1} **[19, 32]**. Above 650 cm^{-1}, some less intense IR peaks are observed at ~811, ~672 and ~846 cm^{-1}. These IR peaks correspond to the trapped NO_3^- ions, OH group vibration of absorbed H_2O and CO_2 from surroundings, when precursor was calcined. However, the broad characteristic band as well as most complex part of the spectrum is the region from 480 to 660 cm^{-1}, which gets less broadened on Ho^{3+} doping.

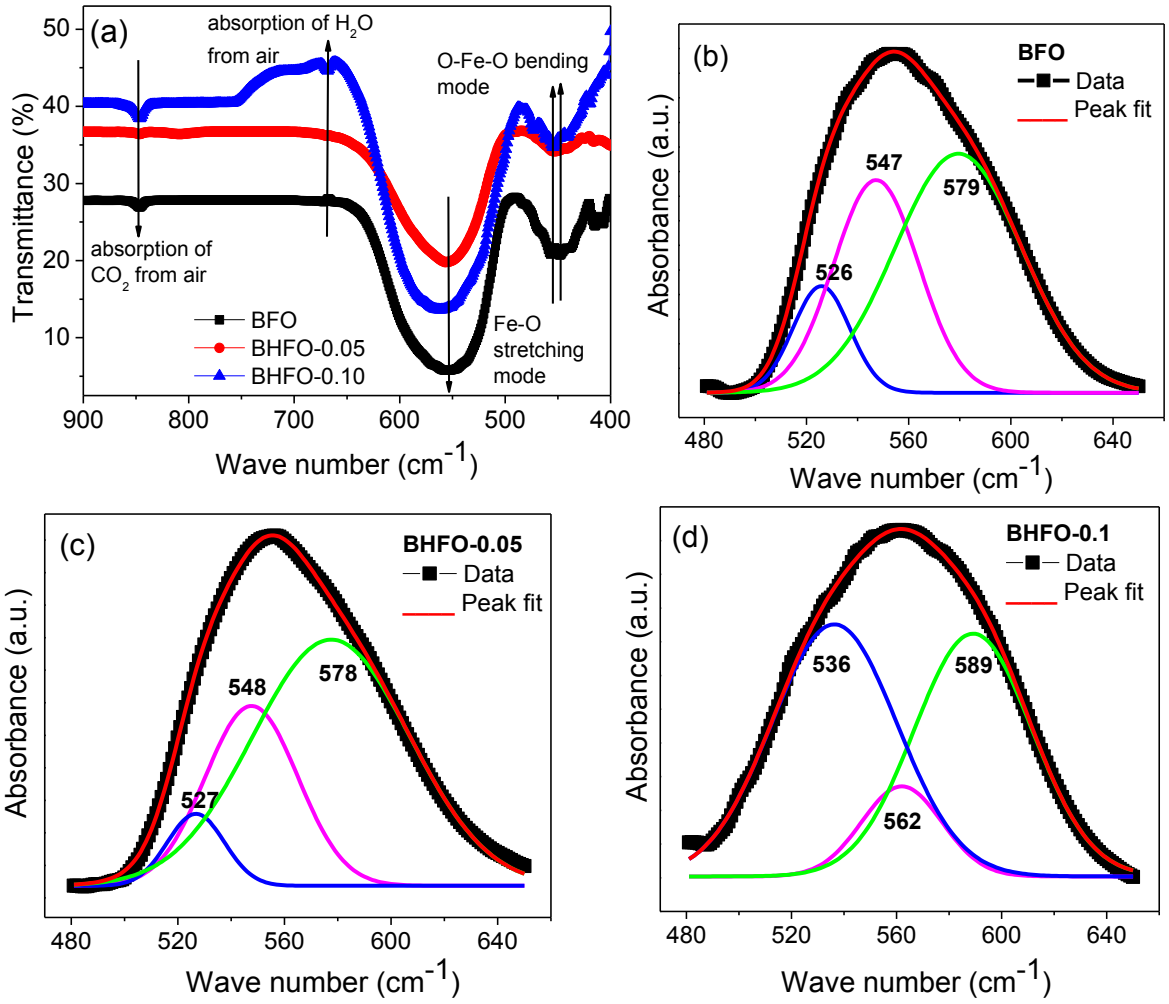

Figure 3.29 (a) FTIR spectra and **(b-d)** Gaussian fitting of FTIR spectra for BFO, BHFO-0.05 and BHFO-0.1 nanoparticles.

For clarity, the spectra were deconvoluted in the wave number range of 470-650 cm^{-1} using the Gaussian type functions and is shown in **Figures 3.29 (b-d)**. The IR peaks located at 526, 527, 536 cm^{-1} are attributed to Bi/Ho-O bond and the peaks at 547, 548, 562 cm^{-1} corresponds to Fe-O bond. In addition, sharp IR peaks located at 579, 578, 589 cm^{-1} are assigned

to out of phase vibrations of oxygen atoms for BFO, BHFO-0.05 and BHFO-0.1 nanoparticles, respectively **[30]**. The observed shift in the position of the peaks with Ho doping could be associated with change in the corresponding ionic sizes as well as the structural change, resulting in changed bond lengths and angles **[33]**. The bond length values of Fe-O and Bi/Ho-O bonds are closely matched with the average bond lengths evaluated from rietveld refinement and are listed in **Table 3.6**.

Table 3.6 Wave number, effective mass, force constant Fe-O and Bi/Ho-O bonds lengths calculated from FTIR spectra for $Bi_{1-x}Ho_xFeO_3$ nanoparticles ($0.0 \leq x \leq 0.1$).

Compositions		**BFO**	**BHFO-0.05**	**BHFO-0.1**
Fe-O bonds	**Wave number (cm^{-1})**	547	548	562
	Effective mass μ (10^{-26} kg)	2.065	2.065	2.065
	Force constant *k* (N cm^{-1})	2.193	2.201	2.315
	Bond Length (Å) (From FTIR)	1.979	1.976	1.943
	Bond Length (Å) (From Refinement)	2.171	2.025	1.992
Bi/Ho-O bonds	**Wave number (cm^{-1})**	526	527	536
	Effective mass μ (10^{-26} kg)	2.467	2.465	2.463
	Force constant *k* (N cm^{-1})	2.422	2.430	2.512
	Bond Length (Å) (From FTIR)	1.914	1.912	1.891
	Bond Length (Å) (From Refinement)	2.166	2.387	2.643

3.2.8 *UV*-VISIBLE ABSORPTION STUDIES

Figure 3.30 (a) shows the *UV*–Vis absorption spectra of BFO, BHFO-0.05 and BHFO-0.1 nanoparticles derived from the absorption spectroscopy. The absorption cut-off wavelength decreases with increasing Ho^{3+} doping content and their corresponding values are calculated as 638.58, 631.56 and 626.91 for BFO, BHFO-0.05 and BHFO-0.1 nanoparticles, respectively. The observed blue shift in cut off wavelength indicates the disturbance in electronic structure and creation of oxygen vacancies in BFO with the addition of Ho^{3+} ions **[35, 36]**.

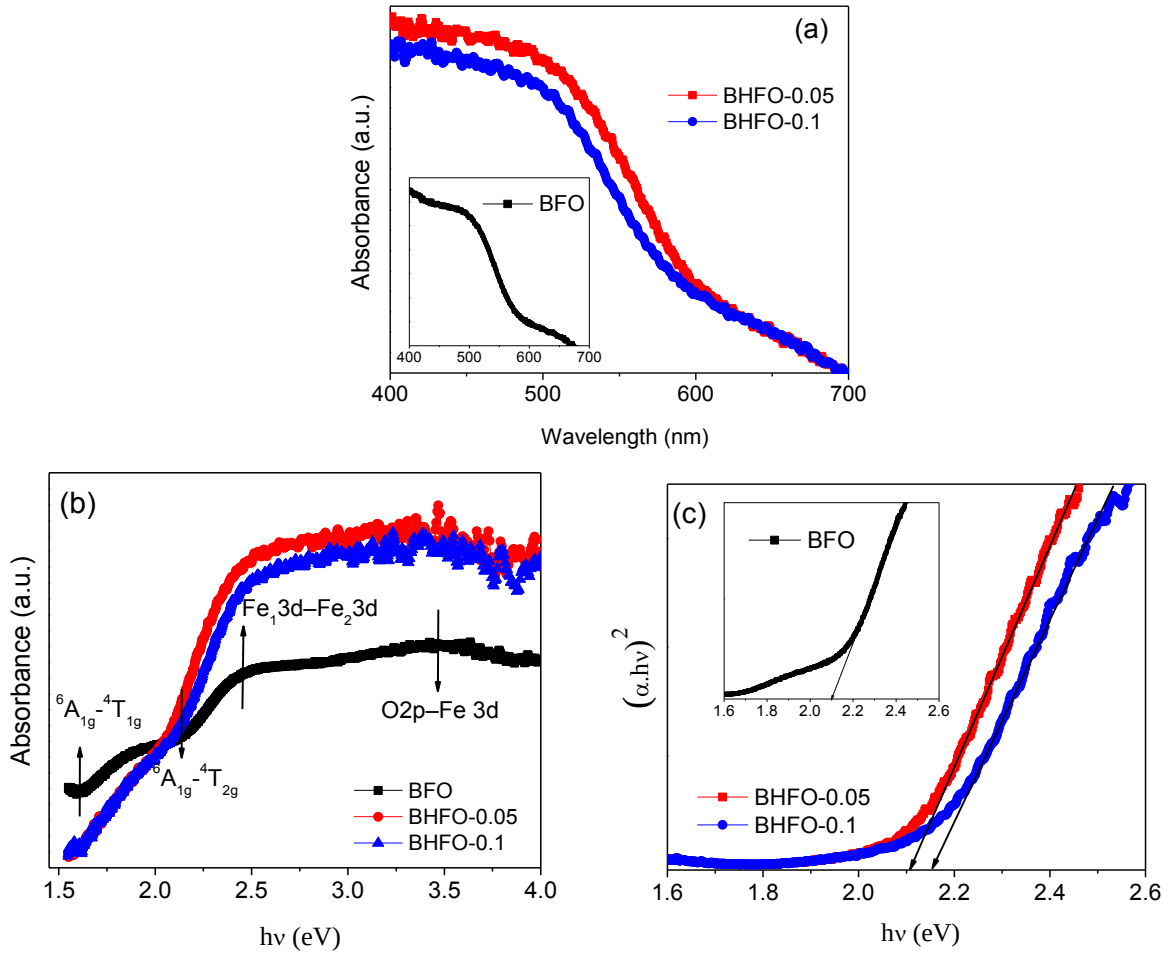

Figure 3.30 (a) *UV* absorption spectra and **(b)** *UV*-Vis absorption spectrum versus energy and **(c)** Tauc's plots for BFO, BHFO-0.05 and BHFO-0.1 nanoparticles.

In general, it is expected to have main six transitions in-between 0 and 3 eV in the electronic structure of BFO using the correlation group and subgroup analysis **[49]**. **Figure 3.30 (b)** shows usual transition states in BFO, BHFO-0.05 and BHFO-0.1 nanoparticles derived from absorption spectra, which is plotted as a function of energy (eV). A broad absorption band located at 3.67 eV is assigned to inter-atomic O 2p–Fe 3d electronic excitations in FeO_6 Octahedral **[50]**. However, a weak shoulder peak besides 3.67 eV is observed, which is associated with the $Fe_1$3d–$Fe_2$3d inter-site electron transfer. The absorption spectrum exhibiting two on-site d to d crystal field transitions of Fe ions positioned at 1.57 and 1.98 eV which are assigned to $^6A_{1g}$-$^4T_{1g}$ and $^6A_{1g}$-$^4T_{2g}$ electronic excitations respectively, caused by the relaxation of spin–orbit coupling **[51]**. A small shift and splitting of strongly hybridized O p to Fe d excitations clearly indicated the distortion in FeO_6 octahedral unit cell induced by Ho^{3+} dopants.

The energy band gap for BFO, BHFO-0.05 and BHFO-0.1 nanoparticles is calculated from classical Tauc's relation and is shown in **Figure 3.30 (c)**. The value of energy band gap is estimated to be 2.04, 2.10 and 2.16 eV for BFO, BHFO-0.05 and BHFO-0.1 nanoparticles, respectively, indicating its photocatalytic ability for visible light exposure **[35, 37-39]**.

3.2.9 PHOTOLUMINESCENCE STUDIES

PL spectra of BFO, BHFO-0.05 and BHFO-0.1 nanoparticles at room temperature are shown in **Figure 3.31**. **Figure 3.31 (a)** shows an intense blue emission around 486 nm may be ascribed to the inter-band transition corresponding to the self-activated center. The emission, corresponding to the 527 nm, can be attributed unambiguously to the transition of an inter-site electron band in BFO nanoparticles **[31]**.

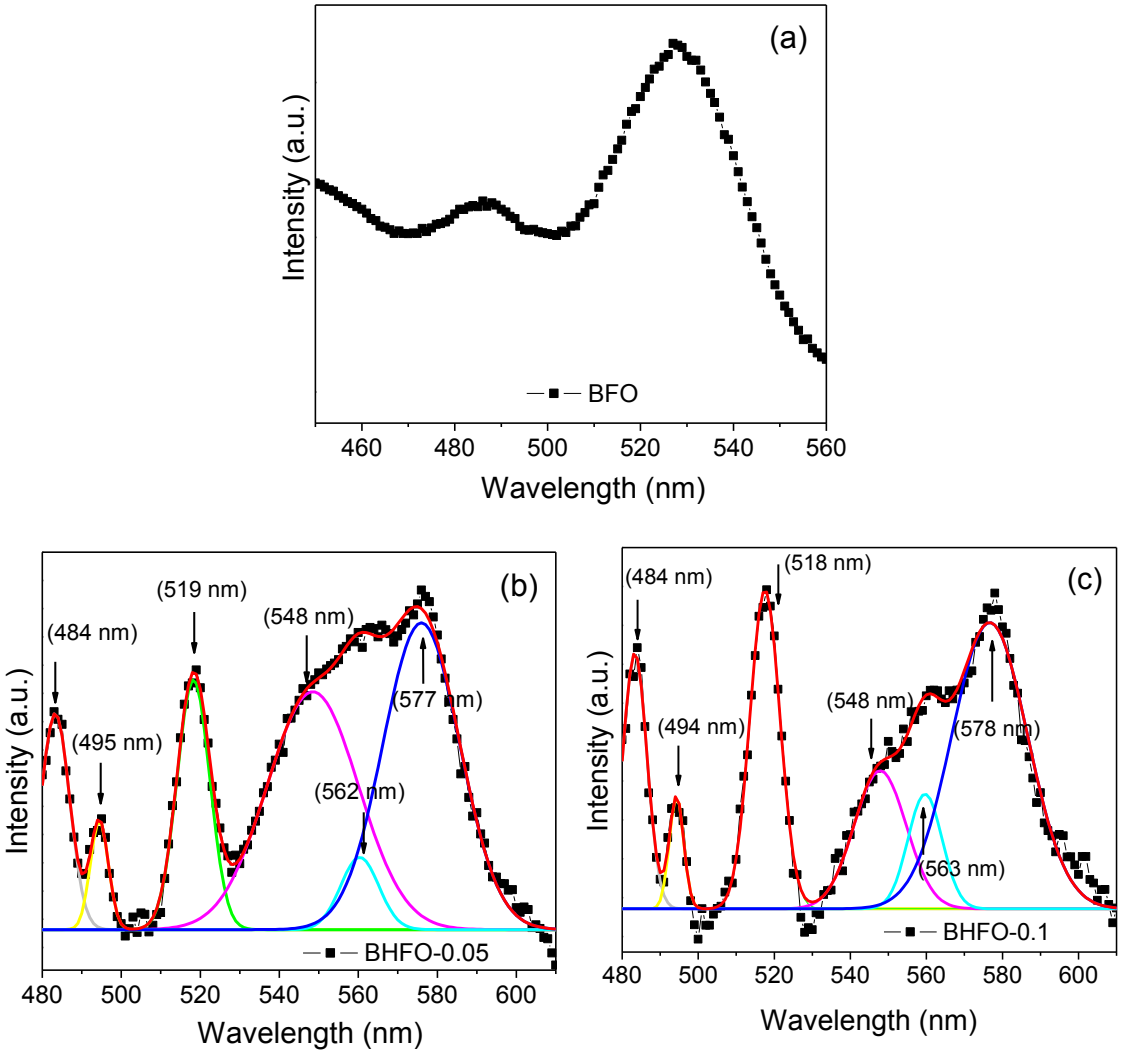

Figure 3.31 Photoluminescence spectra of **(a)** BFO **(b)** BHFO-0.05 and **(c)** BHFO-0.1 nanoparticles.

Ho^{3+} doping arising three emission transitions within 4f-4f levels in BFO are observed for both Ho^{3+} doped samples in visible region of the spectrum as shown in **Figure 3.31 (b and c)**. It is observed that a strong blue emission peak at 484 nm along with a broad hump nearly at 495 nm could be attributed to $^5F_3$-$^5I_8$ transitions **[47, 48]**. An intense yellow-green emission gets broadened due to the overlapping of different Ho^{3+} transitions. The broad yellow–green emission in the wavelength range from 540 to 600 nm can be deconvoluted as centered around 547, 558 and 576 nm in **Figures 3.31 (b and c).** These weak yellow-green emissions may be assigned to electronic transition from the thermalized states $^5F_4$ and $^5S_2$ to $^5I_8$ ground state, respectively **[47]**. Any other emission of lower energies must come from various impurities or defect levels within the energy band gap of the nanoparticles. These blue and yellow emissions lies in the visible region for BFO, BHFO-0.05 and BHFO-0.1 nanoparticles are important for optical electronic device applications.

3.3 $Bi_{1-x}Ba_xFeO_3$ ($0.0 \leq x \leq 0.2$) ceramics

3.3.1 SYNTHESIS

Appropriate amounts of $Bi(NO_3)_3 \cdot 5H_2O$, $Fe(NO_3)_3.9H_2O$ and $Ba(NO_3)_3 \cdot 3H_2O$ and glycine was used to synthesize $Bi_{1-x}Ba_xFeO_3$ (x=0.0, 0.1 and 0.2) ceramics by combustion method. To obtained homogeneous solution, Bismuth nitrate in HNO_3, iron nitrate in deionized water and $Ba(NO_3)_3 \cdot 3H_2O$ were mixed and stirred vigorously for 30 minutes. The temperature of solution was sustained at 80 °C. After few minutes self sustained reaction in the solution occurred because of glycine and brownish color ash was acquired. An electric oven was used to dry the obtained ash. The fine powder obtained after drying was ground using agate mortar and calcined at 500 °C. The powder obtained after calcination was pressed down to pellets at a pressure of 6 MPa. Then, at 520 °C, the pellets were sintered for 2 hours. The compositions of $Bi_{1-x}Ba_xFeO_3$ where x=0.0, 0.1 and 0.2 was signified as BFO, BBFO-0.1 and BBFO-0.2, respectively. The characterization of the prepared samples were done by X-ray diffraction, TEM, FESEM for the investigation of structural properties, dielectric measurement, impedance and ferroelectric analysis for electrical properties, VSM for magnetic behavior, FTIR spectroscopy, *UV*-Visible spectrometer and PL spectroscopy for optical studies.

3.3.2 X-RAY DIFFRACTION STUDIES

XRD plots of $Bi_{1-x}Ba_xFeO_3$ (x=0.0, 0.1 and 0.2) nanoparticles are shown in **Figure 3.32 (a)**. The XRD patterns of Ba^{2+} doped BFO nanoparticles revealed intense diffraction peaks along with the small impurity phase of $Bi_2Fe_4O_9$, $Bi_{25}FeO_{39}$, etc. This is due to the incomplete substitution resulting from the ionic mismatches amongst Ba^{2+} (1.42 Å) and Bi^{3+} (1.17 Å) **[52]**. In order to reconfirm and to extract the structural parameters of $Bi_{1-x}Ba_xFeO_3$ nanoparticles, Reitveld refinement of measured XRD patterns was performed. The refinement of the nanoparticles was carried out using the rhombohedral crystal symmetry. The good agreement between the observed and calculated interplanner spacing of *hkl* planes in BFO confirmed the formation of Ba^{2+} doped BFO, which has a rhombohedrally distorted structure belonging to *R3c* space group. Therefore, the refined pattern of the nanoparticles is indexed according to the rhombohedral system as shown in **Figure 3.32 (b)** and refined structural parameters are tabulated in **Table 3.7**. Similar behavior has also been reported in the literature for rare earth metal doped BFO **[53, 54]**.

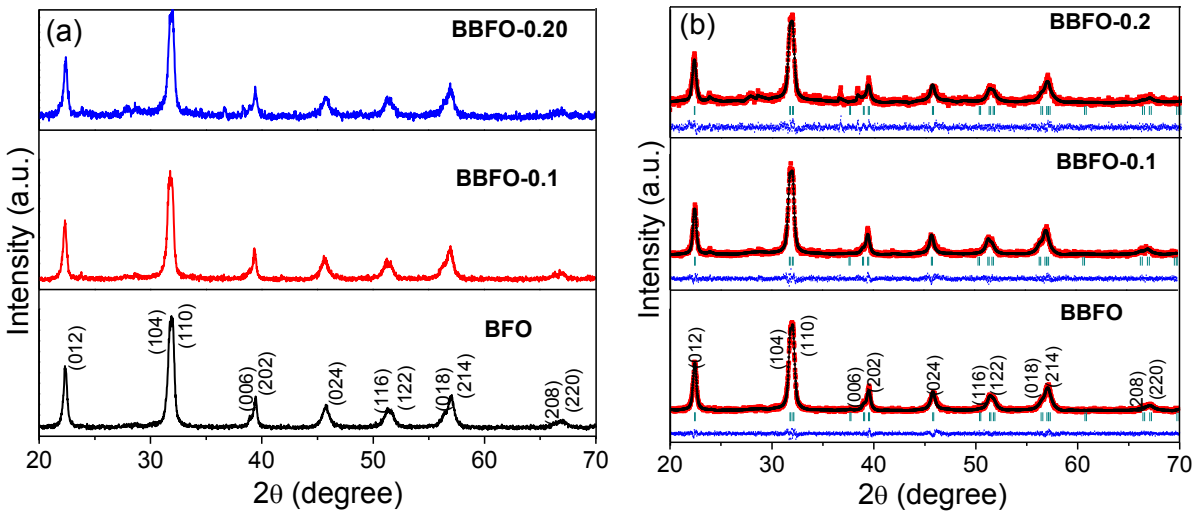

Figure 3.32 (a) X-ray diffraction patterns **(b)** Rietveld refinements of the XRD patterns of $Bi_{1-x}Ba_xFeO_3$ nanoparticles ($0.0 \leq x \leq 0.2$).

The lattice distortion (c/a) is found to increase for BBFO-0.1 and further substitution of Ba^{2+} ions decreases c/a. A reverse trend is followed by unit cell volume for all compositions. The estimated Fe-O-Fe bond angle in nanoparticles is found to increase, which may affect the magnetic structure as well as electric properties in the doped samples **[41, 55-56]**. All these resultant parameters suggested a large distortion which involves Fe^{3+} or Bi^{3+} ion displacement without any structural transformation in BFO with the substitution of Ba^{2+} ions. Therefore, the

degree of distortion in Ba^{2+} doped $BiFeO_3$ nanoparticles was evaluated using Goldschmidt's tolerance factor (t) and is written as follows:

$$t = \frac{\left((1-x)r_{Bi} + xr_{Ba}\right) + r_o}{\sqrt{2}(r_{Fe} + r_o)} \qquad Eq.\ 3.8$$

Here r_{Bi}, r_{Ba}, r_{Fe} and r_O are the effective ionic radii of Bi^{3+}, La^{3+}, Fe^{3+} and O^{2-} ions, respectively **[57]**. The calculated tolerance factor is 0.889, 0.897 and 0.906 for BFO, BBFO-0.1 and BBFO-0.2 nanoparticles, respectively. The calculated values of crystallite size for BFO, BBFO-0.1 and BBFO-0.2 by using Williamson–Hall equation are approximately 43.23 nm, 37.17 nm and 68.98 nm, respectively **[6, 7]**.

Table 3.7 Refined structural parameters for $Bi_{1-x}Ba_xFeO_3$ nanoparticles ($0.0 \leq x \leq 0.2$) obtained by rietveld analysis.

Composition of $Bi_{1-x}Ba_xFeO_3$	***Atom***	***Fractional coordinates***			***Lattice Constant [Å]***	***Bond angle [°]***	***Bond length [Å]***	***Statistical Parameter (%)***
		x	***y***	***z***				
BFO *R3c* V=373.25(Å^3)	Bi Fe O	0.0000 0.0000 0.4167	0.0000 0.0000 -0.04050	0.0000 0.2200 0.0602	a =5.57 c =13.84	Fe-O-Fe =115.10	Bi-O =2.07 Fe-O =1.84	R_p=7.25 *Rwp*=9.25 R_{exp}=8.89 χ^2=1.08
BBFO-0.1 *R3c* V=372.93(Å^3)	Bi/Ba Fe O	0.0000 0.0000 1.1520	0.0000 0.0000 0.7776	0.2888 0.0656 0.5575	a =5.57 c =13.84	Fe-O-Fe =121.00	Bi/Ba-O =3.02 Fe-O =2.71	R_p=10.1 *Rwp*=8.01 R_{exp}=9.36 χ^2=1.17
BBFO-0.2 *R3c* V= 375.37(Å^3)	Bi/Ba Fe O	0.0000 0.0000 0.8448	0.0000 0.0000 0.6403	0.2154 -0.0089 0.4599	a =5.58 c =13.87	Fe-O-Fe =122.00	Bi/Ba-O =1.55 Fe-O =2.75	R_p=9.13 *Rwp*=11.7 R_{exp}=10.4 χ^2= 1.26

3.3.3 MORPHOLOGICAL STUDIES

To reveal the microstructure and particle size of $Bi_{1-x}Ba_xFeO_3$ (x=0.0, 0.1 and 0.2) nanoparticles, TEM micrographs on the scale of 100 nm are shown in **Figures 3.33 (a-c)**. Morphology of the compositions indicated that all the particles were agglomerated and nearly spherical. These agglomerated particles are acquired due to the high surface energy of uniform particles with narrow size. The average particle size of BFO nanoparticles is observed to be ~147 nm. The average particle size of the nanoparticles decreases with the Ba^{2+} doping content in BFO up to BBFO-0.1 and then after increases. The obtained particle size for BBFO-0.1 is ~79 nm and for BBFO-0.2 is ~164 nm.

The SAED pattern shows sharp diffraction rings, confirming the well-developed polycrystalline nature of all the samples shown in **Figures 3.33 (d-f).**

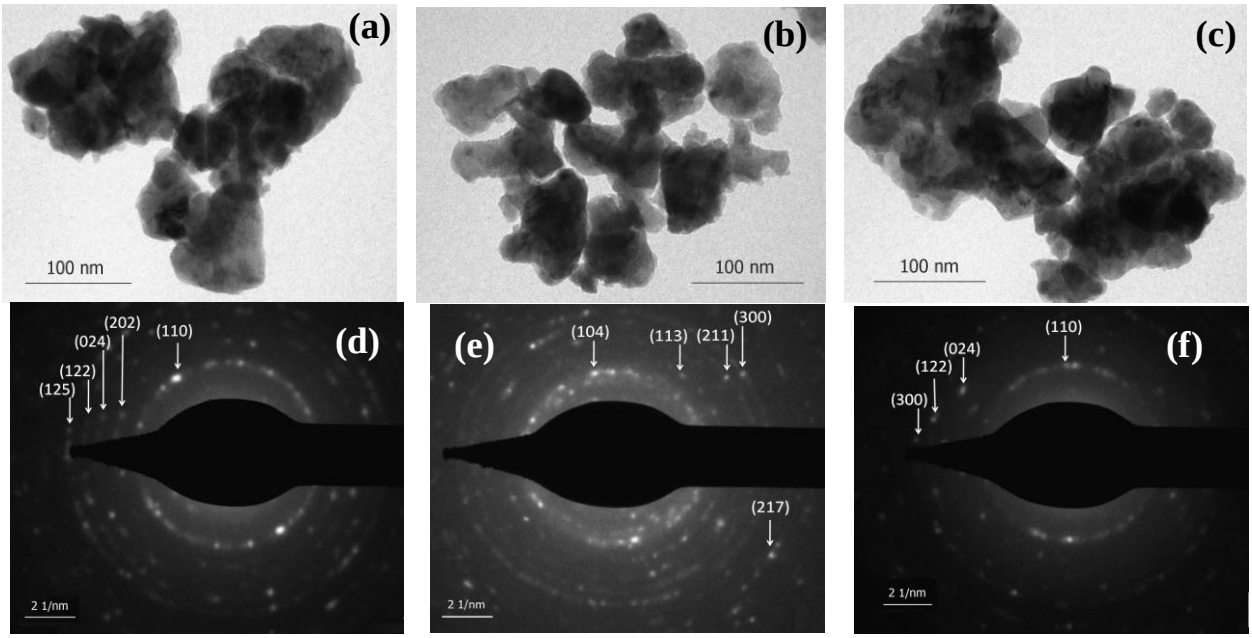

Figure 3.33 TEM images and SAED patterns of **(a, d)** BFO **(b, e)** BBFO-0.1 and **(c, f)** BBFO-0.2 nanoparticles.

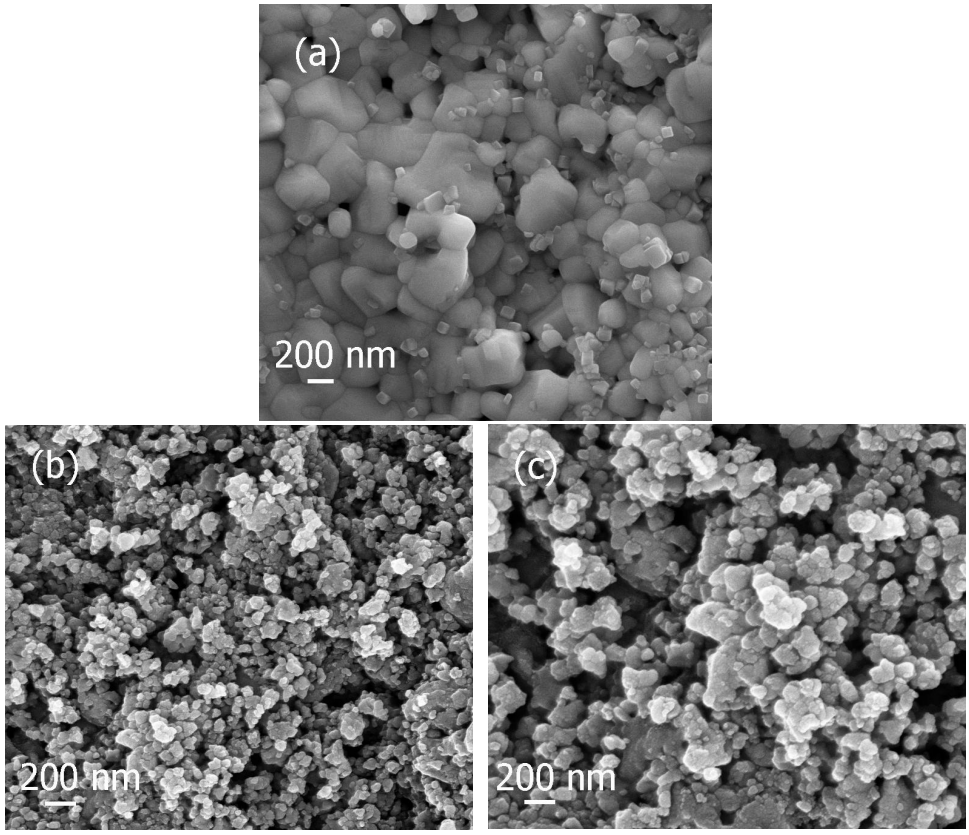

Figure 3.34 FESEM micrographs of **(a)** BFO **(b)** BBFO-0.1 and **(c)** BBFO-0.2 samples.

The FESEM micrographs are shown in **Figures 3.34 (a-c)** reveal the effect of Ba^{2+}-doping on the morphology and the grain size of the $Bi_{1-x}Ba_xFeO_3$ ceramics. It is observed that BFO display regular shaped grains and its average grain size is ~ 422 nm. The grain size is found to decrease with Ba^{2+} substitution for BBFO-0.1 and further increment of Ba^{2+} ions enlarged the size of the grains.

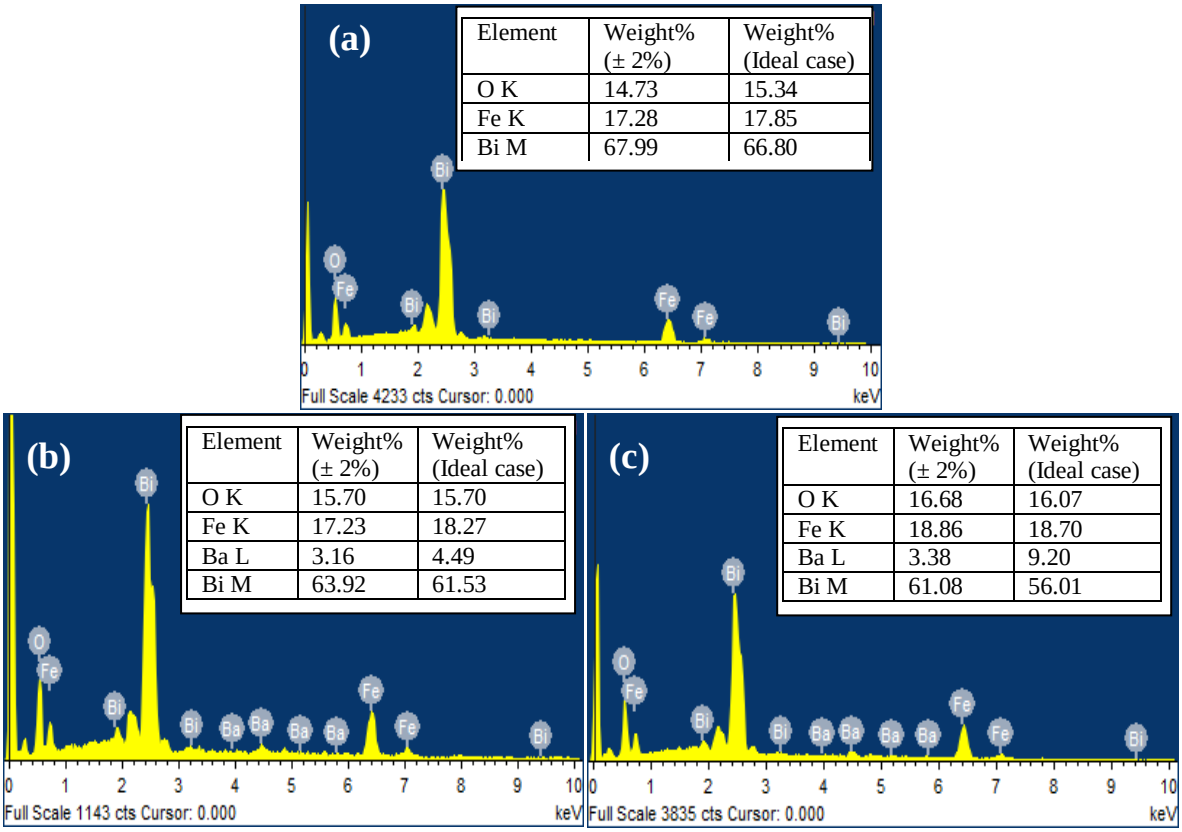

Figure 3.35 EDX patterns of **(a)** BFO **(b)** BBFO-0.1 and **(c)** BBFO-0.2 samples.

The typical EDX spectrum for BFO, BBFO-0.1 and BBFO-0.2 ceramics are shown in **Figures 3.35 (a–c)**. The EDX spectrum verified the chemical homogeneity of each sample as shown in the inset of **Figures 3.35 (a-c)**.

3.3.4 DIELECTRIC STUDIES

The temperature dependence of dielectric constant (ε) for $Bi_{1-x}Ba_xFeO_3$ ceramics at different frequencies (100 Hz to 1 MHz) are shown in **Figure 3.36**. The dielectric constant of BFO demonstrates continuous increment with rise in temperature at lower frequencies as shown in **Figure 3.36 (a).** However, ε increases with increase in temperature up to 380 °C and then it decreases with further increase in temperature for high frequencies.

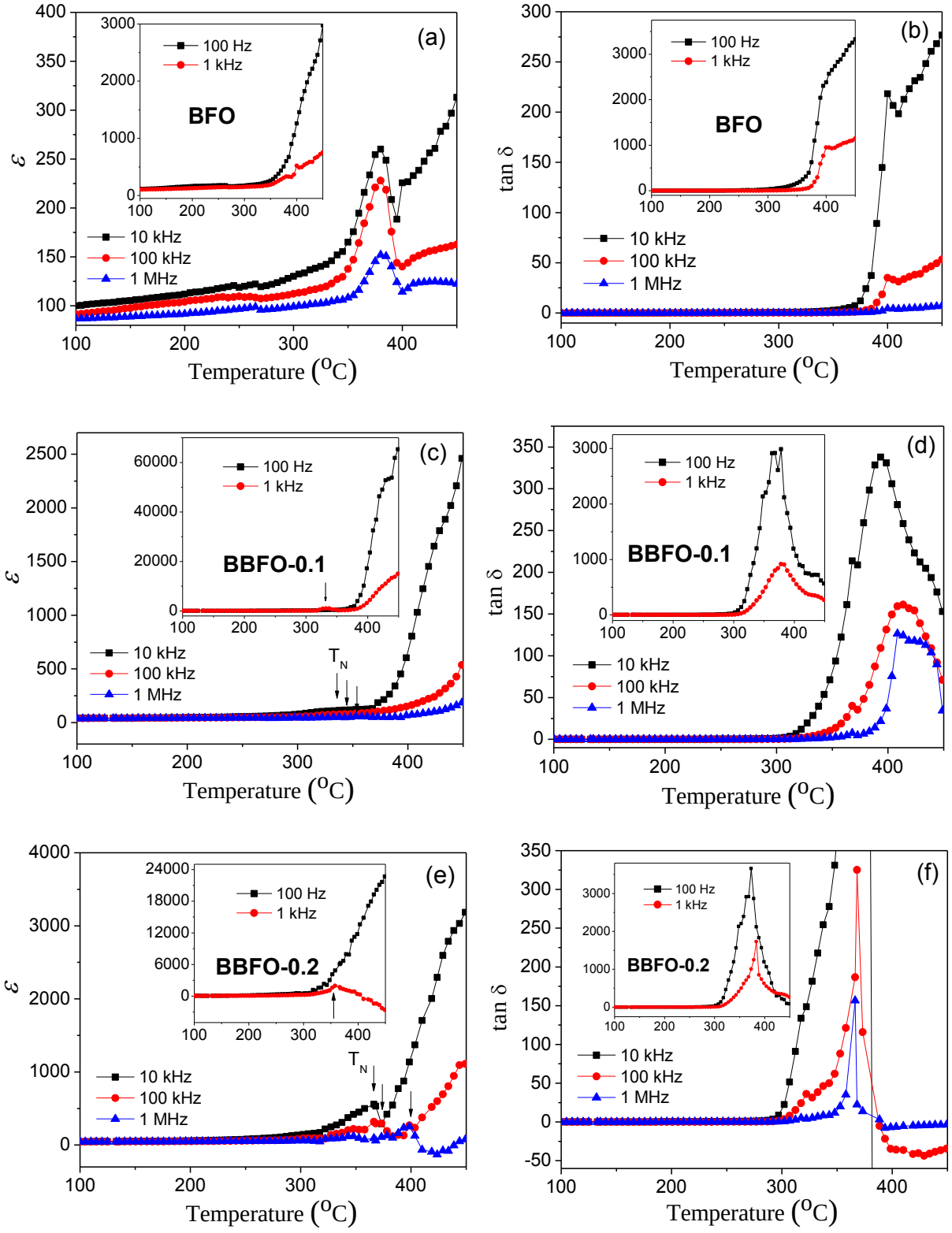

Figure 3.36 Dielectric constant (ε) and dissipation factor (*tan* δ) versus temperature curves for $Bi_{1-x}Ba_xFeO_3$ samples at 100 Hz, 1 kHz, 10 kHz, 100 kHz and 1 MHz.

The obtained peak relates to an antiferromagnetic Neél temperature (T_N) which could be induced by the magnetoelectric coupling between its electric and magnetic orders which was predicted by the Landau-Devonshire theory **[15, 16]**. It is clearly seen that values of ε decreases with increase in frequency. The above behavior is also observed in BBFO-0.1 and BBFO-0.2 ceramics as shown in **Figure 3.36 (c and e),** respectively. It is observed from the figures that T_N shows considerable frequency dispersion with Ba^{2+} ion substitution. It shifts towards higher temperature with the increase in frequency for both BBFO-0.1 and BBFO-0.2 ceramics. Similar behavior was reported by Singh *et al.* in $BiFeO_3$-based systems **[58]**. The variation of *tan* δ with the effect of Ba^{2+} doping has also been studied and is illustrated in **Figures 3.36 (b, d and f).** The above mentioned dielectric anomalies has also been obtained in *tan* δ which may be attributed to the contribution of space charge polarization, which arises because of oxygen vacancies (Vo^{2+}) at high temperature.

Figure 3.37 shows the variation in the real and imaginary part of impedance (Z') for $Bi_{1-x}Ba_xFeO_3$ (x=0.0-0.2) ceramics in terms of frequency at different temperatures (210 °C to 310 °C). A monotonous decrease in Z' for BFO with the increase in frequency at all temperatures showing NTCR behavior, followed by a saturation region at high frequency is observed. This behavior indicates the increase in a.c. conductivity which could be ascribed to the release of space charge polarization, and lowering in the barrier properties of the ceramics **[21, 22]**.

The Z" for BFO is also observed to decrease monotonically with increase in frequency at low temperature range. This observation is a signature of increase in resistive behavior in ceramics. While, at high frequencies, the value of Z" coincide at higher frequencies, which could be ascribed to the occurrence of a thermally activated dielectric relaxation process in the ceramics **[23]**. As temperature increases, the loss spectrum is found to get broader at a particular frequency f_{max} (called relaxation frequency) and shifts towards higher frequency side. The shift of f_{max} suggests the asymmetry in the peak pattern and decrease of relaxation time ($\tau = 1/2\Pi f_{max}$) in the ceramics. Similar behavior of Z' and Z" with frequency and temperature are also observed in BBFO-0.1 and BBFO-0.2 ceramics as shown in **Figures 3.37 (c-f)** respectively.

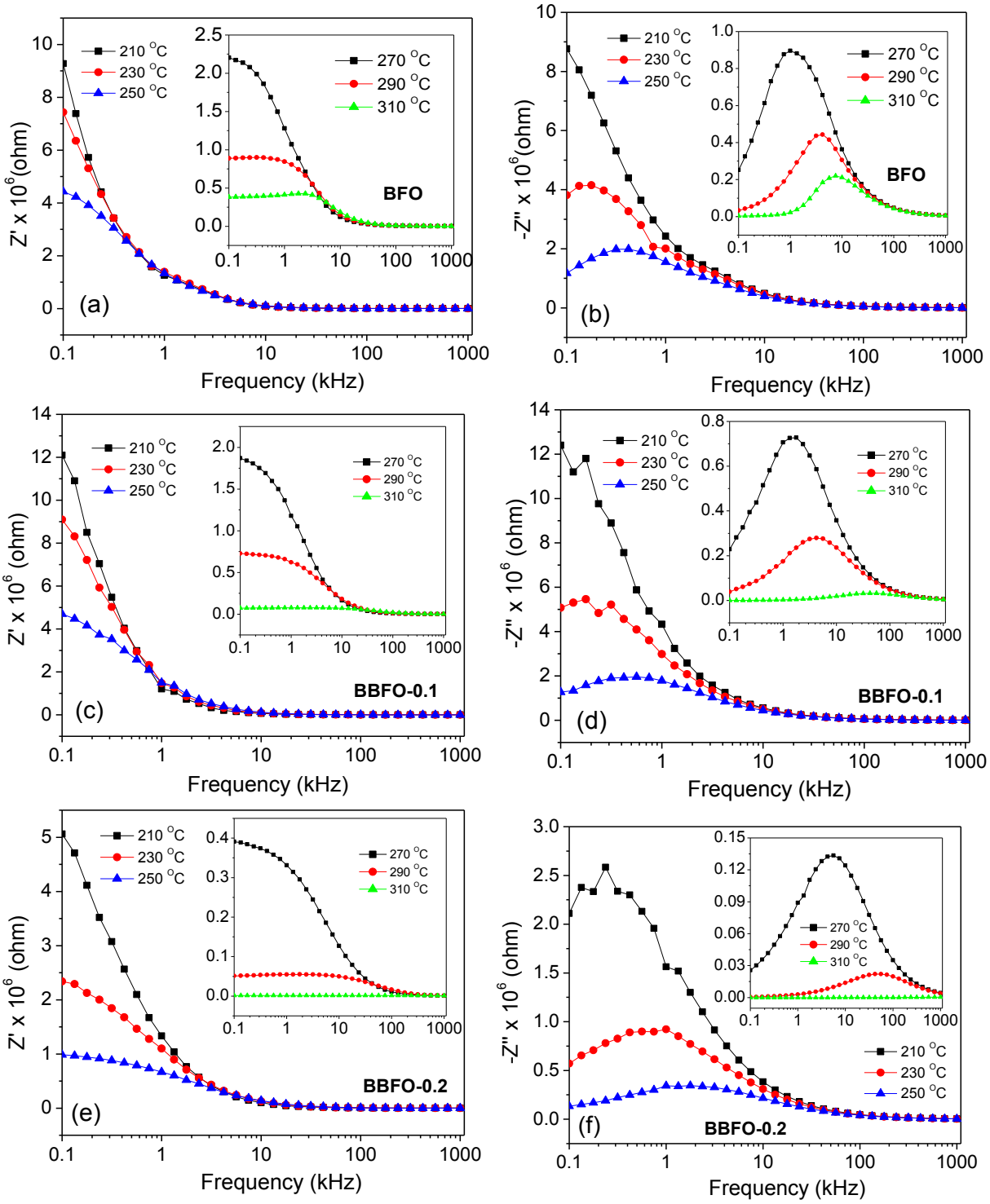

Figure 3.37 Frequency dependent real (Z') and imaginary (Z'') part of impedance for BFO, BBFO-0.1 and BBFO-0.2 samples at 210 °C, 230 °C and 250 °C, the inset shows the variation of impedance at 270 °C, 290 °C and 310 °C.

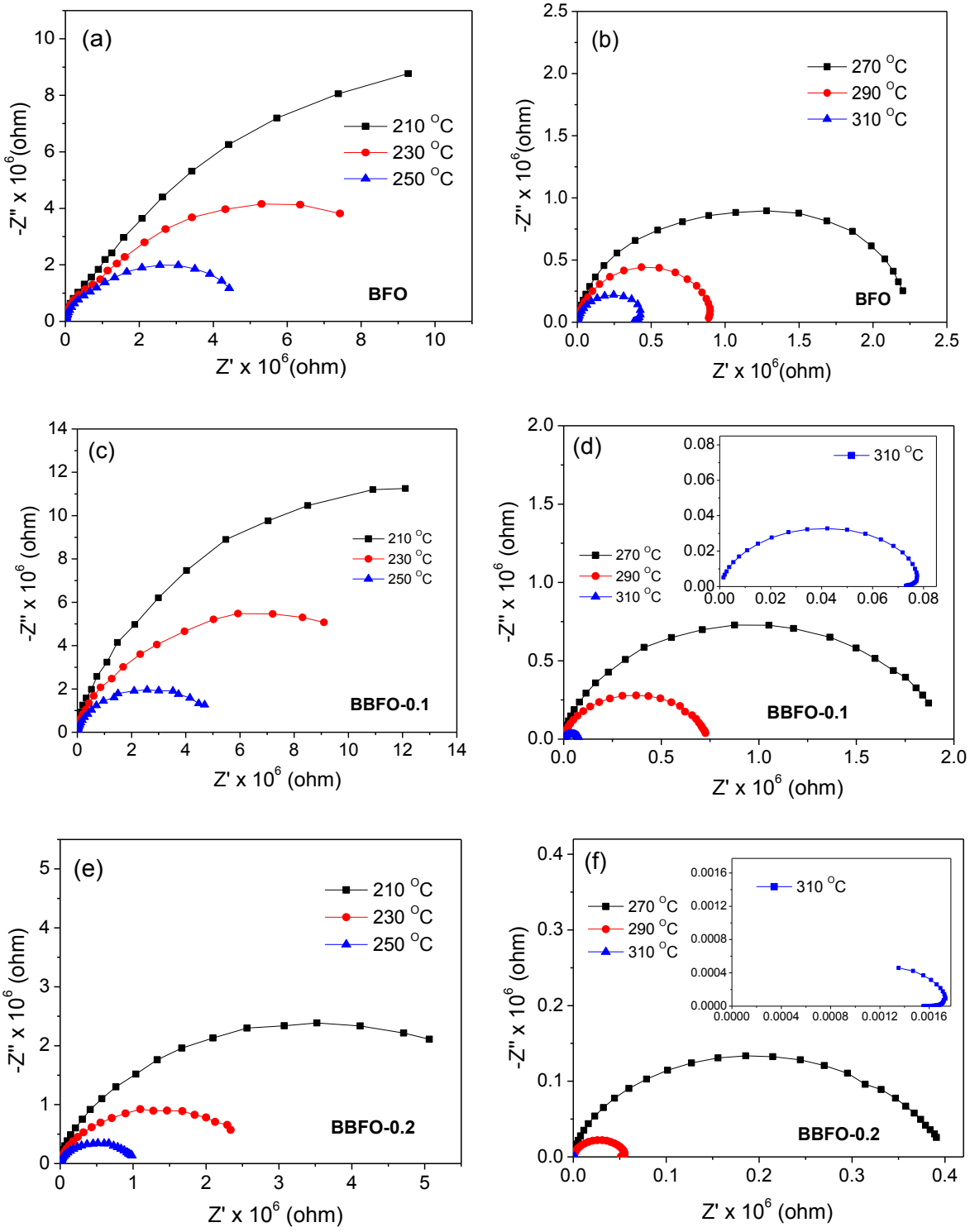

Figure 3.38 Variation of imaginary part Z'' with respect to real part Z' of complex impedance (Nyquist plots) for **(a, b)** BFO **(c, d)** BBFO-0.1 and **(e, f)** BBFO-0.2 samples.

Temperature dependent nyquist plots (Z' vs. Z'') are used to calculate the resistance for $Bi_{1-x}Ba_xFeO_3$ (x=0.0-0.2) ceramics over the wide range of frequency. It is observed from the **Figure 3.38,** the straight lines with large slopes doesn't exhibit a unique relaxation time at low temperature and indicate the insulating behavior of the ceramics. However, the apparent semicircle at high temperature for each composition is indicative of an individual conduction and relaxation process in ceramics. In high temperature zone, value of resistance is obtained through the intercept of semicircles on Z'-axis. The ac conductivity (σ_{ac}) of the prepared Ba^{2+} ions doped ceramics has been calculated from the value of bulk resistance.

The variation of ac conductivity (σ_{ac}) with respect to the inverse of temperature for $Bi_{1-x}Ba_xFeO_3$ (x=0.0-0.2) ceramics is shown in **Figure 3.39.** The activation energy for all compositions was calculated using Arrhenius relations from the slope of the straight line in a plot of In (σ_{ac}) versus 1000/T. The calculated value of activation energy is 0.69 eV for BFO, 0.85 eV for BBFO-0.1 and 1.20 eV for BBFO-0.2 ceramics. The activation energy lie in a temperature range of 510 K-650 K, suggest the conductivity behavior of the ceramics due to the contribution of short range hopping movement of oxygen vacancies **[23]**.

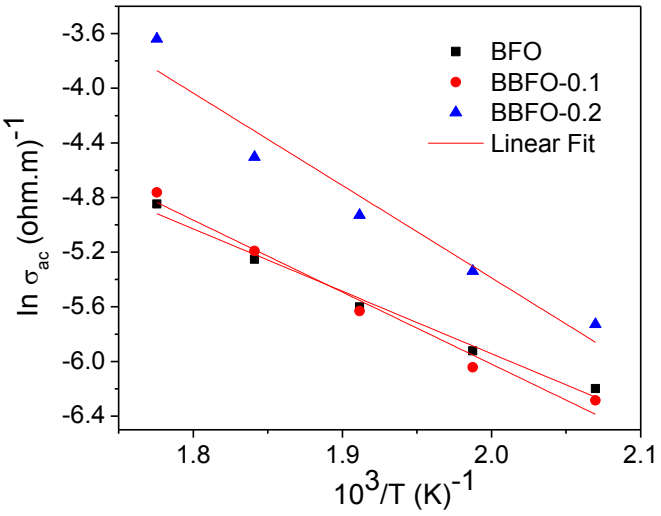

Figure 3.39 Arrhenius plot with temperature for BFO, BBFO-0.1 and BBFO-0.2 samples.

3.3.5 FERROELECTRIC STUDIES

Figure 3.40 shows well established hysteresis loops of $Bi_{1-x}Ba_xFeO_3$ (x=0.0, 0.1 and 0.2) nanoparticles, at applied electric field of 12 kV/cm, were measured. It is clear from the figures that maximum polarization (P_{max}) and remnant polarization (P_r) of BFO decreases from 12.725 μC/cm^2 to 10.349 μC/cm^2 and 7.693μC/cm^2 to 5.141 μC/cm^2, respectively with the addition of

Ba^{2+} ions. This decrement in P_{max} and P_r along with the doping of Ba^{2+} ions could be attributed to the mix valence of Fe ions in BFO. Saturated ferroelectric hysteresis loops of $Bi_{1-x}Ba_xFeO_3$ (x=0.0, 0.1 and 0.2) ceramics can be obtained with the application of higher electric field or by poling the samples with a high voltage.

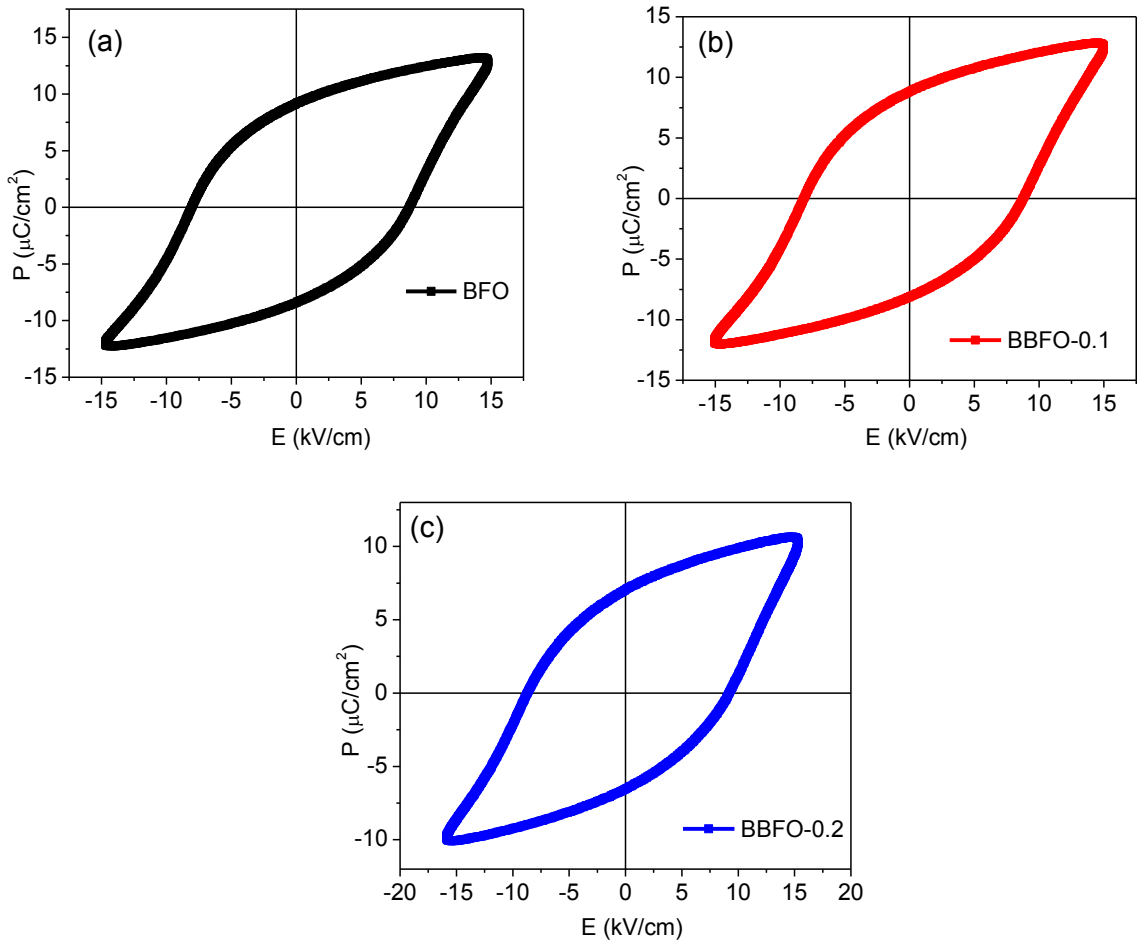

Figure 3.40 Variation of ferroelectric hysteresis loops for **(a)** BFO **(b)** BBFO-0.1 and **(c)** BBFO-0.2 samples.

3.3.6 MAGNETIC STUDIES

The room temperature *M-H* loops of $Bi_{1-x}Ba_xFeO_3$ (x=0.0, 0.1 and 0.2) nanoparticles for the maximum magnetic field of 10 kOe is shown in **Figure 3.41**. A weak ferromagnetic behavior is observed for all the nanoparticles due to the suppression of the space modulated spin structure **[27]**. There is a noticeable change in magnetization observed for BFO, BBFO-0.1 and BBFO-0.2 at room temperature. Magnetization increases monotonically with the Ba^{2+} doping content from 0.180, 0.782 to 1.417 emu/g for BFO, BBFO-0.1 and BBFO-0.2, respectively. *M-H* curves of

BFO nanoparticles show a very narrow magnetic hysteresis loop, with a small but non zero remnant magnetization (M_r) of 0.0077 emu/g and coercive field (H_c) of 145.79 Oe. The H_c is found to decrease from BFO to BBFO-0.1 nanoparticles and then it increases with further increase in Ba^{2+} doping content. The decrease in the coercivity could be attributed to decrease in the particle size from 147.93 nm for BFO to 79.82 nm for BBFO-0.1 and thereafter increases with increase in particle size as evidenced from TEM**.**

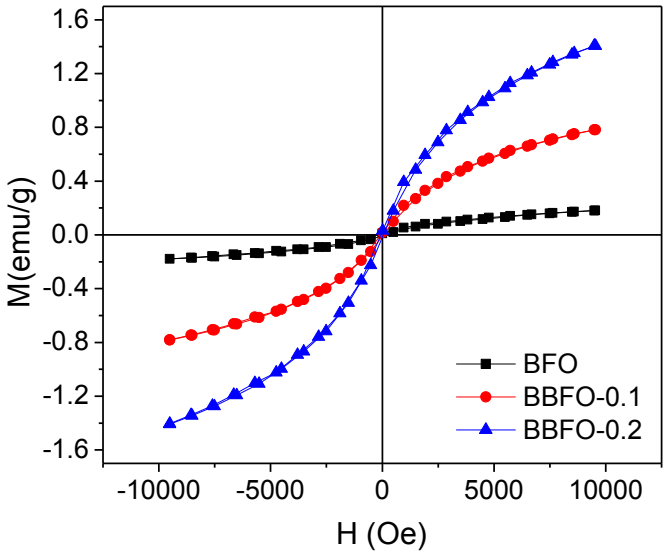

Figure 3.41 Room temperature magnetic hysteresis loops of BFO, BBFO-0.1 and BBFO-0.2 nanoparticles.

Moreover, the obtained magnetization curves of nanoparticles are not saturated. Many reasons could contribute to the enhancement of saturation magnetization when the Ba^{2+} ions are doped in BFO. First, as mentioned in refinement, rhombohedrally distorted BFO allows a weak ferromagnetic ordering due to canting of the spins. The modification of the spin spiral structure into linear, caused by increased in Fe–O–Fe bond angle with Ba^{2+} ions doped BFO nanoparticles, associated with the large distortion due to the considerable ionic mismatches between Bi^{3+} ions and Ba^{2+} ions. As a result large magnetization is observed in the samples. Second, addition of Ba^{2+} to BFO nanoparticles require charge compensation, which can be achieved by formation of Fe^{4+} or oxygen vacancies. If Fe^{4+} exists, the statistical distribution of Fe^{3+} and Fe^{4+} ions in the octahedral may also lead to net magnetization and ferromagnetism. Moreover, the change in electronic density of state distribution between Fe-O driven by the hybridization interaction is also responsible for the magnetization in $BiFeO_3$ system.

3.3.7 *UV*-VISIBLE ABSORPTION STUDIES

Figure 3.42 (a) shows usual transition states in $Bi_{1-x}Ba_xFeO_3$ (x=0.0, 0.1 and 0.2) nanoparticles derived from absorption spectra, which is plotted as a function of energy (eV). Four transition states corresponding to four anomalies are observed in BFO nanoparticles. The one on-site d-to-d crystal field excitations of Fe^{3+} ion's traces at ~1.34 eV and another at ~1.87 eV can be ascribed to $^6A_{1g}$-$^4T_{1g}$ and $^6A_{1g}$-$^4T_{2g}$ electronic energy levels respectively, caused by the relaxation of spin–orbit coupling as shown in **Figure 3.42 (a) [49-51]**. Two other broad charge transfer excitation bands are seen in the absorption spectrum, besides ~1.87 eV. These excitation bands are observed around 2.56 eV and 3.39 eV, which could be attributed to $Fe_1$3d–$Fe_2$3d inter-site electron transfer and inter-atomic O 2p–Fe 3d electronic energy levels, respectively**.** The small amount of Ba^{2+} doping ions in BFO induced more distortion in FeO_6 octahedral accompanied with a slight shift in the charge transfer excitation bands, leading to variation in unit cell volume of Ba^{2+} ion doped BFO nanoparticles. The inset of **Figure 3.42 (a)** shows the *UV*-Vis absorption spectra, where the absorption cutoff wavelengths are seen at 678.32, 639.97 and 689.97 nm for BFO, BBFO-0.1 and BBFO-0.2 nanoparticles respectively. The observed variation in cutoff wavelength indicates the disturbance in electronic structure and the creation of oxygen vacancies in BFO with the addition of Ba^{2+} ions **[35, 36]**.

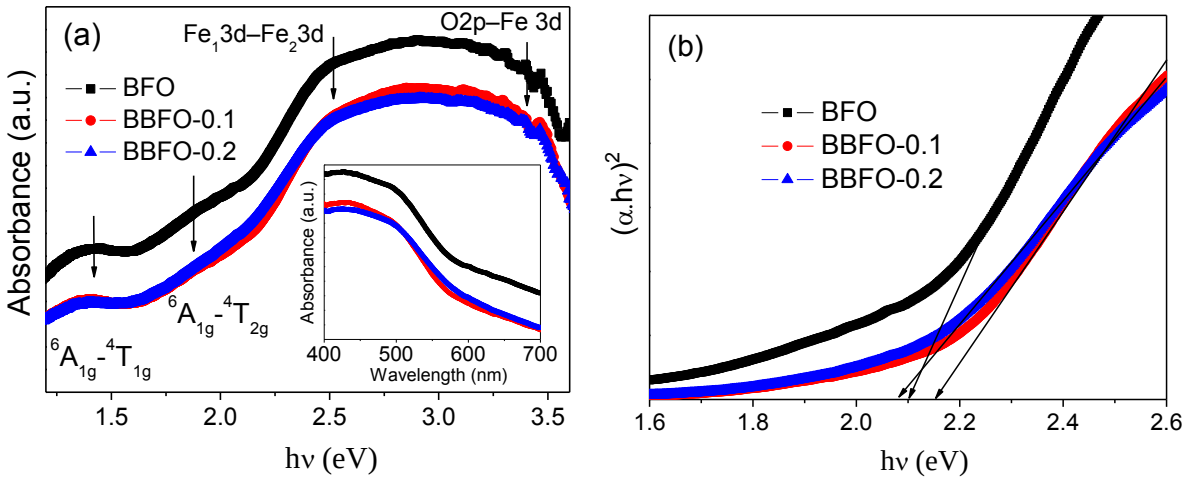

Figure 3.42 (a) *UV*-Vis absorption spectrum versus energy plot. **(b)** Tauc's plots for BFO, BBFO-0.1 and BBFO-0.2 nanoparticles.

The energy band gap of the nanoparticles is calculated by the means of Tauc's relationship as shown in **Figure 3.42 (b)**. The obtained band gap value of nanoparticles increases from 2.09 eV for BFO to 2.15 eV for BBFO-0.1 with Ba^{2+} ions. However, the band gap

decreases to 2.08 eV for BBFO-0.2. As, energy band gaps are particle size dependent, the variation in the band gap could be attributed to the size of the particles, *i.e.* 147.93 nm for BFO, 79.82 nm for BBFO-0.1 and 164.34 nm for BBFO-0.2, obtained from TEM. The decrease in the band gap value can also be due to the existence of defect-induced energy levels between the conduction and valence bands **[59].**

3.3.8 PHOTOLUMINESCENCE STUDIES

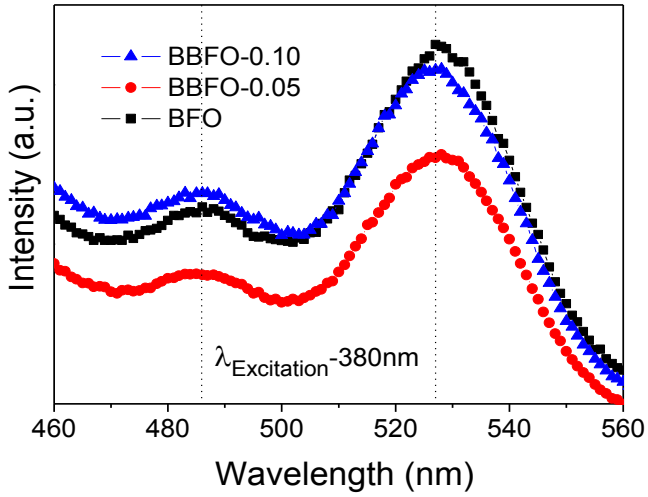

Figure 3.43 Photoluminescence spectra of BFO, BBFO-0.1 and BBFO-0.2 nanoparticles.

The PL spectra for $Bi_{1-x}Ba_xFeO_3$ (x=0.0, 0.1 and 0.2) nanoparticles exhibited several broad and weak emissions, with an excitation wavelength of 380 nm as shown in **Figure 3.43**. A blue emission of nearly 486.95 nm is observed in BFO nanoparticles, which comes from the inter-band transition corresponding to the self-activated center. Another high intensity peak is also seen in the PL spectra; besides 486.95 nm. This green band emission around 527.93 nm can be attributed to the transition of an inter-site electron band. On close observation, with the doping of Ba^{2+} ions in BFO nanoparticles, a noticeable shift is observed in both the emission bands. The shifting of the blue emission band towards lower wavelength from 486.95 nm to 485 nm for BFO and BBFO-0.1 respectively, and then 486.05 nm for BBFO-0.2, could be ascribed to the fluctuation in the energy band gap over doping of Ba^{2+} ions. Also, Ba^{2+} ion content in BFO affects the green band emission by shifting the position of the band a few nm. This shift observed in the green emission band is due to the various defects and/or impurity (or dopant) levels inside the band gap.

References

1. Karimi S., Reaney I. M., Han Y., Pokorny J., Sterianou I., *Journal of Materials Science*, (2009), *44*(19), 5102-5112.
2. Khomchenko V. A., Paixao J. A., Kiselev D. A., Kholkin A. L., M*aterials Research Bulletin*, (2010), *45*(4), 416-419.
3. Zhang Y. J., Zhang H. G., Yin J. H., Zhang H. W., Chen J. L., Wang W. Q., Wu G. H., *Journal of Magnetism and Magnetic Materials*, (2010), *322*(15), 2251-2255.
4. Zhang S. T., Zhang Y., Lu M. H., Du C. L., Chen Y. F., Liu Z. G., Zhu Y. Y., Ming N. B., Pan X. Q., *Applied Physics Letters*, (2006), *88*(16), 162901(1-3).
5. Debye P., *Annalen Der Physik*, (1915), *351*(6), 809-823.
6. Singla G., Singh K., Pandey O. P., *Applied Physics A*, (2013), *113*(1), 237-242.
7. Nalwa K. S., Garg A., *Journal of Applied Physics*, (2008), *103*(4), 044101(1-6).
8. Basiri M. H., Shokrollahi H., Isapour G., *Journal of Magnetism and Magnetic Materials*, (2014), *354*, 184-189.
9. Arora M., Kumar M., *Materials Letters*, (2014), *137*, 285-288.
10. Khodabakhsh M., Sen C., Khassaf H., Gulgun M. A., Misirlioglu I. B., *Journal of Alloys and Compounds*, (2014), *604*, 117-129.
11. Maxwell J. C., Electricity and Magnetism. *Oxford University Press, Oxford*, (1929), Section 328.
12. Koops C. G., *Physical Review*, (1951), *83*(1), 121-124.
13. Sharma P., Varshney D., Satapathy S., Gupta P. K., *Materials Chemistry and Physics*, (2014), *143*(2), 629-636.
14. Pandit P., Satapathy S., Gupta P. K., Sathe V. G., *Journal of Applied Physics*, (2009), *106*(11), 114105(1-7).
15. Singh H., Yadav K. L., *Materials Chemistry and Physics*, (2012), *132*(1), 17-21.
16. Benguigui L., *Solid State Communications*, (1972), *11*(6), 825-828.
17. Cheng Z. X., Li A. H., Wang X. L., Dou S. X., Ozawa K., Kimura H., Zhang S. J., Shrout T. R., *Journal of Applied Physics*, (2008), *103*(7), 07E507(1-3).
18. Das S. R., Choudhary R. N. P., Bhattacharya P., Katiyar R. S., Dutta P., Manivannan A., Seehra M. S., *Journal of Applied Physics*, (2007), *101*(3), 034104(1-7).
19. Sati P. C., Kumar M., Chhoker S., *Ceramics International*, (2015), *41*(2), 3227-3236.

20. Bombik A., Leśniewska B., Mayer J., Pacyna A. W., *Journal of Magnetism and Magnetic Materials*, (2003), *257*(2), 206-219.
21. Behera A. K., Mohanty N. K., Behera B., Nayak P., *Advanced Materials Letters*, (2013), *4*(2), 141-145.
22. Sati P. C., Arora M., Chauhan S., Kumar M., Chhoker S., *Journal of Materials Science: Materials in Electronics*, (2013), *24*(12), 5023-5034.
23. Kumari S., Ortega N., Kumar A., Pavunny S. P., Hubbard J. W., Rinaldi C., Srinivasan G., Scott J. F., Katiyar R. S., *Journal of Applied Physics*, (2015), *117*(11), 114102(1-13).
24. Sharma P., Varshney D., Satapathy S., Gupta P. K., *Materials Chemistry and Physics*, (2014), 143, 629-636.
25. Hwang J. S., Cho J. Y., Park S. Y., Yoo Y. J., Yoo P. S., Lee B. W., Lee Y. P., *Applied Physics Letters*, (2015), 106, 062902(1-5).
26. Mazumder R., Ghosh S., Mondal P., Bhattacharya D., Dasgupta S., Das N., Sen A., Tyagi A. K., Sivakumar M., Takami T., Ikuta H., *Journal of Applied Physics*, (2006), *100*(3), 033908(1-9).
27. Khesro A., Boston R., Sterianou I., Sinclair D. C., Reaney I. M., *Journal of Applied Physics*, (2016), *119*(5), 054101(1-8).
28. Bhushan B., Wang Z., Tol J. V., Dalal N. S., Basumallick A., Vasanthacharya N. Y., Kumar S., Das D., *Journal of the American Ceramic Society*, (2012), *95*(6), 1985-1992.
29. Zalesskii A. V., Frolov A. A., Khimich T. A., Bush A. A., *Physics of the Solid State*, (2003), *45*(1), 141-145.
30. Arya G. S., Negi N. S., *Journal of Physics D: Applied Physics*, (2013), *46*(9), 095004(1-8).
31. Arya G., Kotnala R. K., Negi N. S., *Journal of the American Ceramic Society*, (2014), *97*(5), 1475-1480.
32. Jiang J., Zou J., Anjum M. N., Yan J., Huang L., Zhang Y., Chen J., *Solid State Sciences*, (2011), *13*(9), 1779-1785.
33. Khirade P. P., Birajdar S. D., Raut A. V., Jadhav K. M., *Ceramics International*, (2016), *42*(10), 12441-12451.
34. Chauhan S., Kumar M., Chhoker S., Katyal S. C., Singh H., Jewariya M., Yadav K. L., *Solid State Communications*, (2012), *152*(6), 525-529.

35. Mukherjee A., Hossain S. M., Pal M., Basu S., *Applied Nanoscience*, (2012), *2*(3), 305-310.
36. Som K. K., Molla S., Bose K., Chaudhuri B. K., *Physical Review B*, (1992), *45*(4), 1655-1659.
37. Guo R., Fang L., Dong W., Zheng F., Shen M., *The Journal of Physical Chemistry C*, (2010), *114*(49), 21390-21396.
38. Gao F., Chen X. Y., Yin K. B., Dong S., Ren Z. F., Yuan F., Yu T., Zou Z. G., Liu J. M., *Advanced Materials*, (2007), *19*(19), 2889-2892.
39. Xian T., Yang H., Dai J. F., Wei Z. Q., Ma J. Y., Feng W. J., *Materials Letters*, (2011), *65*(11), 1573-1575.
40. Suresh P., Babu P. D., Srinath S., *Journal of Applied Physics*, (2014), *115*(17), 17D905(1-3).
41. Yang C. H., Kan D., Takeuchi I., Nagarajan V., Seidel J., *Physical Chemistry Chemical Physics*, (2012), *14*(46), 15953-15962.
42. Zheng Q., Luo L., Lam K. H., Jiang N., Guo Y., Lin D., *Journal of Applied Physics*, (2014), *116*(18), 184101(1-11).
43. Hwang J. S., Cho J. Y., Park S. Y., Yoo Y. J., Yoo P. S., Lee B. W., Lee Y. P., *Applied Physics Letters*, (2015), *106*(6), 062902(1-5).
44. Hu Z., Li M., Yu Y., Liu J., Pei L., Wang J., Liu X., Yu B., Zhao X., *Solid State Communications*, (2010), *150*(23), 1088-1091.
45. Yuan G. L., Or S. W., Liu J. M., Liu Z. G., *Applied Physics Letters*, (2006), *89*(5), 052905(1-3).
46. Hasan M., Hakim M. A., Basith M. A., Hossain M. S., Ahmmad B., Zubair M. A., Hussain M. A., Islam M. F., *AIP Advances*, (2016), *6*(3), 035314(1-13).
47. Boyer J. C., Vetrone F., Capobianco J. A., Speghini A., Zambelli M., Bettinelli M., *Journal of Luminescence*, (2004), *106*(3), 263-268.
48. Zhang T., Wang J., Jiang J., Pan R., Zhang B., *Thin Solid Films*, (2007), *515*(20), 7721-7725.
49. Ramirez M. O., Kumar A., Denev S. A., Podraza N. J., Xu X. S., Rai R. C., Chu Y. H., Seidel J., Martin L. W., Yang S. Y., Saiz E., *Physical Review B*, (2009), *79*(22), 224106(1-9).

50. Pisarev R. V., Moskvin A. S., Kalashnikova A. M., Rasing T., *Physical Review B*, (2009), *79*(23), 235128(1-16).
51. Rao T. D., Karthik T., Asthana S., *Journal of Rare Earths*, (2013), *31*(4), 370-375.
52. Luo L., Luo W., Yuan G., Wei W., Yuan X., Zhang H., Shen K., Xu M., Xu, Q., *Journal of Superconductivity and Novel Magnetism*, (2013), *26*(11), 3309-3313.
53. Dhir G., Uniyal P., Verma N. K., *Materials Science in Semiconductor Processing*, (2014), *27*, 611-618.
54. Khomchenko V. A., Kiselev D. A., Kopcewicz M., Maglione M., Shvartsman V. V., Borisov P., Kleemann W., Lopes A. M. L., Pogorelov Y. G., Araujo J. P., Rubinger R. M., *Journal of Magnetism and Magnetic Materials*, (2009), *321*(11), 1692-1698.
55. Singh P., Jung J. H., *Physica B: Condensed Matter*, (2010), *405*(4), 1086-1089.
56. Muneeswaran M., Jegatheesan P., Gopiraman M., Kim I. S., Giridharan N. V., *Applied Physics A*, (2014), *114*(3), 853-859.
57. Shannon R. D., *Acta Crystallographica Section A: Crystal Physics, Diffraction, Theoretical and General Crystallography*, (1976), *32*(5), 751-767.
58. Singh A., Pandey V., Kotnala R. K., Pandey D., *Physical Review Letters*, (2008), *101*(24), 247602(1-4).
59. Mocherla P. S., Karthik C., Ubic R., Ramachandra Rao M. S., Sudakar C., *Applied Physics Letters*, (2013), *103*(2), 022910(1-5).

CHAPTER IV

STUDY OF Ti DOPING AT Fe SITE FOR $Bi_{0.9}A_{0.1}Fe_{1-y}Ti_yO_3$ (A- Ba^{2+}, La^{3+}, Ho^{3+}, 0<y<0.20) CERAMICS

In this chapter the effect of Titanium (Ti^{4+}) substitution at the Fe^{3+} site in modified BFO on the structural, morphological, dielectric, ferroelectric, magnetic and optical properties were examined. The following polycrystalline multiferroic materials have been synthesized in the present chapter:

a)	$Bi_{0.9}La_{0.1}Fe_{1-y}Ti_yO_3$	where y = 0.0, 0.05, 0.10, 0.15 and 0.20
b)	$Bi_{0.9}Ho_{0.1}Fe_{1-y}Ti_yO_3$	where y = 0.0, 0.10 and 0.20
c)	$Bi_{0.9}Ba_{0.1}Fe_{1-y}Ti_yO_3$	where y = 0.0, 0.05, 0.10, 0.15 and 0.20

4.1 $Bi_{0.9}La_{0.1}Fe_{1-y}Ti_yO_3$ ($0.0 \leq y \leq 0.20$) ceramics

4.1.1 SYNTHESIS

$Bi_{0.9}La_{0.1}Fe_{1-y}Ti_yO_3$ ceramics with different composition of y= 0.0, 0.05, 0.10, 0.15 and 0.20 were prepared through combustion technique. $Bi(NO_3)_3 \cdot 5H_2O$, $Fe(NO_3)_3.9H_2O$, $La(NO_3)_3 \cdot 3H_2O$ and [Ti $(OCH(CH_3)_2)_4$] taken as starting materials and glycine as fuel. Then the mixed solution was stirred vigorously using a magnetic stirrer for 30 minutes at 80 °C to obtain a homogeneous transparent solution. Brownish color ash was obtained after auto-ignition of the solution. The ash was then dried at 100 °C in an electric oven for an hour. Agate mortar was used to grind the ash to obtain fine powders. The obtained powder was calcined at 500 °C. The calcined powder was pressed down to pellets of dia. 10 mm and sintered at 520 °C for 2 hours. The compositions of $Bi_{0.9}La_{0.1}Fe_{1-y}Ti_yO_3$ where y= 0.0, 0.05, 0.10, 0.15 and 0.20 was signified as BLFTO-0.0, BLFTO-0.05, BLFTO-0.10, BLFTO-0.15 and BLFTO-0.20, respectively. The characterization of the prepared samples were carried out by X-ray diffraction, TEM, FESEM, dielectric measurement, impedance analysis, ferroelectric measurement, VSM, FTIR spectroscopy, *UV*-Visible spectrometer and PL spectroscopy.

4.1.2 X-RAY DIFFRACTION STUDIES

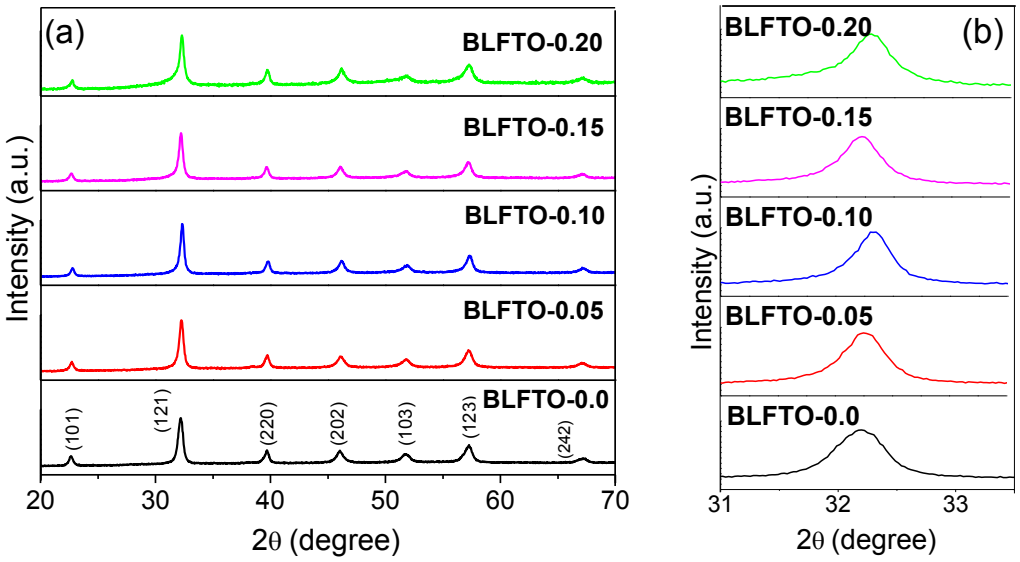

Figure 4.1 (a) X-ray diffraction patterns of $Bi_{0.9}La_{0.1}Fe_{1-y}Ti_yO_3$ nanoparticles ($0.0 \leq y \leq 0.20$) **(b)** Enlarged view of the characteristic peak.

Figure 4.1 (a) shows the XRD patterns of $Bi_{0.9}La_{0.1}Fe_{1-y}Ti_yO_3$ ($0.0 \leq y \leq 0.20$) nanoparticles. It is observed from the figure that all the nanoparticles with a pure phase are successfully synthesized. A magnified pattern shows the substitution effect of Ti^{4+} ions on the crystallization of BLFTO-0.0, BLFTO-0.05, BLFTO-0.10, BLFTO-0.15 and BLFTO-0.20 nanoparticles near 32º is delineated in **Figure 4.1 (b)**. It is observed that the diffraction peaks shift with Ti^{4+} substitution, indicating compressive lattice/structural distortion. Such type of structural distortion may be attributed to the ionic size mismatch of Fe^{3+} ions ($r_{Fe^{3+}}$= 0.645 Å) and Ti^{4+} ions ($r_{Ti^{4+}}$= 0.604 Å) and can be determined by Goldschmidt's tolerance factor (t) **[1]**:

$$t = \frac{\left((1-x)r_{Bi} + xr_{La}\right) + r_o}{\sqrt{2}((1-y)r_{Fe} + yr_{Ti}) + r_o} \qquad Eq.\ 4.1$$

where $r_{Bi^{3+}}$, $r_{La^{3+}}$, $r_{Fe^{3+}}$, $r_{Ti^{4+}}$ and $r_{O^{2-}}$ are ionic radii of Bi^{3+}, La^{3+}, Fe^{3+}, Ti^{4+} and O^{2-} ions, respectively. The calculated tolerance factors are 0.888, 0.8891, 0.8900, 0.8909 and 0.8918 for BLFTO-0.0, BLFTO-0.05, BLFTO-0.10, BLFTO-0.15 and BLFTO-0.20, respectively. The increment in *t* indicates that Ti^{4+} ions with smaller ionic radius than Fe^{3+} help to stabilize the crystal symmetry of $Bi_{0.9}La_{0.1}FeO_3$ nanoparticles.

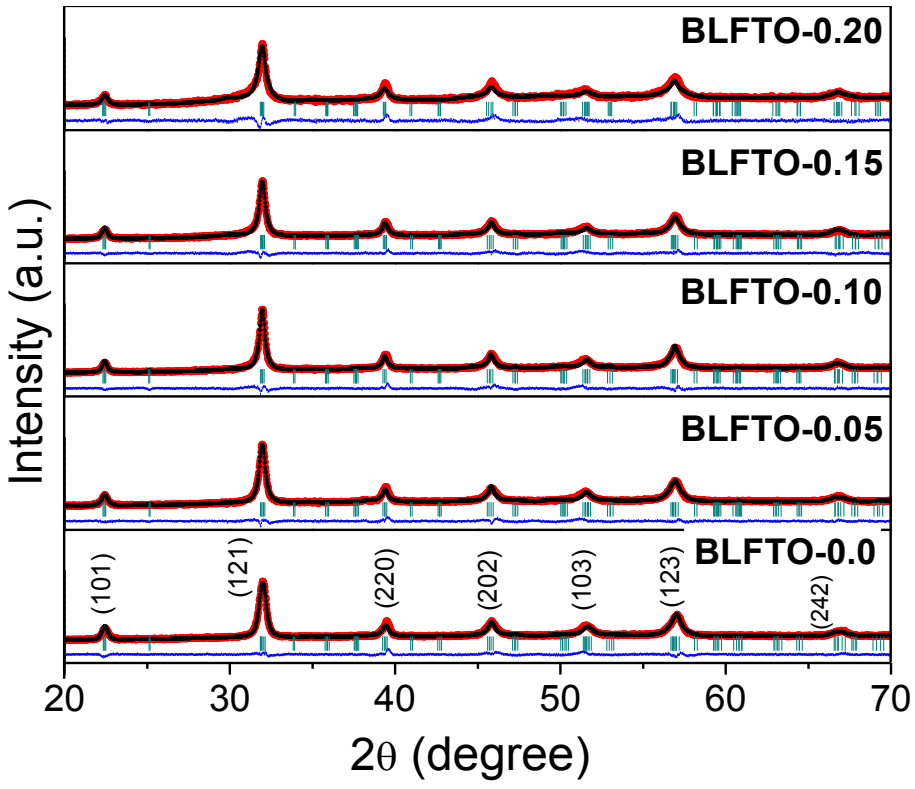

Figure 4.2 Rietveld refinements of the XRD patterns of $Bi_{0.9}La_{0.1}Fe_{1-y}Ti_yO_3$ nanoparticles ($0.0 \leq y \leq 0.20$).

Table 4.1 Refined structural parameters for $Bi_{0.9}La_{0.1}Fe_{1-y}Ti_yO_3$ nanoparticles ($0.0 \leq y \leq 0.20$) obtained by rietveld analysis.

Composition of $Bi_{0.9}La_{0.1}Fe_{1-y}Ti_yO_3$	**Atom**	**Fractional coordinates**			**Lattice Constant [Å]**	**Bond angle [°]**	**Bond length [Å]**	**Statistical Parameter (%)**
		x	**y**	**z**				
BLFTO-0.0 *Pnma* V= 249.15 (Å^3)	Bi/La Fe O1 O2	0.0036 0.0000 0.4744 0.1988	0.2500 0.0000 0.2500 0.5344	0.9976 0.5000 0.1016 0.2050	a =5.61 b =7.95 c = 5.57	Fe-O1-Fe =147.22 Fe-O2-Fe =153.34	Bi/La-O1 =2.24 Bi/La-O2 =2.76 Fe-O1 =2.07 Fe-O2 =2.00	R_p=4.49 R_{wp}=5.87 R_{exp}=3.46 χ^2=2.87
BLFTO-0.05 *Pnma* V= 249.26(Å^3)	Bi/La Fe/Ti O1 O2	0.0126 0.0000 0.4446 0.1988	0.2500 0.0000 0.2500 0.5344	1.0054 0.5000 0.0397 0.1068	a =5.61 b =7.95 c =5.58	Fe-O1-Fe = 158.27 Fe-O2-Fe = 133.98	Bi/La-O1 =2.56 Bi/La-O2 =2.55 Fe/Ti-O1 =2.02 Fe/Ti-O2 =2.47	R_p=4.52 R_{wp}=5.82 R_{exp}=3.60 χ^2=2.62
BLFTO-0.10 *Pnma* V= 249.50(Å^3)	Bi/La Fe/Ti O1 O2	0.0293 0.0000 0.4724 0.1988	0.2500 0.0000 0.2500 0.5344	1.0024 0.5000 0.0750 0.2050	a =5.61 b =7.95 c =5.59	Fe-O1-Fe = 154.64 Fe-O2-Fe = 153.34	Bi/La-O1 =2.38 Bi/La-O2 =2.70 Fe/Ti-O1 =2.03 Fe/Ti-O2 =2.00	R_p=4.86 R_{wp}=6.35 R_{exp}=3.67 χ^2=2.99
BLFTO-0.15 *Pnma* V= 249.16 (Å^3)	Bi/La Fe/Ti O1 O2	0.0284 0.0000 0.5272 0.1988	0.2500 0.0000 0.2500 0.5344	1.0012 0.5000 0.0273 0.2050	a =5.60 b =7.95 c =5.58	Fe-O1-Fe = 167.60 Fe-O2-Fe = 153.34	Bi/La-O1 =2.63 Bi/La-O2 =2.70 Fe/Ti-O1 =2.00 Fe/Ti-O2 =2.00	R_p=4.77 R_{wp}=6.08 R_{exp}=3.61 χ^2=2.83
BLFTO-0.20 *Pnma* V= 249.58(Å^3)	Bi/La Fe/Ti O1 O2	0.0205 0.0000 0.4645 0.1988	0.2500 0.0000 0.2500 0.5344	1.0044 0.5000 -0.0095 0.2050	a =5.60 b =7.96 c =5.59	Fe-O1-Fe = 168.19 Fe-O2-Fe = 153.33	Bi/La-O1 =2.84 Bi/La-O2 =2.71 Fe/Ti-O1 =2.00 Fe/Ti-O2 =2.00	R_p=5.30 R_{wp}=6.75 R_{exp}=3.78 χ^2=3.19

Further, these nanoparticles were analyzed to extract the crystal symmetry and structural parameters by rietveld refinement using FULLProf tool. **Figure 4.2** shows the refined XRD patterns of BLFTO-0.0, BLFTO-0.05, BLFTO-0.10, BLFTO-0.15 and BLFTO-0.20 nanoparticles. The refinement of the diffraction peaks associated with BLFTO-0.0 nanoparticles was carried out via. *R3c* crystal symmetry but the best fit between observed and calculated

interplanar spacing of *hkl* planes was not obtained. Whereas, the required low profile R-factors (<10%) are obtained with orthorhombic crystal symmetry (*Pnma*) which confirms the best fit for BLFTO-0.0 nanoparticles **[2-6]**. In fact, no observed splitting in the diffraction peaks is evident of structural phase transformation with the substitution of Ti^{4+} ions. The observed and refined XRD patterns for BLFTO-0.0, BLFTO-0.05, BLFTO-0.10, BLFTO-0.15 and BLFTO-0.20 nanoparticles using orthorhombic crystal symmetry (*Pnma*) are shown in **Figure 4.2**. The corresponding refined structural parameters are summarized in **Table 4.1**. The crystallite size was calculated to be 29.37 nm, 17.84 nm, 14.04 nm, 19.69 nm and 13.56 nm for BLFTO-0.0, BLFTO-0.05, BLFTO-0.10, BLFTO-0.15 and BLFTO-0.20 nanoparticles, respectively (**Figure 4.3**) **[7, 8]**. The corresponding microstrain values are 0.01037, 0.01298, 0.01425, 0.01143 and 0.01465 for BLFTO-0.0, BLFTO-0.05, BLFTO-0.10, BLFTO-0.15 and BLFTO-0.20 nanoparticles, respectively.

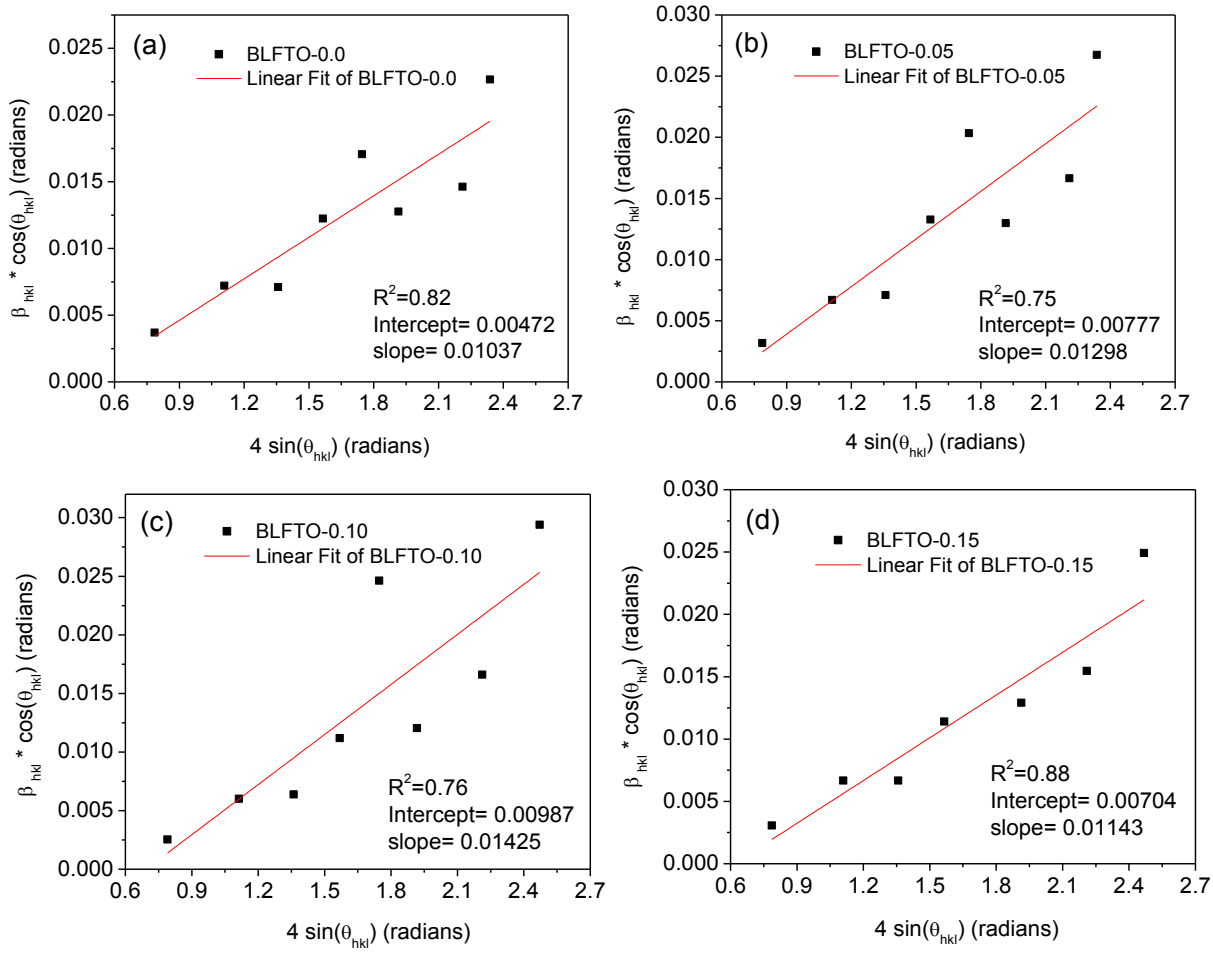

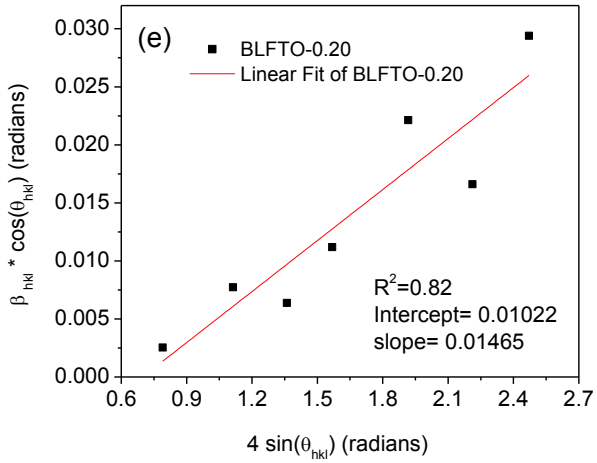

Figure 4.3 Williamson–Hall plots of **(a)** BLFTO-0.0 **(b)** BLFTO-0.05 **(c)** BLFTO-0.10 **(d)** BLFTO-0.15 **(e)** BLFTO-0.20 samples.

4.1.3 MORPHOLOGICAL STUDIES

Representative TEM micrographs of BLFTO-0.0, BLFTO-0.05, BLFTO-0.10, BLFTO-0.15 and BLFTO-0.20 powder samples are shown in **Figures 4.4 (a-e)**. It can be seen that the particle shape is almost spherical and agglomerated at few places due to high surface energy of the nanoparticles **[9, 10]**. The particle size of BLFTO-0.0, BLFTO-0.05, BLFTO-0.10, BLFTO-0.15 and BLFTO-0.20 nanoparticles in agglomerates is in the range of 46 nm to 60 nm, respectively. The trend in variation of particle size of all nanoparticles as observed from TEM images is similar to that of crystallite size as obtained from powder XRD pattern. It is due to Ti^{4+} substitution which restricted the crystal growth and hence, the decrease in particle size is observed. The SAED pattern taken from **Figure 4.4 (a and d)**, illustrated the sharp diffraction rings signifying well developed polycrystalline nature of the nanoparticles as shown in **Figure 4.4 (f-g)**, respectively.

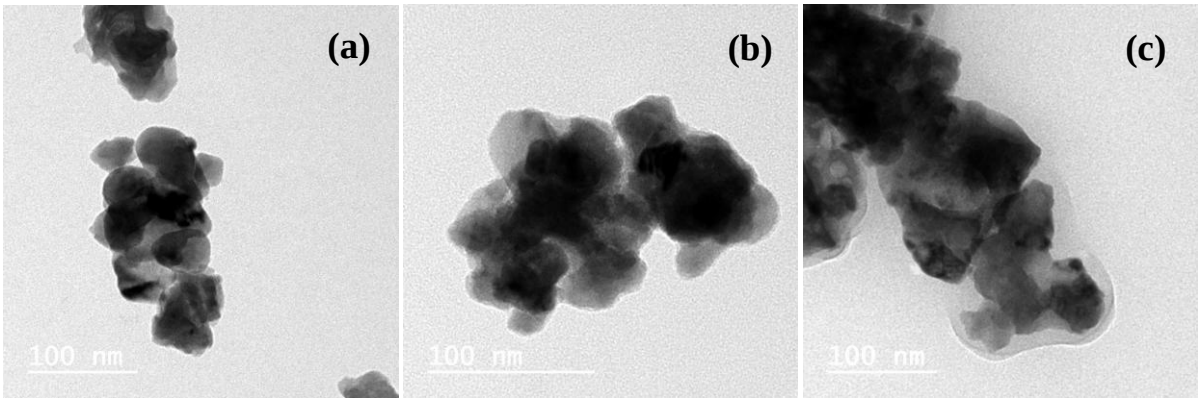

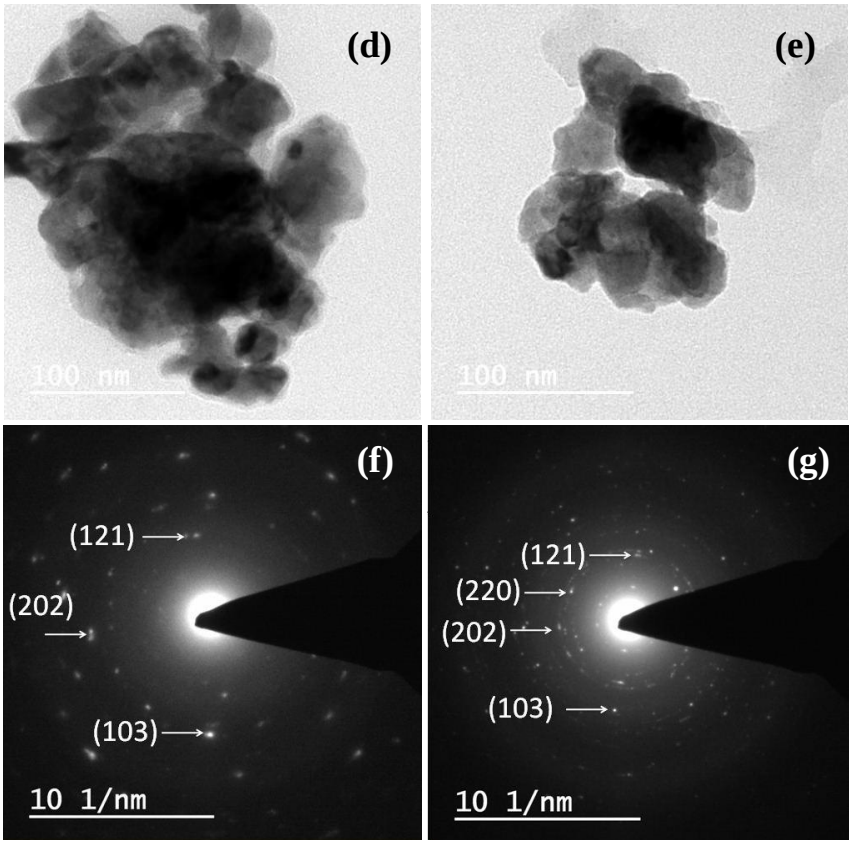

Figure 4.4 TEM images of **(a)** BLFTO-0.0 **(b)** BLFTO-0.05 **(c)** BLFTO-0.10 **(d)** BLFTO-0.15 **(e)** BLFTO-0.20 and SAED patterns of **(f)** BLFTO-0.0 **(g)** BLFTO-0.15 nanoparticles.

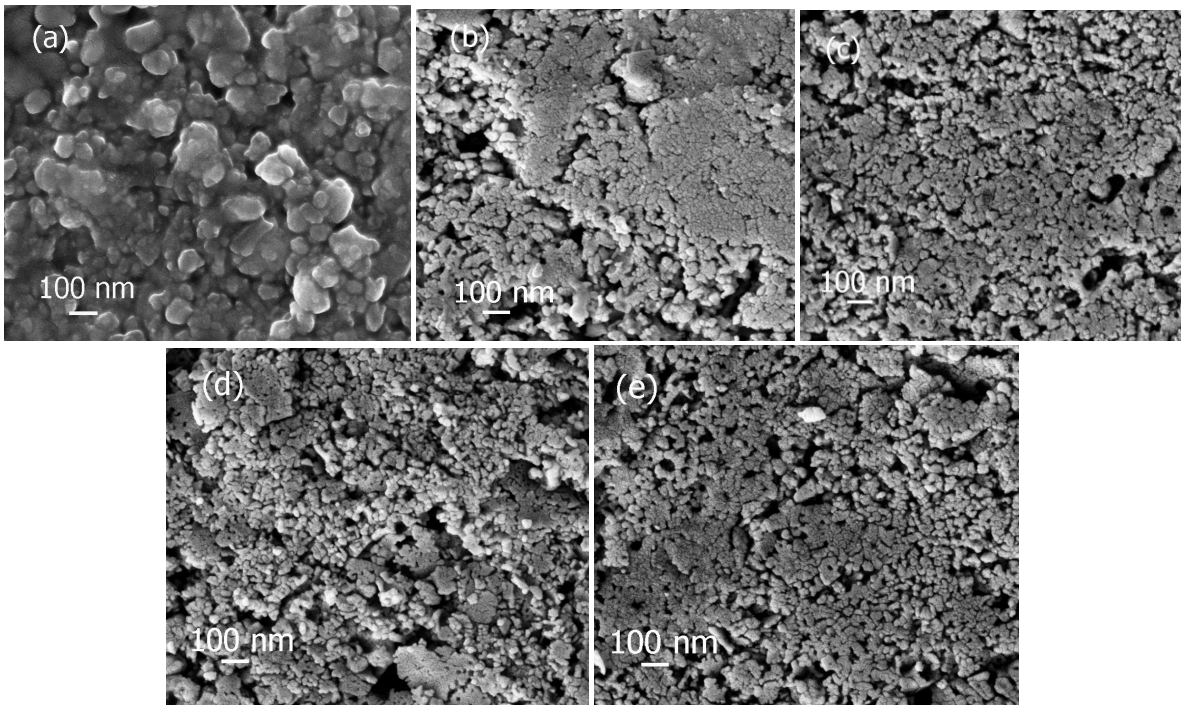

Figure 4.5 FESEM micrographs of **(a)** BLFTO-0.0 **(b)** BLFTO-0.05 **(c)** BLFTO-0.10 **(d)** BLFTO-0.15 **(e)** BLFTO-0.20 samples.

The morphology of sintered pellets of BLFTO-0.0, BLFTO-0.05, BLFTO-0.10, BLFTO-0.15 and BLFTO-0.20 ceramics was analyzed by FESEM. It is observed from **Figure 4.5 (a)** that BLFTO-0.0 ceramics display spherical shaped grains with the average grain size of 98±3 nm. However, the grain size appears to decrease with the addition of Ti^{4+} ions as shown in **Figures 4.5 (b-e) [11]**. The decrease in the size of grains suggests that Ti^{4+} substitution suppress the oxygen vacancies (Vo^{2+}) and consequently inhibit the grain growth **[12, 13].**

4.1.4 DIELECTRIC STUDIES

The substitution effect of Ti^{4+} ions on dielectric characteristics of BLFTO-0.0, BLFTO-0.05, BLFTO-0.10, BLFTO-0.15 and BLFTO-0.20 ceramics has also been investigated. **Figure 4.6** shows the graph of dielectric constant (ε) for BLFTO-0.0, BLFTO-0.05, BLFTO-0.10, BLFTO-0.15 and BLFTO-0.20 ceramics as a function of frequency at room temperature. As predicted, the high values of ε are obtained at lower frequency side and drop off with increasing frequency for BLFTO-0.0 ceramics which is directly attributed to the phenomenon of dipole relaxation **[15, 16]**. However, with the substitution of Ti^{4+} ions, the value of ε is observed to increase for all doped ceramics as compared to BLFTO-0.0 ceramics. Variation of ε values in Ti^{4+} substituted ceramics could be ascribed to size effect of grains **[17, 18]**. A Ti^{4+} doping ion reduces the grain size of ceramics and hence enhanced the volume fraction of grain boundaries which results in high value of ε.

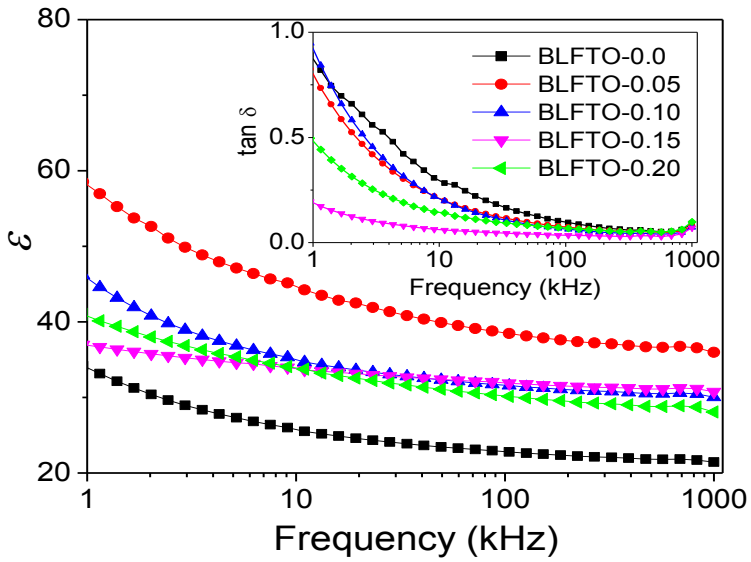

Figure 4.6 Variation of dielectric constant (ε) for BLFTO-0.0, BLFTO-0.05, BLFTO-0.10, BLFTO-0.15 and BLFTO-0.20 samples as a function of frequency, the inset shows the variation of dissipation factor (*tan* δ) as a function of frequency.

Correspondingly, *tan δ* is found to decrease with the substitution of Ti^{4+} ions in $Bi_{0.9}La_{0.1}FeO_3$ ceramics as illustrated in the inset of **Figure 4.6**, indicates that Ti^{4+} doping efficiently suppressed the formation of oxygen vacancies (Vo^{2+}) **[12-14]**.

Figure 4.7 shows thermal dependence of dielectric constant (ε) for BLFTO-0.0, BLFTO-0.05, BLFTO-0.10, BLFTO-0.15 and BLFTO-0.20 at different frequencies (1 kHz-1 MHz). It is observed from the **Figure 4.7 (a)** that the dielectric constant for BLFTO-0.0 increases up to peak temperature (T_p= 379 °C) and then decreases with increase in temperature at 1 kHz. The observed anomaly around 379 °C may correspond to an antiferromagnetic Néel temperature (T_N) which could be induced by the magnetoelectric coupling between its electric and magnetic orders **[19, 20]**. A similar dielectric anomaly at 379 °C is also observed with the change in frequency from 1 kHz to 1 MHz for BLFTO-0.0 ceramics. However, with the addition of Ti^{4+} ions, two dielectric anomalies are observed for BLFTO-0.05 ceramics as shown in **Figure 4.7 (b)**. An anomaly near 309 °C which is far below than T_N (around 375 °C) is normally ascribed to a transient interaction between Fe^{3+}-Fe^{2+} redox couple and oxygen ion vacancies (Vo^{2+}) **[15]**. A repetition pattern of dielectric constant is also followed by BLFTO-0.10, BLFTO-0.15 and BLFTO-0.20 ceramics with temperature as shown in **Figures 4.7 (c-e)**. Whereas, the T_N is found to be shift with the substitution of Ti^{4+} ions and this shift in T_N obtained here may be ascribed to change in spin canted Fe-O-Fe angle due to structural modification (**Table 4.1) [21-24]**. However, similar dielectric anomalies are also evident in dielectric loss for all ceramics as shown in the inset of **Figures 4.7 (a-e).**

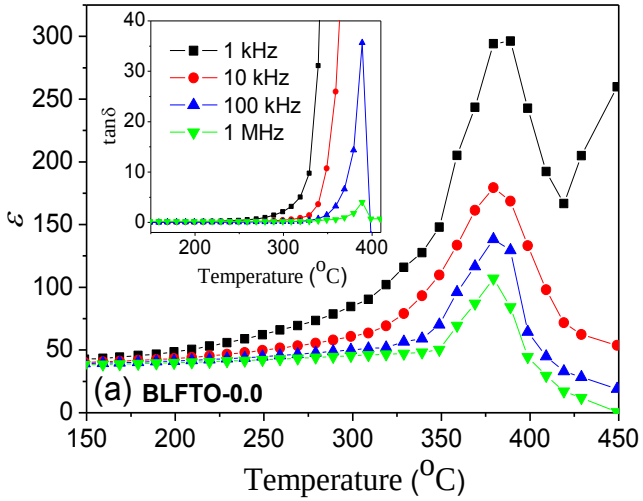

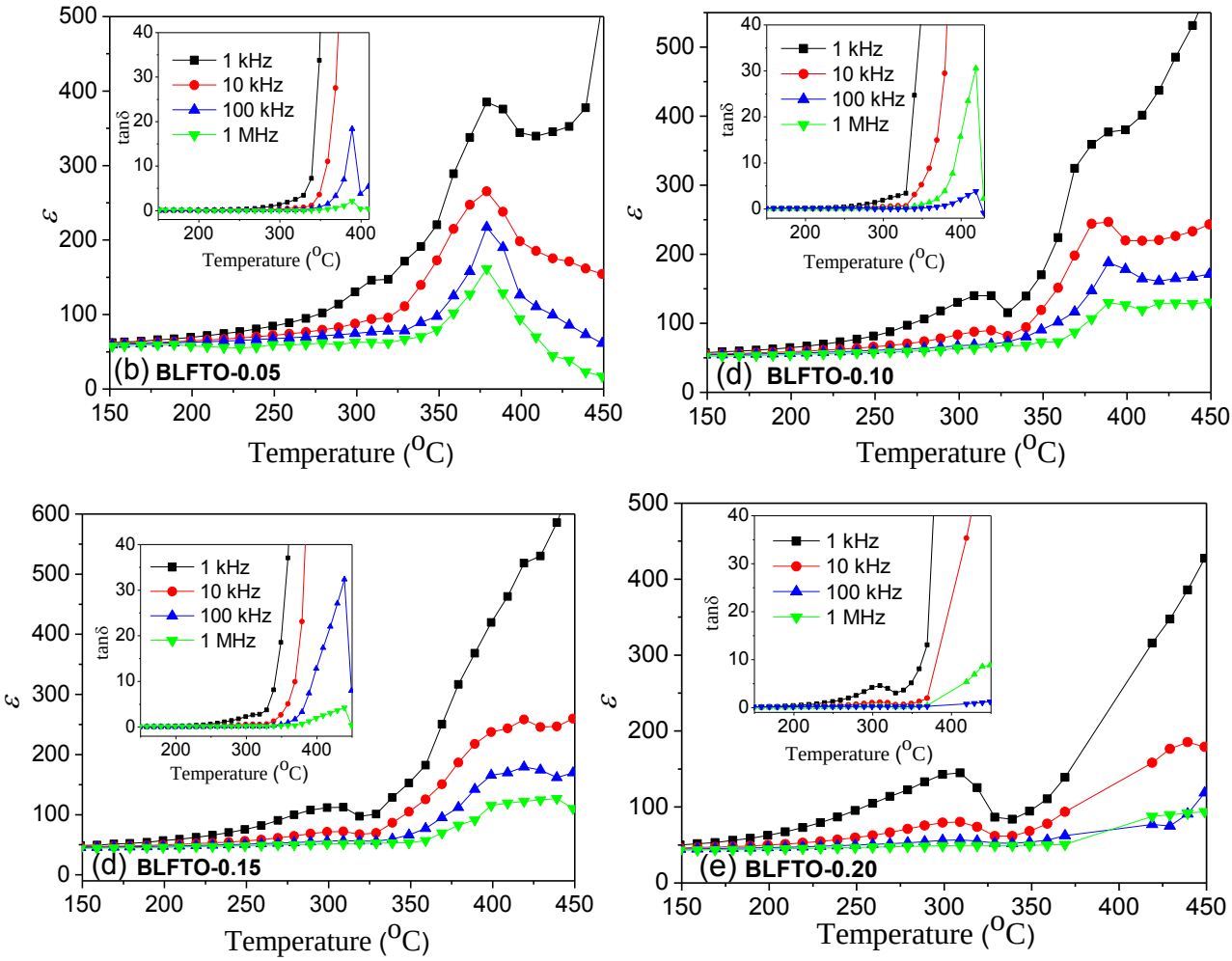

Figure 4.7 Dielectric constant (ε) and dissipation factor (*tan* δ) versus temperature curves for $Bi_{0.9}La_{0.1}Fe_{1-y}Ti_yO_3$ samples at 1 kHz, 10 kHz, 100 kHz and 1 MHz.

Impedance analysis has been carried out in $Bi_{0.9}La_{0.1}Fe_{1-y}Ti_yO_3$ ($0.0 \leq y \leq 0.20$) ceramics to study its conduction mechanism. Temperature dependence of the real part of impedance (Z') in terms of frequency at different temperatures (230 °C to 310 °C) is shown in **Figure 4.8.** An obvious decrease in the values of Z' is observed with increase in frequency, followed by an invariable region, indicates the onset in a.c. conductivity **[25]**. An invariable region at high frequency directly ascribed to the release of space charge polarization in ceramics. Similarly, Z' also decreases with increase in temperature normally show the negative temperature coefficient of resistance (NTCR) nature of the ceramics **[25, 26]**.

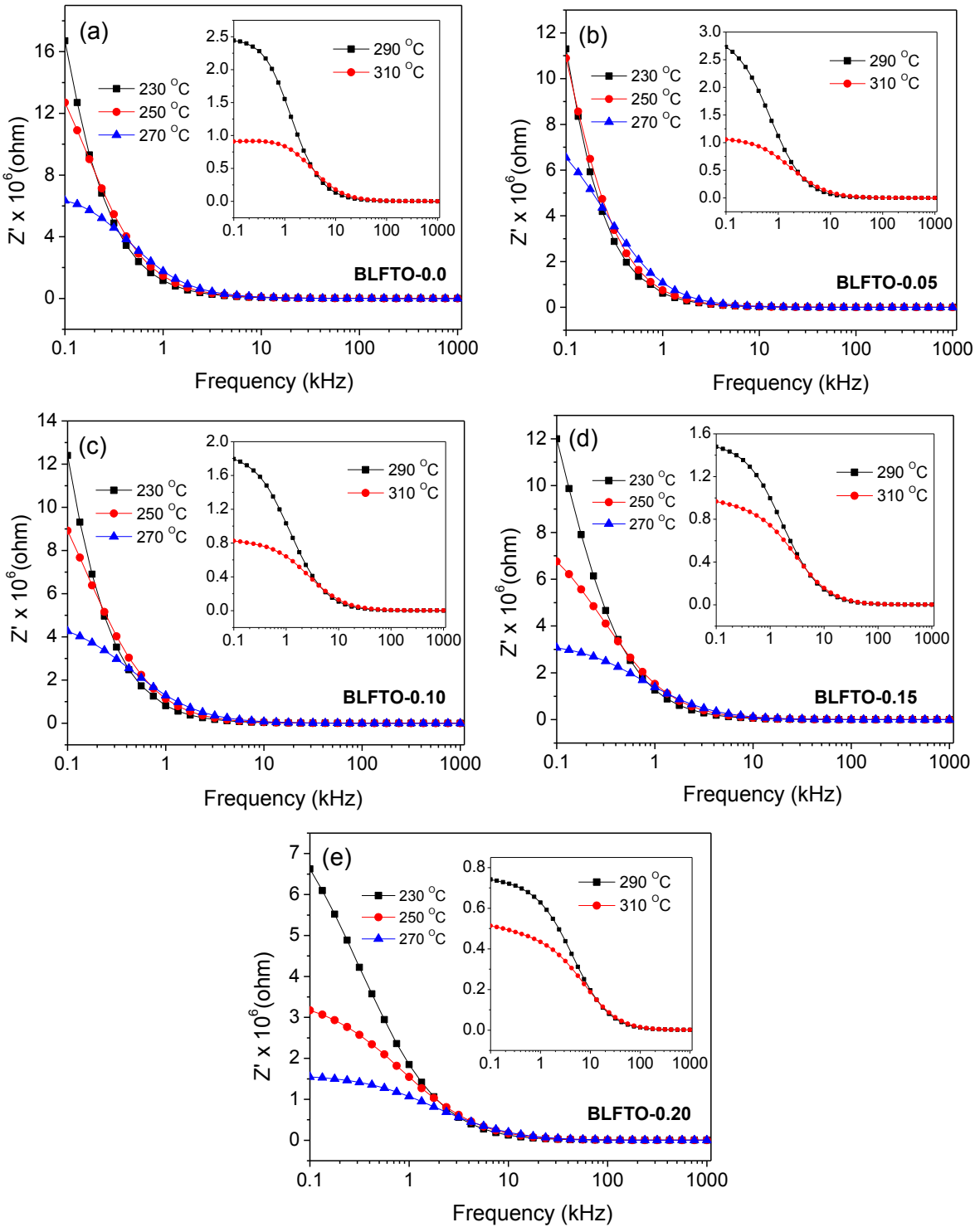

Figure 4.8 Frequency dependent real (Z') part of impedance for **(a)** BLFTO-0.0 **(b)** BLFTO-0.05 **(c)** BLFTO-0.10 **(d)** BLFTO-0.15 **(e)** BLFTO-0.20 samples at 230 °C, 250 °C and 270 °C, the inset shows the variation of impedance at 290 °C and 310 °C.

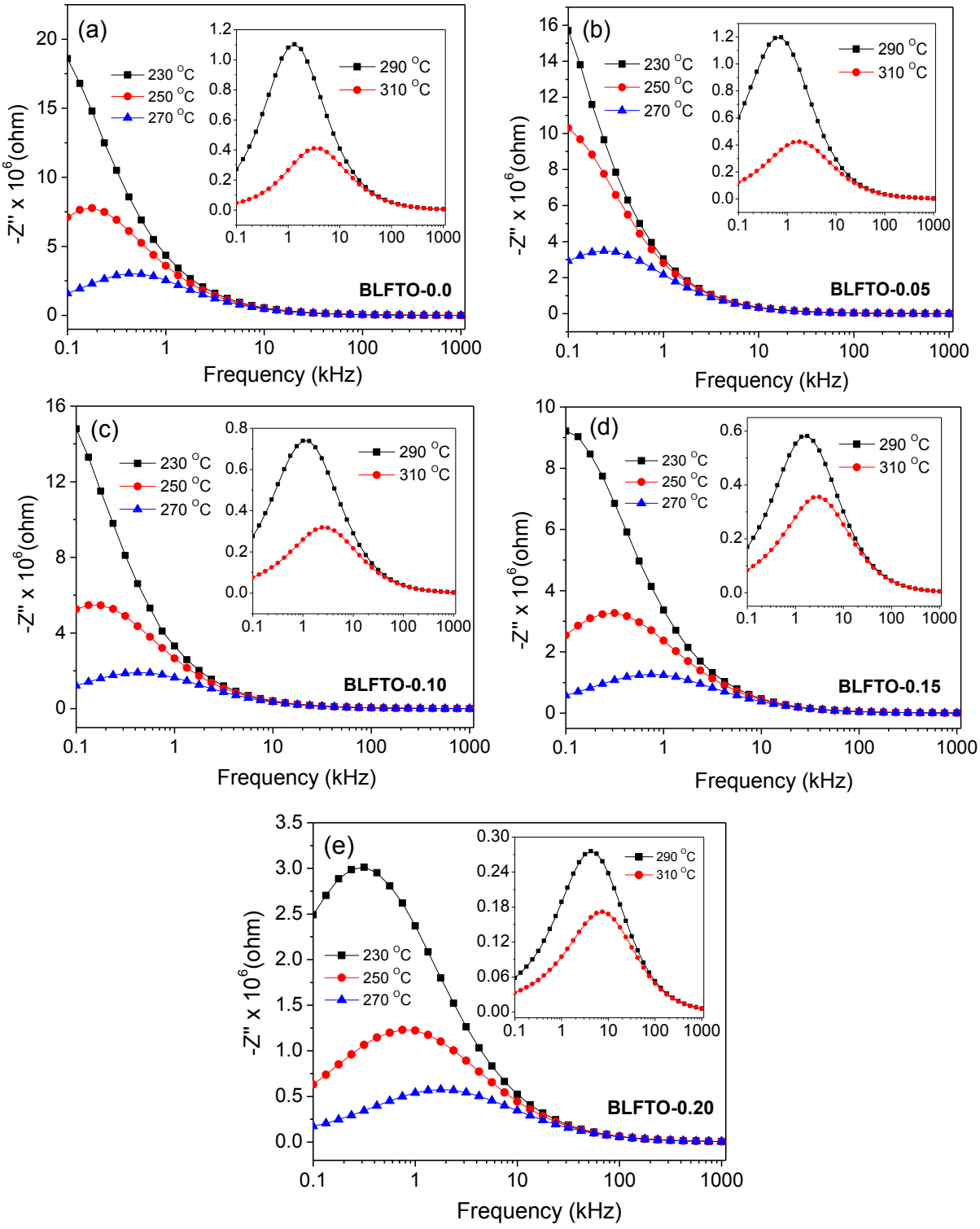

Figure 4.9 Frequency dependent imaginary (Z'') part of impedance for **(a)** BLFTO-0.0 **(b)** BLFTO-0.05 **(c)** BLFTO-0.10 **(d)** BLFTO-0.15 **(e)** BLFTO-0.20 samples at 230 °C, 250 °C and 270 °C, the inset shows the variation of impedance at 290 °C and 310 °C.

Temperature dependence of the imaginary part of impedance (Z") in terms of frequency at different temperatures (230 °C to 310 °C) is shown in **Figure 4.9.** It is observed that Z" frequency pattern for BLFTO-0.0 decreases with increase in frequency at 230 °C. Whereas, at higher temperatures, broad peak at a particular frequency f_{max} (called relaxation frequency) is obtained **[27]**. Even the relaxation frequency is found to shift towards high frequency with rise in temperature which suggests the asymmetry in the peak pattern and decrease of relaxation time ($\tau = 1/2\Pi f_{max}$) in doped ceramics. Similar behavior of Z" with frequency and temperature are also observed in BLFTO-0.05, BLFTO-0.10, BLFTO-0.15 and BLFTO-0.20 ceramics as shown in **Figures 4.9 (b-e)** respectively.

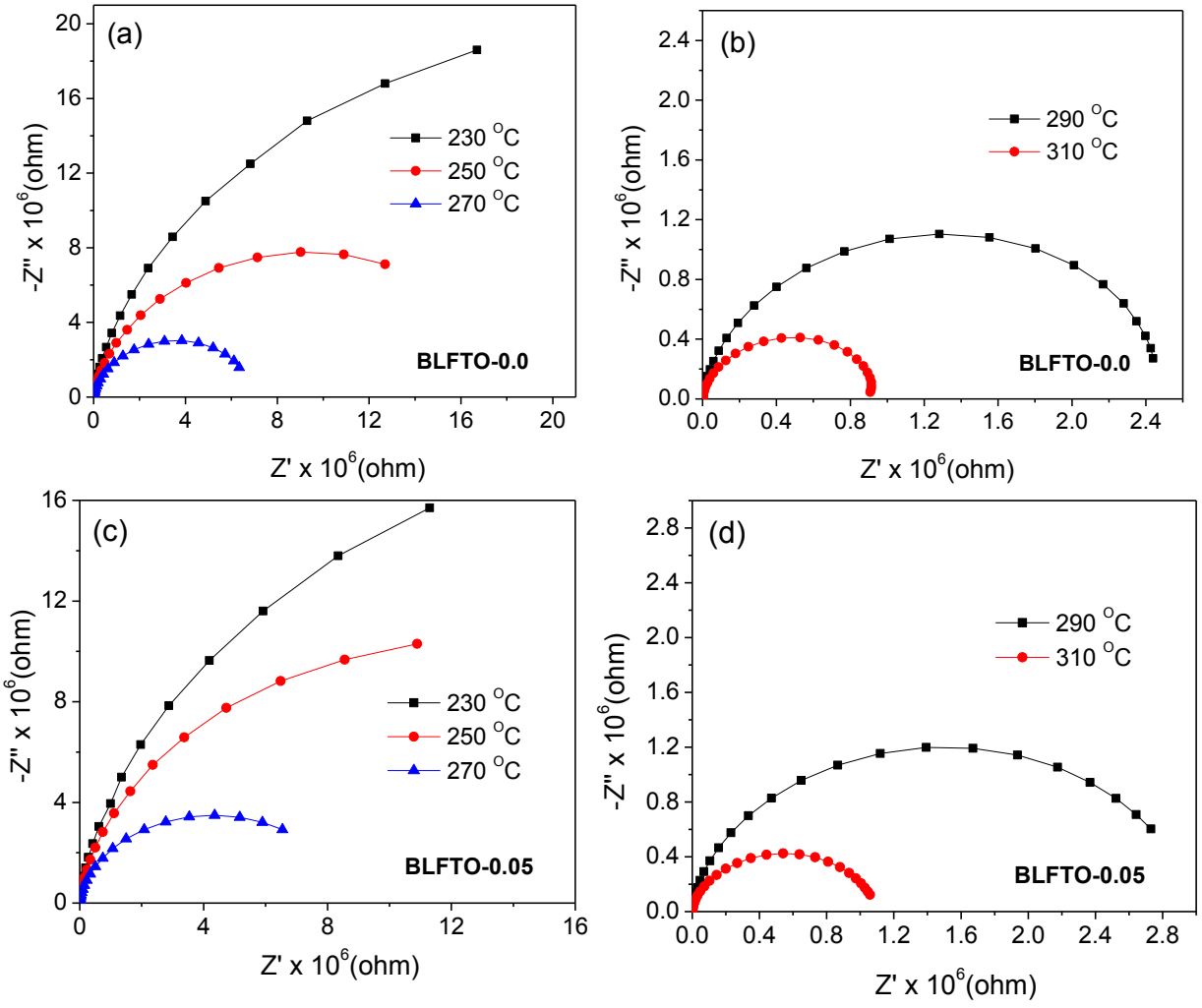

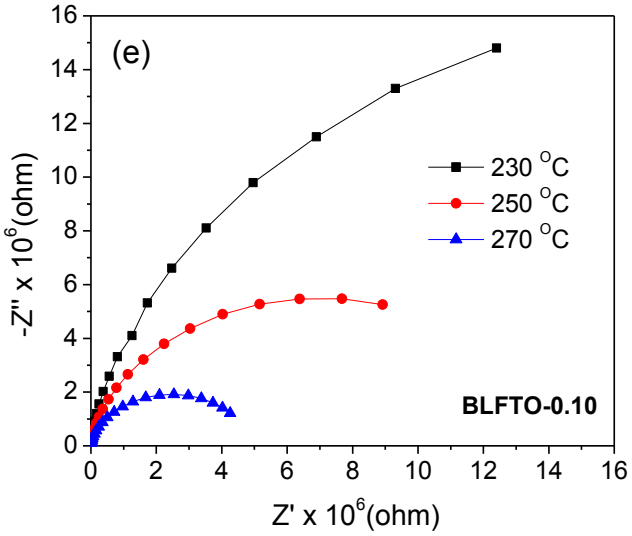
(e)
230 °C
250 °C
270 °C
BLFTO-0.10
-Z'' x 10^6(ohm)
Z' x 10^6(ohm)

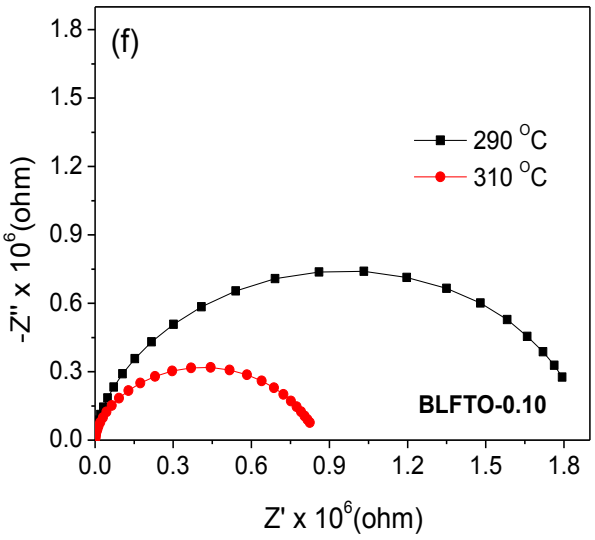
(f)
290 °C
310 °C
BLFTO-0.10
-Z'' x 10^6(ohm)
Z' x 10^6(ohm)

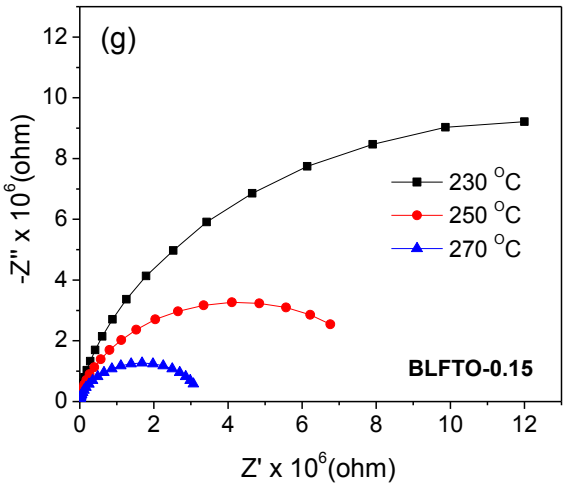
(g)
230 °C
250 °C
270 °C
BLFTO-0.15
-Z'' x 10^6(ohm)
Z' x 10^6(ohm)

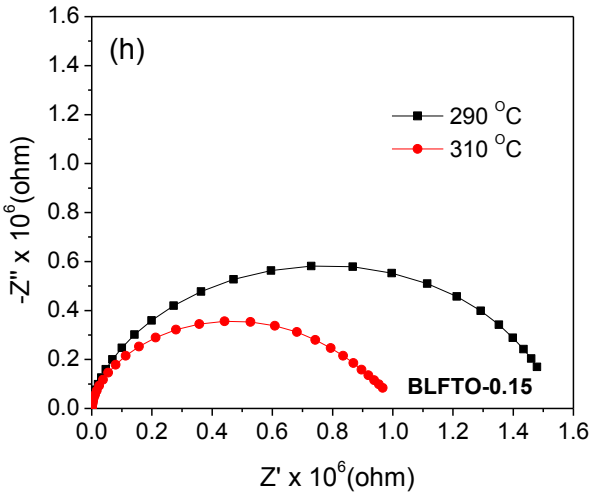
(h)
290 °C
310 °C
BLFTO-0.15
-Z'' x 10^6(ohm)
Z' x 10^6(ohm)

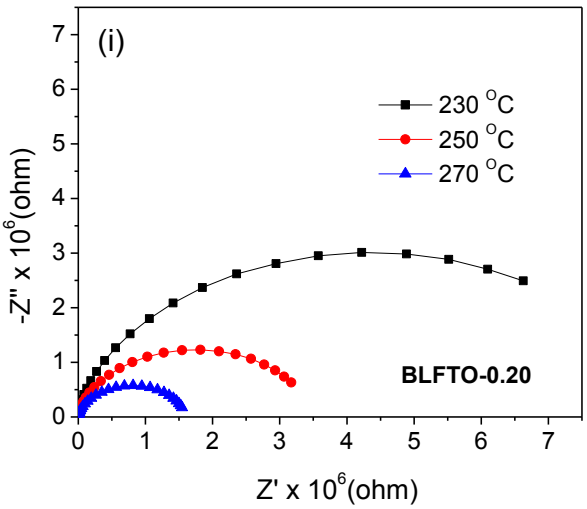
(i)
230 °C
250 °C
270 °C
BLFTO-0.20
-Z'' x 10^6(ohm)
Z' x 10^6(ohm)

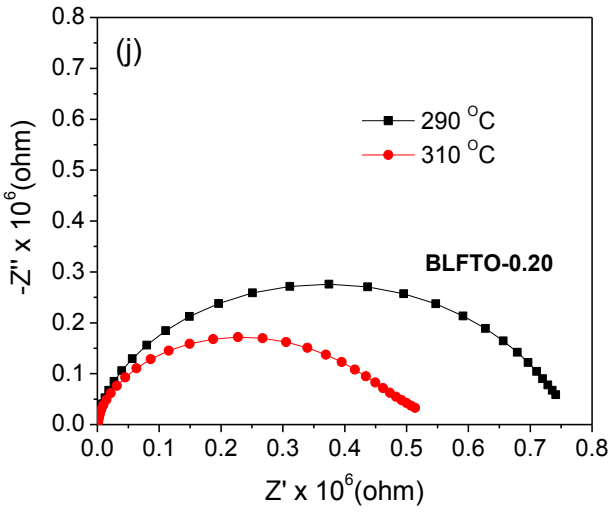
(j)
290 °C
310 °C
BLFTO-0.20
-Z'' x 10^6(ohm)
Z' x 10^6(ohm)

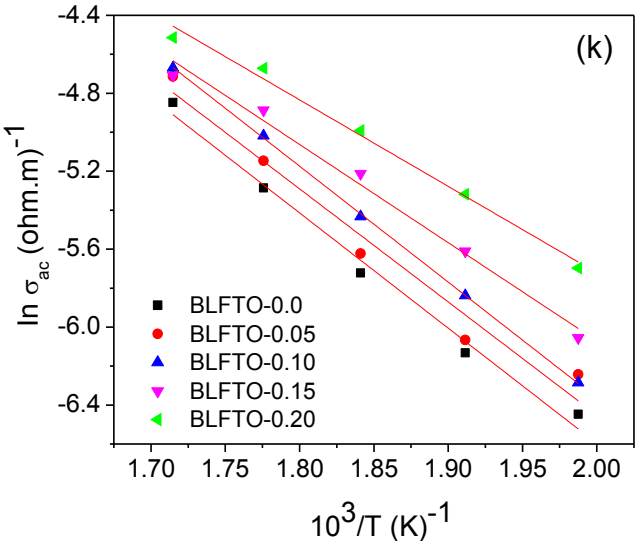

Figure 4.10 (a-j) Variation of imaginary part Z'' with respect to real part Z' of complex impedance (Nyquist plots) **(k)** Arrhenius plot with inverse of temperature for $Bi_{0.9}La_{0.1}Fe_{1-y}Ti_yO_3$ samples.

Figure 4.10 (a-j) shows temperature dependent nyquist plots (Z'' in terms of Z') for $Bi_{0.9}La_{0.1}Fe_{1-y}Ti_yO_3$ ($0.0 \leq y \leq 0.20$) ceramics. It is observed that, at lower temperatures, the onset of a semicircle having large slopes doesn't exhibit a unique relaxation time. This kind of behavior is the direct indication of insulating nature of ceramics. However, the apparent single arc at high temperatures for each composition is indicative of an individual conduction and relaxation process. Moreover, the intercept of semicircles on Z'-axis gives the bulk resistance of the ceramics. These resistance values have been used to calculate the ac conductivity (σ_{ac}) of the ceramics. As, ac conductivity follows the Arrhenius activation law, its plot against inverse of temperature is shown in **Figure 4.10 (k).** The calculated value of activation energy is 0.884 eV for BLFTO-0.0, 0.888 eV for BLFTO-0.05, 0.930 eV for BLFTO-0.10, 0.795 eV for BLFTO-0.15 and 0.710 eV for BLFTO-0.20 ceramics. The activation energy lie in a temperature range of 510 K-650 K, suggest the conducting behavior of the ceramics due to the contribution of short range hopping movement of oxygen vacancies **[27]**.

4.1.5 FERROELECTRIC STUDIES

The polarization–electric field loops of BLFTO-0.0, BLFTO-0.05, BLFTO-0.10, BLFTO-0.15 and BLFTO-0.20 ceramics measured at applied electric field of 9kV/cm. It is observed from the **Figure 4.11** that BLFTO-0.0 ceramics show elliptical shaped *P-E* loop, representing a high conductivity ascribable to the space charge defects, and non-zero remnant

polarization of 0.178 μC/cm^2 **[28]**. The obtained value of maximum polarization for BLFTO-0.0 is 0.227 μC/cm^2. A significantly improved ferroelectric hysteresis loop is observed with the substitution of Ti^{4+} ions in comparison to BLFTO-0.0 ceramics. The observed behavior of increase in polarization with increasing Ti^{4+} ions could be ascribed to the fact that structural distortion increases considerably (as evidenced by c/a ratio) with increase in substitution of Ti^{4+} ions **[29, 30]**. Moreover, with the further substitution of Ti^{4+} ions, ferroelectricity of the ceramics decreases due to the increase in conductivity.

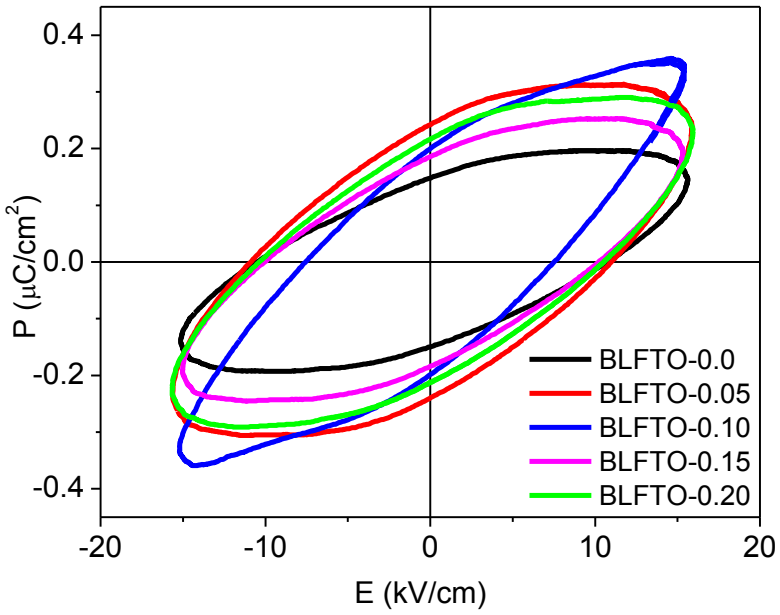

Figure 4.11 Variation of ferroelectric hysteresis loops for BLFTO-0.0, BLFTO-0.05, BLFTO-0.10, BLFTO-0.15 and BLFTO-0.20 samples.

4.1.6 MAGNETIC ANALYSIS

Figure 4.12 (a) shows the magnetization (*M*) versus applied field (*H*) plots for BLFTO-0.0, BLFTO-0.05, BLFTO-0.10, BLFTO-0.15 and BLFTO-0.20 nanoparticles at room temperature. For BLFTO-0.0 nanoparticles, the magnetic hysteresis loop shows a small but nonzero remnant magnetization (M_r) of 0.0143 emu/g and maximum magnetization (M_{max}) of 0.270 emu/g. The obtained value of magnetization (M_{max}) is 0.511, 0.599, 0.531 and 0.508 emu/g at 10 kOe for BLFTO-0.05, BLFTO-0.10, BLFTO-0.15 and BLFTO-0.20 nanoparticles, respectively. It has been observed that M_{max} increases with increase in Ti^{4+} ion substitution for BLFTO-0.05 and BLFTO-0.10. This could be ascribed to suppress in the inhomogeneous magnetic spin structure, and increase in oxygen octahedra tilt angle **[31]**. It may be due to

increase in Dzyaloshinskii-Moriya interactions which cause spin canting. Whereas, for BLFTO-0.15 and BLFTO-0.20 nanoparticles it is significantly lower, which occurred due to the collinear antiferromagnetic ordering and as resultant decreases the M_{max} value **[32, 33]**. It is also clear that the substitution of Ti^{4+} ions significantly increased H_c for BLFTO-0.05, BLFTO-0.10 and BLFTO-0.15 nanoparticles. However, further increment of Ti^{4+} ions, reduced H_c although their net value is still higher than the BLFTO-0.0 nanoparticles. The larger values of H_c in nanoparticles may be related to their magneto-crystalline anisotropy **[34-37]**.

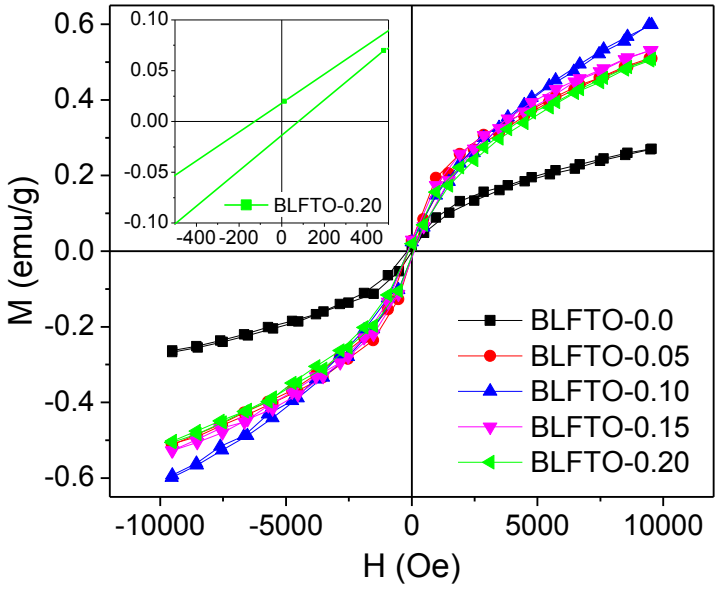

Figure 4.12 Room temperature magnetic hysteresis loops of BLFTO-0.0, BLFTO-0.05, BLFTO-0.10, BLFTO-0.15 and BLFTO-0.20 nanoparticles. Inset shows enlarged view of *M-H* loop for BLFTO-0.2 nanoparticles.

4.1.7 FTIR STUDIES

Figure 4.13 shows the FTIR spectra of BLFTO-0.0, BLFTO-0.05, BLFTO-0.10, BLFTO-0.15 and BLFTO-0.20 nanoparticles. The BLFTO-0.0 nanoparticles exhibit a strong and broad fundamental absorption band in the wavelength region 450-560 cm^{-1} which could be ascribed to the overlapping of Fe-O and Bi-O group vibrations. An absorption peaks at 451 cm^{-1}, 461 cm^{-1} and 568 cm^{-1} are characteristics of O-Fe-O bending and Fe-O stretching vibration of the octahedral FeO_6 group in BLFTO-0.0 structure **[23, 38]**. The weak peak near to 816 cm^{-1} is usually attributed to the trapped NO_3- ions. Besides 816 cm^{-1}, the peak at 847 cm^{-1} is ascribed to OH group vibration of absorbed water and CO_2 from the environment, when precursor was calcined. Carbonate groups are indicated by the broad band at around 1120-1070 cm^{-1}. **Figure**

4.13 also shows shifting of peaks in Ti^{4+} nanoparticles which could be associated with change in the corresponding ionic sizes due to doping.

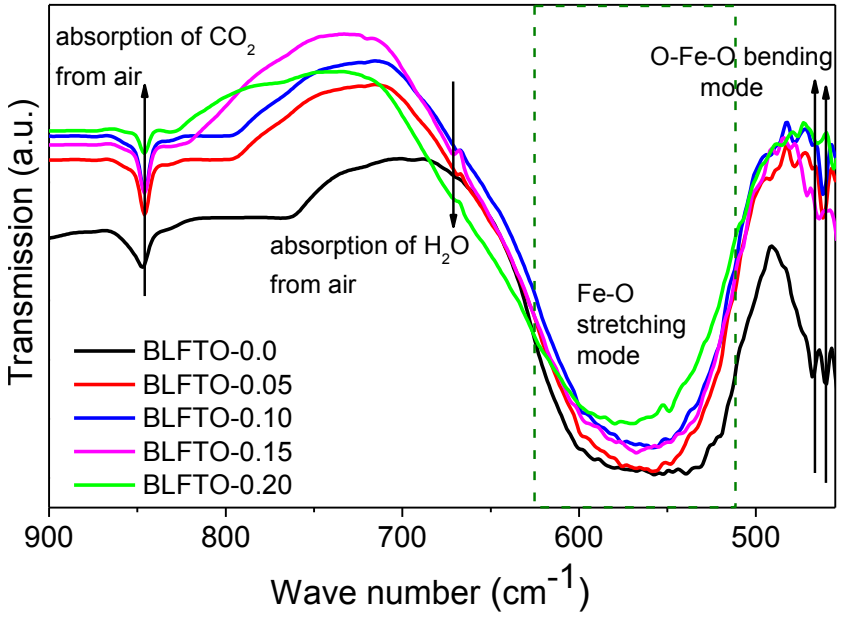

Figure 4.13 FTIR spectra for BLFTO-0.0, BLFTO-0.05, BLFTO-0.10, BLFTO-0.15 and BLFTO-0.20 nanoparticles.

4.1.8 *UV*-VISIBLE ABSORPTION STUDIES

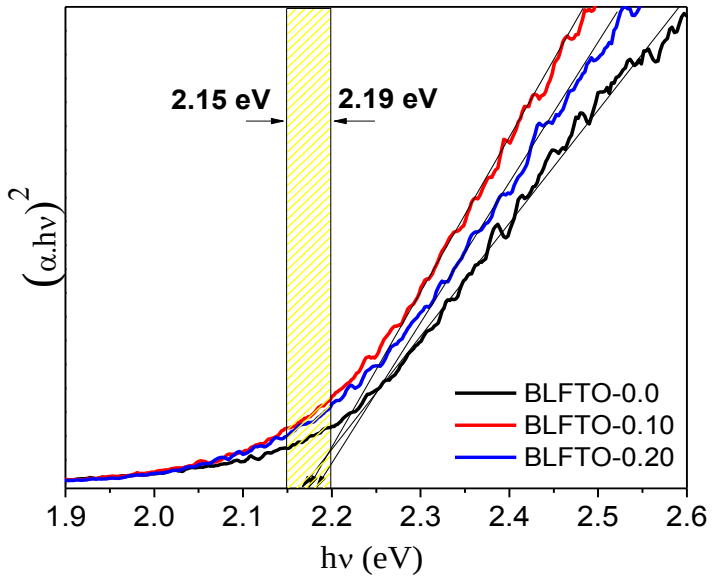

Figure 4.14 Tauc's plots for BLFTO-0.0, BLFTO-0.10 and BLFTO-0.20 nanoparticles.

The energy band gaps (E_g) of these nanoparticles have been calculated from *UV*-Vis absorption spectra using Tauc's relationship as shown **Figure 4.14**. The calculated values of

energy band gap for all the nanoparticles lies between the visible regions of 2.15-2.19 eV. It appears that the energy band gap for Ti^{4+} ions substituted nanoparticles does not change significantly due to lattice distortion.

4.2 $Bi_{0.9}Ho_{0.1}Fe_{1-y}Ti_yO_3$ ($0.0 \leq y \leq 0.20$) ceramics

4.2.1 SYNTHESIS

$Bi_{0.9}Ho_{0.1}Fe_{1-y}Ti_yO_3$ (y=0.0, 0.10 and 0.20) ceramics were prepared using combustion method by using $Bi(NO_3)_3{\cdot}5H_2O$, $Fe(NO_3)_3.9H_2O$, $Ho(NO_3)_3{\cdot}5H_2O$ and [Ti (OCH $(CH_3)_2)_4$]. $Bi(NO_3)_3{\cdot}5H_2O$ in nitric acid HNO_3, iron nitrate in deionized water, $Ho(NO_3)_3{\cdot}5H_2O$ and [Ti (OCH $(CH_3)_2)_4$] were mixed and stirred for 30 minutes to obtain a homogeneous transparent solution. The temperature of the mixed solution was sustained at 80 °C. After auto-ignition, within a few minutes, brownish color ash was acquired. The ash was then dried at 100 °C in an electric oven for an hour and the fine powder obtained after drying was ground and calcined at 500 °C. The powder obtained was palletized to 10 mm with a pressure of 6 MPa and then sintered for 2 hours at 520 °C. The compositions of $Bi_{0.9}Ho_{0.1}Fe_{1-y}Ti_yO_3$ where y= 0.0, 0.10 and 0.20 was signified as BHFTO-0.0, BHFTO-0.10 and BHFTO-0.20, respectively. The prepared samples were characterized with the help of X-ray diffraction, TEM, FESEM, dielectric measurement, impedance analysis, VSM, FTIR spectroscopy, *UV*-Visible spectrometer and PL spectroscopy.

4.2.2 X-RAY DIFFRACTION STUDIES

The XRD analysis of $Bi_{0.9}Ho_{0.1}Fe_{1-y}Ti_yO_3$ nanoparticles and their rietveld refinements were executed to investigate the change in structural parameters and their crystallite sizes as a result of Ti^{4+} doping. The XRD patterns of BHFTO-0.0, BHFTO-0.10 and BHFTO-0.20 nanoparticles are shown in **Figure 4.15 (a).** The diffraction peak positions of BHFTO-0.0 corresponding to the orthorhombic symmetry is observed which is in consistent with earlier report on Ho doped BFO ceramics **[3-5, 39]**. Moreover, a noticeable change in the intensity of diffraction peak and a shift towards higher 2θ for BHFTO-0.10 and BHFTO-0.20 nanoparticles are also observed, indicating lattice/structural distortion (**Figure 4.15 (b))**. The ionic size mismatch among Fe^{3+} ions ($r_{Fe^{3+}}$= 0.645 Å) and Ti^{4+} ions ($r_{Ti^{4+}}$= 0.604 Å) may be the reason of

observed lattice distortion and this distortion can be verified by Goldschmidt's tolerance factor (*t*) **[1]**:

$$t = \frac{\left((1-x)r_{Bi} + xr_{Ho}\right) + r_o}{\sqrt{2}((1-y)r_{Fe} + yr_{Ti}) + r_o} \qquad Eq.\ 4.2$$

where $r_{Bi^{3+}}$, $r_{Ho^{3+}}$, $r_{Fe^{3+}}$, $r_{Ti^{4+}}$ and $r_{O^{2-}}$ are ionic radii of Bi^{3+}, Ho^{3+}, Fe^{3+}, Ti^{4+} and O^{2-} ions, respectively. The calculated tolerance factors are 0.883, 0.885 and 0.887 for BHFTO-0.0, BHFTO-0.10 and BHFTO-0.20 nanoparticles, respectively. The increment in *t* indicates that Ti^{4+} ions with smaller ionic radius than Fe^{3+} help to stabilize the crystal symmetry of $Bi_{0.9}Ho_{0.1}FeO_3$ nanoparticles.

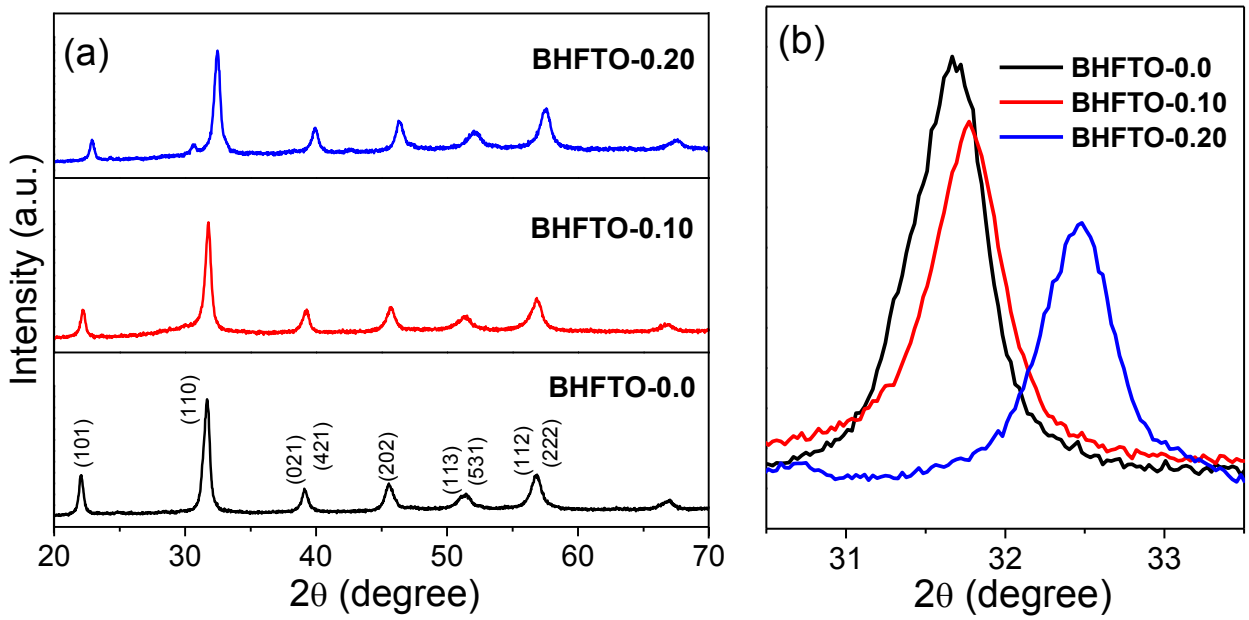

Figure 4.15 (a) X-ray diffraction patterns of $Bi_{0.9}Ho_{0.1}Fe_{1-y}Ti_yO_3$ nanoparticles ($0.0 \leq y \leq 0.20$) **(b)** Enlarged view of the characteristic peak.

A rietveld refinement has also been performed to extract the structural parameters. **Figure 4.16** shows experimental and calculated XRD patterns for BHFTO-0.0, BHFTO-0.10 and BHFTO-0.20 nanoparticles ceramics. The refined structural parameters are tabulated in **Table 4.2**. The increment in volume per unit cell and decrement of c/a ratio indicates a change in crystal anisotropy.

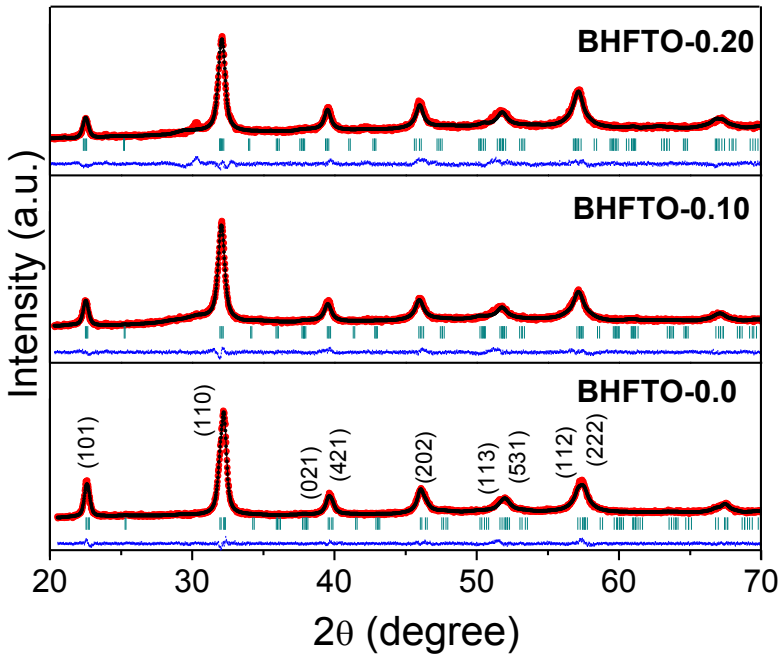

Figure 4.16 Rietveld refinements of the XRD patterns of BHFTO-0.0**,** BHFTO-0.10 and BHFTO-0.20. nanoparticles.

Table 4.2 Refined **s**tructural parameters for $Bi_{0.9}Ho_{0.1}Fe_{1-y}Ti_yO_3$ nanoparticles ($0.0 \leq y \leq 0.20$) obtained by rietveld analysis.

Composition of $Bi_{0.9}Ho_{0.1}Fe_{1-y}Ti_yO_3$	**Atom**	**Fractional coordinates**			**Lattice Constant [Å]**	**Bond angle [°]**	**Bond length [Å]**	**Statistical Parameter (%)**
		x	**y**	**z**				
BHFTO-0.0	Bi/Ho	0.00259	0.25000	1.00082	a= 5.54	Fe-O1-Fe	Bi/Ho-O1=2.39	R_p= 3.37
Pnma	Fe	0.00000	0.00000	0.50000	b= 7.82	= 154.48	Bi/Ho-O2= 2.97	*Rwp*=4.22
V= 242.59 (Å^3)	O1	0.46741	0.25000	0.07225	c= 5.60	Fe-O2-Fe	Fe/Ti-O1= 2.00	R_{exp}=3.24
	O2	0.23941	0.50159	0.19868	c/a ratio- 1.01	= 165.77	Fe/Ti-O2= 2.14	χ^2=1.70
BHFTO-0.10	Bi/Ho	0.00573	0.25000	1.01202	a= 5.57	Fe-O1-Fe	Bi/Ho-O1= 2.35	R_p=3.42
Pnma	Fe/Ti	0.00000	0.00000	0.50000	b= 7.86	= 155.41	Bi/Ho-O2= 2.70	*Rwp*=4.27
V= 245.15 (Å^3)	O1	0.46552	0.25000	0.06840	c= 5.59	Fe-O2-Fe	Fe/Ti-O1= 2.01	R_{exp}=3.22
	O2	0.19880	0.53440	0.20500	c/a ratio- 1.00	= 153.42	Fe/Ti-O2= 2.00	χ^2=1.76
BHFTO-0.20	Bi/Ho	0.00210	0.25000	1.01115	a= 5.59	Fe-O1-Fe	Bi/Ho-O1= 2.34	R_p=4.70
Pnma	Fe/Ti	0.00000	0.00000	0.50000	b= 7.94	= 155.79	Bi/Ho-O2= 2.73	*Rwp*=6.07
V= 247.39 (Å^3)	O1	0.46552	0.25000	0.06828	c= 5.56	Fe-O2-Fe	Fe/Ti-O1= 2.03	R_{exp}=3.68
	O2	0.19880	0.53440	0.20500	c/a ratio- 0.99	= 153.32	Fe/Ti-O2= 2.00	χ^2=2.71

The obtained values of crystallite size using Williamson–Hall equation are 38.83 nm, 29.71 nm and 24.83 nm for BHFTO-0.0, BHFTO-0.10 and BHFTO-0.20 nanoparticles, respectively. The crystallite size follows the decreasing trend with the substitution of Ti^{4+} ions.

4.2.3 MORPHOLOGICAL STUDIES

Figure 4.17 shows the surface morphology of $Bi_{0.9}Ho_{0.1}Fe_{1-y}Ti_yO_3$ (y=0.0-0.20) ceramics. All ceramics show spherical grains in micro range. A higher valance Ti^{4+} ion reduces the average grain size of the ceramics, resulting into less porous surface as shown in **Figure 4.17 (b-c)**. The tendency of decrease in the size of grains with Ti^{4+} ions may be attributed to suppression of oxygen vacancies due to charge compensation mechanism **[12, 13]**.

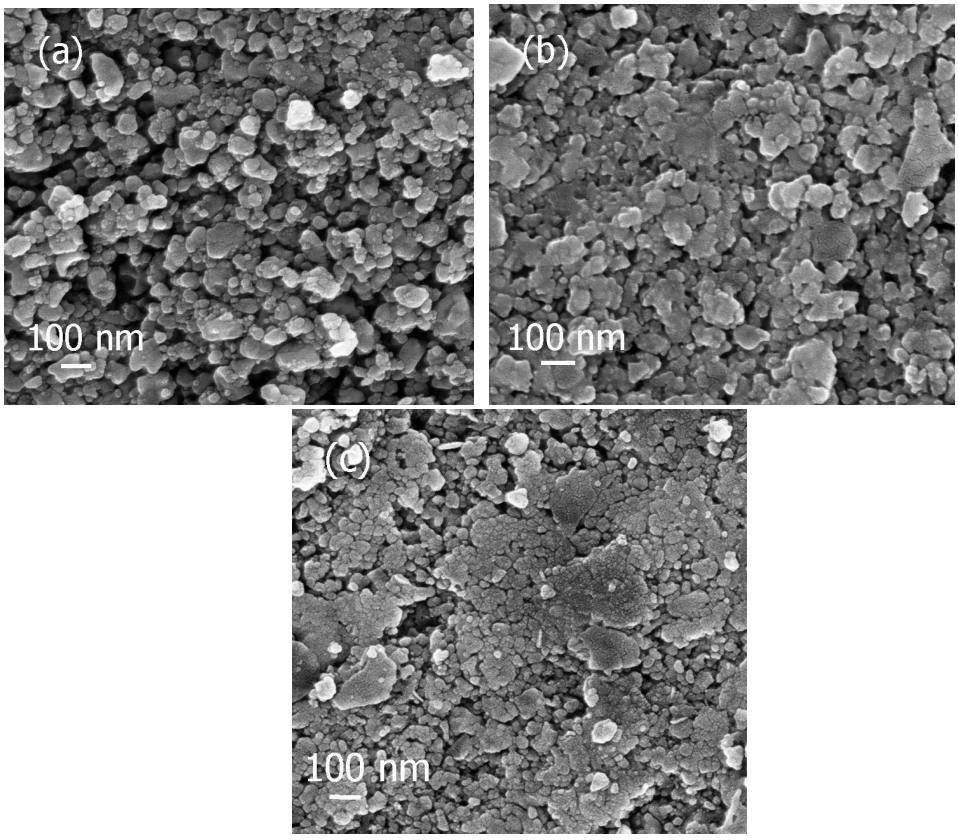

Figure 4.17 FESEM micrographs of **(a)** BHFTO-0.0 **(b)** BHFTO-0.10 **(c)** BHFTO-0.20 samples.

To ascertain the level of Ho^{3+} and Ti^{4+} doping in the synthesized ceramics, EDX analysis was done on co-doped samples as shown in **Figures 4.18 (a-c)**. Spectra taken at a number of selected positions of the sample confirm the presence of expected amounts of all constituents in the synthesized ceramics. The observed percentage of Ho^{3+} and Ti^{4+} value matches well with the

amount of Ho^{3+} and Ti^{4+} used in the respective precursors (inset of **Figures 4.18 (a-c)**).

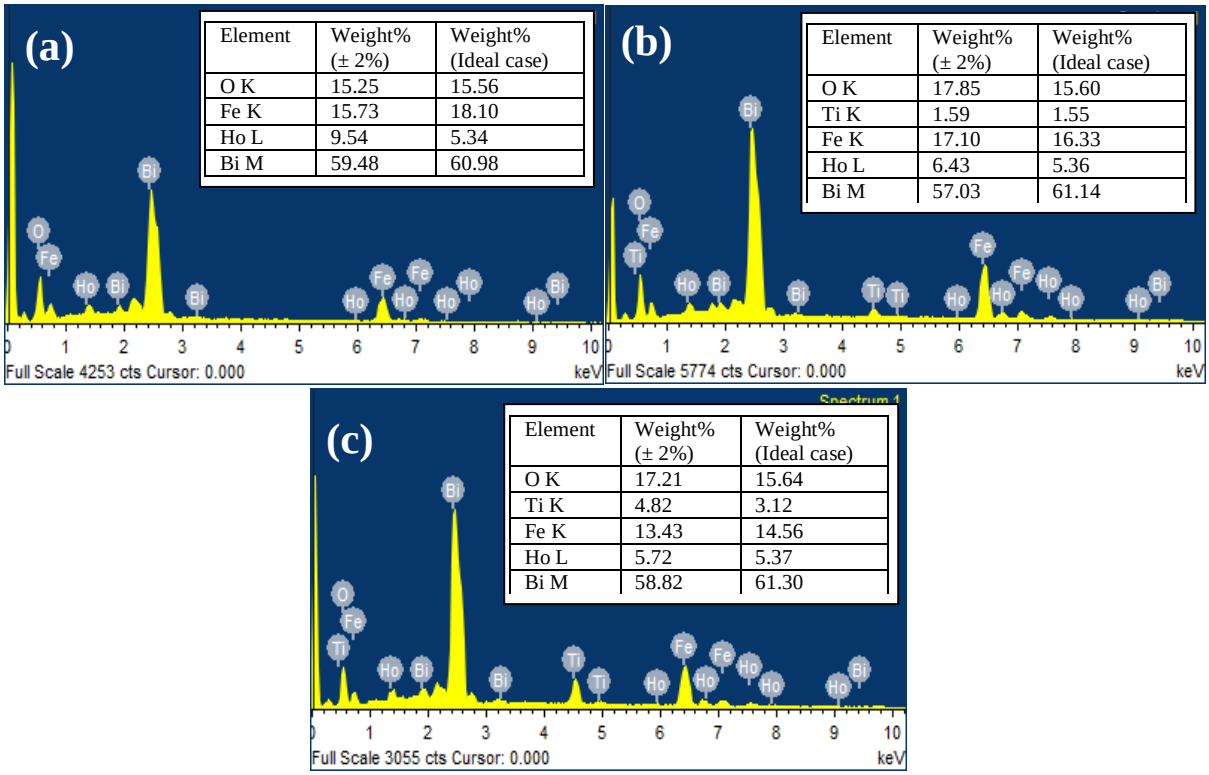

Figure 4.18 EDX patterns of **(a)** BHFTO-0.0 **(b)** BHFTO-0.10 **(c)** BHFTO-0.20 samples.

4.2.4 DIELECTRIC STUDIES

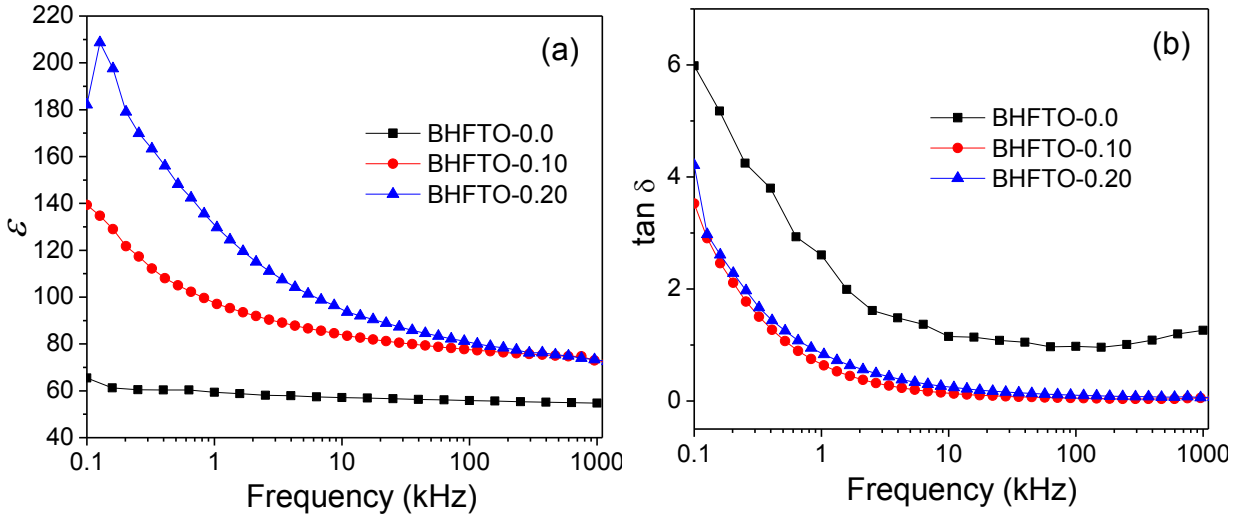

Figure 4.19 Variation of **(a)** relative dielectric constant (ε) and **(b)** dissipation factor ($tan\ \delta$) for BHFTO-0.0, BHFTO-0.10 and BHFTO-0.20 samples as a function of frequency.

Figures 4.19 (a and b) shows the dielectric behavior for $Bi_{0.9}Ho_{0.1}Fe_{1-y}Ti_yO_3$ (y=0.0-0.20) ceramics in terms of frequency in range of 100 Hz-1 MHz. It is clearly seen that both ε and *tan* δ decreases with increase in frequency, followed by a saturation region at higher frequencies. This observation clearly indicates large frequency dispersion, which is ascribed to the Maxwell-Wagner model of interfacial space charge relaxation **[15, 16]**. However, space charge originates in ceramics through oxygen vacancies (Vo^{2+}). It is also important to see that, with increasing Ti^{4+} doping ions, the value of ε is found to increase. The higher values of ε with the substitution of Ti^{4+} ions could be ascribed to the size effect of grains in ceramics **[17, 18]**. Ti^{4+} ions reduces the size of the grains and hence the enhanced volume fraction of grain boundaries which results in high value of ε. Dissipation factor (*tan* δ) follows the reverse trend as ε over the whole frequency range for all compositions.

4.2.5 MAGNETIC ANALYSIS

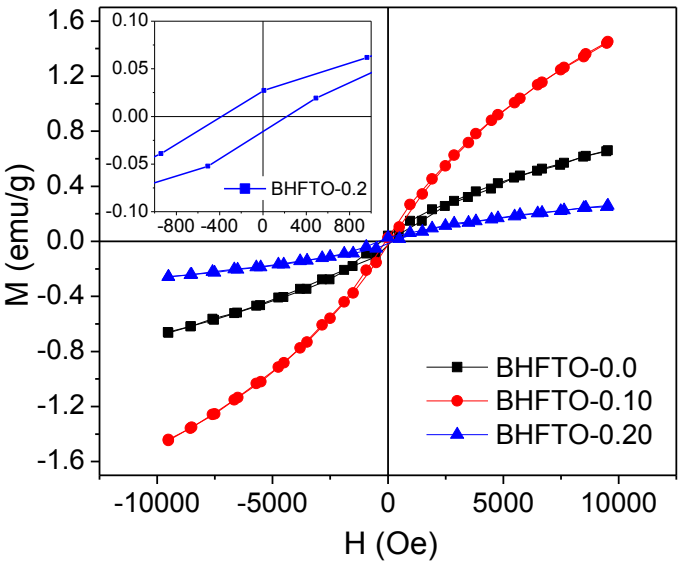

Figure 4.20 Room temperature magnetic hysteresis loops of BHFTO-0.0, BHFTO-0.10 and BHFTO-0.20. Inset shows enlarged view of M-H loop for BHFTO-0.2 nanoparticles.

Figure 4.20 shows the *M-H* loops of $Bi_{0.9}Ho_{0.1}Fe_{1-y}Ti_yO_3$ (y=0.0-0.20) nanoparticles at room temperature. It is observed that BHFTO-0.0 nanoparticles show a weak ferromagnetic behavior at an applied field of 10 kOe due to lattice strain-induced spin canting. The obtained value of maximum magnetization (M_{max}), non zero remnant magnetization (M_r) and coercivity (H_c) for BHFTO-0.0 nanoparticles are 0.66 emu/g, 0.032 emu/g and 224.96 Oe, respectively. Similar ferromagnetic behavior is also observed for Ti^{4+} substituted nanoparticles. In fact, the

value of M_{max} is observed to increase for BHFTO-0.1. Whereas, further substitution of Ti^{4+} ions, reduces its magnetization even than BHFTO-0.0 nanoparticles. The obtained magnetic parameters for BHFTO-0.1 and BHFTO-0.2 nanoparticles are listed in **Table 4.3**. The observed enhancement of magnetism in BHFTO-0.1 nanoparticles could be due to the size effect of the suppression of spiral order **[31]**. The resultant magnetization is decreased for BHFTO-0.2 because of the collinear AFM ordering of orthorhombic crystal symmetry **[32-35]**.

Moreover, coercivity is found to decrease for BHFTO-0.1, while further substitution of Ti^{4+} increased the value of H_c. The larger value of H_c for BHFTO-0.2 nanoparticles may be related to their magneto-crystalline anisotropy along with magnetoelastic anisotropy **[36, 37]**.

Table 4.3 Room temperature magnetic parameters for $Bi_{0.9}Ho_{0.1}Fe_{1-y}Ti_yO_3$ nanoparticles ($0.0 \leq y \leq 0.20$).

Compositions	M_{max} (emu/g)	M_r (emu/g)	H_C (Oe)
BHFTO-0.0	0.66	0.032	224.96
BHFTO-0.10	1.45	0.023	92.93
BHFTO-0.20	0.26	0.021	301.19

4.2.6 *UV*-VISIBLE ABSORPTION STUDIES

The absorption spectrum of BHFTO-0.0, BHFTO-0.10 and BHFTO-0.20 nanoparticles are shown in **Figure 4.21**. It is observed from the **Figure 4.21 (a)** that BHFTO-0.0 nanoparticles exhibit a broad absorption peak at ~642 nm. A significant shift is observed in absorption cut-off wavelength with Ti^{4+} substitution directly indicates the disturbance in electronic structure of BHFTO-0.0 nanoparticles. The electronic transition states in BHFTO-0.0, BHFTO-0.10 and BHFTO-0.20 nanoparticles have also been carried out using absorption spectra. The absorption spectrum as a function of energy (eV) is plotted in **Figure 4.21 (b)**. A broad absorption band located ~3.82 eV is assigned to inter-atomic O 2p–Fe 3d electronic excitations in FeO_6 octahedral. Whereas, a weak shoulder peak towards lower energy side besides 3.82 eV is associated with the $Fe_1$3d–$Fe_2$3d inter-site electron transfer. The spectra also exhibits two on-site d to d crystal field transitions of Fe ions placed ~1.63 and ~1.99 eV which are assigned to $^6A_{1g}$-$^4T_{1g}$ and $^6A_{1g}$-$^4T_{2g}$ electronic excitations respectively, caused by the relaxation of spin–orbit

coupling. A small shift and splitting of strongly hybridized O p to Fe d excitations clearly indicated the distortion in FeO_6 octahedral unit cell induced by Ti^{4+} dopants.

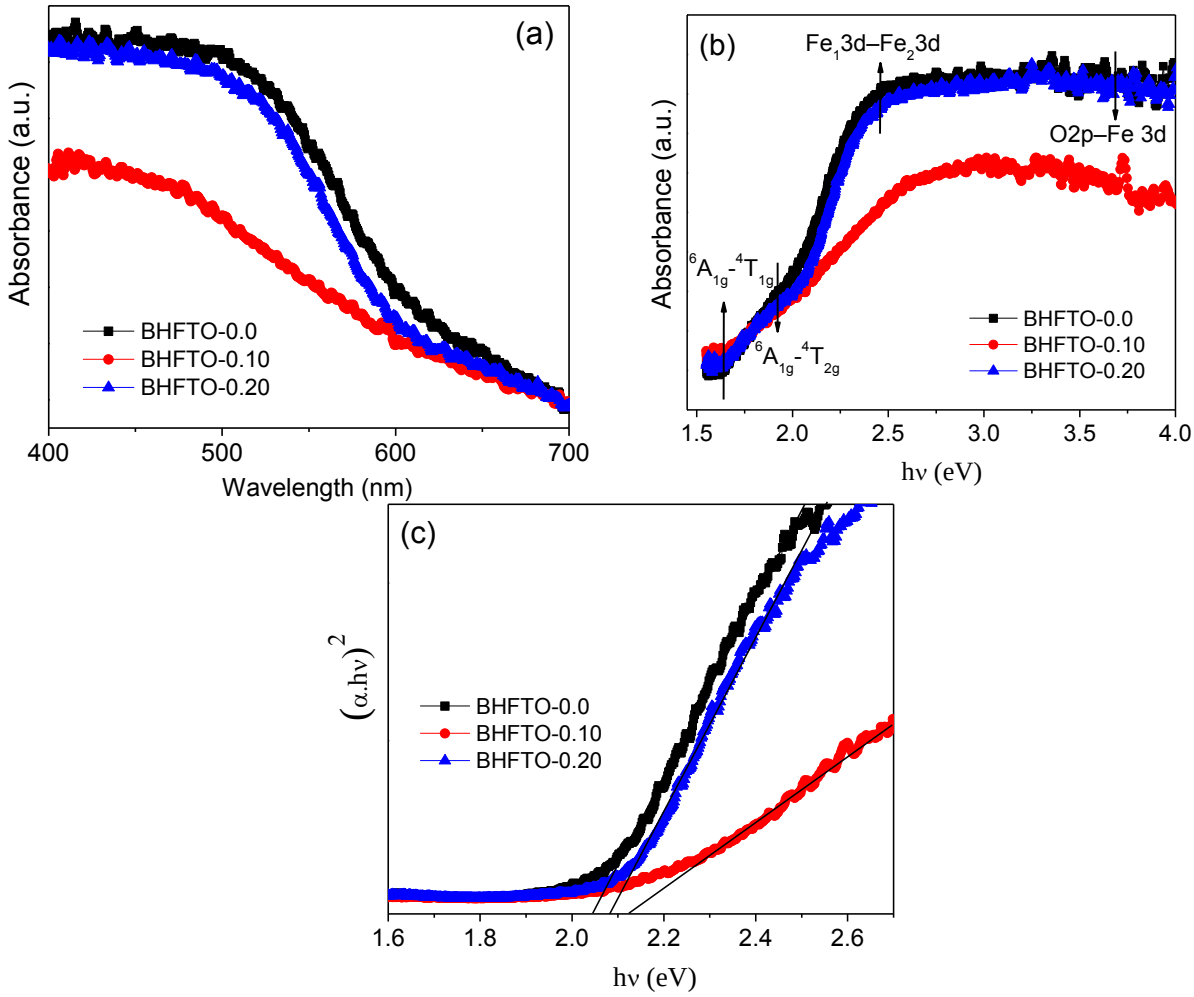

Figure 4.21 (a) UV absorption spectra and **(b)** *UV*-Vis absorption spectrum versus energy and **(c)** Tauc's plots for BHFTO-0.0, BHFTO-0.10 and BHFTO-0.20 nanoparticles.

The energy band gap for BHFTO-0.0, BHFTO-0.1 and BHFTO-0.2 nanoparticles is calculated from classical Tauc's relation and is illustrated in **Figure 4.21 (c)**. The calculated values of energy band gap (E_g) for BHFTO-0.0, BHFTO-0.1 and BHFTO-0.2 nanoparticles are 2.058 eV, 2.131 eV and 2.092 eV, respectively.

4.3 $Bi_{0.9}Ba_{0.1}Fe_{1-y}Ti_yO_3$ ($0.0 \leq y \leq 0.20$) ceramics

4.3.1 SYNTHESIS

$Bi(NO_3)_3 \cdot 5H_2O$ in nitric acid and $Fe(NO_3)_3.9H_2O$ in distilled water, $Ba(NO_3)_3 \cdot 3H_2O$ and [Ti $(OCH(CH_3)_2)_4$] were used to synthesize $Bi_{0.9}Ba_{0.1}Fe_{1-y}Ti_yO_3$ (y=0.0, 0.05, 0.10, 0.15 and

0.20) ceramics. The solution of $Bi(NO_3)_3 \cdot 5H_2O$, $Fe(NO_3)_3.9H_2O$, $Ba(NO_3)_3 \cdot 3H_2O$ and [Ti $(OCH(CH_3)_2)_4$] were mixed vigorously using magnetic stirrer for some time at 80 °C. Eventually, self sustained reaction in the solution occurred and brownish color ash was obtained. The ash was dried and ground to obtain fine powder. Then, at 500 °C, powder was calcined in electric furnace. The powder obtained after calcination was pressed down to pellets at a pressure of 6 MPa. Then, at 520 °C, the pellets were sintered for 2 hours. The compositions of $Bi_{0.9}Ba_{0.1}Fe_{1-y}Ti_yO_3$ where y= 0.0, 0.05, 0.10, 0.15 and 0.20 was signified as BBFTO-0.0, BBFTO-0.05, BBFTO-0.10, BBFTO-0.15 and BBFTO-0.20, respectively. The prepared samples were characterized with the help of X-ray diffraction, TEM, FESEM, dielectric measurement, impedance analysis, ferroelectric measurement, VSM, FTIR spectroscopy, *UV*-Visible spectrometer and PL spectroscopy.

4.3.2 X-RAY DIFFRACTION STUDIES

XRD patterns of BBFTO-0.0, BBFTO-0.05, BBFTO-0.10, BBFTO-0.15 and BBFTO-0.20 nanoparticles are shown in **Figure 4.22.** The intense diffraction peak positions of BBFTO-0.0 corresponding to rhombohedral symmetry are observed. The magnified view of a diffraction peak as shown in **Figure 4.22 (b and c)**, reveals the shift as well as merging of diffraction peaks indicating structural transformation with the substitution of Ti^{4+} ion into BBFTO-0.0 crystal structure. Further, the structural transformation is verified by reitveld refinement using fullprof. **Figure 4.22 (d)** shows the refined XRD pattern of BBFTO-0.0, BBFTO-0.05, BBFTO-0.10, BBFTO-0.15 and BBFTO-0.20 nanoparticles. The crystal structure of BBFTO-0.0 nanoparticles has been refined by using a rhombohedral crystal structure model with *R3c* space group. This structural model consistently replicates all the experimentally observed intense diffraction peaks of BBFTO-0.0 nanoparticles. The structural parameters, ionic positions and reliability parameters of refined BBFTO-0.0 nanoparticles are summarized in **Table 4.4**. Hence, the best profile fits between observed and calculated interplanar spacing of *hkl* planes with low R-factors, confirmed the formation of rhombohedral structure in BBFTO-0.0 nanoparticles. On the contrary, the same structure model could not fit to the experimentally observed diffraction patterns of Ti^{4+} substituted BBFTO-0.05, BBFTO-0.10, BBFTO-0.15 and BBFTO-0.20 nanoparticles. The best fits are obtained for all the refined nanoparticles by using a

tetragonal crystal structure model with space group *P4mm* as shown in **Figure 4.22 (d)**, and refined structural parameters are summarized in **Table 4.4**.

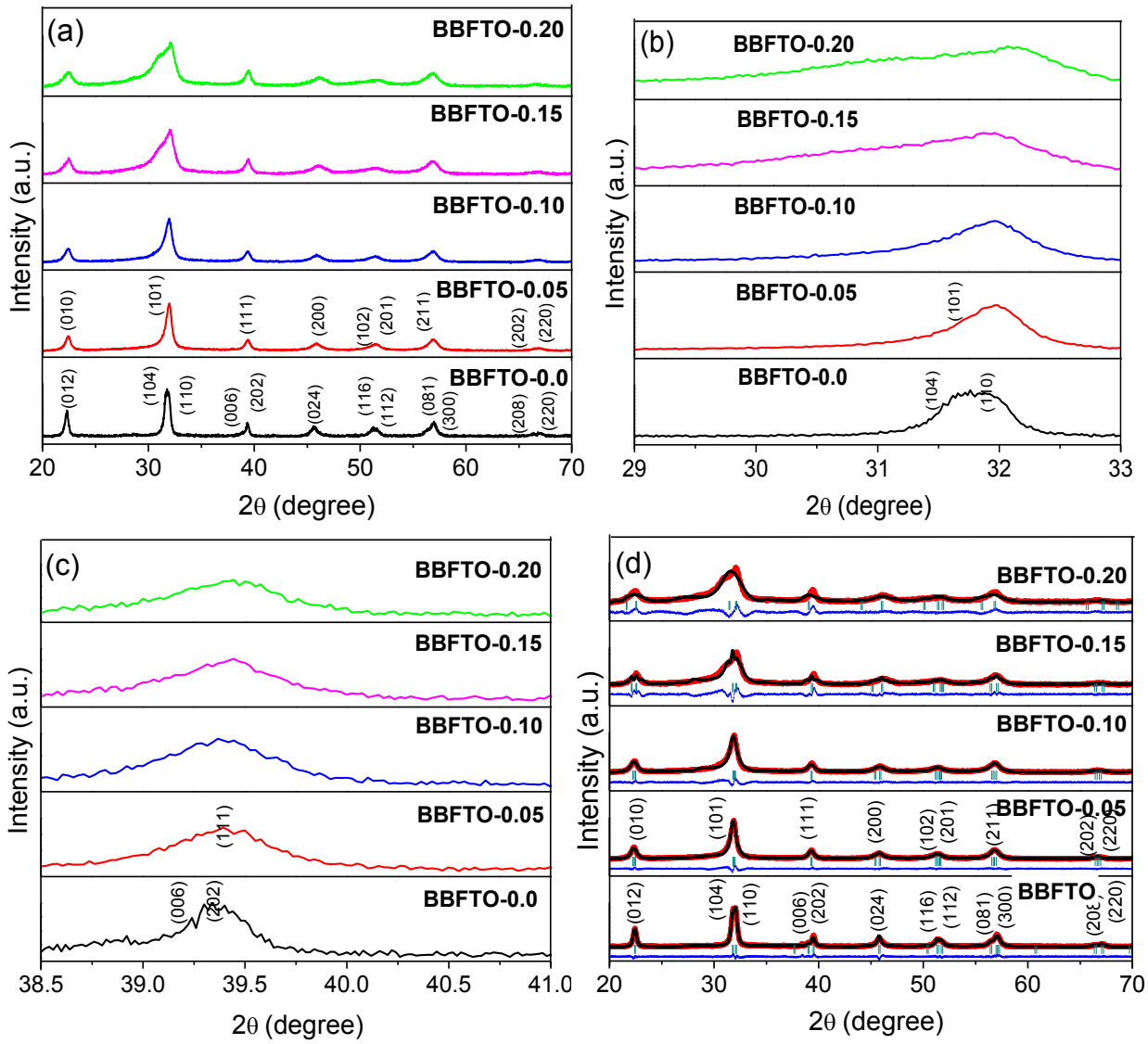

Figure 4.22 (a) X-ray diffraction patterns **(b-c)** Enlarged view of diffraction peaks in 2θ range of 29º -33º and 38.5º -41º, respectively **(d)** Rietveld refinements of the XRD patterns of $Bi_{0.9}Ba_{0.1}Fe_{1-y}Ti_yO_3$ nanoparticles ($0.0 \leq y \leq 0.20$).

Average crystallite sizes were calculated to be 21.96 nm, 15.96 nm, 13.43 nm, 11.69 nm and 11.13 for BBFTO-0.0, BBFTO-0.05, BBFTO-0.10, BBFTO-0.15 and BBFTO-0.20 nanoparticles, respectively. The corresponding lattice strain values are 0.00640, 0.00935, 0.0114, 0.0135 and 0.01515 for BBFTO-0.0, BBFTO-0.05, BBFTO-0.10, BBFTO-0.15 and BBFTO-0.20 ceramics, respectively.

Table 4.4 Refined structural parameters for $Bi_{0.9}Ba_{0.1}Fe_{1-y}Ti_yO_3$ nanoparticles ($0.0 \leq y \leq 0.20$) obtained by rietveld analysis.

Composition of $Bi_{0.9}Ba_{0.1}Fe_{1-y}Ti_yO_3$	Atom	Fractional coordinates x	y	z	Lattice Constant [Å]	Statistical Parameter (%)
BBFTO-0.0	Bi/Ba	0.00000	0.00000	0.1452	a=5.57	R_p=4.32
R3c	Fe	0.00000	0.00000	-0.0793	c=13.85	R_{wp}=5.57
V=373.50(Å^3)	O	0.78170	0.68589	0.3606		R_{exp}=3.95
						χ^2=1.99
BBFTO-0.05	Bi/Ba	0.00000	0.00000	-0.0203	a=3.95	R_p=3.39
P4mm	Fe/Ti	0.50000	0.50000	0.5888	c=3.99	R_{wp}=4.32
V=62.63(Å^3)	O1	0.50000	0.50000	0.2241		R_{exp}=2.95
	O2	0.00000	0.50000	0.5697		χ^2=2.14
BBFTO-0.10	Bi/Ba	0.00000	0.00000	-0.5526	a=3.95	R_p= 3.81
P4mm	Fe/Ti	0.50000	0.50000	0.8507	c=3.99	R_{wp}=4.98
V=62.56(Å^3)	O1	0.50000	0.50000	2.6728		R_{exp}=3.05
	O2	0.00000	0.50000	1.0425		χ^2= 2.67
BBFTO-0.15	Bi/Ba	0.00000	0.00000	-0.3677	a=3.94	R_p= 4.85
P4mm	Fe/Ti	0.50000	0.50000	0.0952	c=4.01	R_{wp}=6.73
V=62.45(Å^3)	O1	0.50000	0.50000	-0.2678		R_{exp}=3.06
	O2	0.00000	0.50000	0.0029		χ^2=4.83
BBFTO-0.20	Bi/Ba	0.0000	0.00000	-0.3950	a=3.94	R_p= 5.14
P4mm	Fe/Ti	0.5000	0.50000	0.2072	c=4.10	R_{wp}=6.81
V=63.85(Å^3)	O1	0.5000	0.50000	-0.3349		R_{exp}=3.13
	O2	0.0000	0.50000	-0.0240		χ^2=4.73

4.3.3 MORPHOLOGICAL STUDIES

Figures 4.23 (a-e) shows the TEM micrographs of the as-prepared nanoparticles. It can be seen that shape of the particles is almost spherical in all compositions. The estimated average particle size of BBFTO-0.0 nanoparticles is ~134 nm. However, the average particle size of BBFTO-0.05, BBFTO-0.10, BBFTO-0.15 and BBFTO-0.20 nanoparticles is in the range of 50 nm to 70 nm.

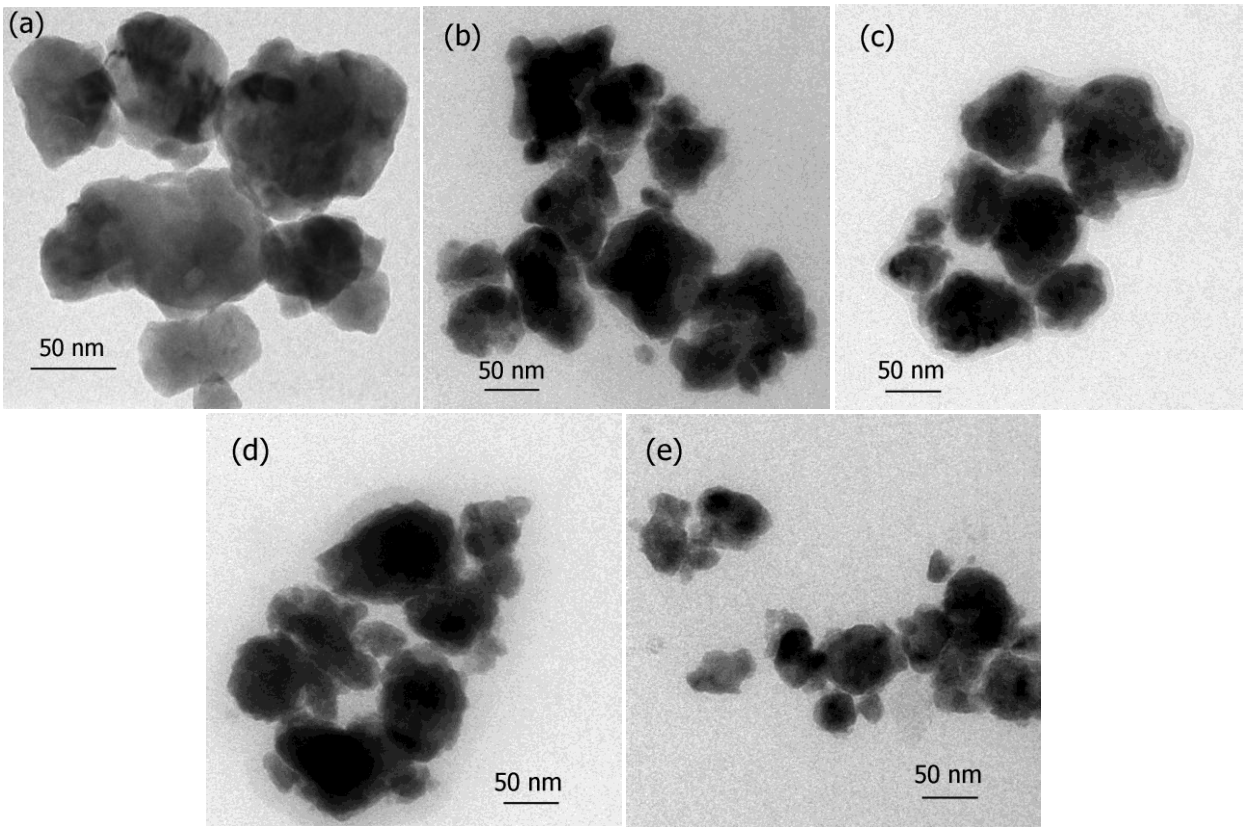

Figure 4.23 TEM images of **(a)** BBFTO-0.0 **(b)** BBFTO-0.05 **(c)** BBFTO-0.10 **(d)** BBFTO-0.15 **(e)** BBFTO-0.20 nanoparticles.

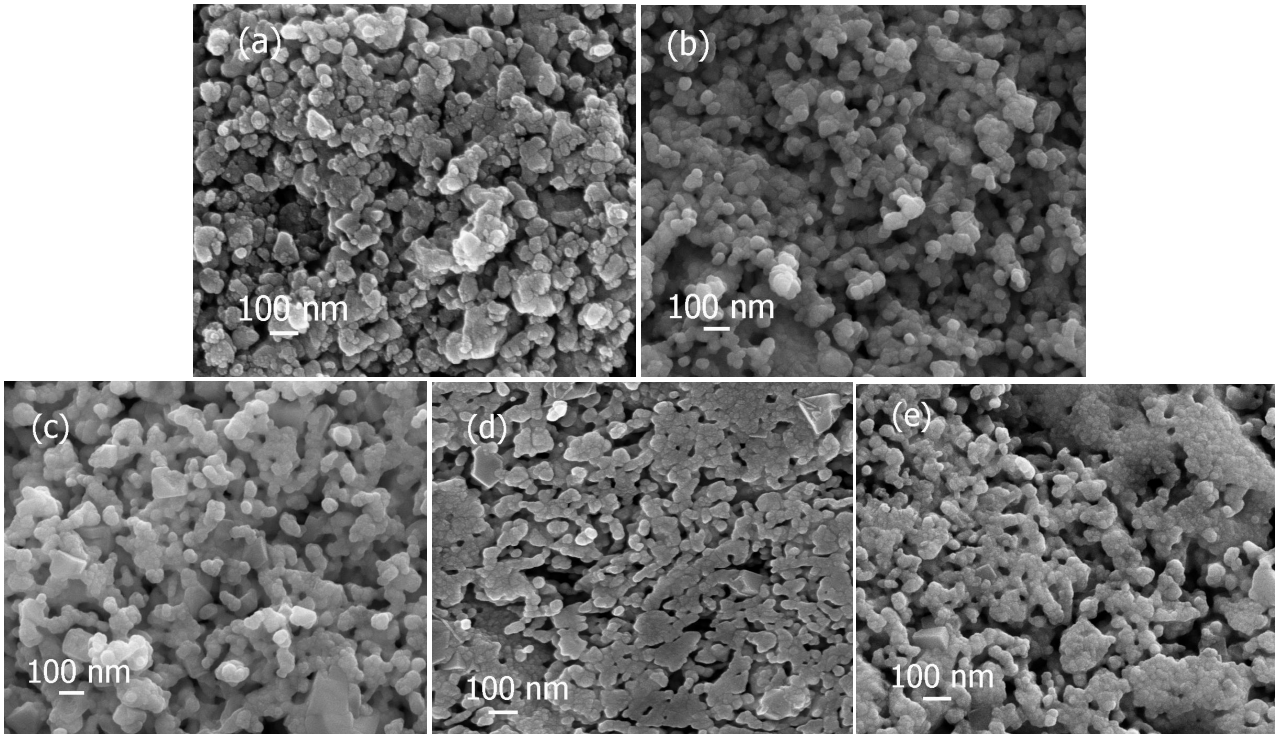

Figure 4.24 FESEM micrographs of **(a)** BBFTO-0.0 **(b)** BBFTO-0.05 **(c)** BBFTO-0.10 **(d)** BBFTO-0.15 **(e)** BBFTO-0.20 samples.

The surface morphology of sintered BBFTO-0.0, BBFTO-0.05, BBFTO-0.10, BBFTO-0.15 and BBFTO-0.20 pellets is shown in **Figure 4.24**. The micrographs show polycrystalline nature of BBFTO-0.0, BBFTO-0.05, BBFTO-0.10, BBFTO-0.15 and BBFTO-0.20 ceramics. **Figure 4.24 (a)** demonstrates the densely packed grains of <0.1 µm are homogeneously distributed over the surface of BBFTO-0.0 ceramics. After substitution of Ti^{4+} ions, the ceramics show an elongated spherical shaped grain, but the grain distribution is not quite homogeneous rather there are couple of grains with larger sizes. The occurrence of larger sized grains is ascribed to the agglomeration of smaller grains. Moreover, the grain size decreases with the substitution of Ti^{4+} ions in BBFTO-0.0 ceramics as depicted in **Figures 4.24 (b-e)**.

4.3.4 DIELECTRIC STUDIES

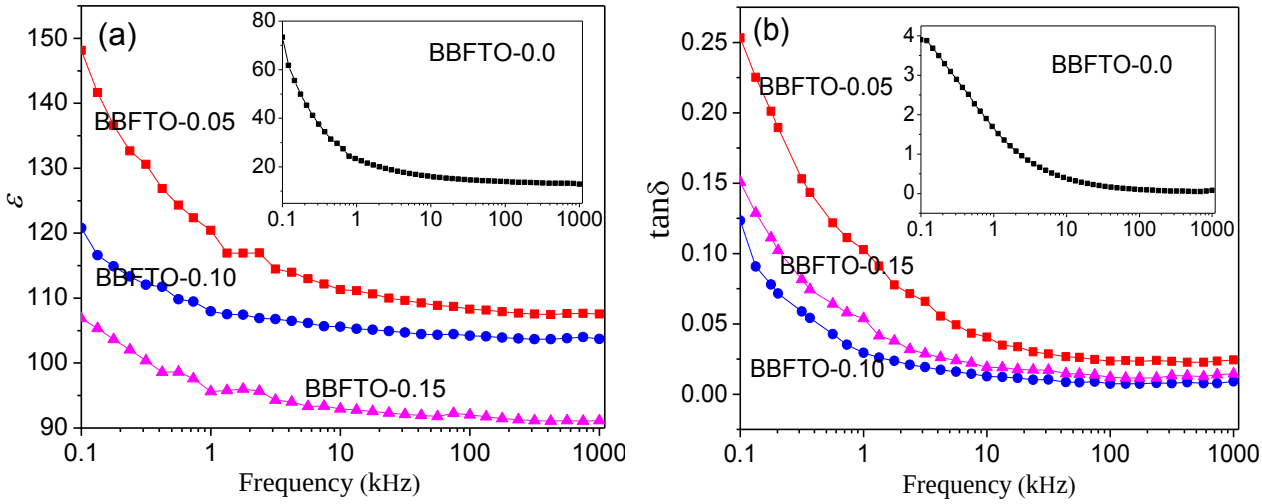

Figure 4.25 Variation of **(a)** dielectric constant (ε) and **(b)** dissipation factor (*tan* δ) for BBFTO-0.0, BBFTO-0.05, BBFTO-0.10 and BBFTO-0.15 samples as a function of frequency.

The effect of Ti^{4+} doping content on the dielectric characteristics of BBFTO-0.0, BBFTO-0.05, BBFTO-0.10, BBFTO-0.15 and BBFTO-0.20 ceramics has also been studied. The variation of ε and *tan* δ for all ceramics in terms of frequency is shown in **Figure 4.25**. It has been observed from the **Figure 4.25 (a)** that ε is strongly frequency dependent at room temperature. ε is in decreasing order as a function of increasing frequency, followed by a saturation region at higher frequencies for all ceramics. The obtained high values of ε at low frequency and vice-versa is based on dipole relaxation phenomenon because of Maxwell–Wagner type of interfacial polarization contribution **[15, 16]**. Similar trend is observed for *tan* δ in terms of frequency as shown in **Figure 4.25 (b)**. It is also observed that ε increases with

increase in Ti^{4+} concentration and it is maximum for BBFTO-0.05. However, a further increment of Ti^{4+} reduced ε, although their net value is still higher than that of BBFTO-0.0. Dielectric loss (*tan δ*) is observed to decrease which indicates the rise in electrical resistivity with increase in Ti^{4+} substitution.

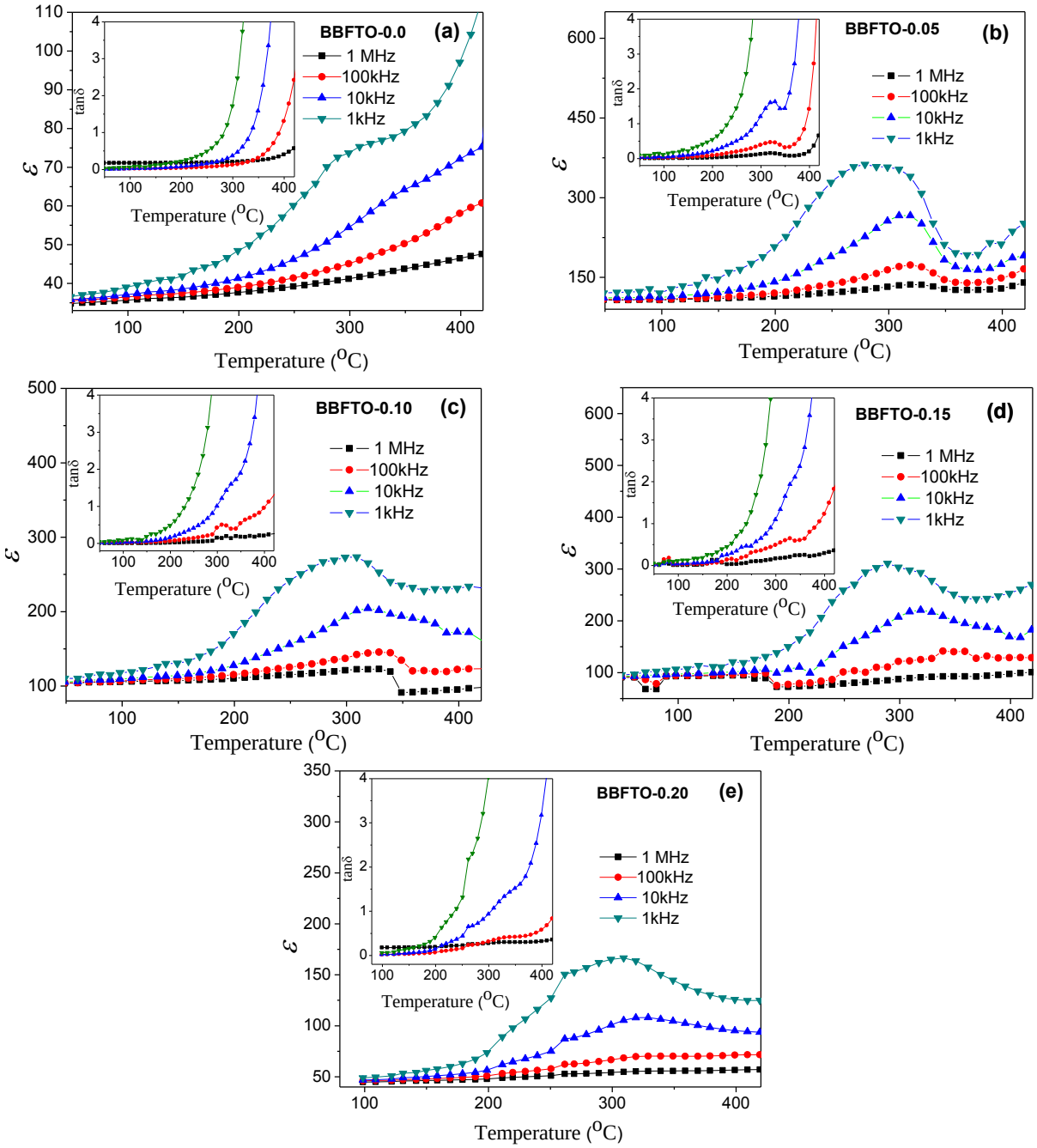

Figure 4.26 Dielectric constant (ε) and dielectric loss (*tan δ*) versus temperature curves for $Bi_{0.9}Ba_{0.1}Fe_{1-y}Ti_yO_3$ samples at 1 kHz, 10 kHz, 100 kHz and 1 MHz.

Figure 4.26 shows the thermally dependent dielectric constant (ε) at various frequencies (1 kHz- 1 MHz) for all ceramics. BBFTO-0.0 ceramics show an anomaly around 298 °C at 1 kHz which is shifted to 329 °C at 10 kHz as shown in **Figure 4.26 (a)**. The observed anomaly in dielectric constant may be attributed to change in electric dipole order from one state to another state because of antiferromagnetic transitions/possible magnetoelectric coupling effect **[19, 20]**. The dielectric constant of BBFTO-0.0 demonstrates continuous increment with rise in temperature at higher frequencies. It is observed from the Figure that peak temperature which may be correlated with T_N shows considerable frequency dispersion. It shifts to higher temperature side with rise in frequency. Similar behavior was reported by Singh *et al*. **[42]** in $BiFeO_3$-based systems. Correspondingly, the dielectric loss also shows a continual increase with temperature at all the frequencies as shown in the inset of **Figure 4.26 (a)**.

The dielectric constant of BBFTO-0.05 is observed to increase up to T_N and then it decreases with further increase in temperature at all frequencies, as shown in **Figure 4.26 (b)**. However, the value of T_N is found to be shifted towards lower temperature with decrease in frequency. The above dielectric anomaly is also observed in dielectric loss as given in the inset of **Figure 4.26 (b).** A similar trend of dielectric constant along with dielectric loss is also observed in BBFTO-0.10, BBFTO-0.15 and BBFTO-0.20 ceramics, as shown in **Figures 4.26 (c-e)**. As compared to BBFTO-0.0, Ti^{4+} ions substitution in place of Fe^{3+} ions has reduced the conductivity of ceramics because of charge compensation. Moreover, smaller grain size results in the increase of grain boundaries acting as scattering center for moving electrons and hence, increases the resistivity. Due to the low loss tangent values at higher frequencies, $Bi_{0.9}Ba_{0.1}Fe_{1-y}Ti_yO_3$ ceramics with higher concentration of Ti^{4+} might have potential applications in high-frequency microwave devices.

Electrical characterization of Ti^{4+} doped BBFTO-0.0 ceramics is carried out using complex impedance spectroscopy. **Figure 4.27** shows the variation of real (Z') and imaginary (Z'') part of impedance with frequency for all the ceramics in the temperature range of 100-250 °C and 300-450 °C in the inset of figures, respectively. Z' for BBFTO-0.0 is found to decrease with the increase in frequency as well as temperature followed by a saturation region at high frequency as shown in **Figure 4.27 (a)**. It indicates the increase in a.c. conductivity with the increase in temperature at high frequency region, which could be ascribed to the release of space

charge, and lowering in the barrier properties of the ceramics **[25]**.

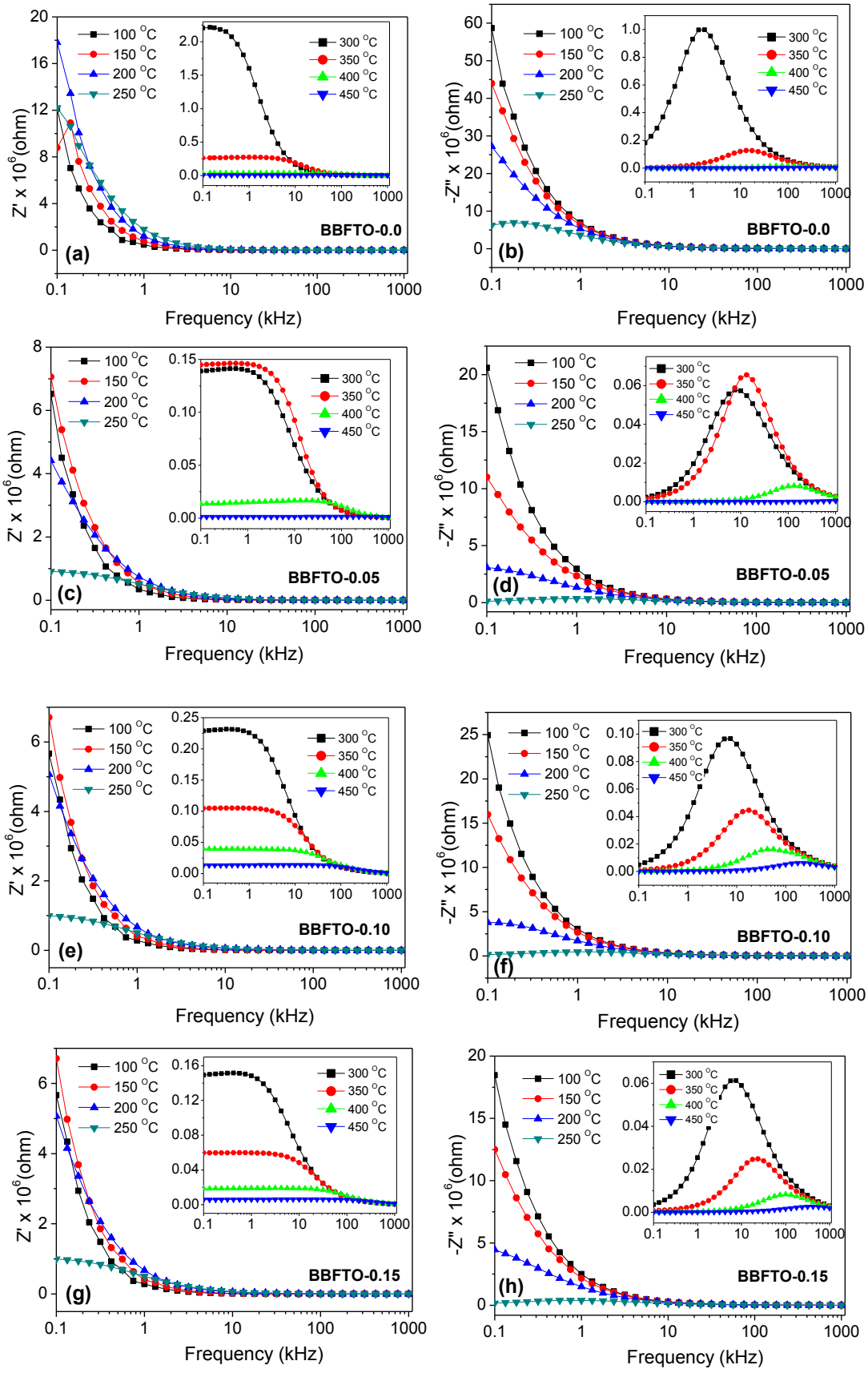

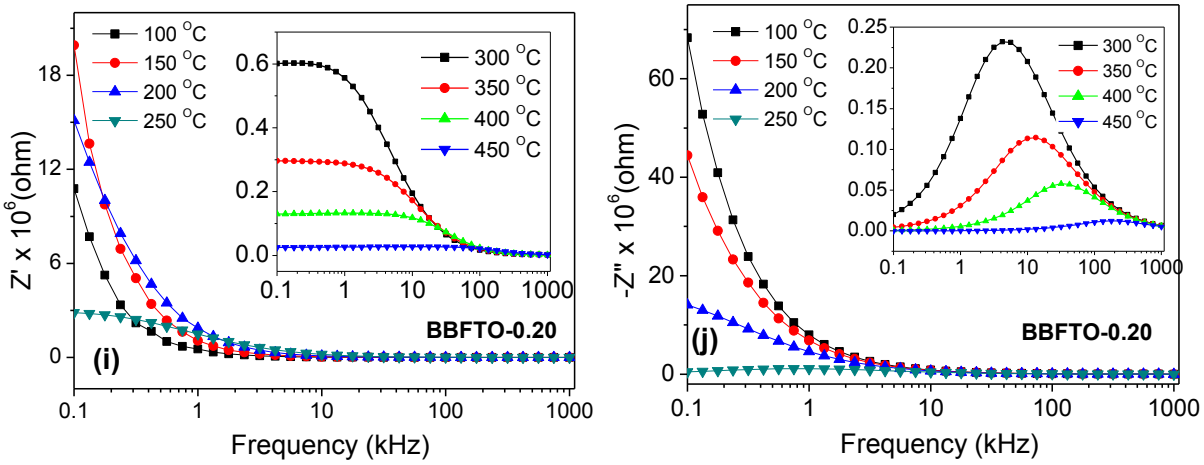

Figure 4.27 Frequency dependent real (Z') and imaginary (Z'') part of impedance for $Bi_{0.9}Ba_{0.1}Fe_{1-y}Ti_yO_3$ ($0.0 \leq y \leq 0.20$) ceramics at 100 °C, 150 °C, 200 °C and 250 °C, the inset shows the variation of impedance at 300 °C, 350 °C, 400 °C, and 450 °C.

Correspondingly, the impedance loss (Z″) values for BBFTO-0.0 ceramic are observed to decrease with increase in frequency up to 250 °C as shown in **Figure 4.27 (b)**. Above 250 °C, the loss curve primarily increases with the increase in frequency, attains a maximum value (Z''_{max}) at a particular frequency known as relaxation frequency **[27]**. Thereafter, it gradually decreases with increase in frequency as shown in the inset of the Figure. The value of Z''_{max} is found to shift towards higher frequency side indicating decrease in relaxation time. Moreover, the value of Z″ is also collapsed at higher frequencies, which could be ascribed to the occurrence of a thermally activated dielectric relaxation process in the ceramics and shows the reduction of bulk resistance with temperature. Similar trends of Z′ and Z″ with frequency and temperature are followed by BBFTO-0.05, BBFTO-0.10, and BBFTO-0.15 and BBFTO-0.20 ceramics as shown in **Figures 4.27 (c-j)**, respectively. The effect of increase in Ti^{4+} doping content on the electrical behavior of the ceramics can be clearly seen in terms of variation in the magnitude of Z′ and Z″. Nyquist plots (Z'' versus Z') are used to calculate the resistance over the wide range of frequency at different temperatures. **Figures 4.28 (a-e)** shows the Nyquist plots of BBFTO-0.0, BBFTO-0.05, BBFTO-0.10, BBFTO-0.15 and BBFTO-0.20 ceramics at lower temperature and proceeds further at higher temperature set in the inset of **Figures 4.28 (a-e).** The straight lines with large slopes are observed at lower temperatures, indicating the insulating behavior of ceramics. However, the bends of the lines decreased and hence, full semicircles were generated at higher temperature. The intercept of the semicircles on the Z'-axis gives the value of resistance. The

resistance is found to decrease with the rise in temperature indicating the negative temperature coefficient of resistance behavior (NTCR) in all ceramics. Some degree of depression is also observed in the semicircles at high temperature which could be ascribed to the distribution of relaxation time phenomena **[25, 26]**. Similar non-Debye relaxation behavior in $BiFeO_3$-$BaTiO_3$ ceramics has also been reported in previous studies **[43, 44].**

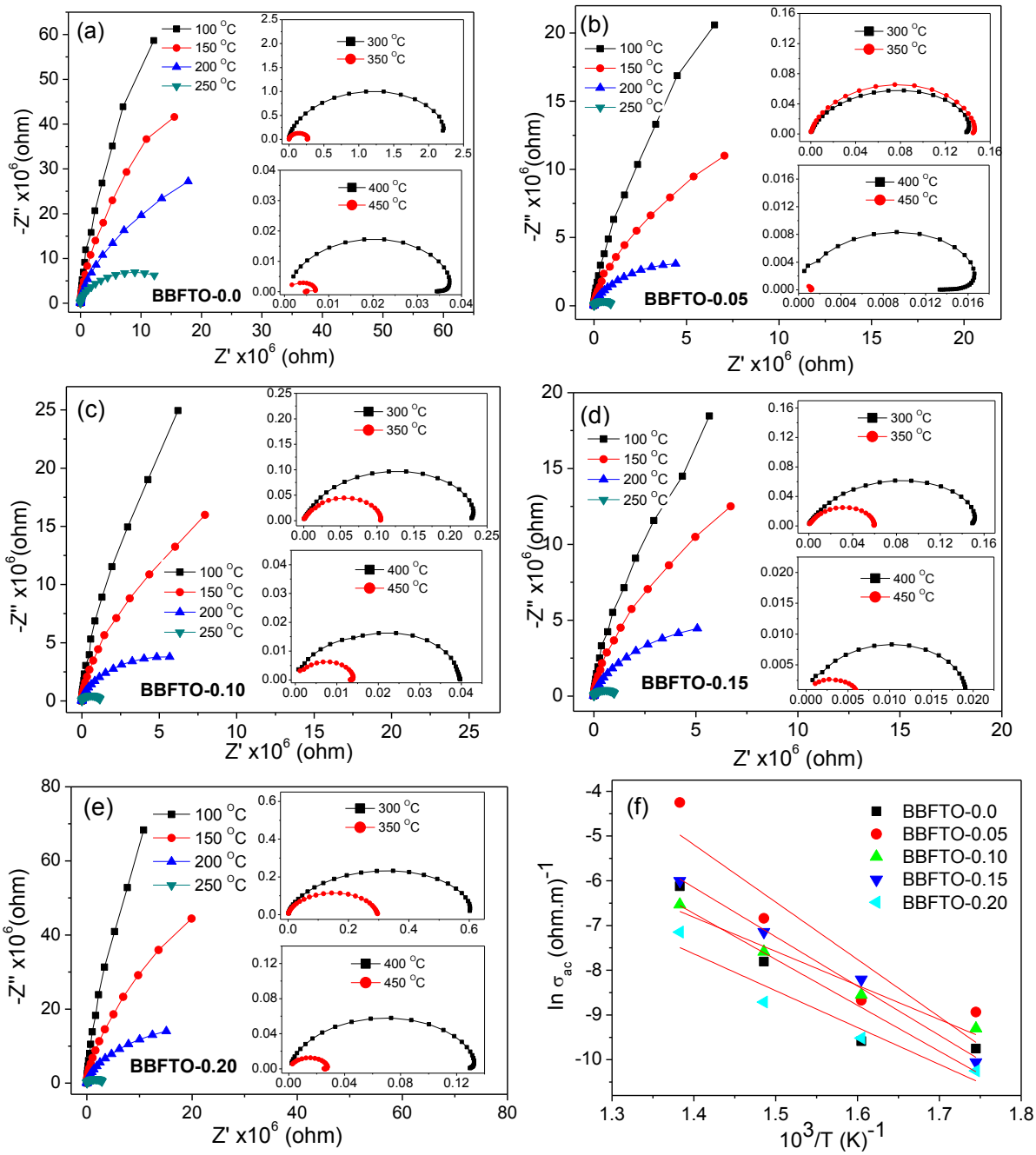

Figure 4.28 (a-e) Variation of imaginary part Z'' with respect to real part Z' of complex impedance (Nyquist plots) and **(f)** Arrhenius plot with temperature for $Bi_{0.9}Ba_{0.1}Fe_{1-y}Ti_yO_3$ ($0.0 \leq y \leq 0.20$) ceramics.

The obtained value of resistance at higher temperatures is used to calculate the ac conductivity (σ_{ac}) of all the ceramics. The temperature dependent ac conductivity follows the Arrhenius activation law and the activation energy can be determined as the slope of the straight line in plot of In (σ_{ac}) versus 1000/T as shown in **Figure 4.28 (f)**. The calculated value of activation energy is 0.744 eV, 0.994 eV, 0.505 eV, 0.841 eV and 0.473 eV for BBFTO-0.0, BBFTO-0.05, BBFTO-0.10, BBFTO-0.15 and BBFTO-0.20 ceramics respectively. The obtained values of activation energy indicate the singly ionized oxygen vacancies and mixed type conducting process due to ionic polaronic in all the ceramics **[27]**.

4.3.5 FERROELECTRIC STUDIES

The *P–E* loops of BBFTO-0.0, BBFTO-0.10, BBFTO-0.15 and BBFTO-0.20 ceramics measured under an electric field are shown in **Figure 4.29.** It is observed from the graph that all ceramics represent ferroelectric behavior which did not yield saturated. This kind of behavior is likely to happen due to the leaky performance of the ceramics. The obtained values of maximum polarization (P_{max}), remnant polarization (P_r), and coercive (E_c) are about 11.13 μC/cm^2, 7.45 μC/cm^2 and 8.30 kV/cm for BBFTO-0.0 ceramic, respectively. The collective value of P_m and P_r is found to be increase after substitution of Ti^{4+} ions in ceramics than BBFTO-0.0 and listed in **Table 4.5**. The obtained ferroelectric hysteresis loop of BBFTO-0.0, BBFTO-0.10, BBFTO-0.15 and BBFTO-0.20 ceramics gives better results with enhanced P_r values than the earlier reported *P-E* measurements of Ba and Ti-doped $BiFeO_3$ ceramics by Deng *at el.* **[45]**. This indicates a reduction in oxygen vacancies due to Ti^{4+} substitution.

Table 4.5 Ferroelectric parameters for $Bi_{0.9}Ba_{0.1}Fe_{1-y}Ti_yO_3$ nanoparticles ($0.0 \leq y \leq 0.20$).

Composition	BBFTO-0.0	BBFTO-0.10	BBFTO-0.15	BBFTO-0.20
Coercivity (kV/cm)	8.30	8.14	6.89	6.15
Remnance (μC/cm^2)	7.45	6.99	9.83	9.77
E_{max} (kV/cm)	14.35	14.05	12.87	11.41
Max polarization (μC/cm^2)	11.13	10.59	14.11	14.02

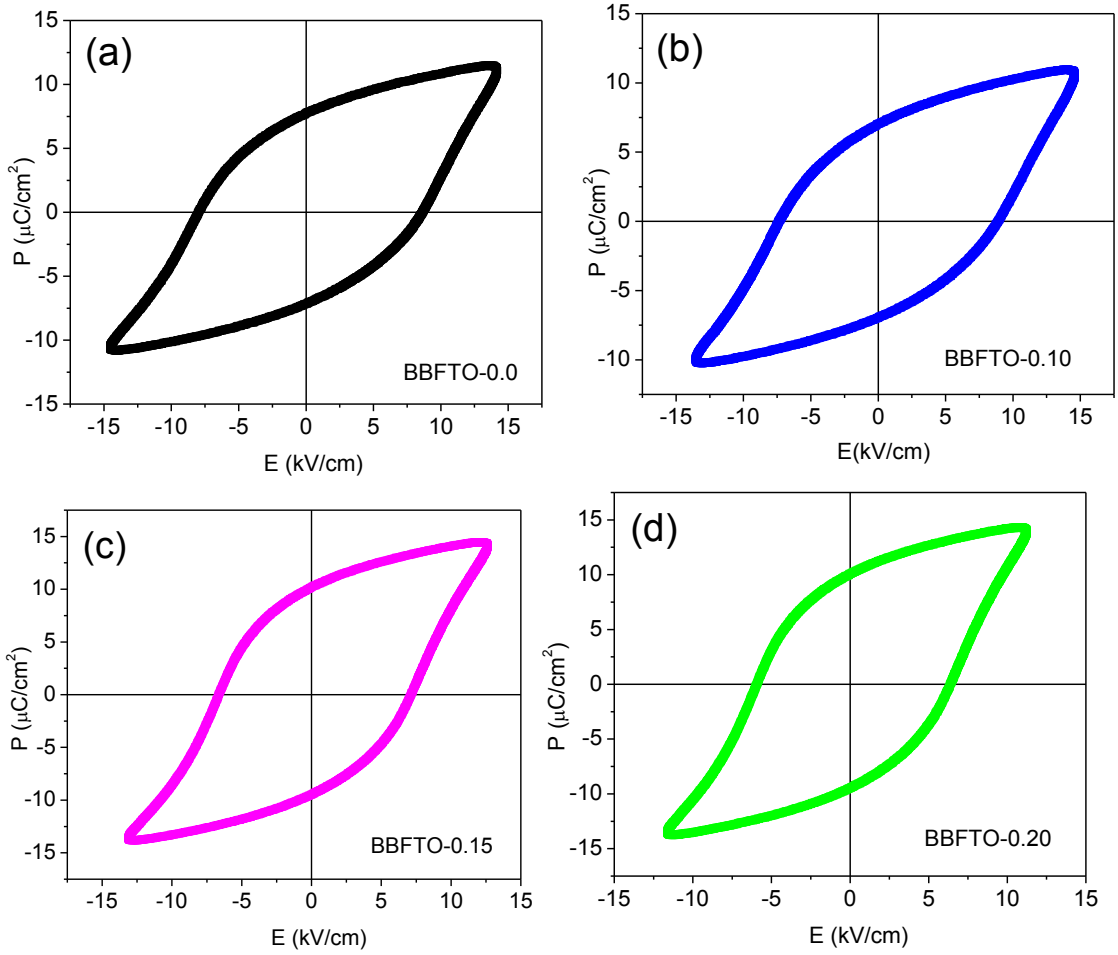

Figure 4.29 Ferroelectric hysteresis loops of **(a)** BBFTO-0.0 **(b)** BBFTO-0.10 **(c)** BBFTO-0.15 and **(d)** BBFTO-0.20 ceramics.

4.3.6 MAGNETIC ANALYSIS

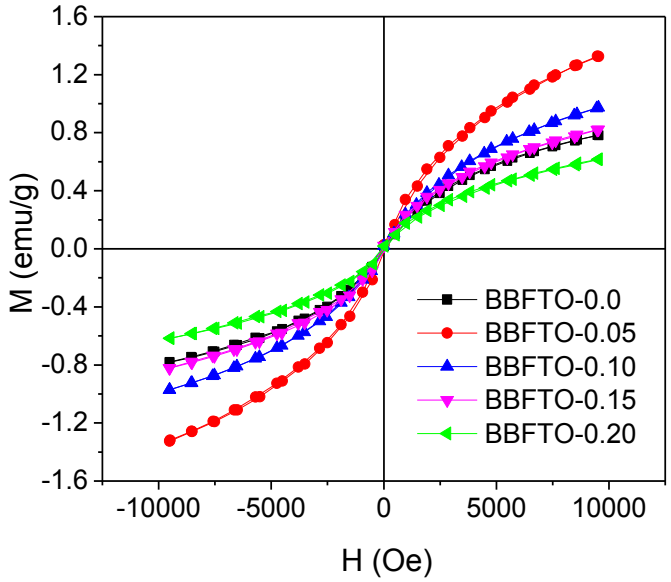

Figure 4.30 Room temperature magnetic hysteresis loops of $Bi_{0.9}Ba_{0.1}Fe_{1-y}Ti_yO_3$nanoparticles.

Figure 4.30 shows *M-H* loops of BBFTO-0.0, BBFTO-0.05, BBFTO-0.10, BBFTO-0.15 and BBFTO-0.20 nanoparticles. BBFTO-0.0 shows a weak ferromagnetic performance like that of pure $BiFeO_3$, with the remnant magnetization of $6.51x10^{-3}$ emu/g. The foremost cause for observed ferromagnetism in ceramics can be ascribed to the size effect of the suppression of spiral order. Meanwhile, the uncompensated spins at the surface contribute to weak ferromagnetism. Similarly, BBFTO-0.05, BBFTO-0.10, BBFTO-0.15 and BBFTO-0.20 nanoparticles show alike behavior of weak ferromagnetism. The obtained value of magnetization (M_{max}) is 0.78, 1.32, 0.97, 0.82 and 0.61 emu/g at 10 kOe for BBFTO-0.0, BBFTO-0.05, BBFTO-0.10, BBFTO-0.15 and BBFTO-0.20 nanoparticles, respectively. The doping of Ti^{4+} ions with molar concentration of 0.05 is found to enhance the magnetization of BBFTO-0.0 ceramics. This could be ascribed to suppression in the inhomogeneous magnetic spin structure, and increase in canted angles. But with further increase of Ti^{4+} doping content, the magnetization is found to decrease which could be attributed to the collinear antiferromagnetic spin ordering as some perovskite compounds with tetragonal symmetry tends to have collinear antiferromagnetic spin structure too, like $BiCoO_3$.

Moreover, the decrease in coercivity could be due to decrease in the particle size and thereafter increases due to much agglomerated nanocluster seen in the micrographs of ceramics. It is observed that the substitution of Ti^{4+} ions significantly increased remnant magnetization (M_r) of the nanoparticles and it is maximum for BBFTO-0.05. However, a further increment of Ti^{4+} reduced M_r, although their net value is still higher than that of BBFTO-0.0 nanoparticles as mentioned in **Table 4.6**.

Table 4.6 Room temperature magnetic parameters for $Bi_{0.9}Ba_{0.1}Fe_{1-y}Ti_yO_3$ nanoparticles ($0.0 \leq y \leq 0.20$).

Compositions	M_{max} **(emu/g)**	M_r **(emu/g)**	H_C **(Oe)**
BBFTO-0.0	0.78	0.012	56.01
BBFTO-0.05	1.32	0.021	60.28
BBFTO-0.10	0.97	0.014	57.88
BBFTO-0.15	0.82	0.015	60.22
BBFTO-0.20	0.61	0.010	57.29

4.3.7 FTIR STUDIES

Figure 4.31 shows the FTIR spectra of BBFTO-0.0, BBFTO-0.05, BBFTO-0.10, BBFTO-0.15 and BBFTO-0.20 nanoparticles. The BBFTO-0.0 nanoparticles exhibit a strong and broad fundamental absorption band in the wavelength region 450-550 cm^{-1} which could be ascribed to the overlapping of Fe-O and Bi-O group vibrations as shown in **Figure 4.31 (a)**.

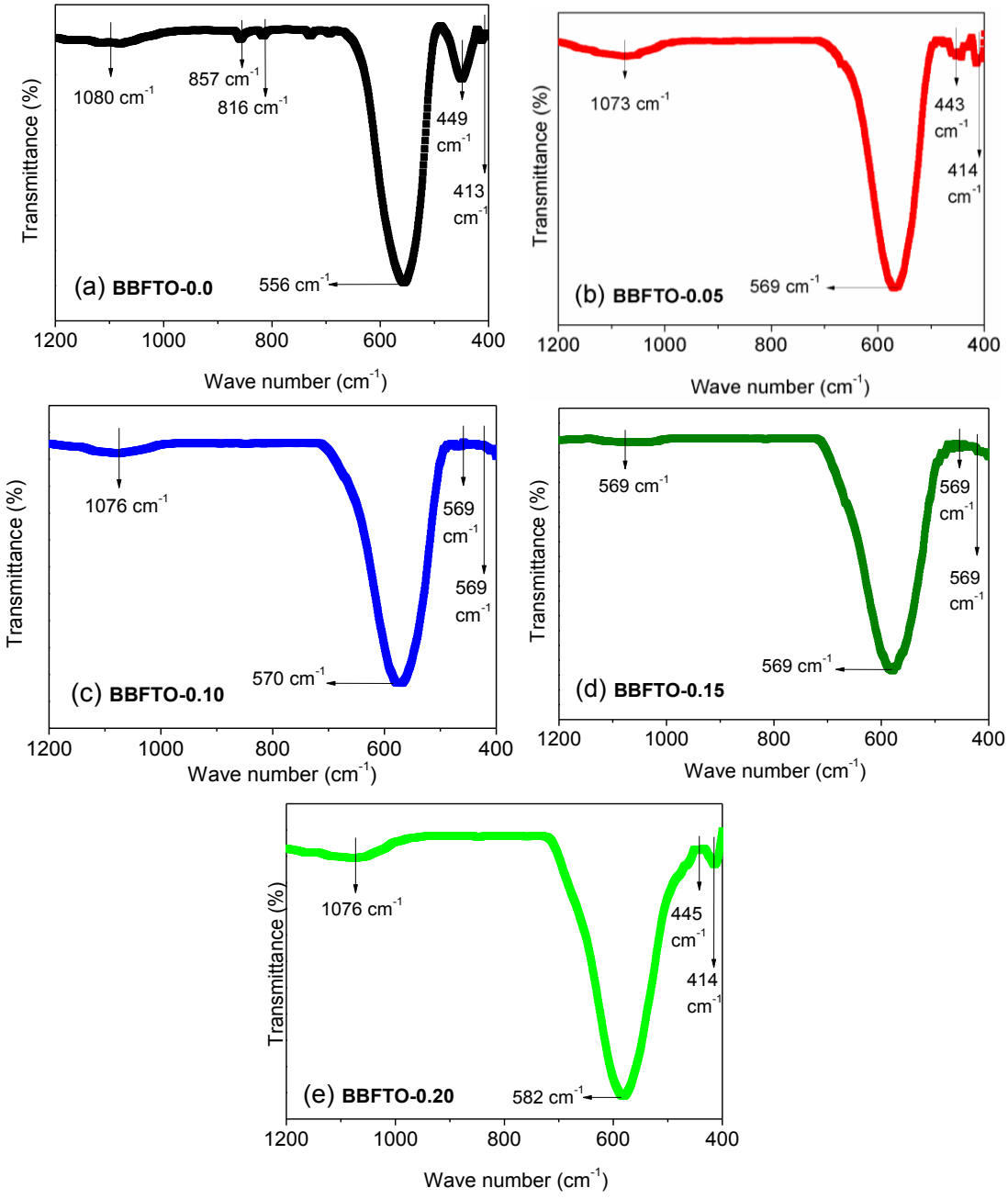

Figure 4.31 FTIR spectra of **(a)** BBFTO-0.0 **(b)** BBFTO-0.05 **(c)** BBFTO-0.10 **(d)** BBFTO-0.15 **(e)** BBFTO-0.20 nanoparticles.

An absorption peak at 413 cm^{-1}, corresponds to the bending and stretching vibrations of BiO_6 octahedra. The absorption peaks at 449 cm^{-1} and 556 cm^{-1} are characteristics of O-Fe-O bending and Fe-O stretching vibration of the octahedral FeO_6 group in BBFTO-0.0 structure **[23, 38]**. The existence of this oxygen-metal bond directly indicates the formation of highly crystalline phase in nanoparticles. The weak peak at about 816 cm^{-1} is usually assigned to the trapped NO_3^- ions. Besides 816 cm^{-1}, the peak at 857 cm^{-1} is attributed to the OH group vibration of absorbed water and CO_2 from the environment, when precursor was calcined. Carbonate groups are indicated by the broad band at around 1120-1070 cm^{-1}. **Figures 4.31 (b-e)** shows shifting of peaks in Ti^{4+} ions substituted nanoparticles which could be associated with change in the corresponding ionic sizes as well as the structural change induced due to doping.

4.3.8 *UV*-VISIBLE ABSORPTION STUDIES

Figure 4.32 shows the absorption spectra of BBFTO-0.0, BBFTO-0.05, BBFTO-0.10, BBFTO-0.15 and BBFTO-0.20 nanoparticles, where the absorption cutoff wavelength is seen in range of 630-680 nm. The observed wavelength region indicates that the nanoparticles can absorb substantial quantity of visible light which is suitable as visible-light driven photocatalyst.

The calculated values of energy band gap increased from 2.09 to 2.16 eV with Ti^{4+} doping ions (as shown in the inset of **Figure 4.32**) which could be attributed to decrease in size of particles as evidenced from TEM. The obtained region of energy band gap for nanoparticles is suitable for the degradation of organic pollutants in visible region.

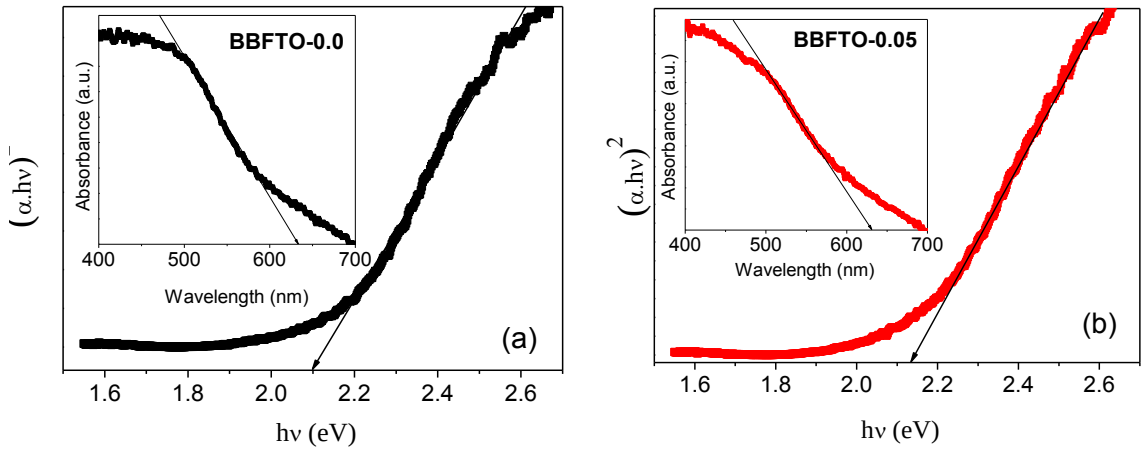

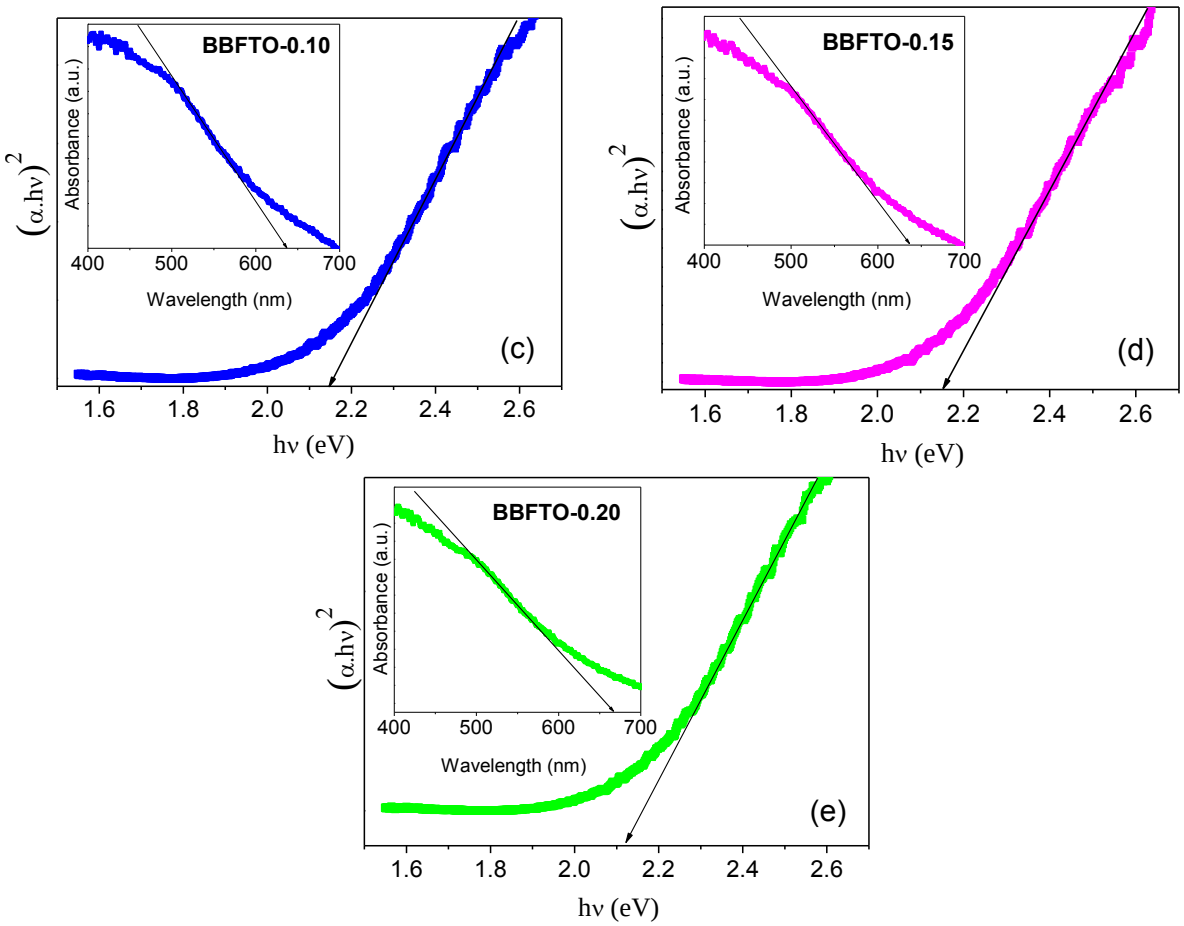

Figure 4.32 Tauc's plots for BBFTO-0.0, BBFTO-0.05, BBFTO-0.10, BBFTO-0.15 and BBFTO-0.20 nanoparticles. Inset shows the *UV*-Vis absorption spectra of nanoparticles.

References

1. Goldschmidt V. M., *Naturwissenschaften*, (1926), *14*(21), 477-485.
2. Kaur M., Yadav K. L., Uniyal P., *Advanced Materials Letters*, (2015), *6*, 895-901.
3. Karimi S., Reaney I. M., Han Y., Pokorny J., Sterianou I., *Journal of Materials Science*, (2009), *44*(19), 5102-5112.
4. Khomchenko V. A., Paixao J. A., Kiselev D. A., Kholkin A. L., *Materials Research Bulletin*, (2010), *45*(4), 416-419.
5. Zhang Y. J., Zhang H. G., Yin J. H., Zhang H. W., Chen J. L., Wang W. Q., Wu G. H. *Journal of Magnetism and Magnetic Materials*, (2010), *322*(15), 2251-2255.
6. Zhang S. T., Zhang Y., Lu M. H., Du C. L., Chen Y. F., Liu Z. G., Zhu Y. Y., Ming N. B., Pan X. Q., *Applied Physics Letters*, (2006), *88*(16), 162901(1-3).

7. Debye P., *Annalen Der Physik*, (1915), *351*(6), 809-823.
8. Singla G., Singh K., Pandey O. P., *Applied Physics A*, (2013), *113*(1), 237-242.
9. Di L. J., Yang H., Hu G., Xian T., Ma J. Y., Jiang J. L., Li R. S., Wei Z. Q., *Journal of Materials Science: Materials in Electronics*, (2014), *25*(6), 2463-2469.
10. Dhir G., Uniyal P., Verma N. K., *Materials Science in Semiconductor Processing*, (2014), *27*, 611-618.
11. Wu J., Wang J., *Journal of the American Ceramic Society*, (2010), *93*(9), 2795-2803.
12. Reetu, Agarwal A., Sanghi S., Ahlawat N., *Journal of Physics D: Applied Physics*, (2012), *45*(16), 165001(1-9).
13. Kumar M., Yadav K. L., *Applied Physics Letters*, (2007), *91*(24), 242901(1-3).
14. Uniyal P., Yadav K. L., *Journal of Physics: Condensed Matter*, (2009), *21*(40), 405901(1-6).
15. Maxwell J. C., Electricity and Magnetism. *Oxford University Press, Oxford*, (1929), Section 328.
16. Koops C. G., *Physical Review*, (1951), *83*(1), 121-124.
17. Sharma P., Varshney D., Satapathy S., Gupta P. K., *Materials Chemistry and Physics*, (2014), *143*(2), 629-636.
18. Pandit P., Satapathy S., Gupta P. K., Sathe V. G., *Journal of Applied Physics*, (2009), *106*(11), 114105(1-7).
19. Singh H., Yadav K. L., *Materials Chemistry and Physics*, (2012), *132*(1), 17-21.
20. Benguigui L., *Solid State Communications*, (1972), *11*(6), 825-828.
21. Cheng Z. X., Li A. H., Wang X. L., Dou S. X., Ozawa K., Kimura H., Zhang S. J., Shrout T. R., *Journal of Applied Physics*, (2008), *103*(7), 07E507(1-3).
22. Das S. R., Choudhary R. N. P., Bhattacharya P., Katiyar R. S., Dutta P., Manivannan A., Seehra M. S., *Journal of Applied Physics*, (2007), *101*(3), 034104(1-7).
23. Sati P. C., Kumar M., Chhoker S., *Ceramics International*, (2015), *41*(2), 3227-3236.
24. Bombik A., Leśniewska B., Mayer J., Pacyna A. W., *Journal of Magnetism and Magnetic Materials*, (2003) *257*(2), 206-219.
25. Behera A. K., Mohanty N. K., Behera B., Nayak P., *Advanced Materials Letters*, (2013), *4*(2), 141-145.

26. Sati P. C., Arora M., Chauhan S., Kumar M., Chhoker S., *Journal of Materials Science: Materials in Electronics*, (2013), *24*(12), 5023-5034.
27. Kumari S., Ortega N., Kumar A., Pavunny S. P., Hubbard J. W., Rinaldi C., Srinivasan G., Scott J. F., Katiyar R. S., *Journal of Applied Physics*, (2015), *117*(11), 114102(1-13).
28. Kumar N., Shukla A., Choudhary R. N. P., *Journal of Materials Science: Materials in Electronics*, (2017), *28*(9), 6673-6684.
29. Yan Z., Wang K. F., Qu J. F., Wang Y., Song Z. T., Feng S. L., *Applied Physics Letters*, (2007), *91*(8), 082906(1-3).
30. Wang Y. P., Zhou L., Zhang M. F., Chen X. Y., Liu J. M., Liu Z. G., *Applied Physics Letters*, (2004), *84*(10), 1731-1733.
31. Kumar P., Panda C., Kar M., *Smart Materials and Structures*, (2015), *24*(4), 045028(1-12).
32. Khesro A., Boston R., Sterianou I., Sinclair D. C., Reaney I. M., *Journal of Applied Physics*, (2016), *119*(5), 054101(1-8).
33. Bhushan B., Wang Z., Tol J. V., Dalal N. S., Basumallick A., Vasanthacharya N. Y., Kumar S., Das D., *Journal of the American Ceramic Society*, (2012), *95*(6), 1985-1992.
34. Kaur M., Uniyal P., *Journal of Materials Science: Materials in Electronics*, (2016), *27*(12), 12539-12549.
35. Arya G. S., Negi N. S., *Journal of Physics D: Applied Physics*, (2013), *46*(9), 095004(1-8).
36. Zalesskii A. V., Frolov A. A., Khimich T. A., Bush A. A., *Physics of the Solid State*, (2003), *45*(1), 141-145.
37. Arya G., Kotnala R. K., Negi N. S., *Journal of the American Ceramic Society*, (2014), *97*(5), 1475-1480.
38. Jiang J., Zou J., Anjum M. N., Yan J., Huang L., Zhang Y., Chen J., *Solid State Sciences*, (2011), *13*(9), 1779-1785.
39. Suresh P., Babu P. D., Srinath S., *Journal of Applied Physics*, (2014), *115*(17), 17D905(1-3).
40. Cheng G. F., Ruan Y. J., Liu W., Wu X. S., *Physica B: Condensed Matter*, (2015), *468*, 81-84.

41. Singh H., Yadav, K. L., *Journal of Physics: Condensed Matter*, (2011), *23*(38), 385901(1-6).
42. Singh A., Pandey V., Kotnala R. K., Pandey D., *Physical review letters*, (2008), *101*(24), 247602(1-4).
43. Singh H., Kumar A., Yadav K. L., *Materials Science and Engineering: B*, (2011), *176*(7), 540-547.
44. Kumar M., Shankar S., Parkash O., Thakur O. P., *Journal of Materials Science: Materials in Electronics*, (2014), *25*(2), 888-896.
45. Deng H., Zhang M., Hu Z., Xie Q., Zhong Q., Wei J., Yan H., *Journal of Alloys and Compounds*, (2014), *582*, 273-276.

CHAPTER V

CONCLUSIONS AND FUTURE SCOPE

This chapter summarizes the key results and conclusions obtained from the above mentioned experimental results. In addition, thesis ends with the future scope and related issues of single-site and double-site doped BFO ceramics.

5.1 CONCLUSIONS

In the present report, the detailed and systematic study of structural, micro-structural, dielectric, magnetic as well as optical properties of $Bi_{1-x}A_xFeO_3$ (A: Ba, La, Ho; $0<x<0.2$) and $Bi_{0.9}A_{0.1}Fe_{1-y}Ti_yO_3$ ($0<y<0.2$) ceramics have been performed. $Bi_{1-x}A_xFeO_3$ (A: Ba, La, Ho; $0<x<0.2$) and $Bi_{0.9}A_{0.1}Fe_{1-y}Ti_yO_3$ ($0<y<0.2$) ceramics were synthesized by sol gel auto-combustion technique. The main observations/findings in the present thesis are highlighted below:

The X-ray diffraction analysis revealed that undoped BFO crystallized in rhombohedral symmetry with space group *R3c*. A compositional phase transformation from *R3c* to *Pnma* was observed for La^{3+} doped BFO at x=0.1 with crystallite size in the nano range of 29–43 nm. Rietveld refinement was used to verify the crystal structure of prepared ceramics. Thermodynamic analysis on the improved phase stability of BFO upon La substitution showed that higher bond strength of I_{La-O} over I_{Bi-O} bond might be instrumental in encouraging the stable perovskitic phase formation. FESEM shows the aggregated grains for BFO together with a grain size ~422 nm. The size of grains decreased for La^{3+} doped BFO ceramics, indicating the suppression of oxygen vacancy (Vo^{2+}) concentration and consequently inhibits the grain growth. Improved dielectric properties with less loss were observed in Bi-site substitution. ε increases for La^{3+} doped BFO at x=0.1, whereas, $tan\ \delta$ follows the reverse trend with subsequent increasing of La^{3+} substitution and its minimum value was ~1.9 for x=0.1 at 100Hz. Moreover, the antiferromagnetic Neél temperature (T_N) is found to decrease towards lower temperature side from 380 °C to 362 °C with La^{3+} substitution. The magnetic studies showed that La^{3+} substitution enhanced the magnetization of BFO ceramics and attains the maximum value of 0.318 emu/g at x=0.1. In addition, FTIR spectra showed the distortion in Fe-O and Bi/La-O bond lengths with La^{3+} substitution and their calculated values are consistent with values calculated from Rietveld analysis. The optical spectra of La^{3+} substituted samples showed a prominent blue shift in the energy band gap.

Ho^{3+} substitution in BFO results in a structural transition from rhombohedral (*R3c)* to orthorhombic (*Pnma)* with crystalline size in the nano range of 37–43 nm. The calculated crystalline size and c/a ratio is found to be reduced with Ho^{3+} substitution. Improved dielectric properties with very less loss have been observed with Ho^{3+} substitution. The dielectric losses observed in BFO (~105) was greatly reduced for Ho^{3+} substituted ceramics with composition

x=0.1 (~5.9) at 100Hz. Detailed magnetic study showed that values of M_r and M_{max} increase with the increment of Ho^{3+} doping content and its maximum values are 0.0122 emu/g and 0.360 emu/g for x=0.1, respectively. However, the larger values of H_c in nanoparticles may be related to their magneto-crystalline anisotropy. In addition, Ho^{3+} doping arising electronic transitions of $^5F_3$-$^5I_8$ at 484 nm, $^5F_4$ and $^5S_2$ to $^5I_8$ around 547, 558 and 576 nm which are detected in PL spectra. The optical studies showed crystal field and charge transfer transitions along with the optical band gap variation in the range 2.18–2.10 eV.

No structural phase transformation is observed with Ba^{2+} substitution, but the particle size gets affected. The areal particle size decreases initially for x=0.1 and then it increases on further increasing Ba^{2+} doping content. It is also is evident from the dielectric behavior that the electrical conductivity of Ba^{2+} substituted ceramics are large as compared to BFO ceramics. T_N shows considerable frequency dispersion with the addition of Ba^{2+} ion. Moreover, doped nanoparticles exhibit larger magnetization (~1.41 emu/g) at room temperature, whereas the electric polarization shows a reverse trend. On the other hand, the optical analysis showed that the band gap of Ba^{2+} ions doped BFO nanoparticles are tuned within the visible spectrum.

Structural refinement reveals that $Bi_{0.9}La_{0.1}Fe_{1-y}Ti_yO_3$ ($0.0 \leq y \leq 0.20$) has crystallized in orthorhombic crystal symmetry with the non-centrosymmetric space group *Pnma*. FESEM shows the aggregated grains of $Bi_{0.9}La_{0.1}FeO_3$ ceramics together with a grain size < 0.1 μm. However, the grain size of co-doped ceramics was observed to decrease with the addition of Ti^{4+} ions, directly indicates that Ti^{4+} ions act as grain growth inhibitor. The maximum obtained value of remnant polarization is 0.289 emu/g for y=0.05 at 11kV/cm. Ti^{4+} substitution increase dielectric constant of the co-doped ceramics. Whereas, dielectric loss (*tan δ*) was observed to decrease over the whole frequency range which indicates the rise in electrical resistivity and the obtained value of resistance is of the order of ~10^7 Ω. The expected dielectric anomaly (T_N) was also found to be shifted towards the lower temperature with increase in Ti^{4+} doping ions in ceramics. The obtained value of magnetization (M_{max}) is 2.21 times higher than $Bi_{0.9}La_{0.1}FeO_3$ ceramics and it is maximum for y=0.10. The optical analysis showed that the energy band gap varies from 2.15-2.19 eV, in La^{3+} and Ti^{4+} ions co-doped BFO nanoparticles are tuned within the visible spectrum.

Ti^{4+} substituted $(Bi_{0.9}Ho_{0.1})(Fe_{1-y}Ti_y)O_3$ ceramics ($0.0 \leq y \leq 0.20$) were also successfully synthesized without changing their orthorhombic symmetry (*Pnma*). The increase in unit cell

volume and lattice constants distributed strongly affects the dielectric and magnetic properties. The decrement in grain size directly indicates that Ti^{4+} ions act as grain growth inhibitor. ε increases and *tan* δ decreases with increase in Ti^{4+} substitution. Detailed magnetic study showed that values of M_{max} increase with the increment of Ti^{4+} substitution and its maximum value is 1.45 emu/g for y=0.10. The optical studies showed crystal field and charge transfer transitions along with the optical band gap variation in the range 2.05–2.13 eV.

Rietveld refinement reveals a transformation from rhombohedral *"R3c"* to tetragonal "*Pnma"* with the Ti^{4+} doping content at y=0.05. The value of lattice parameter a (Å) and unit cell volume V ($Å^3$) is found to decrease with the substitution of Ti^{4+} ions. FESEM reveals the elongated spherical shaped grains. The decrease in the size of grains suggests that Ti^{4+} doping has an obvious effect on the inhibition of grain growth. Both ε and $tan\delta$ are observed to increase at y=0.05, whereas a drop with further increase in Ti^{4+} substitution is observed. The observed anomaly in dielectric constant corresponds to an antiferromagnetic Néel temperature (T_N) and it shifts with the substitution of Ti^{4+} ions. The electrical conductivity of $(Bi_{0.9}Ba_{0.1})(Fe_{1-y}Ti_y)O_3$ ceramics obeys the Arrhenius law and calculated activation energies are 0.744 eV, 0.994 eV, 0.505 eV, 0.841 eV and 0.473 eV for y=0.0, y=0.05, y=0.10, y=0.15 and y=0.20 nanoparticles, respectively. The value of P_m and P_r is found to be increase after substitution of Ti^{4+} ions, indicates a reduction in oxygen vacancies due to Ti^{4+} substitution. The obtained value of magnetization (M_{max}) is 1.7 times higher than $Bi_{0.9}Ba_{0.1}FeO_3$ ceramics and it is maximum for y=0.05 composition. All compositions exhibit strong absorption of light in visible region with energy band gap in range of 2.09 to 2.16 eV.

5.2 FUTURE SCOPE

The observed electric and magnetic properties of doped and co-doped BFO ceramics are so efficient but still its availability in device applications is obscure. However, the optical properties shows that energy band gap varies from 2.04-2.65 eV in doped and co-doped BFO ceramics, are tuned within the visible spectrum and can be utilized in photocatalytic decomposition of organic contaminants in the future and also have potential applications in photonic or optoelectronic devices.